Advancing Super-Resolution Imaging: Innovations for Enhanced Single-Molecule Localisation Microscopy

Matthew Chi-Kan Tang

University of Oxford

Nuffield Department of Medicine

Linacre College

A thesis presented for the degree of

Doctor of Philosophy

Statement of Authorship

All work in this thesis is my own, unless stated otherwise.

The results from Chapter 4 have also been published in:

Qiu, H., Tang, M. C., Roberts, S. K., Li, G., Su, R., Martin-Fernandez, M. L., Clarke, D. T., Liu, S., Liu, X. & Wang, L. Reinforced optical cage systems enable drift-free single-molecule localization microscopy. *Communications Engineering* (2025).

A figure in Chapter 3 has been adapted from the above work which is permitted under a Creative Commons Attribution 4.0 International License (https://creativecommons.org/licenses/by/4.0/). All other work is my own. Where the work of other authors is mentioned, the above publication is cited appropriately.

Acknowledgements

I would like to thank The University of Oxford's Interdisciplinary Bioscience Doctoral Training Programme (now known as ILESA) and the BBSRC for funding this project, and for all the fantastic training opportunities that they have offered. I would also like to thank the various institutions and organisations that have hosted me throughout my DPhil without whom, none of my research would have been possible.

First, thank you to my supervisors at The Rosalind Franklin Institute, Professor Raymond Owens and Dr. Siva Ramadurai for all the help, advice, and support throughout the DPhil. Particular thanks also go to Professor Owens' Nanobody Group at the Rosalind Franklin Institute for running a great lab space and being welcoming.

Second, thank you to Dr Chen Qian at AstraZeneca for supervising, hosting, and helping me out during my internship. I would also like to thank the Phenomics group and QuBi for the various helpful discussions and for having a great working environment.

Finally, thank you to Professor Lin Wang for his help and supervision, as well as Octopus, the Lasers for Science Division, and the Central Laser Facility for hosting me for the majority of my DPhil. It has truly been an excellent experience doing my DPhil within the CLF and LSF and I am deeply grateful for all the assistance, colloborations, and opportunities over the years. Among the Octopus staff, particular thanks go to Hao, Chuan, Connor, Yanru, Sarah B, Ellie, Alix, Stan, Chris, Ben, and Dan with whom I have worked closely at various points throughout the DPhil.

Within the LSF, enormous thanks go to everyone in the G28 early careers office, including past members: Rohan, Holly, Chuan, Yanru, Sever, Sarah B, Timur, Ellie, Jenny, and Jaunti, and current members: Megan P, Oliver, Emily, Alix, Tiff, Bruce, Megan Pr, Kirstie, and Alasdair. My DPhil simply would not have been the same without the support, conversations, cakes, coffee, and distractions in the office!

Outside of work, thank you to Ivy and Ting An for the board games and tabletop games, Evgenii Berestiuk for all the MMO adventures, and Kim for the invaluable friendship

and support from a distance. It would have been a far more stressful DPhil without you guys.

Unfathomable gratitude goes to my partner, Natalie, for being by my side from the start of the DPhil to its end and for helping me along during its lowest points. Thanks to you, this journey has been made less arduous and infinitely more valuable. Thank you also to her family for the visits, support, and company throughout.

Finally, thank you to my family. Without all the valuable lifelong lessons and support, I would have never stood at the starting line of this DPhil, let alone completed it.

Contents

List of Figures

List of Tables

Abstract

Single-molecule localisation microscopy is a super-resolution microscopy method capable of attaining resolutions beyond the diffraction limit of light. Its application to the life sciences has led to unique insights into the functions and organisation of biological molecules in cells.

Despite its benefits, its routine usage faces numerous challenges. This thesis examines several important aspects of these, namely: the detrimental effects of sample drift, insufficient resolution to resolve many different types of protein complexes, the perturbation of native cellular states through fluorescent labelling, and the low signal-to-noise ratio that obfuscates single-molecule detection.

To address sample drift, a novel microscope design is presented and its sample drift is quantified, demonstrating negligible mechanical drift and obviating the need for drift correction methods. This reduces experimental complexity and improves the accessibility and reliability of single-molecule localisation microscopy.

Advances in enhancing resolution are presented through implementing mirror-enhanced fluorescence in combination with a denoising algorithm. Using both technologies conferred an approximately 15 nm enhancement in resolution, allowing a wider range of biological molecules to be visualised.

Different methods to label proteins with nanobodies are compared, thereby outlining the detrimental effects of popular fluorescent labelling methods, as well as highlighting that different experimental outcomes can be achieved by altering the location of the amino acid used to conjugate nanobodies to dyes.

Finally, an evaluation and characterisation of a novel deep learning denoising algorithm is presented, demonstrating that it improves signal-to-noise ratio and resolution for certain types of noise. This evaluation aids other researchers aiming to use denoising algorithms, and underlines the strengths and limits of a state-of-the-art denoising methodology.

Overall, advances to the instrumentation, fluorescent labelling, and software that underpin single-molecule localisation microscopy are presented in this thesis. These advances are expected to aid further methods development, as well as increase the reproducibility and accessibility of applying single-molecule localisation microscopy to investigate biological systems.

1 Introduction

The ability to visualise life at the microscopic level has been paramount in advancing the life sciences. Developments in microscopy methods and technology have expanded and enhanced the toolbox with which researchers investigate biological systems, providing deeper insights into fundamental biology, as well as aiding in the development of novel technologies that benefit public health and the medical sciences. Fluorescence microscopy, in particular, has been key in understanding the organisation, function, and dynamics of biological molecules.

However, the resolution of fluorescence microscopy methods, such as total internal reflection fluorescence microscopy, confocal microscopy, and light-sheet microscopy is physically limited by diffraction [1]. Consequently, the maximum achievable resolution is approximately 200–250 nm [2].

The diffraction limit restricts the available information at the molecular and subcellular levels since many biological structures, such as organelles, viruses, and protein complexes, are smaller than the diffraction limit. While structural biology methods, including X-ray crystallography and cryogenic electron microscopy, achieve molecular resolution (Fig. 1.1), fluorescence microscopy confers high molecular specificity, facile visualisation of molecules inside of cells, and insights into dynamics. The diffraction limit, therefore, restricts the unique strengths of fluorescence microscopy.

1.1 Overview of super-resolution light microscopy

Efforts to overcome the diffraction limit eventually succeeded with the development of super-resolution microscopy, dramatically improving resolutions to approximately 10 nm—a 20-fold increase to that attainable with diffraction-limited methods—thereby opening up new opportunities to investigate biological systems inaccessible with previous methods [2–4] (Fig. 1.1). Indeed, the improved resolution has provided new insights into the functions of biological structures with sizes below that of the diffraction limit

[5]. Examples include the distribution and role of the HIV envelope protein in fusing with host cells, the molecular organisation of neurotransmitters in synapses, and the morphology and dynamics of the peripheral endoplasmic reticulum [6–8].

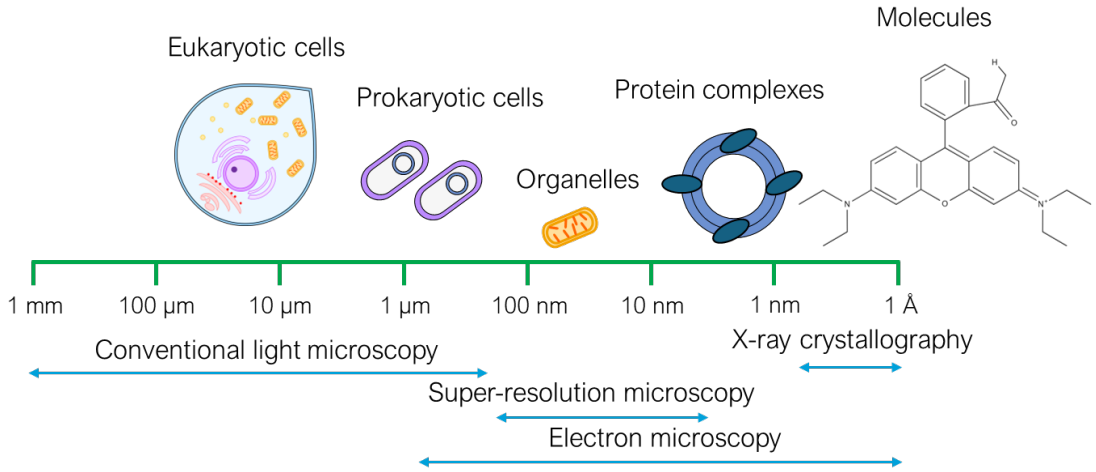

Fig. 1.1: **The approximate length scales of biological systems**. A molecule of rhodamine is depicted as an example.

Super-resolution microscropy encompasses several methods—all of which achieve resolutions beyond the diffraction limit—and can be classified under three broad groups, depending on their underlying principles. The first group, structured illumination microscopy (SIM), relies on illuminating a fluorescently labelled sample with a well-defined periodic pattern, generating a Moiré image that encodes lower spatial frequency information about the sample [9, 10]. Through mathematical recovery of the original sample structure [11], resolutions of up to 100 nm can be obtained.

Expansion microscopy involves the use of a swellable polymer to expand physcially a fluorescently labelled cell or tissue [12]. As a result, structures that were previously close together are brought further apart, allowing them to be resolved. Resolutions of 25 nm can be achieved if the sample is expanded iteratively [13]. However, the chemical treatment applied to cells is necessarily disruptive, limiting expansion microscopy to fixed cells only.

The final major family of super-resolution techniques achieves resolutions beyond the diffraction limit by exploiting the photophysical properties of fluorophores to modulate fluorescence emission. This modulation can be deterministic or stochastic, depending on the mechanism. Deterministic methods use a principle known as RESOLFT (reversible saturable optically linear transitions) [14]. Here, a pair of co-aligned lasers is focused at

the sample where the first laser induces fluorescence excitation while the second laser has zero intensity at its centre and is tuned to a wavelength such that it induces a transition to a nonfluorescent state from the excited state [14, 15]. The diameter of the central zero intensity of the second laser is smaller than the diffraction limit of light, and so scanning this illumination pattern across the sample produces a super-resolution image [16]. The most popular realisation of the RESOLFT concept is stimulated depletion emission (STED) microscopy where fluorophores outside of the central spot are de-excited via stimulated depletion [17].

Single-molecule localisation microscopy (SMLM) methods share the same principle as deterministic methods: transfer all but a fraction of fluorophores to a nonfluorescent state. Instead of using beam shaping and optical methods, however, SMLM uses standard epifluorescent illumination and relies on stochastic processes to ensure only a subpopulation of fluorophores are imaged [18]. Tens of thousands of frames are then collected, resulting in the temporal separation of fluorescent signals. From each frame, the fluorophore positions can be localised with precision beyond that of the diffraction limit by fitting a Gaussian function. Collating all the fluorophore localisations then forms a super-resolution image (Fig. 1.2**b**).

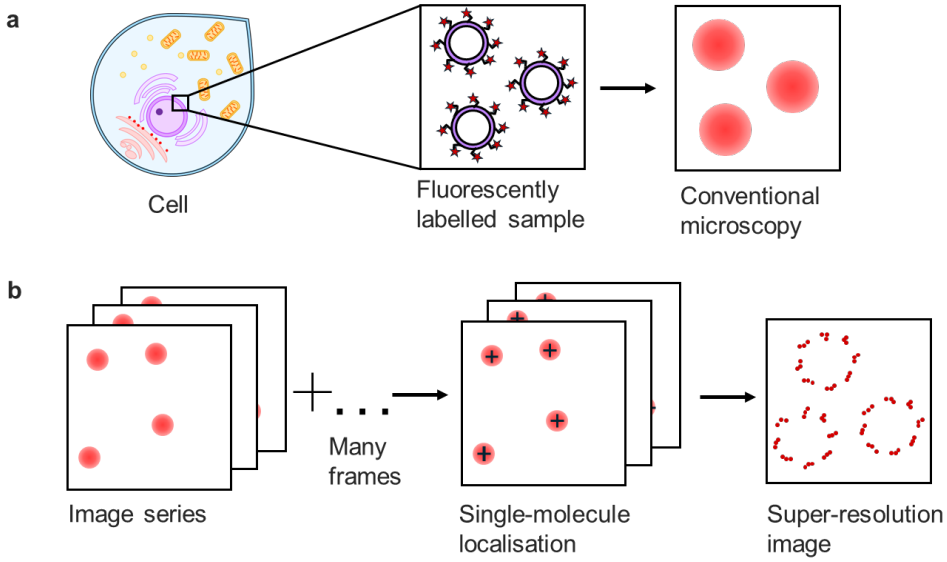

Fig. 1.2: **A comparison between conventional microscopy and SMLM. a** Illustration of the outcome of diffraction-limited imaging of a fluorescently labelled sample with dimensions smaller than the diffraction limit. **b** Illustration of the principle of SMLM.

SMLM techniques differ in the mechanism by which a nonfluorescent state is induced. Stochastic optical reconstruction microscopy (STORM) uses a combination of high-

power laser illumination and a reducing buffer to induce photoswitching in organic dyes [19, 20]. Photoactivated localisation microscopy (PALM) uses photoactivatable proteins or dyes that can be photoinduced into a fluorescent state [21, 22]. Finally, DNA-PAINT relies on diffusion and binding between a pair of oligonucleotides, one of which is conjugated to the reagent used to label a structure while the other is conjugated to a fluorescent dye [23].

With SMLM, resolutions of 20–50 nm are attainable [24]—higher than SIM and comparable to STED and expansion microscopy. However, there is considerable complexity for SMLM in image reconstruction and post-processing [4], as well as greater restrictions in the choice of fluorophore. SMLM, nevertheless, features a relatively straightforward optical setup compared to STED, has greater potential for live-cell imaging than expansion microscopy, and is supported by a range of open-source software [25, 26] which overcome some of the computational complexity associated with the method. Because of these factors, the focus of this thesis, hereon, will be on SMLM.

1.2 Challenges facing single-molecule localisation microscopy

Despite the impressive resolution achievable with SMLM methods, these techniques still face several challenges that limit the localisation precision and accuracy. In SMLM, localisation precision is defined as the spread of the estimated fluorophore positions while localisation accuracy is defined as the discrepancy between the true position of the fluorophore and its estimated position [18]. A measurement with high precision and low accuracy would result in an estimate of the flurophore location far from the true position but with low variance (Fig. 1.3). Likewise, a measurement with low precision and high accuracy would result in the estimated position being near the true position but with high variance (Fig. 1.3). Localising fluorophore signals with both high accuracy and high precision is crucial for extracting valid and reliable biological information from SMLM.

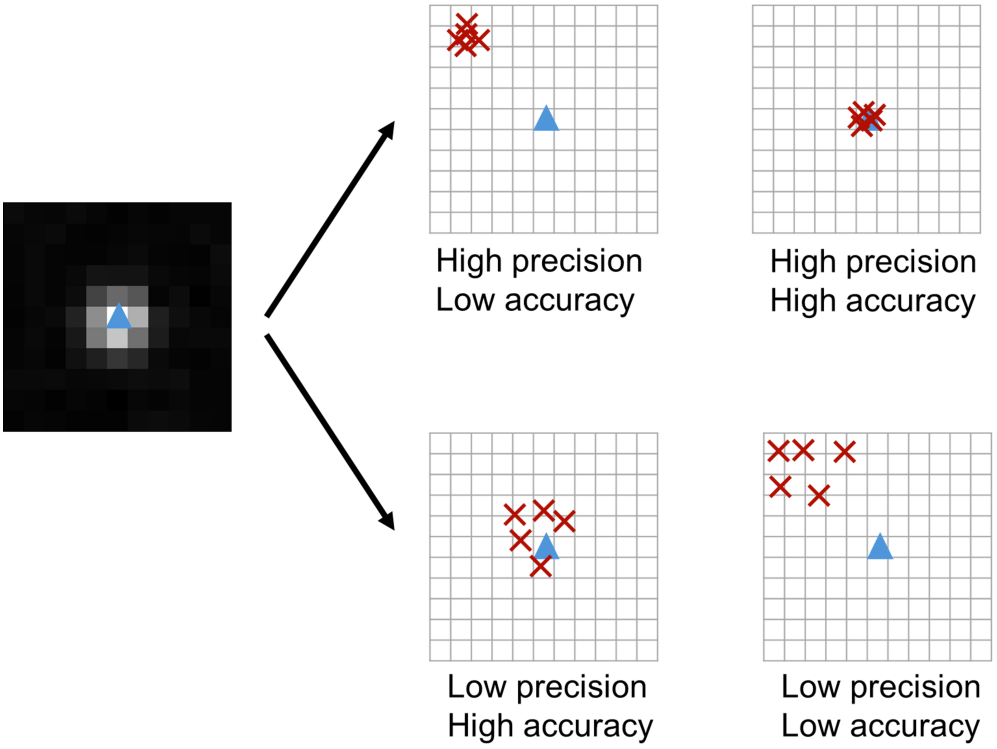

Fig. 1.3: **Illustration of localisation precision and localisation accuracy in SMLM.** An 11 pixel x 11 pixel image of a single-molecule is shown along with the effects of varying localisation precision and localisation accuracy on the estimation of the position of the fluorophore. A blue triangle is used to illustrate the true position of the fluorophore while red crosses are used to indicate estimations of its position.

Numerous experimental factors limit the attainable localisation precision and localisation accuracy in SMLM. These limitations, in turn, increase experimental complexity, reduce reproducibility, decrease broader access beyond specialised laboratories, and hinder biological interpretation of super-resolution data. First, the attainable resolution is, in part, limited by localisation precision, and so is insufficient to be used as a complementary technique to traditional structural biology methods. Second, the long acquisition times necessitated by SMLM methods results in substantial sample drift, compromising image resolution, image fidelity, and decreasing localisation accuracy. Third, conventional fluorescent labelling methods often introduce fluorescent proteins or enzymatic tags as fusion proteins, which can produce experimental artifacts [27, 28], while labelling endogenous structures with antibodies introduces a linkage error of 10–15 nm per antibody [29], worsening localisation accuracy. Finally, the signal-to-noise ratio of SMLM image sequences is often hampered by shot noise, unspecific labelling, and photobleaching [18], all of which are exacerbated in STORM and PALM due to the high laser powers required. The worsened signal-to-noise ratio can lead to imaging artifacts

that obscure accurate interpretation of biological information.

1.2.1 Improvements in hardware

Increasing the resolution in SMLM to less than 20 nm is highly sought after to narrow the resolution difference between fluorescence microscopy and structural biology methods. While X-ray crystallography and cryogenic electron microscopy attain molecular resolution, the available *in situ* biological information is limited by the lack of molecular specificity and the need to average particles or crystallise proteins [30]. Therefore, improving the resolution of SMLM would broaden the scope of biological molecules amenable to investigation using light microscopy, yielding novel insights into *in situ* molecular organisation and function.

To improve resolution, novel microscopy methods have been recently developed that combine different super-resolution imaging modalities. Examples of this include MINFLUX and SIMFLUX [3, 31]. The former combines principles from SMLM and STED while the latter combines concepts from SMLM and SIM. Combining super-resolution methods, however, requires complex optical systems or are only available as closed systems, increasing the cost of implementation and lowering accessibility [32, 33]. Instead, open-source methods that are compatible with existing optical configurations would be highly desirable. One example of this is mirror-enhanced fluorescence, an imaging configuration where a reflective layer is placed behind a fluorescent sample (Fig. 1.4**a**). The presence of the mirror enhances the fluorescence excitation and emission, increasing the number of photons collected by the objective lens [34]. Since the localisation precision in SMLM increases with a higher number of collected photons [18], the resolution is expected to increase with the implementation of mirror-enhanced fluorescence.

The phenomenon of fluorescence at metal interfaces has been characterised theoretically [35–37] and applied to nanometer-level single-molecule distance measurements [38, 39]. By contrast, applications of mirror-enhanced fluorescence to SMLM have been limited, with the sole application (at the time of writing) described by Heil *et al.* 2018 where mirror-enhanced fluorescence was characterised using antibody-labelled samples [40]. As previously described, the large size of antibodies introduces substantial linkage error to SMLM, thus limiting the resolution. Further investigation is, therefore, required to

exploit fully the resolution increase offered by mirror-enhanced fluorescence in SMLM. Nevertheless, mirror-enhanced fluorescence may offer a versatile platform with which to integrate other resolution-enhancing methods.

Besides resolution, the achievable resolution and performance of SMLM can also be hampered by sample drift (Fig. 1.4**b**), where the positions of fluorophores move during image acquisition, owing to the mechanical instability of the microscope [41] and temperature fluctuations, thereby worsening the localisation accuracy. Since SMLM achieves resolutions of 25–50 nm, even drift in the range of hundreds of nanometers—normally negligible in conventional fluorescence microscopy—is sufficient to blur the super-resolution image and obscure the sample structure (Fig. 1.4**b**). To address drift, several methods can be used to correct axial (z-axis) drift and lateral (xy-plane) drift. For example, a common method to correct axial drift is through active stabilisation of the focal plane using a piezoelectric-driven objective lens [42, 43]. Images can be captured throughout the SMLM image sequence and compared to the intensity of the first image to estimate the axial position. From this estimate, the z-position of the objective lens can be adjusted to maintain focusing of the sample.

Popular methods to correct lateral drift include the addition of fiducial markers to the sample, such as fluorescent beads [44], as well as the use of cross-correlation algorithms during post-processing [45]. Methods that use fiducial markers rely on their persistent emission throughout an image sequence. By tracking the lateral position of the markers, the drift trajectory can be quantified and used to correct the xy-localisations of fluorophores. Meanwhile, cross-correlation algorithms correct drift during post-processing by dividing the image sequence into a user-determined number of subsets and comparing fluorophore xy-localisations between the batches [45, 46].

While these methods can correct lateral drift, they are often marred by inconsistency in practice, resulting in tedious protocol optimisation for successful drift correction. For example, using fiducial markers requires additional sample preparation in which determining the appropriate concentration of fiducial markers is a challenging, trial-and-error process [47]. Imaging with a high density of fiducial markers may worsen signal-to-noise ratio since their fluorescence emission is often brighter than the fluorophores, thus

undermining the image quality of an SMLM experiment. Likewise, cross-correlation approaches require parameter tuning to determine the appropriate number of subsets into which to divide the localisation data and may perform poorly if tuned incorrectly. Cross-correlation approaches also assume the drift to be stable and gradual, and so may fail in the presence of abrupt drift. Overall, the additional experimental complexity introduced by drift correction methods decreases accessibility and increases experiment-experiment variation in SMLM, hampering reproducibility. There is, therefore, a need to develop methods capable of addressing drift without requiring additional hardware or experimentation to provide a platform for more consistent results.

1.2.2 Improvements in fluorescent labelling

Besides optics and instrumentation, the accuracy and reliability of SMLM data is also influenced by the choice of fluorophore and labelling method. More specifically, the resolution of SMLM depends on the localisation precision—affected by the number of collected photons [18]—and the fluorophore labelling density [48], both of which are directly affected by the fluorophore properties and the labelling procedure. Thus, the attainable biological information from SMLM depends strongly on the fluorescent labelling strategy.

Ideally, labelling methods should fulfil several criteria to ensure the downstream localisation data are accurate and amenable to valid biological interpretations [18]. First, the fluorophore should be specific to the molecule of interest. Second, the normal physiological state of the biological system should be preserved. Third, the fluorophore should be as physically small as possible to maximise accurate localisation. Finally, the molecule of interest ought to be tagged with exactly one fluorescent label to prevent multiple detections for the same molecule.

Common fluorescent labelling techniques including genetic fusion of the molecule of interest with a fluorescent protein [21], introducing the molecule of interest fused to a dye-reactive enzyme [49, 50], and direct immunolabelling of a molecule using antibodies [19, 51, 52], do not consistently satisfy the above criteria. For instance, fluorescent proteins have a small size, with diameters of 3 nm [53], but may aggregate or perturb physiological functions [54]; recent evaluations of Hsp104-fluorescent-protein fusions and

fluorescent proteins fused to bacterial flagellar motor proteins both demonstrated alterations to normal molecular behaviour [27, 28]. Similar concerns also apply to proteins fused to dye-reactive enzymes, such as the SNAP-tag and Halo-tag. While antibodies circumvent these problems by binding to endogenous structures, their large size of 10–15 nm produces a large linkage error. The fluorescent signal may, therefore, be recorded relatively far from the protein of interest [29]—particularly when using both primary and secondary antibodies—thereby decreasing localisation accuracy. The large systematic error introduced by antibodies also worsens the accuracy of any downstream spatial analysis methods, limiting biological insight. Furthermore, there can often be large variation in the specificity of commercial antibodies [55, 56], reducing the reproducibility of SMLM experiments.

The use of single-domain antibodies (nanobodies) has emerged as a labelling method to address the above concerns. These are a unique variant of antibodies produced by camelids and sharks that contain only a single variable heavy chain domain (Fig. 1.4**c**) [57, 58], resulting in smaller sizes ($\sim$ 2.5 nm), lower linkage error (Fig. 1.4**c**) [59], and higher localisation accuracy. Nanobodies also retain the advantages of antibodies, namely their high affinity for native proteins and amenability to dye conjugation, and so they have been increasingly used for fluorescent labelling in SMLM [60].

Despite these advantages, the widespread adoption of nanobodies for SMLM has been slow, owing to their limited availability for biological targets. While the use of anti-GFP nanobodies for SMLM has been widely reported [59, 61], the need to engineer cells to express GFP fusion proteins ablates a key advantage of nanobodies—their ability to bind endogenous molecules. As such, the best practices, challenges, and pitfalls are poorly outlined for labelling native structures with nanobodies for SMLM. In addition, cell fixation and permeabilisation remain the routine methods for nanobody delivery into cells [60–63]. Thus, better characterisation and investigation of the experimental outcomes of different live-cell-compatible labelling methodologies would be beneficial for the development of nanobody technology in SMLM.

1.2.3 Denoising in SMLM

Finally, the reliability of SMLM data can be worsened by a poor signal-to-noise ratio (SNR). Low SNR can result in worse localisation precision and may also lead to false positives (noise detected as a single-molecule signal) or false negatives (single-molecule signals that are missed), resulting in more artifacts and decreased localisation accuracy.

Noise in SMLM originates from a diverse array of sources that can be broadly divided into three categories (Fig. 1.4**d**). The first example is background fluorescence which is generated from out-of-focus cellular structures, as well as autofluorescence from residual transfection reagents and fixatives [64, 65]. Another example is unspecifically bound fluorophores which result in prominent non-uniform background fluorescence for STORM and PALM, and elevated background for DNA-PAINT [66]. Finally, different types of noise can arise from the cameras used to image single-molecules [67]. Camera noise sources include read noise, which is generated by the camera electronics; dark current noise, arising from thermally generated electrons; amplification noise, caused by the signal amplification process in EMCCD cameras; finally, shot noise arises from the stochasticity of photon emission and detection, causing statistical fluctuations in the number of photons that arrive at the camera [68].

Given the detrimental effects of noise in SMLM, the application of denoising algorithms to improve localisation precision and localisation accuracy is an attractive solution, particularly for live-cell imaging where concerns over phototoxicity necessitate low-power illumination and, therefore, poorer SNR [69]. To this end, several denoising methods for fluorescence microscopy have been developed [68, 70]. However, noise has a greater influence on the raw images from SMLM than those from conventional fluorescence microscopy [71], meaning that classical denoising algorithms may not generalise well to SMLM or may not generalise well between different SMLM samples [72].

In contrast, the application of deep learning may have greater potential for achieving generalisability. With deep learning, a denoising model may be trained using a supervised learning approach or an unsupervised learning approach. The former involves mapping an input to a known output while the latter does not require a known output

[73]. For denoising, supervised learning requires pairs of noisy and denoised images [74–76], thus imposing limitations for biological SMLM data since a denoised ground truth is rarely attainable. This problem is circumvented by unsupervised approaches where algorithms for image denoising rely on temporal redundancy between adjacent frames [77, 78] or spatial redundancy between adjacent pixels in the same frame [79, 80]. However, these approaches may not generalise well to SMLM given that images change rapidly between frames, reducing temporal redundancy, while using spatial redundancy alone discounts long-range temporal correlations which may improve denoising in time series data [81]. Furthermore, current deep learning denoising algorithms use convolutional neural network (CNN) architectures. These architectures have been widely applied to SMLM [82–85], but suffer from a low effective receptor field [86], meaning that they are unable to leverage all the available information in an SMLM dataset, as well as spectral bias [87], resulting in CNNs preferentially incorporating low spatial frequency information which can lead to oversmoothed images.

Recently, Li *et al.* 2023 [81] developed a denoising algorithm for SMLM named SRDTrans that aimed to address the issues highlighted above using a combination of spatial sampling and an unsupervised transformer network. Unlike CNNs, the receptive field of transformers uses the whole image [73], thus utilising all available spatiotemporal information in SMLM data to learn a more accurate denoising model. Moreover, SRDTrans has been designed with lower model complexity compared to other transformer networks [88–90], thus easing its wider adoption for SMLM.

Despite the merits of the deep learning architecture of SRDTrans, evidence of its effectiveness for biological data was not demonstrated by Li *et al.* 2023 [81]. For example, the denoising effectiveness was quantified by measuring the full width at half-maximum (FWHM) of microtubule line profiles before and after denoising as an indicator of image resolution. FWHMs of 188 $\pm$ 22 nm were recorded for microtubule filaments prior to denoising which disagrees with well-established literature values of 50–60 nm—from a 25 nm diameter in addition to antibody linkage errors—for microtubule FWHMs [51, 91, 92]. Additionally, microtubules are not ideal resolution standards as under-labelled—and hence, lower resolution—samples can give narrow FWHMs; the selection of filaments from which to evaluate resolution is also subjective, increasing the risk of biased analyses

[93, 94]. Examination of additional biological samples is needed for denoising evaluation and to ascertain the effectiveness of denoising across different types of noise in SMLM, particularly because of the heterogeneity of sources of noise.

Overall, a more rigorous assessment of the denoising ability of SRDTrans is required. The wider SMLM community has historically benefitted from transparent evaluations of localisation software [25, 26] and clustering algorithms [95]. Further, characterising the performance of SRDTrans may highlight the limitations and areas of improvement for further development of denoising algorithms, and may also demonstrate the feasibility of applying transformer architectures to SMLM since deep learning algorithms based on transformers have not yet been widely adopted.

1.3 Scope and organisation of the thesis

Several challenges in SMLM have been highlighted in the previous section (summarised in Fig. 1.4), all of which hinder the acquisition of reliable and accurate biological information, thereby decreasing reproducibility and limiting the acquisition of useful biological insight. A secondary effect of the highlighted challenges is the increased experimental complexity of SMLM and the need for a high level of expertise required to apply SMLM effectively, both of which decrease access for the broader biological imaging field.

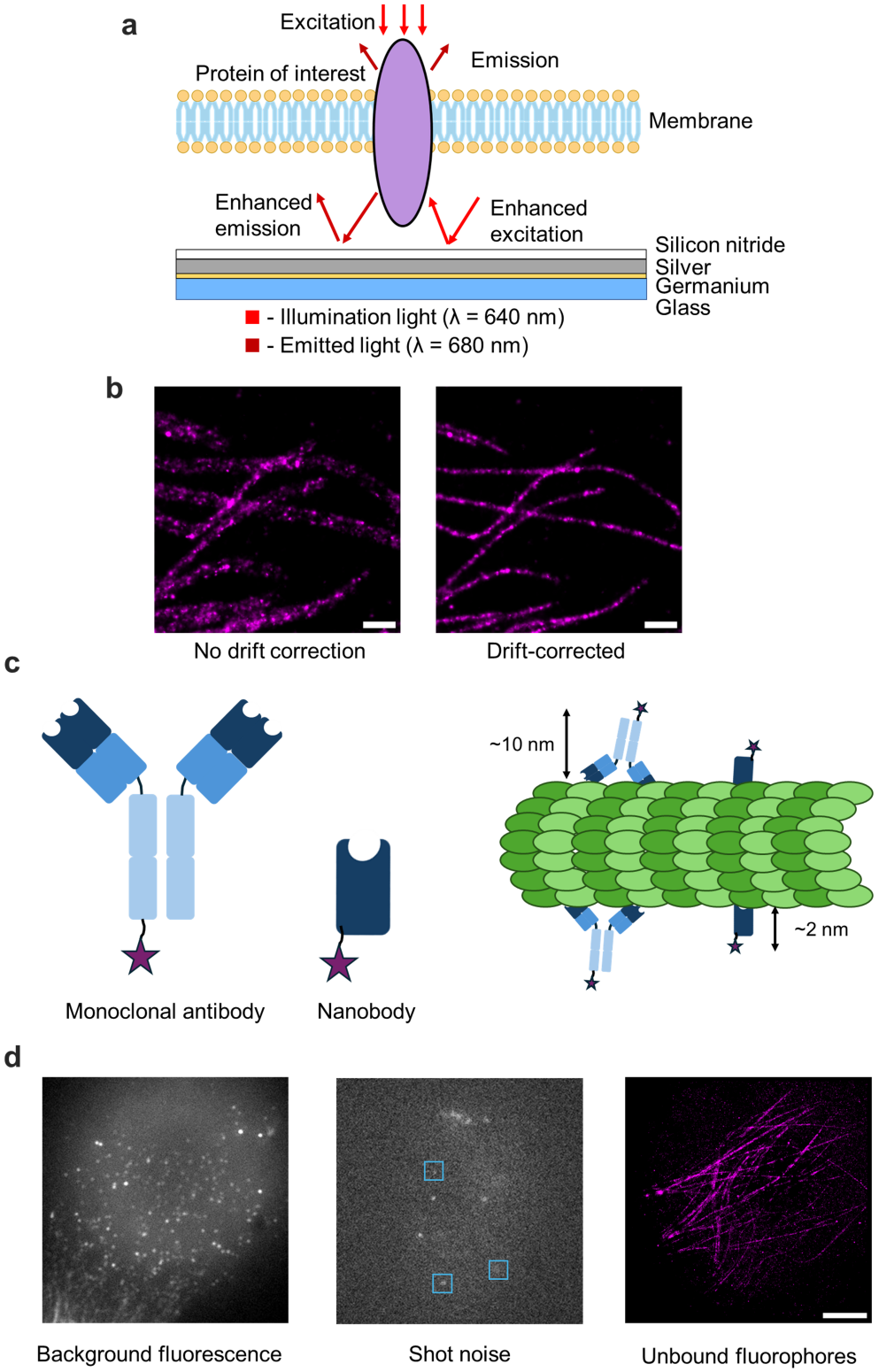

Fig. 1.4: **Project summary.** **a** Diagram of mirror-enhanced fluorescence. **b** The detrimental effects of sample drift in STORM images of immunolabelled microtubules; the filaments have a smeared appearance without drift correction. Scale bars: 1 µm. **c** The size difference between antibodies and nanobodies and the effects on labelling. The purple star represents a conjugated fluorophore. The linkage error for antibodies is shown above the semi-hollow green cylinder while the linkage error for nanobodies is shown below. **d** Different types of noise in SMLM. The areas enclosed by blue squares represent pixels where distinguishing between signal and noise is difficult due to shot noise.

As such, the aim of this project is to develop and evaluate new methods in each of the challenge areas highlighted above. More specifically, this project has the following aims:

1. Develop and quantify the drift of a novel microscope design capable of negating drift through its mechanical construction alone, obviating the use of drift correction methods and enabling high localisation accuracy to be achieved with simpler experimental workflows.
2. Implement mirror-enhanced fluorescence as a photonic platform for SMLM to increase the localisation precision and achievable resolution.
3. Assess the labelling efficiency of labelling intracellular proteins in live cells using nanobodies, as well as different nanobody-dye conjugates.
4. Evaluate the denoising performance of SRDTrans across a range of biological samples and different types of noise.
5. Apply the above developments through SMLM imaging of a range of biological samples.

It is anticipated that these developments will both advance the technologies for SMLM and provide informative guidelines for current technologies, thereby facilitating the acquisition of more reliable, more accurate, and easier-to-interpret SMLM data, all of which will aid in gaining novel biological insights.

1.3.1 Organisation of the thesis

The remainder of this chapter details the biological samples that are used for benchmarking throughtout the thesis. Chapter 2 provides a detailed overview of STORM—the primary modality of SMLM used in this work—and the methods with which resolution and drift are quantified. Methods for extracting quantitative information from localisation data and denoising methods are also introduced. Chapter 3 is a comprehensive description of the experimental methodologies. In Chapter 4, the drift quantification of a novel microscope design is presented, addressing Aim 1. Chapter 5 describes the implementation of mirror-enhanced fluorescence and attempts to increase the resolution of SMLM, addressing Aim 2. In Chapter 6, an evaluation of the application of different

nanobody labelling methods to SMLM is presented (Aim 3). Chapter 7 is a detailed evaluation, characterisation, and expansion of SRDTrans (Aim 4). Finally, Chapter 8 describes the application of SMLM to investigate the internalisation of SARS-CoV-2 spike protein.

1.4 Biological Imaging Applications

To evaluate potential improvements from new technologies, a range of biological structures will be imaged, including well-characterised reference standards, as well as samples without a well-known structural characterisation. The following section contains a brief description of each sample and its utility for benchmarking in SMLM.

1.4.1 Microtubules

Microtubules are filamentous polymers that consist of α-tubulin and β-tubulin subunits and form part of the cytoskeleton in eukaryotic cells. Microtubules have a diameter of approximately 25 nm [96, 97], and so additional structural insights can be gained through SMLM compared to diffraction-limited imaging.

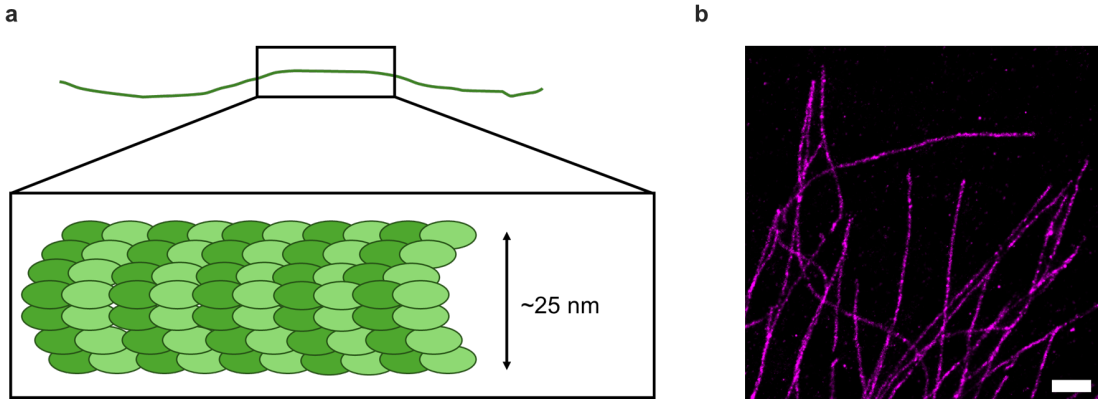

Fig. 1.5: **The structure of tubulin.** **a** Cartoon representation of a zoomed-in view of a semi-hollow microtubule filament. **b** Super-resolution image of microtubules in HeLa cells immunolabelled with antibodies conjugated to Alexa Fluor 647 acquired using STORM. The scale bar is 1 µm.

Furthermore, their long and continuous filaments are easily identifiable in an SMLM reconstruction (Fig 1.5**b**) and are, therefore, conducive to visual assessments of image quality. While microtubules do not often appear as smooth filaments in SMLM due to the unevenness of labelling, they nonetheless serve as quick and effective indicators of image fidelity deterioration from sample drift or labelling errors. For example, filaments

will appear smeared because of drift and will appear fragmented if the fixation process has affected their structural integrity [98]. As such, assessments of sample drift and denoising in later chapters will include microtubules.

1.4.2 Nuclear pore complexes

Nuclear pore complexes (NPCs) are large protein assemblies situated on the nuclear membrane that mediate translocation of molecules into and out of the nucleus. Structurally, NPCs consist of approximately 500 proteins arranged in a cylindrical array [99]. Out of these proteins, nucleoporin Nup96 is particularly well-suited for fluorescent labelling; Nup96 is arranged in two eight-cornered ring structures—a cytoplasm-facing ring and a nucleoplasm-facing ring with each corner containing two copies of Nup96 12 nm apart, resulting in a total of 32 copies of Nup96 per NPC [100]. 16 copies can be visualed in a 2D SMLM experiment. The diameter of the ring is approximately 120 nm for *Homo sapiens* (Fig. 1.6**a**) [101].

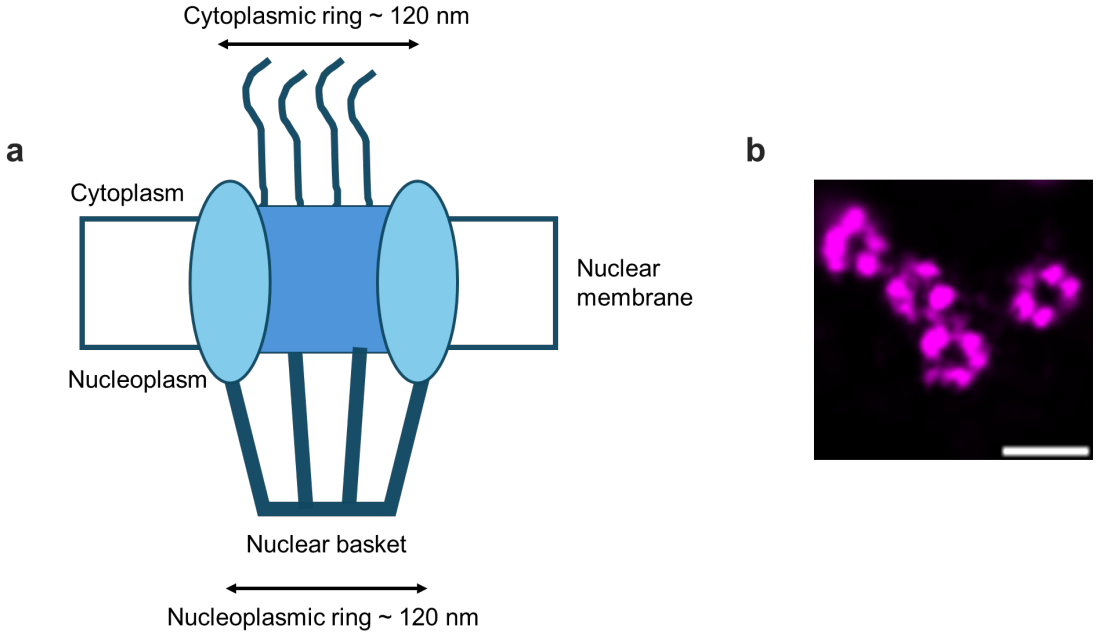

Fig. 1.6: **The structure of nuclear pore complexes.** **a** Cartoon representation of the vertical cross-section of a nuclear pore complex embedded in the nuclear membrane. **b** Super-resolution image of nuclear pore complexes in U2OS cells where nucleoporin 96 (Nup96) is labelled with Alexa Fluor 647. The scale bar is 1 µm.

The eight-fold symmetry of the ring is, therefore, discernible in SMLM (and other super-resolution methods) but indiscernible in diffraction-limited microscopy. Thus, the extent to which the eight discrete corners of the rings can be visualised serves as a reference

standard for image resolution (Fig. 1.6**b**) [93]. NPCs also permit facile visualisation of resolution enhancement beyond conventional SMLM since the two Nup96 subunits in each corner are better resolved with improved resolution [102]. Finally, similar to microtubules, NPC rings will appear smeared if image fidelity has been degraded by drift and will not be visible at all if the SNR is poor.

1.4.3 Vimentin

Vimentin is an intermediate filament that has a diverse array of cellular functions [103]. The diameter of vimentin is approximately 10 nm [104] which is beyond the resolution of SMLM but additional insights can still be gained compared to conventional microscopy.

Similar to microtubules, the filaments are easily identifiable in SMLM. Thus, the ability to resolve distinct filaments serves as a visual readout of labelling efficiency, for example from using a dye-conjugated anti-vimentin nanobody. There has also been a renewed interest in the cellular function of vimentin, with recent work highlighting its role in cancer metastasis, pathogen responses, and wound healing [105, 106]. However, vimentin imaging thus far has typically involved fixed cells [107, 108]. Thus, improvements in nanobody labelling may facilitate further functional insights into vimentin.

1.4.4 The internalisation of SARS-CoV-2 spike protein

SARS-CoV-2 is an RNA virus responsible for the COVID-19 pandemic. Like other viruses, its mechanism of infection relies on successful viral entry into cells through receptor binding [109]. For SARS-CoV-2, virus uptake is initiated by interactions between the viral spike protein and angiotensin-converting enzyme 2 (ACE-2) receptor at the cell surface [110]. Internalisation then proceeds along two different pathways. If transmembrane protease, serine 2 (TMPRSS) is present, the spike is cleaved, exposing a fusion peptide that facilitates entry into the cell [111, 112]. If TMPRSS is absent, internalisation occurs through clathrin-mediated endocytosis, resulting in spike protein cleavage in endosomes by Cathepsin L [113, 114].

Despite the extensive characterisation of SARS-CoV-2 entry and internalisation using biochemical and structural biology methods [110], there are fewer studies that examine

the molecular organisation of ACE-2 and spike protein during internalisation, particularly at the resolutions achievable through SMLM. Moreover, there is an increasing awareness that oligomerisation of ACE-2 and spike protein plays a crucial role in internalisation [115]. Thus, compared to microtubules and nuclear pore complexes—which represent well-characterised one-dimensional and two-dimensional structures, respectively—the ACE-2 and spike interaction represents a biological system without a well-defined structure. Such a system is particularly informative for assessing technological improvements in SMLM since it more realistically resembles addressing a biologically driven research question where the cellular structure of the sample will likely be unknown *a priori*.

2 Theory

The purpose of this chapter is to outline the principles of single-molecule fluorescence and localisation that underpin the work to be presented in later chapters, as well as the principles behind the novel methods and the methods used to evaluate potential improvements. Henceforth, discussion will mostly be restricted to direct stochastic optical reconstruction microscopy (dSTORM) as this imaging modality is used for the majority of experimental data presented in the thesis.

2.1 Single-molecule fluorescence

Fluorescence is a process where a molecule emits light following absorption of light at a specific wavelength. Irradiation of a molecule excites an electron from the S_0 ground state to a higher energy state (Fig. 2.1) [116]. From this state, the molecule undergoes vibrational relaxation and solvent relaxation to the S_1 excited state where de-excitation occurs, resulting in emission of a photon. Because of vibrational relaxation and solvent relaxation, the emission wavelength is red-shifted relative to the absorption wavelength.

The majority of molecules cycle between the S_0 and S_1 states upon irradiation. However, it is possible for a molecule to relax to the ground state via intersystem crossing to the first triplet state, T_1, followed by quenching by molecular oxygen, O_2 (Fig. 2.1). This pathway is exploited in dSTORM to generate stable nonfluorescent, dark states, and induce photoswitching in fluorophores [24].

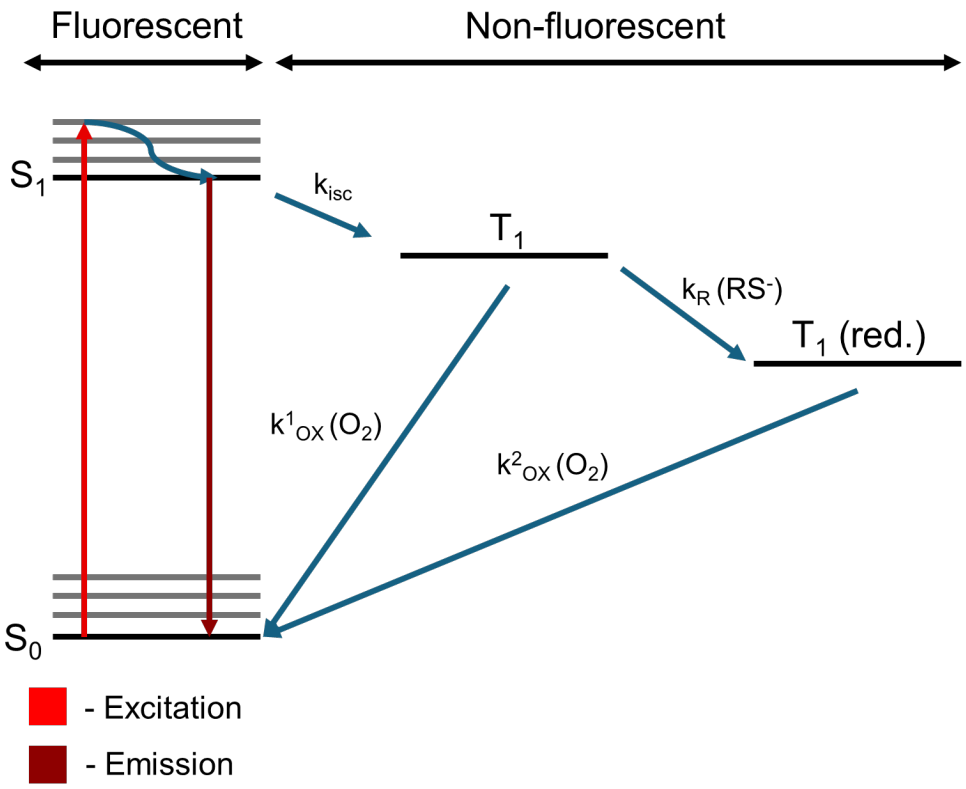

Fig. 2.1: **Jabłonski diagram of the underlying photochemistry in dSTORM**. S_0 and S_1 denote the ground state and first excited state, respectively. T_1 denotes the first triplet state while T_1 (red.) denotes the reduced triplet state. RS^- represents the thiolate anion. k is used to denote rate constants with isc, R, and OX used to abbreviate intersystem crossing, reduction, and oxidation, respectively.

Typically, a buffer containing an oxygen-scavenging system and a mild reducing agent is used in dSTORM. The oxygen-scavenging system prevents quenching of the triplet state by molecular oxygen—improving its photostability since reactive oxygen species are produced in reactions with molecular oxygen [117]. One example of such a system consists of catalase, glucose oxidase, and glucose. The following reactions are catalysed by this system:

$$C_6H_{12}O_6 + O_2 \xrightarrow{\text{Glucose oxidase}} C_6H_{10}O_6 + H_2O_2 \tag{2.1}$$

$$H_2O_2 \xrightarrow{\text{Catalase}} H_2O + \frac{1}{2}O_2\,. \tag{2.2}$$

Glucose is oxidised into D-glucono-1,5-lactone and hydrogen peroxide by glucose oxidase. Catalase then decomposes the hydrogen peroxide into water and oxygen. Notably, the oxygen produced from breaking down hydrogen peroxide is half the number of moles of oxygen that is input, resulting in a net decrease in oxygen.

The reducing agent is typically a thiol that facilitates the photoreduction of the triplet

state to form a stable dark state (Fig. 2.1) [118]. The chemical characteristics of the dark state differ depending on the fluorophore but generally, its formation involves disruption to π-electron conjugated systems. For example, the dark state of Alexa Fluor 647, the most popular fluorophore for dSTORM, is a nonemissive thiolate-dye adduct where the thiol group disrupts the chromophoric polymethine chain [119]. From this dark state, fluorophores return to the ground state via stochastic thermal elimination, or photoinduced elimination of the thiolate with a 405 nm wavelength laser, thus completing the photoswitching cycle [120].

The criterion of a stable dark state is a key factor in the performance of dSTORM [91]. More precisely, a fluorophore requires a low duty cycle which is given by:

$$\mathrm{DC} = \frac{\tau_{\mathrm{on}}}{\tau_{\mathrm{off}}} \,. \tag{2.3}$$

τ_{on} is the time the fluorophore resides in a fluorescent state while τ_{off} is the time the fluorophore resides in the dark state. The photoswitching kinetics, as well as the on-times and off-times, can be modulated by the laser power or reducing agent concentration [120, 121].

Fluorescent signals from fluorophores spaced at a distance below the diffraction limit are unresolvable in conventional fluorescence microscopy. However, with a sufficiently low duty cycle—and therefore, sufficiently stable dark states where $\tau_{\mathrm{off}} >> \tau_{\mathrm{on}}$—the majority of fluorophores will reside in a dark state. Since dark state lifetimes are on the order of 10s or 100s of seconds, imaging with frame rates of 10–100 Hz enables the temporal separation of fluorescent signal from fluorophores spaced closer than the diffraction limit. Modulation of photoswitching is, therefore, of critical importance to the outcome of a dSTORM imaging experiment and, in practice, restricts the number of available fluorophores since not all fluorophores are amenable to photoswitching.

2.2 Single-molecule imaging

Given a sample labelled with a fluorophore capable of photoswitching, and other desirable properties such as a high molar extinction coefficient (ϵ), the fluorescent signal is typically imaged with a standard, epifluorescent microscope (Fig. 2.2**c**) for a dSTORM

experiment. Here, the sample is plated on a glass coverslip, immersed with an appropriate buffer, and sandwiched between the coverslip and a coverslide. For imaging, the sample is illuminated evenly with high power density (>1 kW/cm^2) and the emission light is filtered by a dichroic mirror and bandpass filter—maximising detection efficiency—before being focused onto a camera by a tube lens.

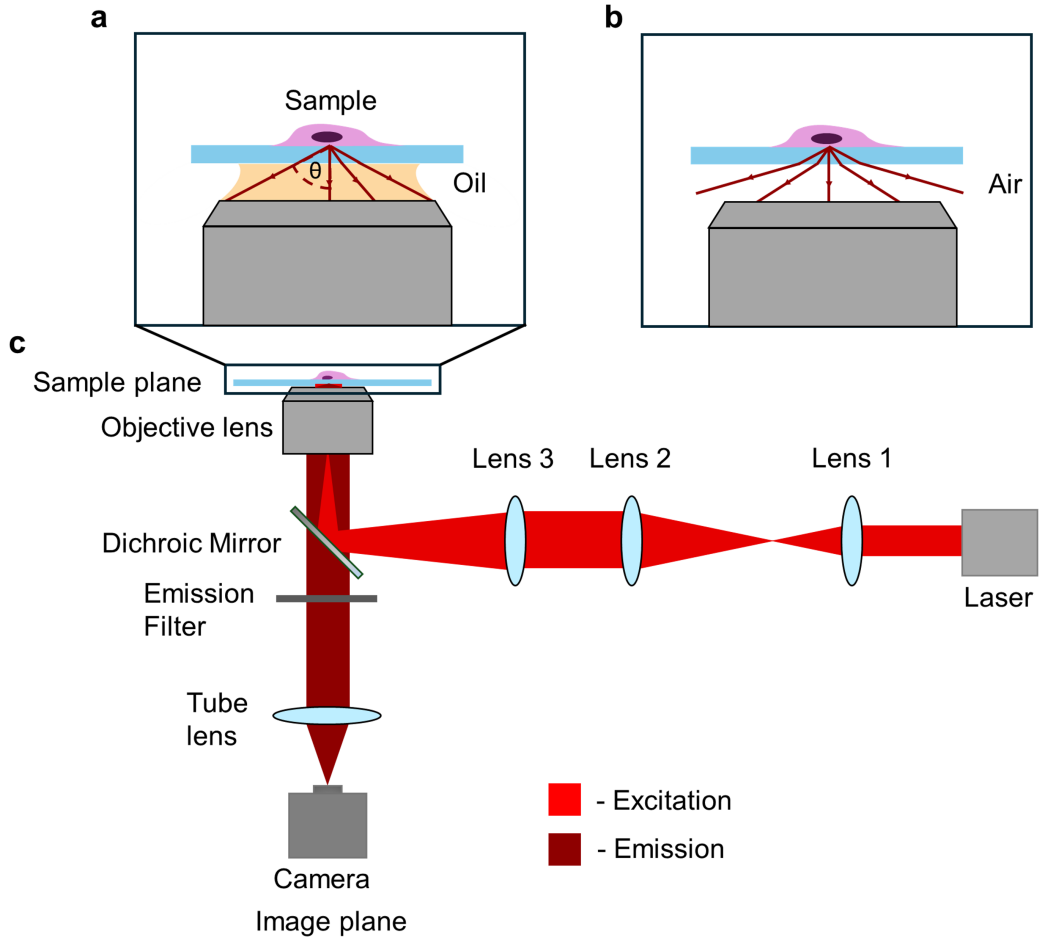

Fig. 2.2: **Simplified optical layout of a typical epifluorescent microscope for dSTORM. a** Ray tracing of photon detection by an oil-immersion objective lens for a sample plated on a glass coverslip. θ denotes the collection angle. The coverslide is not drawn for simplicity. **b** Ray tracing of photon detection by an air objective for a sample on a glass coverslip. The detection efficiency is lower due to refractive index mismatch. **c** Optical layout of an inverted epifluorescent microscope. Collimated laser light is expanded by lens 1 and lens 2 before focusing onto the objective lens back focal plane by lens 3. The emitted light is filtered with a dichroic mirror and emission filter before focusing onto a camera.

dSTORM-capable microscopes must satisfy several further criteria to maximise detection efficiency. The first is that the immersion medium of the objective ought to minimise refractive index mismatch. Since samples are plated on glass, the absence of an immersion medium would result in refraction of the emitted fluorescence away from the collection angle of the objective lens (Fig. 2.2**b**). To alleviate this, oil-immersion objec-

tive lenses with high numerical apertures (NA) are used (Fig 2.2**a**) since immersion oils have a similar refractive index to glass [122]. The NA is expressed as:

$$\mathrm{NA} = n \sin \theta, \tag{2.4}$$

where n is the refractive index of the immersion medium and θ is the collection angle of the objective [123], and so the use of high-NA lenses in SMLM (NA $>$ 1.4) maximises the photon detection from the fluorophores and, therefore, the achievable resolution, thus facilitating downstream single-molecule localisation.

The second consideration is the magnification achieved by the objective lens and tube lens. Imaging fluorophores onto a camera discretises the fluorescent signal into pixels. In order to resolve this signal, it must be sampled at a rate of at least twice the minimum size, as stated by the Nyquist-Shannon sampling theorem [124]. For example, for a maximum resolution of 250 nm, the magnification must be chosen such that the pixel size corresponds to less than or equal to 125 nm on the image plane. A poorly selected pixel size can result in low localisation accuracy in downstream analyses.

2.3 From single-molecules to super-resolution

With a bright, photoswitching dye and a calibrated optical system, a small subpopulation of single-molecules are imaged per frame in a dSTORM experiment. However, as previously stated, the spatial resolution is limited by diffraction, given by [123]:

$$d = \frac{\lambda}{2\mathrm{NA}} \, . \tag{2.5}$$

d is the size of the resolvable structure and λ is the emission wavelength. To achieve super-resolution, the fluorescent signal must be localised with an accuracy greater than the resolution limit.

When imaging with a microscope, the emitted fluorescence undergoes Fraunhofer diffraction through a circular aperture, producing a blurred spot at the image plane [122]. The blurring of an object by an imaging system is formally described by the point spread

function (PSF). The relationship between the image, object, and PSF is given as:

$$\mathrm{Im}(x, y) = \mathrm{Obj}(x, y) \ * \ \mathrm{PSF}(x, y) \,, \tag{2.6}$$

where $\mathrm{Im}(x, y)$, $\mathrm{Obj}(x, y)$, and $\mathrm{PSF}(x, y)$ denote the image, object, and PSF, respectively, on a 2D plane while $*$ denotes the convolution operator [125]. A definition of convolution is given in Appendix: A.1.1.

To localise single-molecules, a mathematical description of the PSF is required. For Fraunhofer diffraction through a circular aperture, a common model is the Airy disk (Fig. 2.3**a**) [126], given as:

$$I(r) = I_0 \left[\frac{2J_1(k\mathrm{NA}r)}{k\mathrm{NA}r} \right]^2 , \tag{2.7}$$

with

$$k = \frac{2\pi}{\lambda} \,. \tag{2.8}$$

J_1 is a first order Bessel function of the first kind, I_0 is the maximum intensity, NA is the numerical aperture, and r is the radius from the centre. Aside from the Airy disk, A 2D Gaussian function (Fig. 2.3**b**) is also a popular model [127]:

$$I(x, y) = \frac{I_0}{2\pi\sigma} \exp\left(\frac{-(x - x_0)^2 - (y - y_0)^2}{2\sigma^2} \right) . \tag{2.9}$$

σ is the standard deviation of the 2D Gaussian fit and also is a measure of the PSF width. x_0 and y_0 are the centre coordinates of the Gaussian. exp denotes the exponential function, $f(x) = e^x$. This notation is used throughout this work.

Neither function is an accurate description of the true PSF—the Gaussian function is a simplified model and the Airy function is only accurate for NAs < 0.7 [127–129] which are not used in dSTORM. While more complex mathematical expressions provide more accurate descriptions of the PSF [129–131], Gaussian approximations still achieve reasonable accuracy when emitter dipole orientations are distributed isotropically [128], and have advantages due to simplicity and ease of computation.

With a suitable mathematical description of the PSF, single-molecule localisation first involves approximate localisation of single molecule positions through image filtering

and local maxima detection (Fig. 2.3**c**). This step typically involves smoothing the image for feature enhancement, detecting single-molecules using an intensity threshold, and extraction of small (6–12 pixel radius) regions of interest wherein each region of interest contains the fluorescent signal from one molecule (Fig. 2.3**d**).

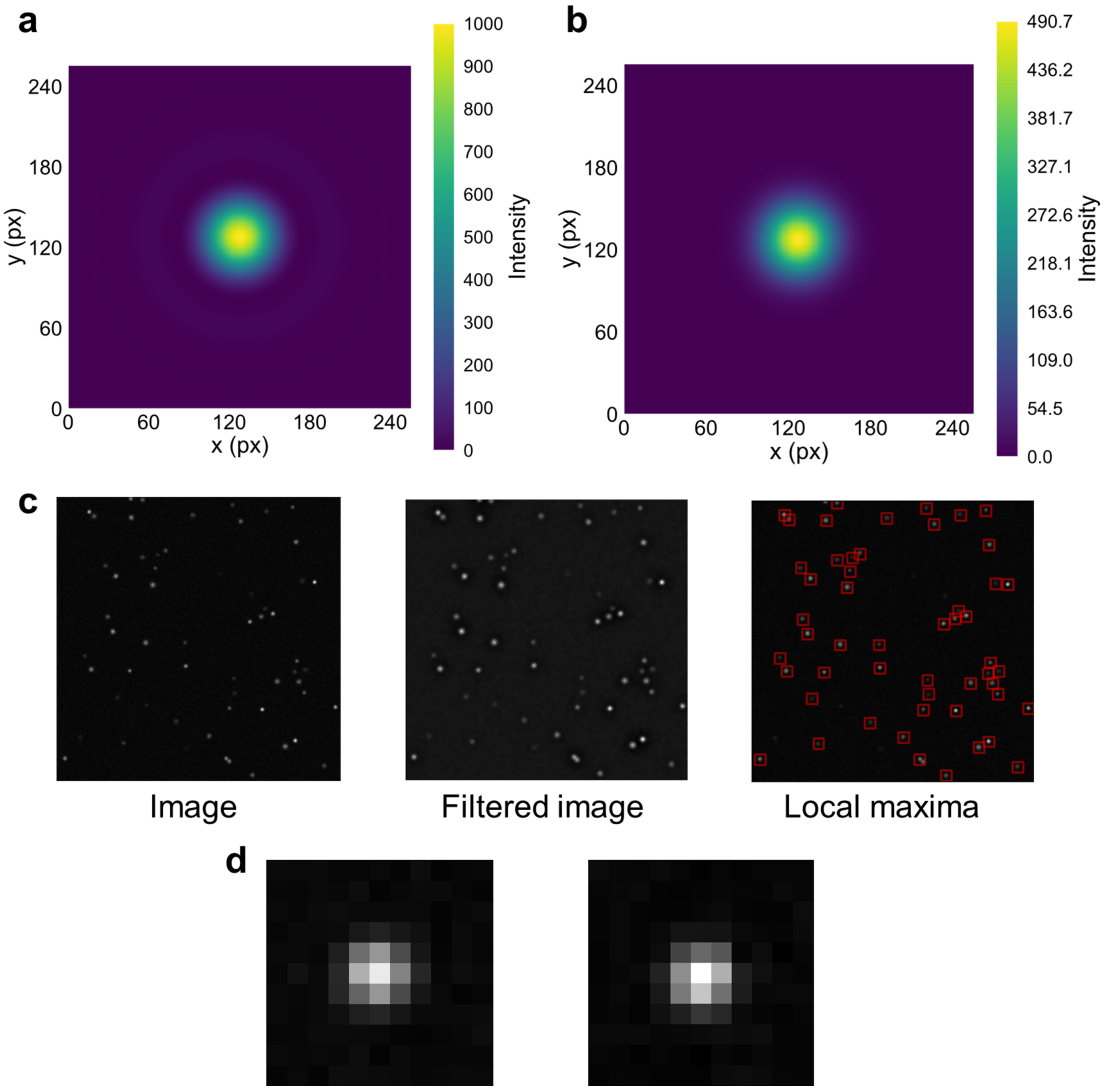

Fig. 2.3: **Point spread function models and approximate localisation of single-molecules.** The PSFs in **a** and **b** have been simulated to be unrealistically large (256 pixels x 256 pixels) and are unrepresentative of real PSFs. **a** Airy disk simulation of a PSF using Eq. 2.7, upscaled to a 256 x 256 image with parameters of: $I_0 = 1000$, $r = 50$ pixels. The PSF was generated using the Astropy package in Python 3.13 [132]. **b** Gaussian PSF simulation using Eq. 2.9, upscaled to a 256 x 256 image, with parameters of $I_0 = 1000000$ and $\sigma = 18$ pixels. The PSF was generated using the Python packages listed in Methods: 3.11. **c** Approximate localisation of single-molecules through image filtering and local maxima detection using the scikit-image package [133] in Python 3.13. The image of single-molecules is synthetic data generated from the ThunderSTORM plugin in ImageJ 1.54f [134, 135]. The image was filtered with a difference-of-Gaussians filter using convolution kernels of size $\sigma = 1$ and $\sigma = 6$ while local maxima were detected with an intensity threshold of 3 times the root mean square intensity. **d** Representative 11 x 11 regions of interest of the fluorescent signal from single-molecules, cropped from the original image in **c**.

In this work, a 2D integrated Gaussian function was fit to the PSF for all molecules

which is better adapted to the pixelation of fluorescent signal compared to the Gaussian function described in Eq. 2.9 [127, 136]. Here, the PSF is given as:

$$\mathrm{PSF}(x, y) = I_0 \Delta \mathrm{E}_x \Delta \mathrm{E}_y + b \,, \tag{2.10}$$

where

$$\Delta \mathrm{E}_x = \frac{1}{2} \operatorname{erf}\left(\frac{x - x_0 + \frac{1}{2}}{\sqrt{2}\sigma} \right) - \frac{1}{2} \operatorname{erf}\left(\frac{x - x_0 - \frac{1}{2}}{\sqrt{2}\sigma} \right), \tag{2.11}$$

$$\Delta \mathrm{E}_y = \frac{1}{2} \operatorname{erf}\left(\frac{y - y_0 + \frac{1}{2}}{\sqrt{2}\sigma} \right) - \frac{1}{2} \operatorname{erf}\left(\frac{y - y_0 - \frac{1}{2}}{\sqrt{2}\sigma} \right). \tag{2.12}$$

erf is the error function (Appendix: A.1.2), b is the background intensity, and all other parameters are as stated in Eq. 2.8. Eqs. 2.11, and 2.12 essentially describe the difference in the Gaussian cumulative distribution function over one pixel for both the x-coordinate and y-coordinate.

In single-molecule localisation, the PSF centre coordinates (x_0, y_0), intensity (I_0), standard deviation (σ), and background intensity (b) are unknown and must be estimated for each fluorophore from its image (Fig. 2.3**d**). Maximum likelihood estimation (MLE) is used throughout this work for parameter estimation since it achieves accuracies close to the theoretical limit for SMLM [127, 128, 137].

The aim of MLE is to estimate parameter values which maximise the likelihood of observing a given set of data (Fig. 2.4**b**) [73, 138]. For SMLM, the data corresponds to the observed image of a single molecule (Fig. 2.3**d**) while the parameters are:

$$\boldsymbol{\theta} = [\theta_x, \theta_y, \theta_I, \theta_\sigma, \theta_b] \,,$$

which denote estimates for x_0, y_0, I_0, σ, and b, respectively. The MLE procedure is then repeated for every detected molecule for all frames.

For MLE, the photon detection is modelled as a Poisson process [139, 140], generally given as [138]:

$$p(n \,|\, \mu) = \frac{\mu^n \, \exp(-\mu)}{n!} \,. \tag{2.13}$$

$p(n \,|\, \mu)$ denotes the probability of observing n photons given an expected photon count,

μ. Given:

$$n = \mathrm{Im}(x, y)\,, \tag{2.14}$$

$$\mu = \mathrm{PSF}(x, y \mid \boldsymbol{\theta}) = I_0 \Delta \mathrm{E}_x \Delta \mathrm{E}_y + b\,, \tag{2.15}$$

where $\mathrm{Im}(x, y)$ denotes the intensity for a pixel at x, y, single-molecule localisation can be formulated as a parameter optimisation problem stated as following:

$$\hat{\boldsymbol{\theta}} = \arg\max_{\boldsymbol{\theta}} \mathcal{L}(\boldsymbol{\theta} \mid \mathrm{Im})\,. \tag{2.16}$$

With $\hat{\boldsymbol{\theta}}$ denoting the optimal parameters and $\mathcal{L}(\boldsymbol{\theta} \mid \mathrm{Im})$ denoting the likelihood of obtaining a set of parameters given the observed data [128, 141]. Using the Poisson distribution outlined by Eq. 2.13, Eq. 2.14, and Eq. 2.15, the likelihood is written as:

$$\mathcal{L}(\boldsymbol{\theta} \mid \mathrm{Im}) = \prod_{x,y \,\in\, \mathrm{Im}} \frac{\mathrm{PSF}(x, y \mid \boldsymbol{\theta})^{\mathrm{Im}(x,y)} \exp\left(-\mathrm{PSF}(x, y \mid \boldsymbol{\theta})\right)}{\mathrm{Im}(x, y)!}\,. \tag{2.17}$$

In practice, however, the log-likelihood is used due to improved numerical stability [73], resulting in:

$$\ln[\mathcal{L}(\boldsymbol{\theta} \mid \mathrm{Im})] = \ln\left[\prod_{x,y \,\in\, \mathrm{Im}} \frac{\mathrm{PSF}(x, y \mid \boldsymbol{\theta})^{\mathrm{Im}(x,y)} \exp\left(-\mathrm{PSF}(x, y \mid \boldsymbol{\theta})\right)}{\mathrm{Im}(x, y)!}\right]. \tag{2.18}$$

This equation, when ignoring terms that do not explicitly depend on $\boldsymbol{\theta}$, then simplifies to:

$$\ln[\mathcal{L}(\boldsymbol{\theta} \mid \mathrm{Im})] = \sum_{x,y \,\in\, \mathrm{Im}} \mathrm{Im}(x, y) \ln\left[\mathrm{PSF}(x, y \mid \boldsymbol{\theta})\right] - \mathrm{PSF}(x, y \mid \boldsymbol{\theta})\,. \tag{2.19}$$

Finally, substituting the log-likelihood into Eq. 2.16 leads to:

$$\hat{\boldsymbol{\theta}} = \arg\max_{\boldsymbol{\theta}} \sum_{x,y \,\in\, \mathrm{Im}} \mathrm{Im}(x, y) \ln\left[\mathrm{PSF}(x, y \mid \boldsymbol{\theta})\right] - \mathrm{PSF}(x, y \mid \boldsymbol{\theta})\,. \tag{2.20}$$

In other words, single-molecule localisation involves determining the values of $\boldsymbol{\theta}$ (i.e. the xy-position and photophysical properties of the fluorophore) that maximise the log-likelihood (see Fig. 2.4 for a visual representation). A variety of optimisation algorithms may be used to determine the values of $\boldsymbol{\theta}$, such as the Nelder-Mead method, Newton-Raphson methods, or Levenberg-Marquadt [142–144].

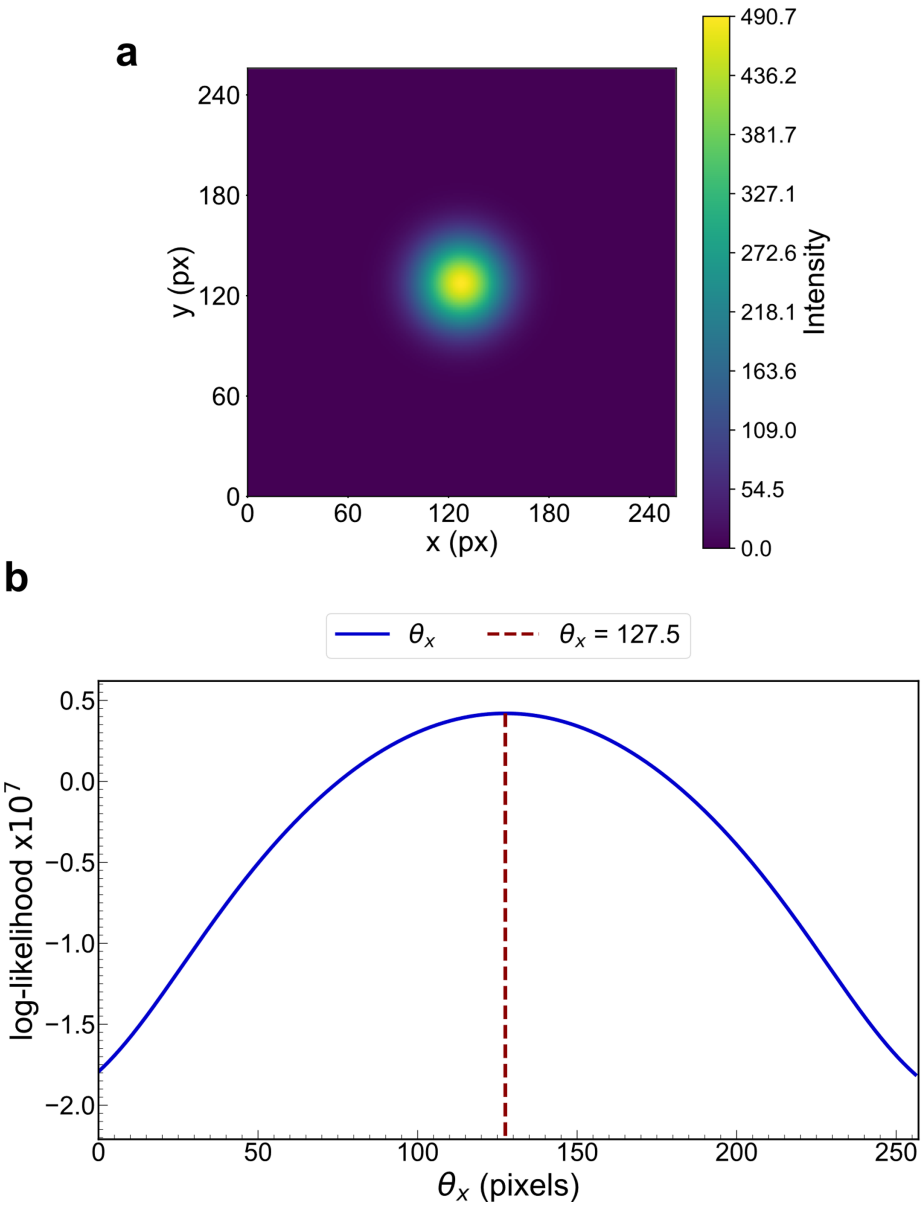

Fig. 2.4: **Visual representation of maximum likelihood estimation in SMLM for a single variable.** Similar to Fig. 2.3, the PSF simulation is unrealistically large and does not represent real PSFs. **a** Integrated Gaussian PSF simulation from Fig. 2.3**b**. **b** Plot of the log-likelihood against different values of θ_x—the estimated x-coordinate of the Gaussian function centroid. The log-likelihood values have been scaled down by a factor of 10^7 to facilitate visualisation. A value of 127.5 pixels maximises the log-likelihood, as expected from the parameters used to initialise the simulation as given in Fig. 2.3**b**. The optimal value is shown with a dashed red line.

Carrying out this optimisation routine for all single-molecules then produces a localisation table containing the subpixel xy-coordinates of all detected fluorophores, as well as other information including the intensity, background, PSF width, and localisation precision. This localisation table is the final output from single-molecule localisation from which a super-resolution image can be reconstructed.

2.4 Resolution limit in SMLM

Of critical importance in determining the resolution of SMLM is the precision at which single-molecules are localised (Introduction: 1.2, Fig. 1.3). In general, the limit to the precision of estimating a parameter is given by the Cramér-Rao lower bound (CRLB) [137], a quantity determined by inverting the Fisher information matrix—a measure of how much information is available in the data with which to estimate the parameters [140]—followed by taking the diagonal entries of the inverted matrix. More specifically for the ith parameter [145],

$$\mathrm{var}(\hat{\theta}_i) \geq \mathbf{I}_{ii}^{-1}(\boldsymbol{\theta})\,. \tag{2.21}$$

$\mathrm{var}(\hat{\theta}_i)$ is the variance of the ith estimated parameter, and $\mathbf{I}_{ii}(\boldsymbol{\theta})$ is the ith diagonal entry of the Fisher information matrix for a parameter vector, $\boldsymbol{\theta}$, of length, n. The full Fisher information matrix, with elements along row i and column j, is given by [145]:

$$\mathbf{I}_{ij}(\boldsymbol{\theta}) = \mathrm{E}\left[\frac{\partial \ln\left[\mathcal{L}(\mathrm{Im}(x,y)\mid\boldsymbol{\theta})\right]}{\partial\boldsymbol{\theta}_i}\cdot\frac{\partial \ln\left[\mathcal{L}(\mathrm{Im}(x,y)\mid\boldsymbol{\theta})\right]}{\partial\boldsymbol{\theta}_j}\right],\ i,j\in\{1,2,\ldots n\}\,. \tag{2.22}$$

E is the expectation value and all other terms are as previously stated. Substituting the log-likelihood from Eq. 2.19 then leads to:

$$\mathbf{I}_{ij}(\boldsymbol{\theta}) = \sum_{x,y\,\in\,\mathrm{Im}} \frac{1}{\mathrm{PSF}(x,y,\boldsymbol{\theta})}\frac{\partial\,\mathrm{PSF}(x,y,\boldsymbol{\theta})}{\partial\boldsymbol{\theta}_i}\frac{\partial\,\mathrm{PSF}(x,y,\boldsymbol{\theta})}{\partial\boldsymbol{\theta}_j}\,, \tag{2.23}$$

with a derivation given in Appendix: A.1.3. In practice, Eq. 2.23 is used to calculate the Fisher information matrix.

Intuitively, higher values in the Fisher information matrix correspond to greater steepness in the log-likelihood function which facilitates more precise estimates of $\boldsymbol{\theta}$, resulting in lower variance in parameter estimation, and greater precision.

Alternatively, several single-molecule localisation software, such as ThunderSTORM, use a simplified analytical equation derived from least-squares fitting of a Gaussian PSF to calculate the localisation precision [18, 128, 146]. This has the form:

$$\sigma_{xy} = \sqrt{\frac{\hat{\theta_\sigma^2} + \frac{a^2}{12}}{\hat{\theta_I}} + \frac{8\pi\,\hat{\theta_\sigma^4}\,\hat{\theta_b^2}}{a^2\hat{\theta_I^2}}}\,. \tag{2.24}$$

$\hat{\theta_\sigma}, \hat{\theta_I}$, and $\hat{\theta_b}$ correspond to the best estimates for the standard deviation, fluorophore intensity, and background intensity, respectively, of the 2D Gaussian PSF. a is the pixel size, while σ_{xy} is the localisation precision. Eq. 2.24 summarises the essential photophysical parameters that affect localisation precision in SMLM; higher photon counts increase localisation precision while higher background decreases localisation precision.

However, localisation precision is not the sole measure of resolution in SMLM. The labelling density is also critical to resolving a structure at sub-diffraction resolution [21, 147]. For example, if the minimum distance between any two fluorophores is 50 nm, the resolution will be limited to 50 nm, irrespective of the localisation precision. Apart from labelling density, other experimental factors influence the resolution, including linkage error, the choice of PSF model, and the localisation method [48].

To account for these different factors, the Fourier ring correlation (FRC) resolution was introduced to provide a standardised resolution metric [48]. This methodology shares the same principles as Fourier shell correlation in cryogenic electron microscopy [148, 149], wherein a dataset is split into two independent halves, an image or 3D structure is reconstructed for each half, and a Fourier transform (Appendix: A.1.4) is applied to both images or structures (Fig 2.5). The correlation in Fourier space between the pixels bounded by a circle of fixed radius is then calculated. This calculation is written as:

$$\mathrm{FRC}(q) = \frac{\sum_q \hat{f}_1(q)\hat{f}_2^*(q)}{\sqrt{\sum_q |\hat{f}_1(q)|^2}\sqrt{\sum_q |\hat{f}_2(q)|^2}}\ ,\ q\ \in \text{circle}\,. \tag{2.25}$$

Here, q denotes the radius of the bounding circle in spatial frequency units; $\hat{f}_1$ and $\hat{f}_2$ denote the Fourier transforms of the two images, and $*$ denotes the complex conjugate.

The resolution is determined by increasing the Fourier space radius, q, and repeating the correlation calculation (Eq. 2.25) until the correlation falls below a threshold, usually chosen to be 1/7 (≈ 0.143) (Fig 2.5) [48, 150]. The correlation curve is typically smoothed to facilitate this process.

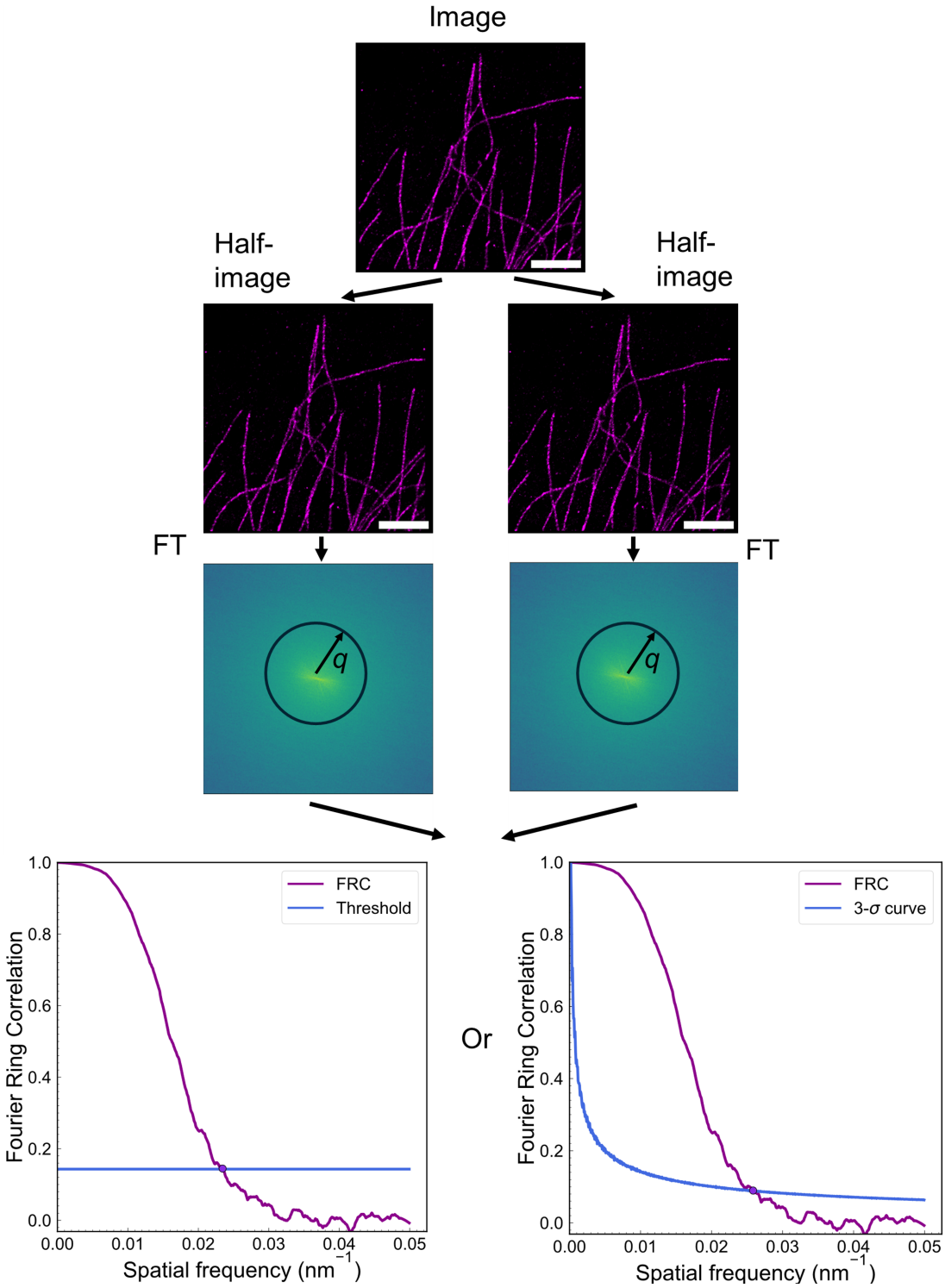

Fig. 2.5: **Example Fourier ring correlation measurement on experimental data.** An image reconstructed from SMLM data is split into two independent images. Both images are Fourier transformed (FT) and the correlation between pixels bounded by a circle of radius q is calculated. The resolution can then be measured as the spatial frequency at which the correlation decreases below a threshold or the three-sigma curve. A threshold of 0.143 is used. The SMLM data are microtubules immunolabelled with antibodies conjugated to Alexa Fluor 647.

Alternatively, the resolution may be evaluated as the point where the correlation decreases below a sigma-factor curve which is given as [151–153]:

$$\sigma_q = \frac{\sigma_{factor}}{\sqrt{\frac{N_q}{2}}} \, . \tag{2.26}$$

σ_q is the sigma curve at radius q, N_q is the number of pixels bounded by the circle with radius q, and σ_{factor} is an integer value that is typically = 3. Since $\frac{1}{\sqrt{N}}$ describes an FRC curve of pure noise [152], a curve with a sigma factor of three thus delineates FRC values as significant when they are at least three times higher than that of noise. Hence, the resolution is determined from the point at which the FRC falls below the three-sigma curve.

Taken together, the localisation precision is a useful metric for assessing the performance of SMLM in relation to measurable photophysical properties of the fluorophores. However, the FRC resolution provides a more holistic performance metric and will thus be used for resolution evaluation throughout this work.

2.5 Drift Quantification in SMLM

Drift is generally defined as the displacement of a fluorophore away from the initial position it held at the beginning of an image acquisition. This displacement can occur in the lateral direction—i.e. along the xy-plane—or in the axial direction—along the z-axis. The consequence of lateral drift is to blur an image (Fig. 2.6) while the effect of axial drift is to defocus the single-molecule fluorescent signal (Fig. 2.6). Drift quantification is of importance for Chapter 4 which describes the development and evaluation of a drift-free microscope.

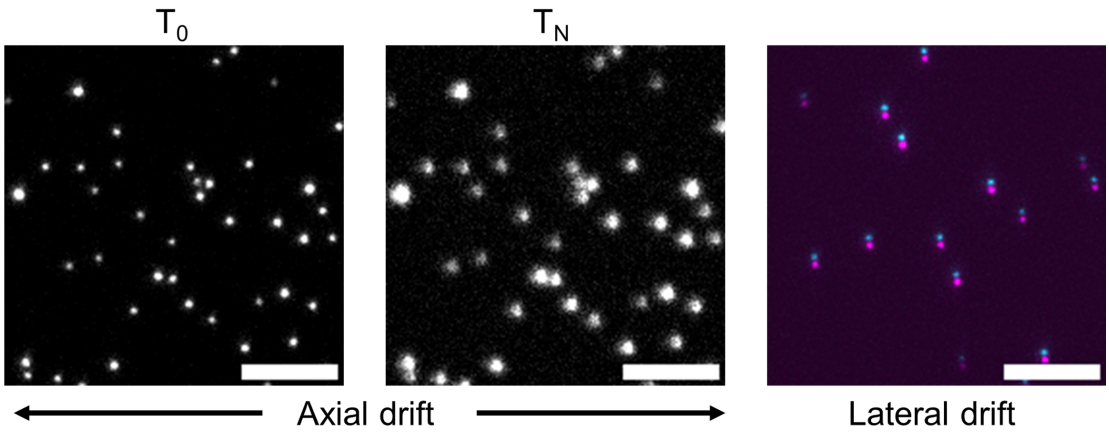

Fig. 2.6: **Effects of sample drift visualised through widefield imaging of 100 nm fluorescent beads.** Axial drift defocuses the fluorescent signal. Here, T_0 denotes the first frame of an image series and T_N denotes the final frame of an image series. For the lateral drift, magenta is used to mark the first frame of an image series while cyan is used to mark the final frame. Scale bars: 5 µm. Widefield images were acquired using a Zeiss AxioObserver Z1 microscope.

To quantify axial drift, the width of the PSF serves as an approximate measure of z-axis deviation from the focal plane since deviations from the focal plane increase the PSF width (Fig. 2.6). Here, the PSF width is taken to be its full width at half-maximum (FWHM) which can be calculated from the best estimate of the standard deviation of the 2D Gaussian fit from Eqs. 2.10, 2.11, 2.12 using the following relation:

$$\mathrm{FWHM} = 2\hat{\theta_\sigma}\sqrt{\ln 2}\,. \tag{2.27}$$

Using the first frame as a reference, the axial drift was estimated as $\Delta\mathrm{FWHM}_t$, where $t \in \{2, 3, \ldots, T\}$. To assess whether the axial position over time deviates significantly beyond that expected from measurement error, a 95% confidence interval was calculated as:

$$\left[\Delta\mathrm{FWHM}_{t=1} - \mathrm{t}_c\,\frac{s_{t=1}}{\sqrt{n_{t=1}}}\,,\ \Delta\mathrm{FWHM}_{t=1} + \mathrm{t}_c\,\frac{s_{t=1}}{\sqrt{n_{t=1}}}\right]\,. \tag{2.28}$$

$\Delta\mathrm{FWHM}_{t=1}$ is the change in the FWHM for the first frame, and so is equal to zero. t_c is the critical value for the t-distribution for a 95% confidence interval, $s_{t=1}$ is the standard deviation for the FWHMs in frame one, and $n_{t=1}$ is the number of localisations in the first frame.

Built-in algorithms from ThunderSTORM and SMAP (single-molecule analysis platform) were used to carry out lateral drift correction via fiducial marker tracking and

redundant cross-correlation (RCC), respectively [46, 135, 154], as well as to quantify the lateral drift. The lateral drift correction for fiducial markers is implemented as following for a time series $t \in \{1, 2, \ldots, T\}$:

$$\bar{x}_t = \sum_{i=1}^{N} \frac{1}{N}(x_{i,t} - \theta_i). \tag{2.29}$$

$\bar{x}_t$ denotes the average drift at frame t, N denotes the number of fiducial markers in the frame, $x_{i,t}$ is the absolute position of the ith fiducial marker in frame t, and θ_i is an unknown relative offset in the fiducial marker position. The θ_i for all beads—$\hat{\boldsymbol{\theta}} = [\hat{\theta_1}, \hat{\theta_2}, \ldots \hat{\theta_N}]$—is estimated through least squares optimisation:

$$\hat{\boldsymbol{\theta}} = \arg\min_{\boldsymbol{\theta}} \sum_{t=1}^{T} \sum_{n=1}^{N} ((x_{i,t} - \theta_i) - \bar{x}_t)^2. \tag{2.30}$$

An equivalent routine is carried out for the y-coordinate. The values of $\bar{x}_t$ and $\bar{y}_t$ calculated with $\hat{\boldsymbol{\theta}}$ can then be used to estimate the lateral drift through the following procedure,

$$\langle \bar{x} \rangle = \frac{1}{T} \sum_{t=1}^{T} |\bar{x}_t| \,, \tag{2.31}$$

$$\langle \bar{y} \rangle = \frac{1}{T} \sum_{t=1}^{T} |\bar{y}_t| \,. \tag{2.32}$$

$\langle \bar{x} \rangle$ and $\langle \bar{y} \rangle$ denote the mean absolute drift over the image acquisition period, T. Absolute values are used so that only the magnitude of the drift is quantified.

If fiducial markers are not used, the lateral drift can be estimated using RCC. The principle of this technique is to split the localisations into a number of subsets (n), calculate the correlation for all pairs of subsets, and estimate lateral drift from this correlation. It is formulated as:

$$S_n(\mathbf{x}) = S_{true}(\mathbf{x} - \mathbf{D_n}). \tag{2.33}$$

Here, $S_n(\mathbf{x})$ denotes the *nth* subset from the localisation table where x is a vector of the xy-localisations; $S_{true}(\mathbf{x})$ is the drift-free xy-positions, and $\mathbf{D_n}$ is the estimated lateral drift of the *nth* subset. The drift estimates are derived from the xy-position of the cross-correlation peak between two image subsets [46], and therefore can be used to estimate lateral drift in dSTORM.

2.6 Colocalisation and cluster analysis

Multi-colour dSTORM enables colocalisation analysis of multiple biological molecules, giving insights into their organisation and interactions. Here, two-colour dSTORM is applied to understanding the interaction between SARS-CoV-2 spike protein and ACE-2 receptor in Chapter 8. This section will outline an analysis approach similar to that described by Malkusch *et al.* 2012 [155].

Prior to colocalisation analysis, channel registration must be carried out to correct for chromatic aberrations which cause wavelength-dependent distortions in single-molecule localisations [156]. A common practice for this is to acquire images of multi-colour fluorescent beads in two different channels, determine the subpixel xy-localisations, and calculate an affine transformation matrix between the localisations which compensates for the chromatic aberrations. The matrix is formulated as:

$$\begin{bmatrix} 1 & 0 & \Delta x \\ 0 & 1 & \Delta y \end{bmatrix} \begin{bmatrix} x & y & 1 \end{bmatrix}^T = \begin{bmatrix} x' \\ y' \end{bmatrix}. \tag{2.34}$$

Δx and Δy are the xy shifts that must be estimated in channel registration; x and y are the xy-localisations from one channel, T is the transpose, while x' and y' are the xy-localisations from a second channel. A channel registration error was also calculated by taking the median of the nearest neighbour Euclidean distances from the registered bead localisations of one channel to the localisations of the second channel.

Following channel registration, a coordinate-based colocalisation (CBC) value is determined for each localisation in each channel (Fig. 2.7). The first step in this process is the calculation of the radial distribution of both molecular species around a localisation. The distribution of species A from the localisations of species A is given as:

$$D_{A_i,A}(r) = \frac{N_{A_i,A}(r)}{\pi r^2 N_{A_iA}(R)} \,/\, \frac{1}{\pi R^2}. \tag{2.35}$$

The distribution of species B from the localisations of species A is:

$$D_{A_i,B}(r) = \frac{N_{A_i,B}(r)}{\pi r^2 N_{A_iB}(R)} \,/\, \frac{1}{\pi R^2}. \tag{2.36}$$

$D_{A_i,A}(r)$ is the distribution of species A from the localisations of species A around a

series of radii r, where $r = [r_1, r_2, .., R]$ and R is the maximum radius size. $D_{A_i,B}(r)$ is the distribution of species B from the localisations of species A. $N_{A_i,A}(r)$ is the number of molecules of species A around the localisations of species A. $N_{A_i,B}(r)$ is the number of molecules of species B around species A. Effectively, the distribution captures the number of molecules normalised by area and the maximum molecule count—normalised by the area of the maximum molecule count. The distribution calculations are then repeated for species B, i.e. $D_{B_iB}(r)$ and $D_{B_iA}(r)$.

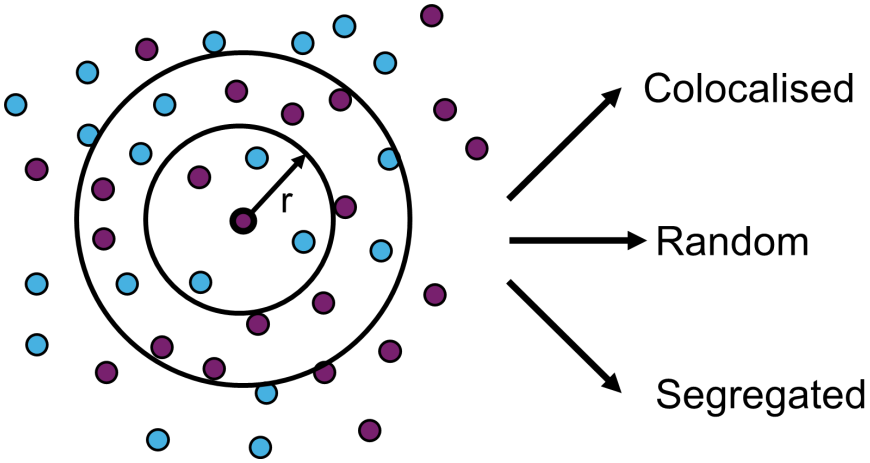

Fig. 2.7: **Illustration of colocalisation analysis.** For each localisation, the number of molecules in each channel within a radius, r, are counted. Depending on whether the distributions of molecules in each channel are correlated, anti-correlated, or not correlated, a localisation can be classified as colocalised, randomly distributed, or segregated with respect to localisations from the second channel. The localisations of one channel are depicted as blue circles while the localisations of the second channel are depicted as purple circles.

The correlation between the two distributions is calculated through the Spearman rank correlation coefficient:

$$\rho_{A_i} = \frac{\sum_{r_j=1}^{R}(O_{D_{A_iA}}(r_j) - \bar{O}_{D_{A_iA}}) \cdot (O_{D_{A_iB}}(r_j) - \bar{O}_{D_{A_iB}})}{\sqrt{\sum_{r_j=1}^{R}(O_{D_{A_iA}}(r_j) - \bar{O}_{D_{A_iA}})^2} \cdot \sqrt{\sum_{r_j=1}^{R}(O_{D_{A_iB}}(r_j) - \bar{O}_{D_{A_iB}})^2}} \,. \tag{2.37}$$

ρ_{A_i} is the Spearman rank correlation coefficient for the ith localisation from species A and O is used to denote the ranks of the radial distributions along r. Again, the calculation is repeated for species B.

Finally, the CBC value is calculated for a localisation by weighting the Spearman rank correlation coefficient by the nearest neighbour distance for species B.

$$CBC_{A_i} = \rho_{A_i} \cdot \exp\left(-\frac{s_{A_iB}}{R}\right) . \tag{2.38}$$

s_{A_iB} denotes the nearest neighbour distance and other variables are as previously stated.

With this weighting, CBC values range from -1 to 1, describing perfect anti-correlation to perfect correlation, respectively (Fig. 2.7).

2.6.1 Cluster analysis

After colocalisation, molecules can be filtered depending on their degree of colocalisation for further analysis. One such analysis method is cluster analysis [95, 157, 158], wherein molecules within a certain spatial proximity are grouped, and various cluster descriptors—such as size, area, and circularity—can be calculated to quantify and interrogate the spatial organisation of molecules.

Prior to cluster analysis, the existence of clusters must be verified. For this purpose, Ripley's K-function can be used which gives the expected number of points, N, around a point within a circle with radius, r [159, 160]. The K-function is expressed as:

$$K(r) = \frac{\sum_{i=1}^{n} N_{p_i}}{nA} \, . \tag{2.39}$$

n is the number of points, p_i is the ith point, and A is the area. For a random distribution the expected value of $K(r)$ is πr^2 while clustering or dispersion will show deviations away from this. For convenience, the Ripley K-function is often normalised to the L-function, which has an expected value of r, and the H-function, which has an expected value of 0 [160]. These are given by:

$$L(r) = \sqrt{\frac{K(r)}{\pi}} \, , \tag{2.40}$$

$$H(r) = L(r) - r \, , \tag{2.41}$$

where $L(r)$ and $K(r)$ denote the L-function and H-function, respectively. With the normalised H-function, positive values indicate clustering while negative values indicate dispersion.

Once the presence of clustering has been confirmed, clustering algorithms can be applied to localisations [161]. Here, hierarchical density-based spatial clustering of applications with noise (HDBSCAN) is used which classifies clusters based on a minimum number of points [162]. The number of molecules, radius, area, density, and circularity of each cluster are then calculated (Fig. 2.8). The radius, r, is taken to be the maximum

distance of the distances between all points within a cluster and the cluster centre (Fig. 2.8). In other words,

$$r = \max\{d_{ic}\}\,, i \in \{1, 2, \ldots, N\} \tag{2.42}$$

where,

$$d_{ic} = \sqrt{(x_i - x_c)^2 + (y_i - y_c)^2}\,, \tag{2.43}$$

and the cluster centre, (x_c, y_c), is taken to be the cluster centroid:

$$(x_c, y_c) = \left(\frac{1}{N} \sum_{i=1}^{N} x_i\,,\ \frac{1}{N} \sum_{i=1}^{N} y_i \right)\,. \tag{2.44}$$

x_i and y_i denote the x-coordinate and y-coordinate of the ith localisation in a cluster of N points.

The cluster area and perimeter are estimated by determining the convex hull of the cluster (Fig. 2.8) which is the smallest area that can be bound by line segments between points [163]. The circularity is then calculated as [164]:

$$C = \frac{4\pi A}{P^2}. \tag{2.45}$$

With A and P being the area and perimeter, respectively. Values closer to 1 indicate higher circularity and values closer to 0 indicate lower circularity. The number of molecules is determined by counting the number of localisations. Finally, the density is calculated by dividing the total number of molecules by the area.

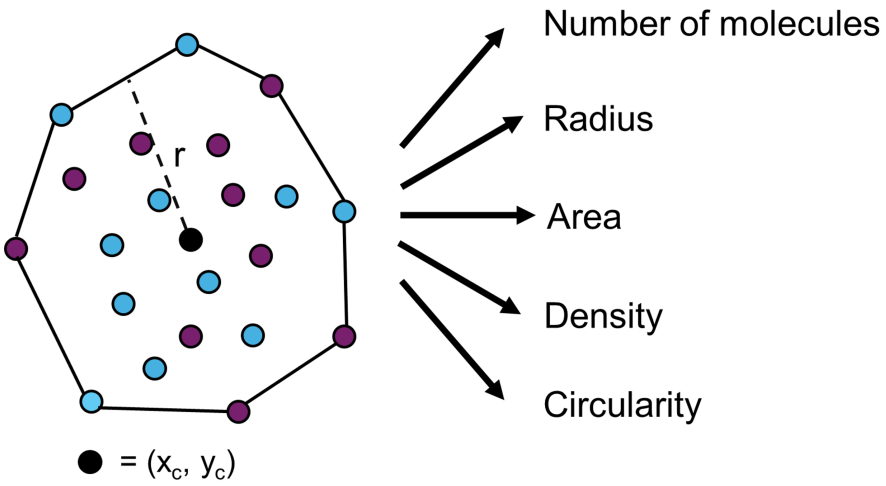

Fig. 2.8: **An example cluster and illustration of cluster properties.** Once clusters have been identified, five cluster properties are calculated. Here, the convex hull is depicted with solid black lines which is used to calculate the area and perimeter. The cluster centroid, (x_c, y_c), is shown with a black circle. These parameters are then used to calculate several cluster properties. The cluster radius is depicted with a dashed line.

Further cluster analysis can be carried out using principal component analysis (PCA) which is a dimensionality reduction technique that reduces the cluster data into fewer variables—termed principal components—based on maximising the variance of the original variables [165, 166]. Each principal component is a linear combination of the original variables.

The variance in cluster data with n clusters and k cluster descriptors, $[X_1, X_2, \ldots, X_k]$ where X denotes a vector, is given by the $k \times k$ covariance matrix, $\mathbf{\Sigma}$, [138]:

$$\mathbf{\Sigma} = \begin{bmatrix} \mathrm{var}(X_1) & \mathrm{cov}(X_1, X_2) & \ldots & \mathrm{cov}(X_1, X_k) \\ \mathrm{cov}(X_2, X_1) & \mathrm{var}(X_2) & \ldots & \mathrm{cov}(X_2, X_k) \\ \vdots & \vdots & \ddots & \vdots \\ \mathrm{cov}(X_k, X_1) & \ldots & \ldots & \mathrm{var}(X_k) \end{bmatrix} . \tag{2.46}$$

var and cov denote the variance and covariance, respectively, with the covariance given by,

$$\mathrm{cov}(X_1, X_2) = \frac{\sum_{i=1}^{n} (X_{1_i} - \bar{X}_1)(X_{2_i} - \bar{X}_2)}{n-1} . \tag{2.47}$$

The principal components can be found through eigenvalue decomposition of the covariance matrix which gives the eigenvectors, $\mathbf{v}_1, \mathbf{v}_2, \ldots \mathbf{v}_k$, and their corresponding

eigenvectors, $\lambda_1, \lambda_2, .., \lambda_k$.

$$\mathbf{\Sigma v} = \lambda \mathbf{v} \, . \tag{2.48}$$

The eigenvalues each give a proportion of explainable variance while the elements of the eigenvector give the coefficients for the linear combination of variables that define the principal components. For example, the first principal component of the cluster data can be given as [166]:

$$\mathrm{PC1} = v_1 \cdot \mathrm{N} + v_2 \cdot r + v_3 \cdot A + v_4 \cdot D + v_5 \cdot C \, , \tag{2.49}$$

where $v_1, \ldots, v_5$ denote the elements of the first eigenvector, $\mathbf{v_1}$, and N, r, A, D, and C denote the number of molecules, cluster radius, area, density, and circularity, respectively.

This analysis approach facilitates the visualisation, interpretation, and comparison of cluster data that originate from different experimental treatments of a biological system.

2.7 Denoising with a spatial redundancy transformer

The denoising algorithm, SRDTrans, developed by Li *et al.* 2023 is an unsupervised deep learning method that uses a combination of spatial redundancy sampling and a shifted windows transformer [81, 167, 168]. A systematic characterisation and evaluation of its denoising effectiveness for SMLM data is provided in Chapter 7.

The spatial redundancy sampling strategy involves dividing each frame of the input $h \times w \times t$ ($height \times width \times time$) SMLM image stack into a series of 2x2 pixel patches. From each patch, a random pixel is selected and extracted, along with the horizontally adjacent pixel and the vertically adjacent pixel. All the central pixels are collated to form a substack with dimensions $h/2 \times w/2 \times t$ while the horizontally adjacent and vertically adjacent pixels are collated to form a substack each with the same dimensions, ultimately resulting in three image substacks. It is assumed that the intensities of pixels corresponding to noise will be independent while intensities corresponding to signal will be correlated, thus allowing for discrimination between signal and noise without ground truth data.

For model training, the central stack is input into the transformer network which uses the parameters $\boldsymbol{\theta}$ for denoising, while the remaining two substacks are used as training pairs to determine the optimal values of $\boldsymbol{\theta}$. This training procedure resembles that of Eq. 2.16 and Eq. 2.20, except that the goal is to determine the values of $\boldsymbol{\theta}$ that minimise the loss function, $L(\boldsymbol{\theta})$ [73], rather than maximise the log-likelihood:

$$\hat{\boldsymbol{\theta}} = \arg\min_{\boldsymbol{\theta}} \; L(\boldsymbol{\theta}) \, . \tag{2.50}$$

$\hat{\boldsymbol{\theta}}$ are the optimal parameters for denoising which are determined following model training. For SRDTrans, the loss function is a linear combination of mean squared error (L_2) and mean absolute error (L_1) for both the vertically adjacent and horizontally adjacent substacks, S_{ver} and S_{horiz}, respectively. More precisely [169],

$$L_{1,\text{ver}}(\boldsymbol{\theta}) = \sum_{i=1}^{N} |(\text{f}[S_i, \boldsymbol{\theta}] - S_{\text{ver}})| \, , \tag{2.51}$$

$$L_{2,\text{ver}}(\boldsymbol{\theta}) = \sum_{i=1}^{N} (\text{f}[S_i, \boldsymbol{\theta}] - S_{\text{ver}})^2 \, , \tag{2.52}$$

$$L_{\text{ver}} = \frac{1}{2} L_1 + \frac{1}{2} L_2 \, , \tag{2.53}$$

$$L_{\text{total}} = \frac{1}{2} L_{\text{ver}} + \frac{1}{2} L_{\text{horiz}} \, . \tag{2.54}$$

$\text{f}[S_i, \boldsymbol{\theta}]$ is a shorthand for the output of the transformer network and S_i is the ith batch for the central substack. N is the batch size—a proportion of the total number of training pairs. The loss function for the horizontally adjacent substack, L_{horiz} is identical to Eqs. 2.51, 2.52, and 2.53, except with S_{horiz}. Once the optimal parameters, $\hat{\boldsymbol{\theta}}$, have been obtained, they can be used for model inference, i.e. denoising other SMLM image stacks.

To address some of the shortcomings of SRDTrans for denoising persistent emission, two new loss functions were introduced to penalise the denoising model for temporal smoothness and low variance for the brightest pixels, both of which are indicative of abnormal photoswitching for dSTORM. The temporal smoothness loss function is first calculated by taking the pixel-wise absolute difference for each frame, $t \in \{1, 2, 3, \ldots, T\}$, to its preceding frame,

$$\Delta\text{Im}(x, y)_{i,t+1} = |\text{Im}(x, y)_{i,t+1} - \text{Im}(x, y)_{i,t}| \, , \tag{2.55}$$

followed by taking the negative mean for all images in the substack and for all batches,

$$L_3 = -\frac{1}{NT}\sum_{i=1}^{N}\sum_{t=1}^{T}\Delta\mathrm{Im}(x,y)_{i,t}\,. \tag{2.56}$$

$\mathrm{Im}(x,y)_{i,t+1}$ denotes an image at frame $t+1$ from the ith batch and the loss function is denoted by L_3.

Meanwhile, the loss function that penalises low variance in bright regions, L_4, first involves calculating the pixel-wise mean intensity, $\bar{I}$, and variance, $\mathrm{var}(I)$, over the time dimension of the image substack composed of the central pixels,

$$\bar{I}_i = \frac{1}{T}\sum_{t=1}^{T}\mathrm{Im}(x,y)_{i,t}\,, \tag{2.57}$$

$$\mathrm{var}(I_i) = \frac{1}{T}\sum_{t=1}^{T}[\mathrm{Im}(x,y)_{i,t} - \bar{I}]^2\,. \tag{2.58}$$

Given a threshold I_T , the mask is given as:

$$M(x,y)_i = \begin{cases} 1, & \text{if } \bar{I}_i > I_{T_i} \\ 0, & \text{otherwise}\,. \end{cases} \tag{2.59}$$

The mask is applied to the temporal variance, retaining values where the mean intensity was above the threshold. The loss, L_4, is taken to be the negative mean of the retained variance values,

$$L_4 = -\frac{1}{N}\sum_{i=1}^{N}[M(x,y)_i \cdot \mathrm{var}(I_i)]\,. \tag{2.60}$$

Finally, the total loss is given as,

$$L_{\mathrm{total}} = \frac{1}{2}L_{\mathrm{ver}} + \frac{1}{2}L_{\mathrm{horiz}} + 0.3\cdot L_3 + 0.2\cdot L_4\,. \tag{2.61}$$

The results from SRDTrans were evaluated by comparing the FRC resolutions (Eq. 2.25) with and without denoising.

3 Methods

3.1 Optical setup of ROCS-SMLM

A four-colour, 50 mW laser engine with 405 nm, 488 nm, 561 nm, and 640 nm laser lines (Toptica, iCHROME-CLE50) was used as the illumination source. The laser light was emitted via a polarisation-maintaining single-mode fibre and collimated using an achromatic objective lens (Leica, 20X, 0.25 NA). An achromatic doublet lens (f = 60 mm) was then used to focus the collimated laser light into a multi-mode fibre (Thorlabs, M72L01), transforming the laser from a Gaussian beam profile to a top-hat beam profile. Due to challenges in aligning the fibre, it could not be angled to achieve a true top-hat beam, resulting in an illumination profile in between that of a tophat and a Gaussian (Appendix: Fig. A.1**b, d**). To achieve a true top-hat profile, fine instrumental control of the positioning of the multimode fiber would be required. However, in practice, rough alignment resulted in a useable illumination profile with sufficient power density for STORM.

The laser light emanating from the multi-mode fibre was collimated by a second achromatic objective lens (Olympus, 20X, 0.4 NA) and expanded by a pair of achromatic doublet lenses (f = 30 mm, f = 50 mm). Following this, the laser light was reflected by a quad-edge dichroic mirror (Semrock, Di01-R405/488/561/635-25x36) to a high-NA, oil-immersion (Thorlabs, MOIL-30, n = 1.518, Olympus Type F) objective lens (Olympus, 60XOTIRF, 60X, 1.42 NA). The collimated light was focused by an achromatic doublet lens (f = 250 mm) onto the back focal plane of the objective lens to produce Köhler illumination on the sample plane. Samples were mounted on a custom-designed sample stage with a 10 µm translation range along the x-axis and y-axis. z-axis control of the objective lens was achieved using a piezoelectric electric stage (Physik Instrumente, E709) mounted underneath the objective lens. Micromanager 2.0 was used to adjust the axial position of the piezoelectric stage during image acquisition [170].

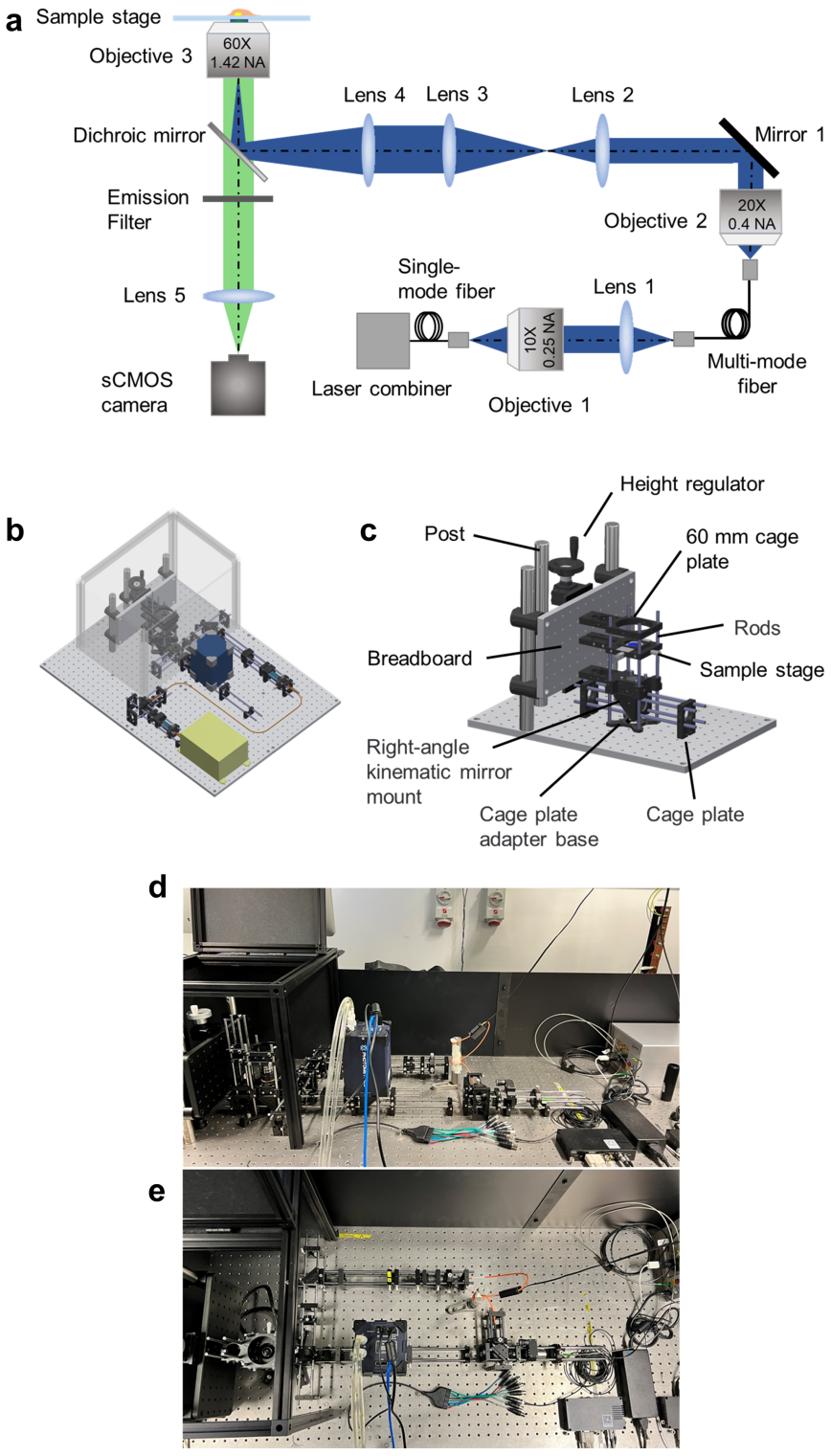

Fig. 3.1: **Schematics and pictures of the ROCS optical setup.** All optomechanical components are unique to the ROCS design except the cage plate adapter base. **a** Optical layout of the ROCS microscope. **b** Computer-aided design (CAD) rendering of the microscope. **c** CAD rendering of the components that make up the sample stage. **d** Side view of the ROCS microscope on an optical table. **e** Top view of the ROCS microscope.

In the imaging path, the fluorescence emission was collected by the 1.42 NA objective lens, passed through an emission filter (Chroma, ET525/50m or ET690/50m), and fo-

cused by an achromatic doublet lens (f = 200 mm) onto an sCMOS camera (Teledyne Photometrics, 01-Prime-BSI-R-M-16-C). The camera has a chip size of 2048 pixels x 2048 pixels, with a pixel size of 6.5 µm x 6.5 µm. The images projected onto the camera have a pixel resolution of 97.5 nm, resulting in a 200 µm x 200 µm field-of-view. The field of illumination following beam shaping was 38 µm x 38 µm. Micromanager 2.0 was used for camera control and image acquisition.

3.2 Microscope construction and characterisation

The ROCS-SMLM microscope was constructed on an optical table with active vibration isolation and in a temperature- and humidity-controlled laboratory. It was built as a 30 mm optical cage system with an inverted epifluorescence design using optomechanical components from RayCage Photoelectric Technology (unless noted otherwise) with two ancillary components from Thorlabs. These components included a cage plate adapter base (Thorlabs, LCP4S) and three 30 mm cage xy translators (Thorlabs, CXY1A) that were used to mount the single-mode fibre and multi-mode fibre. The ROCS microscope was built as part of a previous project carried out by Hao Qiu (Octopus, Central Laser Facility) and Professor Lin Wang (Octopus, Central Laser Facility). Construction was followed by optical alignment to ensure all optomechanical components were centred on the optical axis and the lenses were arranged as $4f$ systems.

3.2.1 Measuring microscope specifications

Following construction, the pixel resolution of projected images, the size of the field of illumination, the power density at the focal plane, and the size of the point spread function (PSF) were measured to ensure accuracy in downstream image analyses. The pixel resolution was measured through brightfield illumination of a patterned microscope slide (Psyer Optics, S8) containing a series of graticules with a length of 1 mm in 10 µm divisions (Fig. A.1**a**). From an image of the graticules, the number of pixels between two adjacent graticules was measured in ImageJ (version 1.54f) [134]. Dividing 10 µm by the number of pixels yielded a pixel resolution of 97.5 nm/pixel.

The size of the field of illumination (FOI) was measured by acquiring an image of the laser spot illuminating a coloured fluorescent slide (Thorlabs, FSK5) using a low

power density (20 W / cm^2) and a camera exposure time of 3 ms. The diameter of the illumination spot, and thus the field of illumination, was measured in ImageJ by plotting a line profile across the centre of the spot, fitting a one-dimensional Gaussian function, and calculating the full width at half-maximum (FWHM). While the beam profile was expected to be a top-hat, in practice it was a widened Gaussian profile, thereby allowing the FOI to be measured from its FWHM.

With the FOI known, the power was calibrated by setting the laser power at 0 mW and increasing the power to its maximum in 5 mW increments. The output laser power at the objective lens was measured at the back focal plane using a power meter and power sensor (Thorlabs, PM100D and S121C). Finally, the power density was obtained by dividing the measured laser powers by the FOI.

The size of the point spread function was measured by imaging 100 nm-diameter Tetraspeck^{TM} beads (Invitrogen, T7279), which were used as a point source approximation, with a power density of 0.008 kW/cm^2. From a widefield image of fluorescent beads, a two-dimensional Gaussian function was fit to the emission profile of each fluorescent bead using ThunderSTORM version 1.3 [135]. The standard deviations of the fitted Gaussian functions were then averaged and used to calculate the FWHM of the PSF (Theory: Eq. 2.27).

3.3 Molecular Biology and Biochemical Methods

Molecular biology methods were employed to generate fusion proteins tagged with SNAP or fluorescent proteins, and to generate plasmids for protein expression and purification. All plasmids contained the *ampR* gene, which regulates ampicillin resistance, as a selection marker, and *lacZ*α for blue-white screening. The pOPINE plasmid was used for mammalian cell transfection and the pOPINVHH plasmid with a polyhistidine tag was used for protein purification [171, 172]. The DNA sequences of different proteins of interest are given in Appendix: A.5 and Appendix: A.7. Biochemical methods were used to purify nanobodies for downstream fluorescent labelling.

3.3.1 Polymerase chain reaction

Polymerase chain reactions were carried out in 50 µL reaction volumes containing: 1 µL of 100 ng/µL template DNA, 1 µL each of 100 µM forward and reverse primer, 25 µL of Phusion Flash High-Fidelity PCR Master Mix (Invitrogen, F548S), and nuclease-free water. The thermocycling conditions were as following: denaturation at 98°C for 10 s, primer annealing at 98°C for 10 s, elongation at 55°C for, and final elongation at 72°C for 20 s. The size of PCR products was verified by adding 10 µL of TriTrack loading dye (Thermo Scientific, R1161) and carrying out agarose gel electrophoresis at 90 V for 40 minutes with 1% (w/v) agarose. SYBR™ Safe (Invitrogen, S33102) was used for DNA visualisation and the HyperLadder™ 1 kb molecular weight marker (Meridian Bioscience, BIO-33053) was used to estimate the size of the PCR product. The PCR products were purified using a nucleoSpin® gel and PCR clean-up kit (Bioanalysis, 740609.50). Mutagenesis of single amino acids in nanobodies was carried out using primers encoding the mutation.

3.3.2 Expression vector construction

Restriction cloning was carried out to transfer either a gene of interest or genetically encoded tag from one plasmid to another. A 100 µL reaction mixture containing 1X rCutSmart™ buffer (New England Biolabs, B6004S), 2.5 µL of each restriction enzyme, 1 µg of DNA, and nuclease-free water was used for DNA digestion. The restriction enzymes NcoI (New England Biolabs, R0193S) and PmeI (New England Biolabs, R0560S) were used to excise the gene of interest while PmeI and Bsu36I (New England Biolabs, R0524S) were used to excise genetic tags. Restriction digests were carried out at 37°C for 1 h and the size of reaction products were verified with agarose gel electrophoresis as previously described.

Ligation-independent cloning was carried out between a digested plasmid and a PCR product to produce a new plasmid construct. A 10 µL reaction mixture containing 1X CE II buffer (Vazyme, C112-01), 2 µL of digested plasmid DNA, 2 µL of PCR product, 1 µL of Exnase II (Vazyme, C112-01), and nuclease-free water. Reactions were carried out at 42°C for 30 minutes. 10 µL Tris-EDTA buffer was added after the reaction ended

to prevent further reaction.

3.3.3 Transformation and plasmid extraction

To introduce recombinant plasmid DNA into bacteria, DNA transformation was carried out using *Escherichia coli* Stellar^{TM} Competent Cells (Takara Bio, 636763). 2 µL of plasmid DNA were added to 20 µL of cells on ice. The cell-DNA mixture was then incubated on ice for 30 minutes. The *E. coli* cells were heatshocked at 42 °C for 30 s and incubated on ice for 2 minutes. 200 µL of SOC medium (Invitrogen, 15544034) was then added and the cells were incubated at 37°C and 200 rpm for 1 h. Following incubation, 100 µL of cells were added to 1% (w/v) LB agar plates containing 100 µg/mL of ampicillin, 2 mM isopropyl β-D-1-thiogalactopyranoside (IPTG), and 40 µg/mL 5-bromo-4-chloro-3-indolyl-β-D-galactopyranoside (X-gal). The cells were then streaked and incubated overnight at 37°C for blue/white screening. White colonies—those containing the gene of interest—were selected, transferred into 4 mL or 50 mL of terrific broth (TB) containing 100 µg/mL of ampicillin, and incubated overnight at 37°C and 200 rpm. Following overnight incubation, plasmid DNA was extracted from *E. coli* using either the Miniprep kit (Qiagen, 12123) or Midiprep kit (Qiagen, 12143) for higher yields.

3.3.4 Protein expression

Recombinant *E. coli* were incubated overnight in 10 mL TB broth supplemented with 0.1% glucose, 1 mM $MgCl_2$, and 100 µg/mL ampicillin at 37°C and 225 rpm. The *E. coli* liquid culture was then upscaled to 1 L of TB broth culture with the same supplementation. Protein expression was induced with 1 mM IPTG at an OD_{600} of 0.8 followed by overnight incubation at 28°C, 225 rpm.

3.3.5 Protein purification

Nanobodies were purified from cells grown in TB broth using osmotic shock. Cultures were centrifuged at 5000 rpm, 4°C for 30 minutes to pellet cells which were then resuspended in TES buffer (0.2 M Tris, 0.5 mM EDTA, 500 mM sucrose, pH 8) and 50 mg of DNAase I overnight. The following day, two volumes of TES/4 (0.05 M Tris, 125

mM sucrose, pH 8) without EDTA were added and the suspension centrifuged at 12000 rpm, 4°C for 45 minutes. The supernatant was filtered with a 0.8 µm filter and diluted with 4 volumes of PBS. Nanobodies were purified from the supernatant via nickel affinity chromatography and gel filtration using an ÄKTA pure™. The wash buffer for affinity chromatography was: 50 mM Tris, 500 mM NaCl, 30 mM imidazole, pH 7.5, while the elution buffer was the same composition but with 500 mM imidazole. The buffer for gel filtration was: 20 mM Tris, 200 mM NaCl, pH 7.5. The proteins were then concentrated with a 5 kDa molecular weight cutoff filter (Sartorius, Vivaspin® 20) at 4000 g for 30 minutes. The size of the product was verified using SDS-PAGE with a NuPAGE™ 4–12% bis-tris gel (Thermo Scientific) and a PAGERuler™ Plus ladder (Thermo Scientific, 26634).

3.3.6 Fluorescent labelling of nanobodies at cysteine residues

Nanobodies were first incubated for 10 minutes on ice with 15 mM TCEP. 10 uL of 1 mM AF647-maleimide (Invitrogen, A20347) was then added and the nanobody-dye mixture was incubated at 4°C for two hours. Nanobody-dye conjugates were purified using Pierce™ dye removal columns (Thermo Scientific, 22858).

3.4 Sample preparation and fluorescent labelling

To quantify and compare the effects of different resolution-enhancing methods, a variety of proteins in different cells were fluorescently labelled. Typically, U2OS (ATCC, HTB-96) or HeLa (ATCC, CCL-2) cells were fixed and permeabilised prior to labelling. However, streptolysin-O was used to label live cells in culture. The Calu-3 cell line (ATCC, HTB-55) was also used to investigate the internalisation of SARS-CoV-2 spike protein. The labelling procedures for these samples is described in this section. All common chemical reagents were purchased from Sigma-Aldrich unless otherwise specified.

3.4.1 Fluorescent beads

200 µL of 0.01 % (w/v) poly-L-lysine was dispensed onto a 22 mm x 22 mm, #1.5 glass coverslip (VWR, 631-0124) and incubated for 1 hour at ambient temperature. 100 nm Tetraspeck™ beads were diluted in Milli-Q® water at a 1:100 ratio. The poly-L-lysine

was then removed and dried before the addition of the diluted bead solution. The beads were left to attach to the glass for 30 minutes at ambient temperature. Following this, the dilute bead solution was removed, and the coverslip was mounted onto a 25 mm x 76 mm coverslide (Scientific Laboratory Supplies, MIC3028).

3.4.2 Cell culture

The cell lines used in this project were: HeLa cells, U2OS cells stably expressing Nup96-SNAP, U2OS cells stably expressing Nup96-GFP, and Calu-3 cells. All cell lines were maintained at 37°C and 5% CO_2. HeLa cells and Calu-3 cells were maintained in high-glucose Dulbecco's Modified Eagle Medium (Gibco, 21063029) while U2OS cells were maintained in McCoy's 5A (modified) medium (Gibco, 16600082). All media was supplemented with 10% foetal bovine serum (Gibco, 16000044), 50 units/mL of penicillin (Gibco, 15070063), and 50 µg/mL of streptomycin (Gibco, 15070063). McCoy's 5A (modified) medium was further supplemented with minimum essential media with non-essential amino acids (Gibco, 11140050). Cells were passaged every 2–4 days using 1X Trypsin (Gibco, 11140050) to detach cells followed by splitting them at a ratio of 1:5 or 1:6. Prior to cell fixation or transfection, cells were plated onto coverslips sterilised with 70% (v/v) ethanol, 4-well glass bottom slides (Ibidi, 80427), or 8-well glass bottom slides (Ibidi, 80807) at a ratio of 1:4–1:6 and grown for 24–48 h.

3.4.3 Cell transfection

24 h after cell plating, cells were transfected using Fugene® HD Transfection Reagent. Plasmid DNA and transfection reagent were added to Opti-MEM (Gibco, 15392402) at a ratio of 1 µg of DNA to 2 µL of transfection reagent to a final volume of 100 µL per well and incubated at ambient temperature for 10 minutes. Half of the media was then removed from a well and 100 µL of the DNA-Fugene mixture was added. Cells were then incubated for 24–48 h before imaging or fixation.

3.4.4 Fluorescent labelling of Tubulin

Following incubation for 24 h, α-tubulin in HeLa cells was labelled according to ref. [173]. In summary, cells were first incubated for 30 s at 37°C with extraction buffer (0.25% [v/v]

Triton-X100 and 0.1% [v/v] glutaraldehyde) dissolved in PEM buffer (80 mM PIPES, 5 mM EGTA, 2 mM $MgCl_2$, pH 6.8) to remove cytosolic proteins. The extraction buffer was removed and cells were fixed with fixation buffer (0.25% Triton-X100 and 0.5% glutaraldehyde dissolved in PEM buffer) at 37°C for 10 minutes. The fixation solution was then removed and 0.1% $NaBH_4$ (w/v, dissolved in PBS) was added and incubated at ambient temperature for 7 minutes. $NaBH_4$ was then removed, and the cells were washed twice with PBS. Cells were subsequently blocked at ambient temperature for 2 h with blocking buffer which consisted of 0.22% (w/v) gelatin and 0.1% Triton-X100 dissolved in PBS. Following blocking, primary antibody solution (monoclonal anti-α-tubulin [Sigma-Aldrich, T5168] dissolved in blocking buffer) at a concentration of 1:200 was added and incubated overnight at 4°C. Afterwards, cells were washed three times with blocking buffer for 10 minutes each. Secondary antibody solution (donkey anti-mouse IgG (H+L) conjugated to Alexa Fluor 647 [Invitrogen, A32787] dissolved in blocking buffer) was added at a final concentration of 5 µg/mL. The secondary antibody was incubated for 1 h at ambient temperature after which cells were washed once with blocking buffer and twice with PBS. Cell samples were imaged immediately or stored at 4°C in 0.1% (w/v) sodium azide.

3.4.5 Nup96-SNAP labelling

All solutions were dissolved in PBS unless otherwise specified and all steps were performed at ambient temperature. U2OS cells stably expressing Nup96-SNAP were pre-fixed in 2.4% (v/v) paraformaldehyde (PFA) for 30 s before permeabilisation with 0.4% (v/v) Triton-X100 for 3 minutes. The cells were then washed with PBS and fixed for 30 minutes using 2.4% PFA. The PFA was subsequently quenched with 50 mM NH_4Cl for 5 minutes and washed twice with PBS. 500 µL of Image-iT^{TM} FX Signal Enhancer (Invitrogen, I36933) was then added and incubated for 30 minutes. Following this, cells were labelled with 1 µM SNAP-Surface® Alexa Fluor® 647 (New England Biolabs, S9136S, dissolved in 1 mM dithiothreitol [DTT] and 0.5% [w/v] bovine serum albumin [BSA]) for 2 h. Cells were then washed three times with PBS before imaging or storage in 0.1% (w/v) sodium azide at 4°C.

3.4.6 Nup96-GFP labelling

All solutions were dissolved in transport buffer (20 mM HEPES, 110 mM potassium acetate, 1 mM EGTA, 250 mM sucrose, pH 7.5) unless otherwise specified. U2OS cells stably expressing Nup96-GFP were pre-fixed in 2.4% (v/v) PFA for 30 s. The cells were then washed twice with transport buffer and the plasma membrane was permeabilised by adding 25 µg/mL digitonin to the cells on ice. Following permeabilisation, the cells were washed twice with 1% (w/v) BSA and incubated for 30 minutes on ice with the anti-GFP nanobody (dissolved in 1% BSA solution) at a concentration of 2 µM. After labelling, excess nanobodies were removed by washing twice for 5 minutes each with 1% BSA. The cells were fixed again in 3% PFA for 10 minutes and the nuclear membrane was subsequently permeabilised by adding 0.4% (v/v) Triton-X100 (dissolved in PBS). The cells were then washed twice with PBS and incubated on ice for 30 minutes with the anti-GFP nanobodies at a concentration of 1 µM. Excess nanobodies were washed by rinsing the cells twice with PBS for 15 minutes each. The labelled cells were stored in 0.1% (w/v) sodium azide at 4°C before imaging.

3.4.7 Streptolysin-O labelling

Streptolysin-O (SLO) is pore-forming protein secreted by *Streptococcus pyogenes* that facilitates pathogenesis [174]. Here, SLO was used as a method to deliver fluorescent tags into live cells. Labelling was carried out on cells with at least 75% confluency. 0.3 µL of 10 mM tris(2-carboxyethyl)phosphine (TCEP) was added to SLO for 20 minutes at 37°C for activation. The activated SLO and fluorescent nanobody were diluted with PBS for a total volume of 120 µL for 8-well slides and 300 µL for 4-well slides. The final concentrations of nanobody were 4–5 µM and the final concentrations of SLO ranged from 50–100 units in 120 µL. The mixture of SLO and fluorescent nanobody was added to cells for 8 minutes at 37°C. The mixture was then removed, and cells were washed once with PBS supplemented with 3 mM $MgCl_2$. DMEM supplemented with recovery buffer (1% FBS, 2 mM ATP, 2 mM GTP, and 2 mg/mL glucose) was added to cells for 30 minutes at 37°C. Following this, cells were imaged immediately or were fixed with 4% PFA for 10 minutes prior to imaging.

3.4.8 Vimentin labelling

HeLa cells or U2OS were fixed with 4% PFA for 10 minutes and permeabilised with 0.1% Triton-X100 for 3 minutes. The cells were then washed with PBS and blocked with 5% BSA for 2 h. Vimentin was then labelled overnight with the anti-vimentin nanobodies, VB3 or VB6 (dissolved in blocking buffer), conjugated to Alexa Fluor 647. The nanobody concentrations for purified nanobody was of 2–5 mg/ml and the nanobody was diluted at a 1:100 or 1:200 ratio for labelling. Following labelling, excess nanobodies were removed by washing once with PBS-T (0.1% [v/v] Tween 20) and twice with PBS.

3.4.9 ACE-2-SNAP labelling

24 h after transfection with the pOPINE-ACE-2-SNAP plasmid, Calu-3 cells were fixed with 4% PFA for 10 minutes and permeabilised with 0.05% Triton-X100 for 3 minutes. The cells were then washed with PBS and blocked with Image-iT^{TM} FX Signal Enhancer for 30 minutes before labelling for 2 h with 1 µM SNAP-Surface® ATTO 488 (New England Biolabs, S9136S, dissolved in 1 mM DTT and 0.5% BSA) for single-colour imaging. Finally, cells were washed thrice with PBS prior to imaging.

For two-colour imaging with AF647-labelled SARS-CoV-2 spike protein, 5 µL of purified spike protein, with a concentration of 2 mg/mL, was added to cell media and incubated for either 5, 15, or 30 minutes before fixation, permeabilisation, and SNAP labelling.

3.4.10 STORM buffer

STORM buffer was prepared from stock solutions of 1 M mercaptoethylamine (MEA) (Sigma-Aldrich, M6500), 10 mg/mL catalase (Sigma-Aldrich, C1345), 35 mg/mL glucose oxidase (Sigma-Aldrich, G7141), and 10% (w/v) glucose solution. All stock solutions were dissolved with a base buffer of 50 mM Tris-HCl and 10 mM NaCl at pH 7.5. The final concentration of MEA in the STORM buffer ranged from 35–100 mM while the final concentrations of catalase and glucose oxidase were 0.04 mg/mL and 0.5 mg/mL, respectively.

3.5 Conventional fluorescence microscopy

3.5.1 ROCS microscope: imaging fluorescent beads

A bead-coated coverslip was mounted on a coverslide such that the beads were sandwiched between the coverslip and coverslide. Duplicating silicone glue (Picodent, Twinsil 20) was spread around the edges of the coverslip to seal the sample. Fluorescent beads were illuminated with a 488 nm laser for excitation using a power density of 0.01 kW/cm^2. The fluorescence emission was filtered by a Chroma ET 525/50m bandpass filter before detection by the sCMOS camera. Images of beads were recorded with an exposure time of 100 ms.

For assessing drift, an image series of 240 frames, with images recorded every 30 s, was acquired. For this image series, image acquisition was synchronised with laser illumination such that the laser was only turned on during image acquisition, i.e. every 30 s, thereby minimising drift from thermal expansion introduced by laser heating and allowing mechanical drift to be assessed in isolation. The built-in autofocus function in Micromanager [175] and the piezoelectric stage were used for real-time correction of axial drift with the exception of when axial drift was quantified.

3.5.2 ZEISS AxioObserver Z1: imaging fluorescent beads

Fluorescence microscopy of 100 nm fluorescent beads was carried out with a high-NA, oil-immersion objective (ZEISS, α Plan-Apochromat, DIC M27, 100X, 1.46 NA) with an excitation wavelength of 488 nm and a power density of 0.01 kW/cm^2. The fluorescence emission passed through an MBS-488 dichroic mirror and a BP495-550/LP750 emission filter before detection by the EMCCD camera (Andor, iXon DU 897). Images were recorded with an exposure time of 100 ms and an EM gain of 300. As with the ROCS microscope, lateral drift was quantified from an image series where an image was recorded every 30 s for 2 h, resulting in an image series of 240 frames. Axial drift was corrected in real-time using the built-in definite focus functionality of the microscope with the exception of during axial drift quantification.

3.6 STORM image acquisition

3.6.1 ROCS microscope

Following preparation of STORM buffer, the buffer was dispensed into the cavity of a concave coverslide (Thorlabs, MS15C1) and a coverslip with fixed cells on its surface was mounted. The edges were sealed with duplicating silicone glue. The sample was then excited with the appropriate wavelength for the dye (488 nm for ATTO 488, 640 nm for Alexa Fluor 647) and a widefield image was acquired with a camera exposure time of 100 ms and a power density of 3 W/cm^2. A region of interest was then selected and cropped from the field of view. To transfer most fluorophores to a dark state and to establish a stable blinking state, the power was increased to roughly 4 kW/cm^2 and the exposure time was decreased to 20–30 ms. For image acquisition, the power was lowered to 1.6–2.4 kW/cm^2 and 30000–60000 frames were collected. The fluorescence emission was filtered by an appropriate bandpass filter (Chroma ET525/50m for green-fluorescing dyes, Chroma ET 690/50m for far-red-fluorescing dyes) before being detected by the sCMOS camera. For samples with low blinking density, illumination with the 405 nm laser was also used at a power density of 3 W/cm^2

3.6.2 Two-colour STORM

Prior to two-colour STORM, widefield images of 100 nm Tetraspeck^{TM} beads were recorded in the appropriate channels with the same power and exposure time as for the widefield image in STORM. Two-colour STORM was then performed sequentially, with a change in emission filter following image acquisition in the first channel. The Chroma ET525/50m bandpass filter was used for green-fluorescing dyes while the Chroma ET 690/50m bandpass filter was used for far-red-fluorescing dyes. 20000 frames were recorded for each channel with the power densities and exposure times as described above.

3.6.3 Zeiss Elyra PS.1 microscope

Samples were mounted with the same method as the ROCS microscope prior to imaging and illuminated with the appropriate excitation wavelength. Imaging was carried out

with a high-NA oil-immersion objective lens (ZEISS, α Plan-Apochromat, DIC M27, 100X, 1.46 NA) along with an MBP 405/488/642 dichroic mirror (ZEISS, 1784-996), a BP420-480/BP495-550/LP650 multi-bandpass emission filter (Carl Zeiss 1769-207) in the imaging path, and an EMCCD camera (Andor, iXon DU897) for detection. Wide-field images of the samples were collected with an exposure time of 200 ms, power density of 0.1 kW/cm^2, and EM gain of 50. The power density was increased to 14 kW/cm^2 to achieve a stable blinking state while the exposure time was decreased to 30 ms and the EM gain was lowered to 50. The power density was then decreased to 3.8 kW/cm^2 for image acquisition and the EM gain was increased to 250. The built-in definite focus functionality was used to correct axial drift in real-time during image acquisition.

3.7 Image processing and post-processing

3.7.1 Single-molecule localisation

The image sequences from SMLM and bead imaging were saved as 16-bit TIFF stack files. In the ROCS microscope, the following camera settings were used: offset = 100, pixel resolution = 97.5 nm, and 0.59 e$^-$ per analogue-digital unit. In the ZEISS Elyra microscope and ZEISS AxioObserver, the offset = 100, pixel resolution = 100 nm, 15.3 e$^-$ per analogue-digital unit, and gain = 250.

Sub-pixel localisation of fluorophores was carried out using ThunderSTORM in ImageJ. The images were filtered with a B-spline wavelet filter [176] with a third-order basis function and scaling factor of 2. The fluorophores were then located by detecting local intensity maxima with a threshold of 1.5σ—where σ is the standard deviation of intensity from the first wavelet level. Following this, the lateral positions of fluorophores were estimated by fitting a 2D integrated Gaussian PSF model via maximum likelihood estimation [128] (Theory: 2.3). A standard deviation of 1.62 pixels and a fitting radius of 5 pixels was used to define the approximate location of a fluorophore prior to Gaussian fitting. Parameter optimisation via maximum likelihood estimation (Theory: 2.3, Eq. 2.20) was carried out using the Nelder-Mead method [142]. The localisation precision was calculated as described by Theory: Eq. 2.24. The Normalized Gaussian setting was used for visualisation with a pixel size of 9.75 nm/pixel.

3.7.2 Postprocessing: filtering and drift correction

After sub-pixel localisation of fluorophores, abnormal data were first filtered by removing localisations with a localisation precision above 200 nm. The Remove Duplicates settings in ThunderSTORM was also used which groups fluorophores if their mutual distance is less than a specified threshold. Here, a threshold of 2*localisation precision was used.

Sample drift from STORM image sequences was corrected following filtering and removal of duplicates. The redundant cross-correlation [46] feature packaged in the Super-resolution Microscopy Analysis Platform (SMAP) [154] was used. Between 12–25 bins were typically used for drift correction.

3.7.3 Resolution quantification

The resolution from super-resolution images was quantified using the Fourier ring correlation method with FIRE—an ImageJ plugin provided by Nieuwenhuizen *et al.* 2013 [48], or with a custom routine [177] written in Python 3.13 based on the equations in Theory: 2.4. A custom routine was developed due to its greater ease in batch comparisons, customising input parameters, and so that analysis and visualisation could be carried out using the same software. For FRC calculations, the localisation data were split into two datasets either at the midpoint or by splitting via odd and even frames. A threshold of 1/7 was used. The pixel size for all FRC calculations was 10 nm/pixel. FRC curves were plotted using custom code in Python 3.13.

3.7.4 Drift quantification

The axial drift from the image sequence of beads was quantified from the estimated point spread function width, given as σ in the localisation table. For each frame, the average FWHM was calculated. The value of the average FWHM of the first frame was then used as a reference and the changes in FWHM with respect to this reference were calculated, resulting in a measure of axial drift over time.

The lateral drift from the image sequence of beads was quantified using a bead tracking algorithm in ThunderSTORM. This algorithm first automatically identifies the beads

from localisations that continuously fluoresce for a substantial amount of time. The drift trajectory for one image frame is then calculated by averaging the positions of all beads. This process is repeated for the entire image series, yielding the drift trajectory and bead positions as the output. The mean drift for an image series was quantified by averaging the drift trajectory over time. The positions of beads were plotted as scatter points while the drift trajectory was plotted as a curve.

For STORM image sequences, the lateral drift was quantified using the differences in xy-positions obtained from RCC. The mean drift for an image sequence was quantified by averaging the absolute values of the bins. Drift calculations and plotting were carried out using Python 3.13.

3.8 Single-molecule analysis

3.8.1 Quantification of photophysical parameters

Photoswitching kinetics were characterised from an SMLM image sequence as outlined by Bittel *et al.* 2016 [178]. In summary, single-molecules from the first 10000 frames of an image sequence were identified by filtering images with a difference of Gaussians filter using standard deviations of 2 pixels and 6 pixels, followed by local maxima identification with a threshold of 6 times the root mean square (RMS) intensity—both of which were standard procedures used by single-molecule localisation algorithms. An 8-pixel x 8-pixel region of interest containing the single-molecule was then extracted along the image series, resulting in an image substack for each molecule with dimensions of 8 pixels x 8 pixels x t, where t denotes the acquisition length for an image sequence. From this substack, the photons per switching cycle, number of switching cycles, total photon count, photoswitching time, and on/off duty cycle were calculated.

The number of switching cycles was calculated by counting the number of frames where the signal was above 6 times the RMS. Switching cycles were determined by identifying consecutive frames where the signal was above 3 times the RMS. The photons per switching cycle were calculated by summing the signal over each switching cycle. Total photon count was calculated by multiplying the number of photon cycles with the pho-

tons per switching cycles. The photoswitching time was determined by determining the time difference between the first switching cycle and the final switching cycle. Finally, the duty cycle was calculated by dividing the number of on frames with the number of off frames. All photophysical calculations were carried out using an analysis routine written in Python 3.13 [179].

3.8.2 Multi-colour analysis

After postprocessing, colocalisation analysis of two-colour STORM data was carried out using the algorithms described in Malkusch *et al.* 2012 [155]. In brief, channel registration was performed using widefield image of 100 nm diameter fluorescent beads that have been acquired with excitation wavelengths of 488 nm and 640 nm. The registration error was taken to be the median nearest neighbour distance from one channel to another following registration. A coordinate-based colocalisation (CBC) value was then calculated for all localisations in both channels (see Theory: section 2.6 for a more detailed description) where the maximum radius was 120 nm and the increment used was 15 nm. Multi-colour analysis was carried out using custom scripts in Python 3.13 [180].

3.8.3 Cluster analysis

The presence of clusters was determined by calculating Ripley's H-function [160], $H(r)$, along a search radius of 500 nm with an increment of 10 nm (Theory: 2.6.1). Clusters were then identified using hierarchical density-based spatial clustering with noise (HDBSCAN) [162], resulting in a cluster value assigned to each localisation. All localisations belonging to a particular cluster were subsequently extracted and cluster parameters—number of ACE-2 molecules, radius, area, density, and circularity—were calculated. From these parameters, dimensionality reduction was carried out using principal component analysis (PCA) to facilitate interpretation and visualisation of the cluster data. Cluster analysis was carried out using custom scripts in Python 3.13 [180].

3.9 Mirror-enhanced fluorescence imaging

22 mm x 22 mm x 5 mm glass slides coated with 10 nm silicon nitride, 50 nm silver, and 2 nm of germanium were purchased from Nanjing Bote Electro-Optics Co., Ltd. The slides were coated with 100 nm diameter fluorescent beads as previously described (3.4.1). The beads were imaged as described in Methods: 3.5.1. However, a widefield image was acquired instead of an image sequence.

U2OS cells stably expressing Nup96-SNAP were grown on the mirror-coated slides with the conditions as described in Methods: 3.4.2. Fluorescent labelling was carried out as previous (Methods: 3.4.5), except all reagents were made to a volume of at least 3 mL to ensure the cells on the slide were coated. STORM buffer was prepared as previous (Methods: 3.4.10) and dispensed onto a 22 mm x 50 mm #1.5 glass coverslip (VWR, 16004-336). The mirror-coated slide was then mounted such that the cells (middle) were sandwiched between the slide (top) and the coverslip (bottom, in contact with the objective lens). STORM imaging, single-molecule localisation, and postprocessing were carried out as previous (Methods: 3.6.1, 3.7.1, 3.7.2). Signal-to-noise ratio calculations of fluorescently labelled nuclei were carried out from widefield images by using a custom Python script to segment nuclei using the implementation of Otsu's method in the scikit-image Python package [133, 181]. The signal was taken to be the difference in mean intensity between the nuclei and the background while the noise was taken to be the standard deviation in intensity of the background.

3.10 Denoising with a Spatial redundancy transformer

3.10.1 Training and inference

The detailed implementation of the model is specified in Li *et al.* 2023 [81]. The denoising model was trained in all cases with the following settings: 6000 3D (xyt) training pairs, a patch size of 128 x 128 x 128 pixels, and the Adam optimiser [182]. The loss function for each training pair was a linear combination of L1-norm loss and L2-norm loss (Theory: 2.7). 1–4 NVIDIA A100-SMX4-80GB GPUs were used for training. The same settings and GPUs were used for inference, whereby the output was a denoised

image stack. Single-molecule localisation and postprocessing for denoised image stacks was carried out as previous (Methods: 3.7.1, 3.7.2). The deep learning architecture was implemented in Python 3.9.

Two custom loss functions were included to remove noise from unspecifically bound or out-of-focus fluorophores. The first loss function calculated the negative mean of the pixelwise absolute difference between adjacent frames, resulting in lower (more negative) loss if adjacent frames had low similarity and higher (less negative) loss if adjacent frames were very similar. Since the goal of training is to minimise loss, the aim of this loss function was to penalise the model for retaining pixels with little change in intensity, and therefore, slow photoswitching kinetics.

The second loss function first identified bright regions of the image substacks by applying a mask that retained pixels where the mean intensity over time was greater than 2.5% of the maximum intensity of each image. From these bright regions, the temporal variance was calculated for each pixel. Finally, the negative mean of the temporal variance was calculated, meaning that the loss was lower if the bright regions were photoswitching and higher if the bright regions were not photoswitching which may have corresponded to noise from out-of-focus fluorophores or aggregated unspecifically bound fluorophores.

3.10.2 Denoising evaluation

Denoising was evaluated on three independent image sequences of microtubules and nuclear pore complexes labelled with AF647, as well as three image sequences of ACE-2-SNAP labelled with ATTO 488 that had been incubated with SARS-CoV-2 spike protein. For the low-power NPC image sequence, the power density was 0.8 kW/cm^2. Subpixel localisation of the denoised image sequences was carried out using the settings specified in 3.7.1. The postprocessing procedures described in 4.8.2 were also applied to the denoised data. The FRC resolution comparisons were evaluated with the custom routine described above in Section: 3.7.3. The PANELJ plugin in Fiji was used for the evaluation of nuclear pore complex data using the rolling FRC algorithm [153]. Here, the settings were: a fixed threshold of 0.143 as the resolution criterion, a block size of 64 pixels, a background intensity of 15, and a pixel size of 10 nm.

The photon counts of denoised, and non-denoised image sequences were evaluated on three independent datasets of microtubules and nuclear pore complexes labelled with AF647. To ensure the same molecules were compared across the original and denoised image sequences, a custom localisation routine [183] was written in Python 3.13 with a similar algorithm to ThunderSTORM as outlined in Theory: 2.3. This custom routine differed in the choice of image filter, the threshold calculation for detecting single molecules, and the localisation precision calculation. A difference of Gaussians filter was used instead of a wavelet filter due to differences between wavelet filter implementations in Python and Java (which ThunderSTORM is written in). The threshold was based on a user-specified multiple of the RMS intensity of the filtered image, and the localisation precision was estimated by calculating and inverting the Fisher information matrix to obtain the Cramér-Rao lower bound, as described in Theory: Eqs. 2.21, 2.22, and 2.23. An intensity threshold of $3.5 * \text{RMS}$ was used.

3.11 List of Python packages

Several custom-written Python 3.13 analysis routines have been described, all of which depend on a number packages. These include: NumPy (version 2.2.6) [184], Matplotlib (version 3.10.6) [185], OpenCV (version 4.12.0.88) [186], SciPy (version 1.16.2) [187], scikit-learn (version 1.5.2) [188], Seaborn (version 0.13.2) [189], Numba (version 0.61.2) [190], Pandas (version 2.3.2) [191], Tifffile (version 2025.9.9) [192], PyArrow (version 21.0.0) [193], and RipleyK (version 0.0.3) [194]. In addition, SRDTrans uses the following packages: PyTorch (version 2.4.0) [195], timm (version 1.0.15) [196], einops (version 0.8.1) [197], and Scikit-image (version 0.24.0) [133]. The custom routines also contain the various dependencies which the above packages rely on.

4 Drift-free SMLM

4.1 Overview

As highlighted in Introduction: 1.2.1, sample drift presents major problems in the acquisition of reliable and reproducible SMLM data due to its worsening of localisation accuracy and necessitation of additional experimental procedures to correct drift. To overcome this limitation, a novel microscope design, termed reinforced optical cage systems (ROCS), is presented in this chapter. The results of this chapter have also been published in ref. [198]. However, all work presented herein is my own work.

The ROCS are inspired by reinforced concrete structures in civil engineering, where concrete is embedded with steel bars to improve resistance to shear, tensile, and compressive stresses [199]. Following this blueprint, the ROCS feature perforated optomechanical components that are directly affixed to an optical bench, and are rigidly interconnected with and supported by tungsten steel rods, thus preventing mechanical drift of the optical components—for example, lenses, mirrors, and filters—housed inside. In contrast, conventional optical cage systems use non-perforated optomechanical components that are affixed to an optical bench by an optical post and are neither interconnected nor supported by steel rods. As such, the mechanical stability of conventional optical cage systems is hypothesised to be worse than a ROCS microscope.

Prior to the results presented in this chapter, Hao Qiu (Octopus, Central Laser Facility) and Professor Lin Wang (Octopus, Central Laser Facility) had designed and constructed an SMLM-capable microscope using ROCS to overcome the instability inherent to conventional optical cage system microscopes, the design of which is described in Methods: 3.1. Guoli Li and Rong Su (Shanghai Institute of Optics and Fine Mechanics, Chinese Academy of Sciences) had also conducted vibrational mode analysis simulations [200] to compare the mechanical stability of the ROCS microscope compared to conventional optical cage system microscopes [198]. These simulations compared specific optical components, including the sample stage and right-angle kinematic mirrors, and demon-

strated that the mechanical stability was worse for conventional optical cage systems compared to the ROCS.

Following the simulation results, the goal of this chapter is to assess experimentally the ability of the ROCS microscope to negate drift by quantifying sample drift from widefield imaging of fluorescent beads. The drift quantification is then extended to direct stochastic optical reconstruction microscopy (dSTORM) of microtubules and nuclear pore complexes which represent a well-characterised one-dimensional and two-dimensional sample, respectively.

4.2 Mechanical stability in conventional fluorescence microscopy

To evaluate the mechanical stability of the ROCS microscope, 100 nm fluorescent beads were imaged using widefield microscopy. In this experiment, the laser was only turned on during image acquisition, allowing mechanical drift to be assessed in isolation. The autofocus function in Micromanager—which is responsible for active stabilisation of the focal plane during acquisitions—was also turned off to allow quantification of axial drift.

4.2.1 Evaluation of axial mechanical drift

The beads were imaged using a 488 nm laser over two hours, with one frame acquired every 30 s, resulting in a 240-frame image sequence. Single-molecule localisation was then carried out for each fluorescent bead in the image sequence, according to Theory: 2.3 and Methods: 3.7.1, to determine the xy localisations (x_0, y_0), PSF size (σ), background (b), and intensity (I_0), where the terms in brackets are from Theory: Eqs. 2.10, 2.11, 2.12. From the PSF size, the axial drift was quantified, as described in Theory :2.5 and Methods: 3.7.4. In total, five independent image sequences were acquired, resulting in five independent measures of axial drift.

The results from axial drift quantification using the ROCS microscope are shown in Fig. 4.1. Here, the mean change in PSF size over 240 frames ($\Delta\overline{\text{FWHM}}$) (Fig. 4.1**c**), using the first frame as a reference frame, was quantified, along with a 95% confidence interval. As the z-position of the microscope moves away from the focus, $\Delta\overline{\text{FWHM}}$

would be expected to increase or decrease [201]. The presence of axial drift, therefore, would result in a gradual increase or decrease in $\Delta\overline{\text{FWHM}}$.

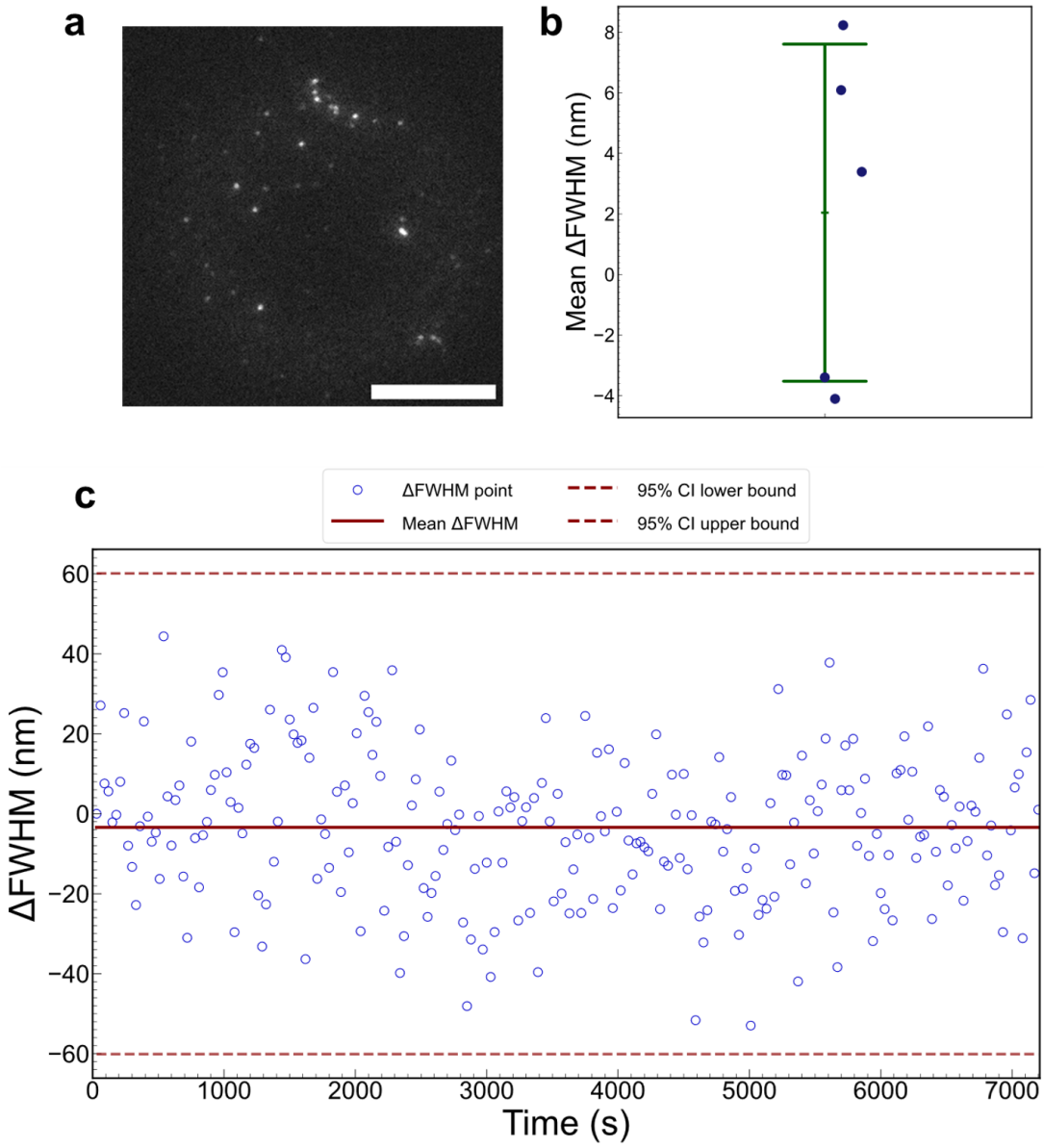

Fig. 4.1: **Axial drift quantification in conventional widefield microscopy using the ROCS microscope**. **a** Widefield image of the fluorescent beads. Scale bar: 10 µm. **b** Dotplot of $\Delta\overline{\text{FWHM}}$ for all five experimental repeats, where each dot represents one experiment. The central bar represents the mean of the five experiments which was 2.0 ± 5.6 nm. The upper and lower bars represent one standard deviation. **c** The mean change in the PSF sizes of the fluorescent beads in each frame, relative to the first frame, for one image sequence. The blue dots represent the average change in PSF size at each time point. The solid red line is the mean change in PSF size and was -3.4 ± 18.6 nm. The dashed red lines represent the upper and lower bounds of the 95% confidence interval which are -60.1 nm and 60.1 nm, respectively.

The mean change in PSF size was -3.4 ± 18.6 nm over 240 frames for the example shown in Fig. 4.1 and was 2.0 ± 5.6 nm for all five experimental repeats 4.1**b**. All values of $\Delta\overline{\text{FWHM}}$ also lay within the 95% confidence interval (Fig. 4.1**c**), indicating that there was no significant change in PSF size over time and that changes in PSF size could be

attributed to measurement variability rather than axial drift. Furthermore, the changes in PSF size were an order of magnitude below the depth of field of the microscope (∼500 nm), implying that the microscope had sufficiently high mechanical stability to prevent loss of focus in conventional fluorescence microscopy over two hours.

Similar axial drift was observed for other experimental repeats. All mean values of $\Delta\overline{\mathrm{FWHM}}$ were between -10 nm to 10 nm (Fig. 4.1**b**) and were also two orders of magnitude below the depth of field of the microscope. Therefore, it was unlikely that there was any measurable axial drift in the ROCS microscope over two hours.

As a comparison, the axial drift was evaluated on image sequences of 100 nm fluorescent beads, acquired using the ROCS microscope with autofocus turned on. In other words, with active stabilisation of the focal plane, to provide a reference standard for the measurement result from Fig. 4.1. This image sequence was acquired by Hao Qiu (Octopus, Central Laser Facility). The same analysis approach as presented in Fig. 4.1 was used, and five independent repeats were carried out.

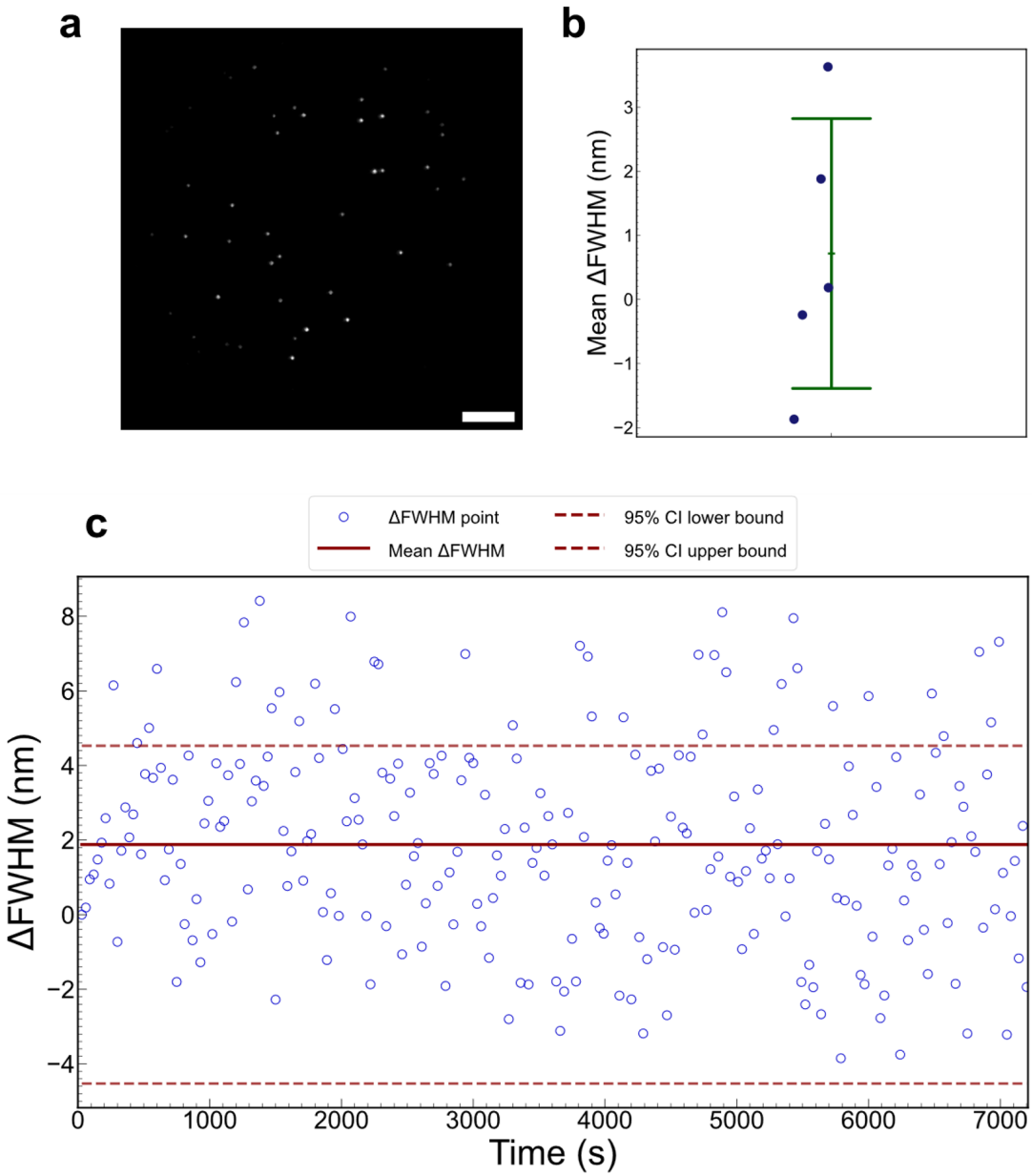

Fig. 4.2: **Axial drift quantification of fluorescent beads with autofocus enabled. a** Widefield image of the fluorescent beads. Scale bar: 10 µm. **b** Dotplot of $\Delta\overline{\text{FWHM}}$. The mean for all five experimental repeats was 0.7 ± 2.1 nm. **c** The mean change in the PSF sizes of the fluorescent beads over time. The mean was -1.9 ± 2.9 nm and the upper and lower bounds of the confidence interval was -10.0 nm and 10.0 nm, respectively.

From the axial drift quantification with active drift stabilisation (Fig. 4.2), the change in the PSF sizes for all five experimental repeats was 0.7 ± 2.1 nm (Fig. 4.2**b**). Similar to the results shown in Fig. 4.1, all of the PSF size changes were below the depth of focus of the microscope, and do not show an overall increase or decrease over the two hours of image acquisition (Fig. 4.2**c**), as would be expected from having active drift stabilisation. The similarity of the results with and without active stabilisation further supported the observation that the ROCS microscope did not exhibit significant axial

drift.

To further evaluate the stability exhibited by the ROCS microscope, the axial drift of fluorescent beads was quantified with a commercial ZEISS AxioObserver Z1 microscope. Again, image sequences were acquired without active z-axis stabilisation. However, unlike the ROCS microscope, clear axial drift was observed after five minutes (Fig. 4.3**a**). The same image acquisition settings from the ROCS microscope image sequences (one frame every 30 s for 240 frames total), therefore, could not be used. Instead, a camera exposure time of 100 ms was used with a total of 3000 frames, resulting in five minutes of image acquisition.

A substantially different pattern for $\Delta\overline{\text{FWHM}}$ was observed from the bead image sequences acquired with a commercial microscope (Fig 4.3). The mean $\Delta\overline{\text{FWHM}}$ across five experiments (Fig 4.3**c**) was 148.2 $\pm$ 54.3 nm which was two orders of magnitude higher compared to the same results from the ROCS microscope, with and without autofocus (Fig. 4.1**b**, Fig. 4.2**b**). The overall trajectory of the axial drift (Fig. 4.3**b**) also differed, with a clear increase in ΔFWHM, as opposed to the fluctuations in ΔFWHM observed from the ROCS microscope data (Fig. 4.1**c**, Fig. 4.2**c**). Of further note is the ΔFWHM reaching $\sim$ 380 nm—a value slightly exceeding the microscope depth of focus—after only five minutes (Fig. 4.3**b**), while the maximum ΔFWHM from the ROCS microscope was always at least one order of magnitude below the depth of focus over two hours. Therefore, the performance of STORM would likely be degraded without the use of active focal plane stabilisation.

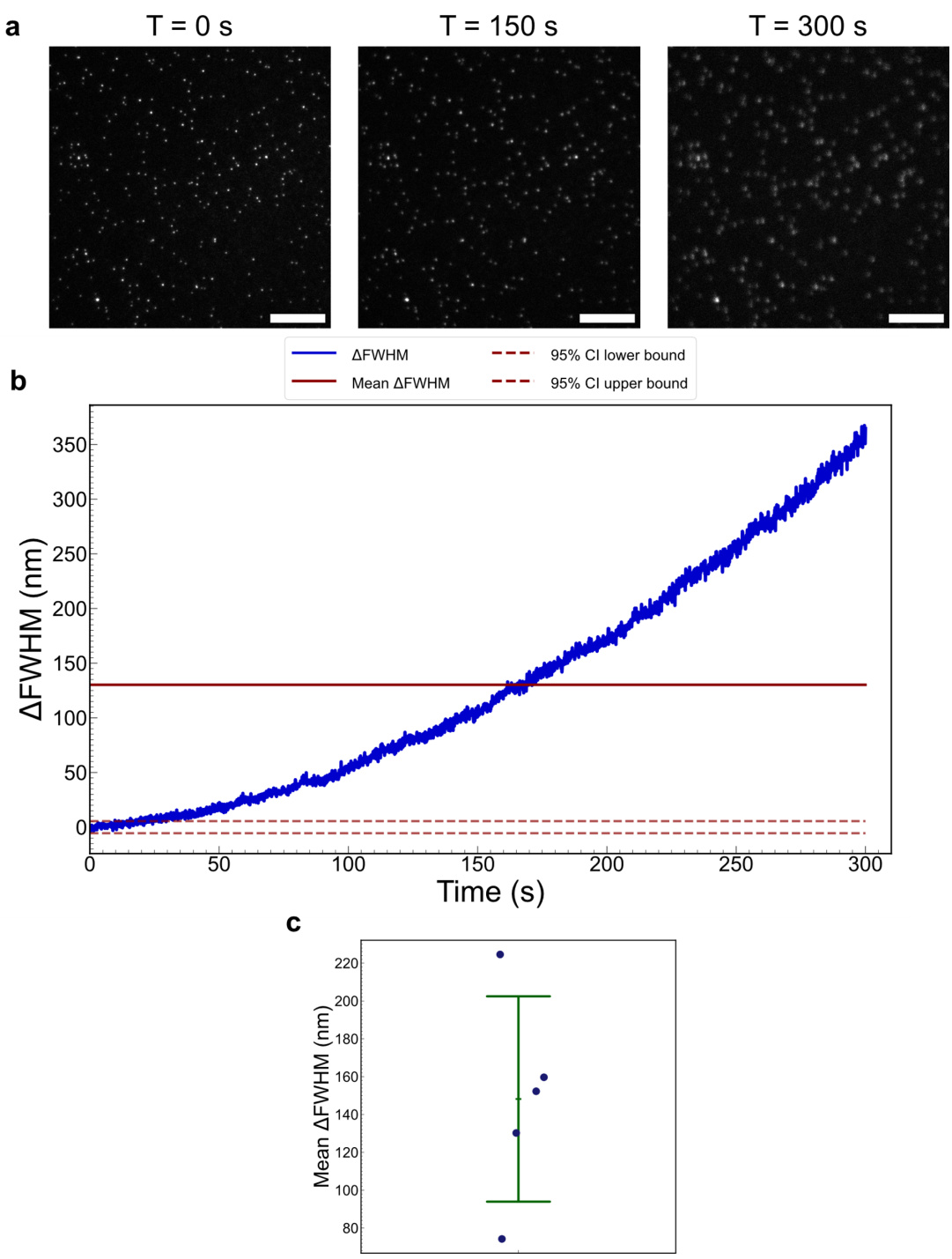

Fig. 4.3: **Axial drift quantification of fluorescent beads without active stabilisation using a commercial microscope. a** Widefield images of the fluorescent beads representing the start (T = 0 s), middle (T = 150 s), and end (T = 300 s) of the image acquisition, respectively. Slight defocus is visible at T = 150 s while clear loss of focus is observed at T = 300 s. Scale bar: 10 µm. **b** Change in the PSF sizes of fluorescent beads over five minutes of image acquisition. The mean $\Delta\overline{\mathrm{FWHM}}$ was 159.7 ± 127.8 nm while the upper and lower bounds for the confidence interval are -6.7 nm and 6.7 nm, respectively. The mean for all five experimental repeats was 0.7 ± 2.1 nm. **c** Dotplot of $\Delta\overline{\mathrm{FWHM}}$ for all five experimental repeats. The mean was 148.2 ± 54.3 nm.

In conclusion, these results demonstrated that the ROCS microscope could negate mechanical drift in the axial direction over two hours, thus offering an exceptional level of stability compared to commercial microscopes.

4.2.2 Evaluation of lateral mechanical drift

The lateral drift was quantified (Theory: 2.5, Methods: 3.7.4) using the same image sequences presented in Fig. 4.1 and Fig. 4.2. Here, the xy localisations were used to estimate the x and y drift trajectories of the beads from the image sequences, resulting in a drift value for x and y each for every frame, $\bar{x}_t$, $\bar{y}_t$. From the trajectories, the drift was quantified along x and y by taking the mean absolute value for all 240 frames to produce $\langle \bar{x} \rangle$, $\langle \bar{y} \rangle$. The trajectories—along with the xy positions of beads $(x_{i,t} - \theta_i \, , \, y_{i,t} - \theta_i)$—are plotted, as well as the distributions of the drift values $(\bar{x}_t \, , \, \bar{y}_t)$ of all frames.

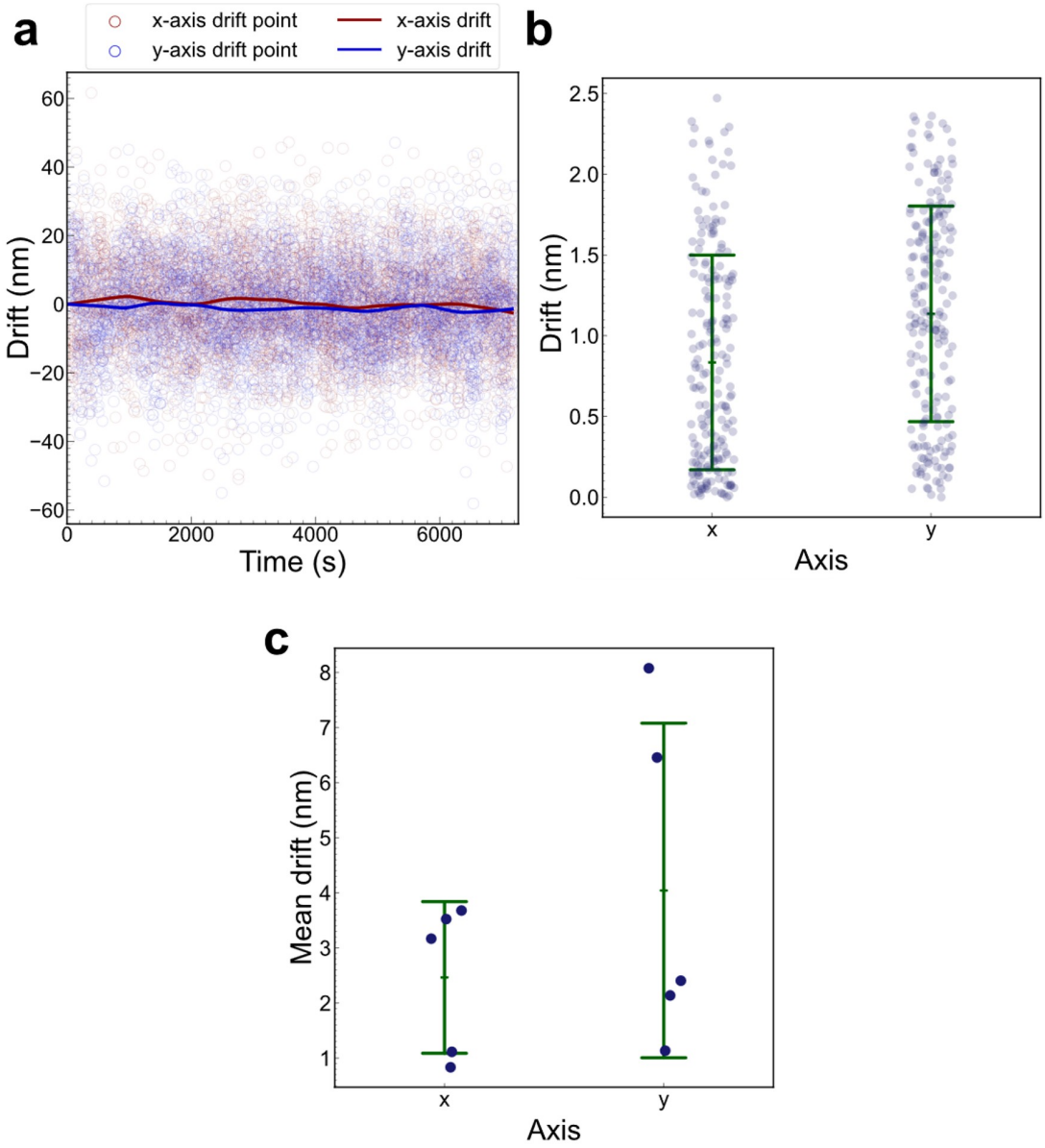

Fig. 4.4: **Lateral drift quantification of fluorescent beads without active stabilisation using the ROCS microscope. a** Lateral drift trajectory over two hours from the same image sequence as Fig. 4.1. The scatter points represent the bead xy positions, $x_{i,t} - \theta_i$, $y_{i,t} - \theta_i$ (see Theory: 2.5 for more details). The curves represent the overall trajectory, i.e. all values of $\bar{x}_t$, $\bar{y}_t$. **b** Dotplot of the absolute drift values for all frames from the drift trajectory plotted in **a**. The dots represent the absolute drift values for each frame. The central bar represents the mean drift which was 0.8 ± 0.7 nm along the x-axis and 1.1 ± 0.7 nm along the y-axis. The upper and lower bars represent one standard deviation. **c** Dotplot of the mean absolute drifts for all five experimental repeats. Each dot represents the mean absolute drift, $\langle \bar{x} \rangle$, $\langle \bar{y} \rangle$, for one experiment. The central bar is the mean which was 2.5 ± 1.4 nm along the x-axis and 4.0 ± 3.0 nm along the y-axis.

From the five image sequences acquired without autofocus, the overall lateral drift was 2.5 ± 1.4 nm along the x-axis and 4.0 ± 3.0 nm along the y-axis (Fig. 4.4**c**). For the example image sequence in Fig 4.4, the lateral drift was 0.8 ± 0.7 nm and 1.1 ± 0.7 nm

along the x-axis and y-axis, respectively, over two hours of imaging (Fig. 4.4**b**). Both drift measurements were at least two orders of magnitude below the diffraction limit of conventional fluorescence microscopy and were one order of magnitude lower than typical localisation precision values ($\sim$ 20 nm) attainable from STORM [19]. These results, combined with the axial drift measurements, demonstrate that the ROCS microscope exhibits negligible drift in all three dimensions over extended imaging periods.

The potential effects of active focal plane stabilisation on lateral drift of the ROCS microscope were also investigated. The same analysis approach from Fig. 4.4 was applied to the image sequences from Fig. 4.2.

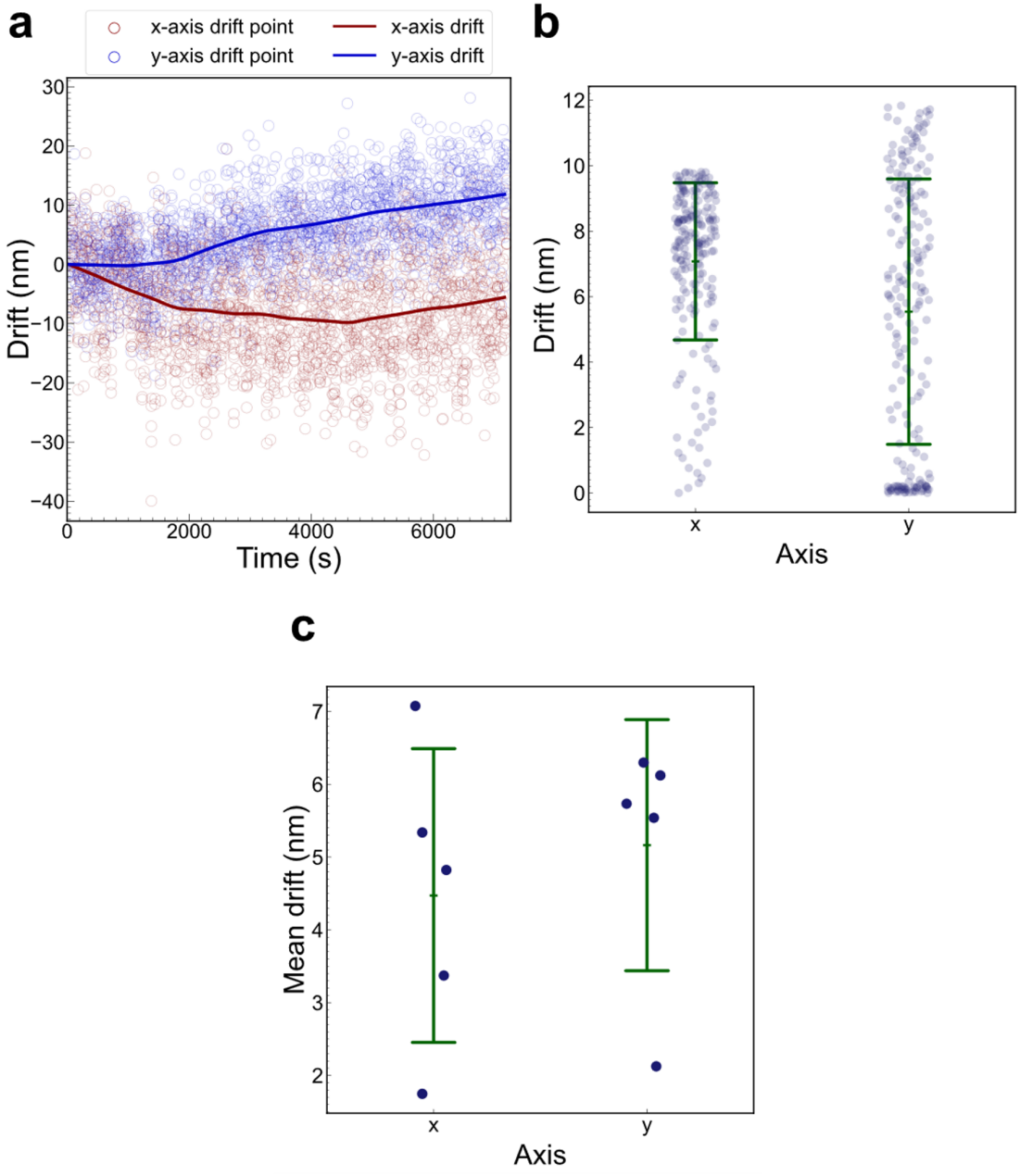

Fig. 4.5: **Lateral drift quantification of fluorescent beads with active stabilisation using the ROCS microscope. a** Lateral drift trajectory over two hours from the same image sequence as Fig. 4.2. The scatter points represent the bead xy positions. The curves represent the overall trajectory, i.e. all values of $\bar{x}_t$, $\bar{y}_t$. **b** Dotplot of the absolute drift values for all frames from the drift trajectory plotted in **a**. The dots represent the absolute drift values for each frame. The central bar represents the mean drift which was 7.1 ± 2.4 nm along the x-axis and 5.5 ± 4.0 nm along the y-axis. The upper and lower bars represent one standard deviation. **c** Dotplot of the mean absolute drifts for all five experimental repeats. Each dot represents the mean absolute drift for one experiment. The central bar is the mean which was 4.5 ± 2.0 nm along the x-axis and 5.2 ± 1.7 nm along the y-axis.

With active stabilisation, the lateral drift of the example bead image sequence from the ROCS microscope (Fig. 4.5**a**, Fig. 4.5**b**) was 7.1 ± 2.4 nm and 5.5 ± 4.0 nm along the x-axis and y-axis, respectively. For all five experimental repeats, the mean drift was 4.5

$\pm$ 2.0 nm along the x-axis and 5.2 $\pm$ 1.7 nm along the y-axis (Fig. 4.5**c**). The similarity of these results to those acquired without active axial drift stabilisation shows that the use of active stabilisation does not affect lateral drift. Together with the quantification of axial drift with and without active stabilisation (Fig. 4.1, Fig. 4.2), the lateral drift measurements demonstrated that the ROCS is capable of drift-free imaging without the use of additional software or hardware for real-time active drift stabilisation. The ROCS thereby offers a potential route to reduce cost and simplify hardware requirements without compromising performance.

As a final comparison to evaluate mechanical drift, the lateral drift of the commercial microscope used to obtain the results in Fig. 4.3 was also quantified with active drift stabilisation. The same experimental conditions and analysis approach as previous were used.

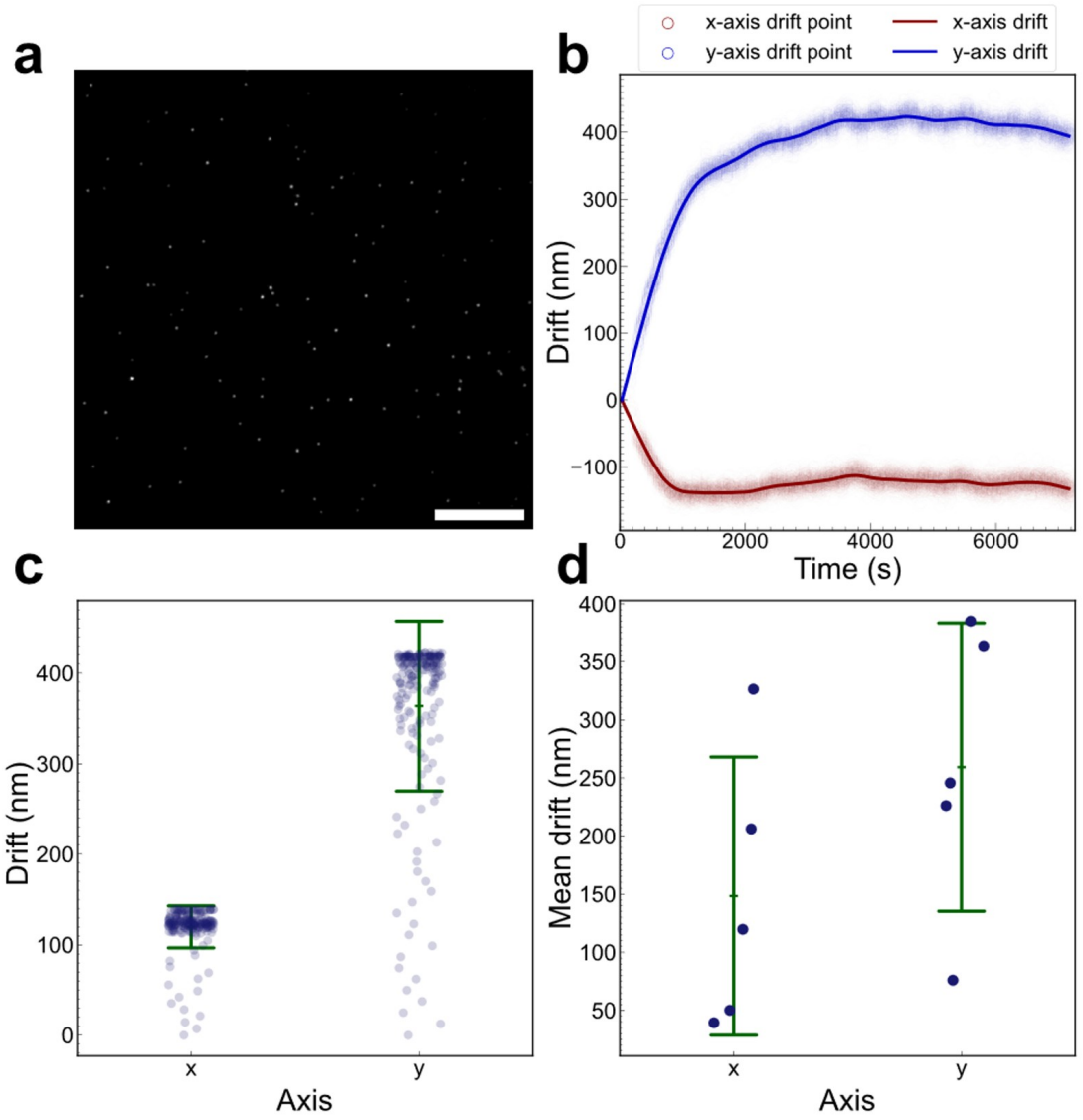

Fig. 4.6: **Lateral drift quantification of fluorescent beads with active stabilisation using the AxioObserver commercial microscope. a** Representative widefield image. Scale bar: 10 µm. **b** Lateral drift trajectory over two hours from a representative image sequence. The scatter points are the bead xy positions while the curves are the drift trajectory. **c** Dotplot of the drift values from **b** with the central bars denoting mean values of 119.7 ± 23.1 nm and 363.8 ± 93.7 nm along the x-axis and y-axis, respectively. **d** Dotplot of the lateral drift measurements from all five experimental repeats. The mean drift was 148.3 ± 119.8 nm along the x-axis and 259.4 ± 124.1 nm along the y-axis.

Quantification of lateral drift using the commercial microscope yielded values of 119.7 ± 23.1 nm and 363.8 ± 93.7 nm along the x-axis and y-axis, respectively, for the example image sequence (Fig. 4.6**b**, Fig. 4.6**c**), while mean drift values of 148.3 ± 119.8 nm and 259.4 ± 124.1 nm along the x-axis and y-axis, respectively, were calculated for all five experimental repeats (Fig. 4.6**d**). These drift measurements were two orders of magnitude greater than those in Fig. 4.4 and Fig. 4.5 and are substantially beyond typical lateral localisation precision values attainable in STORM.

In conclusion, the evidence from widefield imaging of beads over two hours supports the hypothesis that the ROCS can negate lateral and axial drift. The ROCS thus confers a level of mechanical stability unachievable even with a high-end commercial microscope. From the drift quantification, it is also hypothesised a negligible level of drift would be observable in STORM imaging, particularly because typical STORM image acquisitions are substantially shorter (15–30 minutes vs 2 hours [18]) than the acquisition times used to measure drift from fluorescent beads.

4.3 Evaluating sample drift in ROCS-STORM

The evidence from drift quantification in widefield microscopy suggested that mechanical drift would be negligible in STORM. In particular, the axial drift would have to exceed the depth of field of the microscope ($\sim$ 450 nm) to have a detrimental effect on the localisation precision. Since the recorded axial drift over two hours was two order of magnitude below this value, it was unlikely that the axial drift of the ROCS microscope would have affected STORM imaging. Furthermore, the severity of the axial drift of the commercial microscope relative to the ROCS microscope may have necessitated shorter acquisition times in STORM, potentially undersampling the structure of interest. As such, it would have likely been challenging to compare the ROCS and commercial microscopes solely on axial drift. For these reasons, the evaluation of sample drift in STORM was focused only on lateral drift and the Fourier ring correlation (FRC) resolution (Theory: 2.4).

The experimental approach for drift quantification was to carry out three independent repeats each of STORM imaging for microtubules and nuclear pore complexes (NPCs), the characteristics of which are described in Introduction: 1.4.1 and Introduction: 1.4.2, respectively. Both samples are common reference standards in SMLM [52, 93].

For drift quantification, the super-resolution image was first drift corrected by applying redundant cross-correlation (RCC) using the super-resolution microscopy analysis platform (SMAP) [154]. Qualitative assessments of super-resolution image quality before and after drift correction, as well as between the ROCS microscope and a commercial microscope (ZEISS Elyra PS.1), were first carried out, followed by quantitative assess-

ments of the lateral drift from the drift trajectories obtained from RCC (see Theory: 2.5 and Methods: 3.7.4 for more details). Finally, the image resolutions were compared by computing the FRC resolutions. The results of this analysis are sensitive to the method by which the localisation table is split to form two image halves, and the resolution criterion. In this chapter, the localisations were split at their midpoint to allow potential resolution degradation by sample drift to be assessed—an effect which would not be assessable by splitting the data by odd and even frames. A fixed FRC threshold of 1/7 (≈ 0.143) was also used to assess the resolution.

4.3.1 Evaluating sample drift from STORM imaging of microtubules

Microtubules in HeLa cells were immunolabelled according to Methods: 3.4.4 with an anti-α-tubulin primary antibody and a secondary antibody conjugated to Alexa Fluor 647 (AF647). STORM imaging was carried out over 15 minutes (33000 frames) as described in Methods: 3.6.1 and Methods: 3.6.3 for the ROCS microscope and commercial microscope, respectively. Single-molecule localisation was carried out as described in Theory: 2.3 and Methods: 3.7.1. The qualitative assessment from a representative STORM image acquired using the ROCS microscope is shown in Fig. 4.7 while the remaining ROCS STORM images are shown in Appendix: Fig. A.4 and the remaining commercial microscope STORM images are shown in Appendix: Fig. A.5.

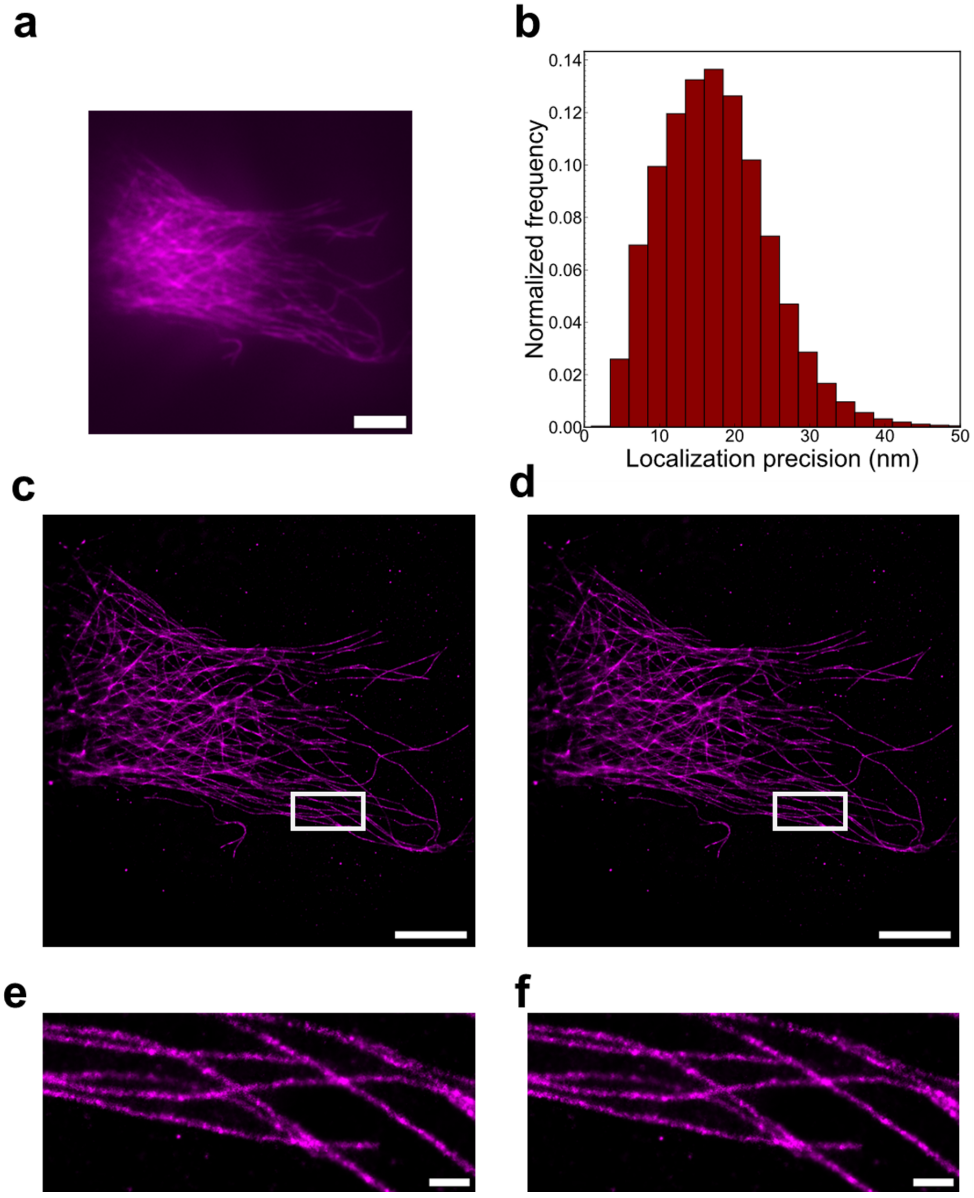

Fig. 4.7: **STORM imaging of immunolabelled ∝-Tubulin in HeLa cells using the ROCS-STORM microscope. a** Widefield image of microtubules. Scale bar: 5 µm. **b** Localisation precision histogram from the localisation data. The mean localisation precision was 17.5 ± 7.3 nm. **c** Super-resolution reconstruction from the first STORM image sequence without RCC drift correction. Scale bar: 5 µm. The remaining reconstructions are shown in Appendix: Fig. A.4. **d** Super-resolution reconstruction with RCC drift correction. Scale bar: 5 µm. **e** Magnified view of the region of interest enclosed by a white rectangle in **c**. Scale bar: 1 µm. **f** Magnified view of the region of interest enclosed by a white rectangle in **d**. Scale bar: 1 µm.

From the qualitative assessment of STORM image quality, more details of the microtubules were visible in the super-resolution images (Fig. 4.7**c**, Fig. 4.7**d**) compared to the widefield image (Fig. 4.7**a**). This observation, combined with a reasonable localisation precision of 17.5 ± 7.3 nm (Fig. 4.7**b**), confirmed that the ROCS was capable of STORM imaging with a similar performance to that described in the literature [18,

52, 202]. Further, there was little visible difference in the appearance of microtubules in the STORM images following drift correction (Fig. 4.7**e**, Fig. 4.7**f**, Appendix: Fig. A.4), implying that lateral drift did not adversely affect the image quality from STORM imaging using the ROCS microscope.

In comparison, the qualitative assessment of STORM image quality from the same biological structure using the commercial microscope revealed that while details of the microtubules not visible in the widefield image could be visualised with STORM (Fig. 4.8), they were blurred and indiscernible without RCC (Fig. 4.8**c**, 4.8**e**, Appendix: A.5). Differences in illumination and detection optics between the ROCS and commercial microscope were unlikely to have contributed to the difference in experimental outcomes due to the similarity in localisation precisions (19.0 $\pm$ 5.2 nm with the commercial microscope, compared to 17.5 $\pm$ 7.3 nm with the ROCS), indicating that single-molecule detection and fitting were of similar accuracy.

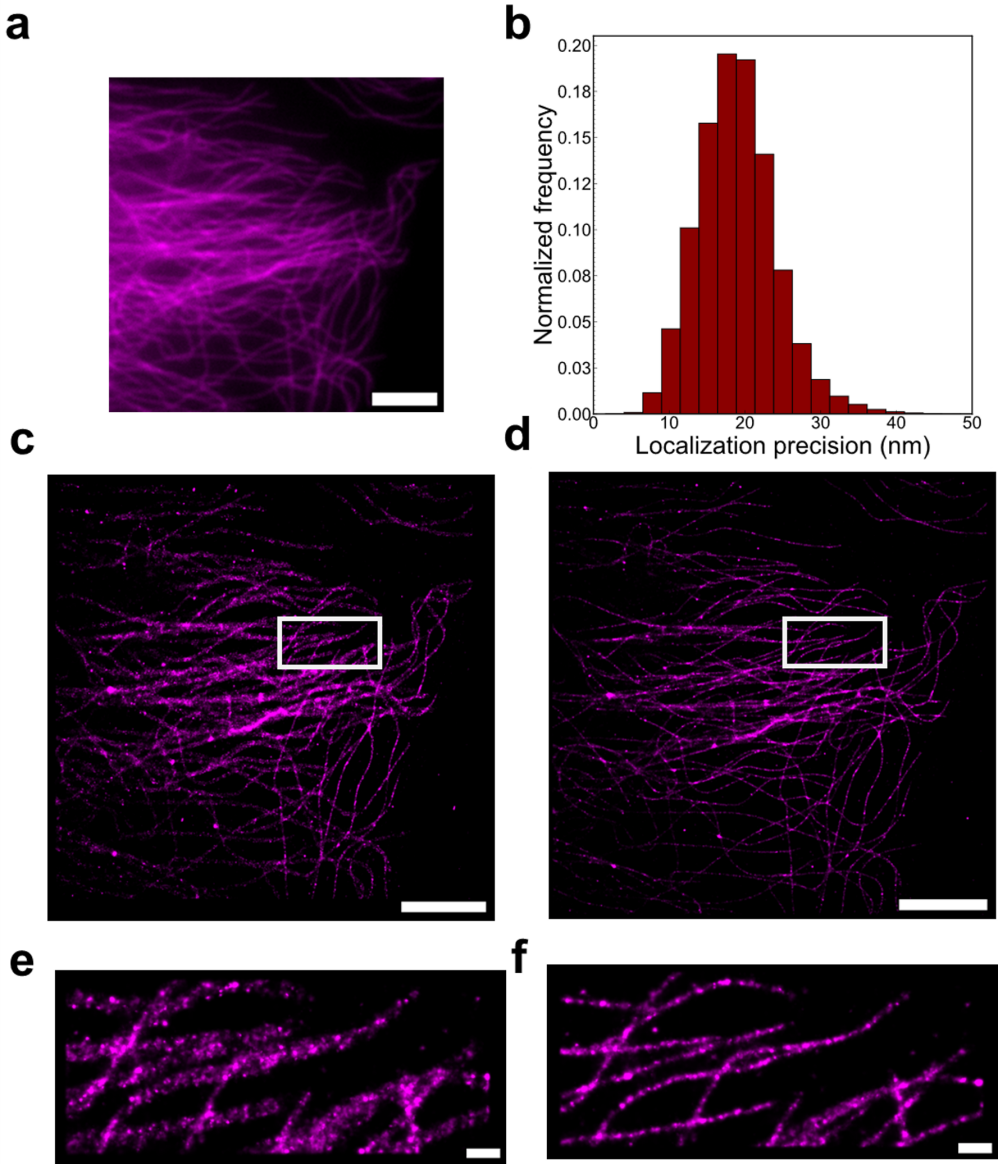

Fig. 4.8: **STORM imaging of immunolabelled α-Tubulin in HeLa cells using the commercial ZEISS Elyra PS.1 microscope. a** Widefield image of microtubules. Scale bar: 5 µm. **b** Localisation precision histogram from the localisation data. The mean localisation precision was 19.0 ± 5.2 nm. **c** Super-resolution reconstruction from the first STORM image sequence without RCC drift correction with clear blurring from sample drift. Scale bar: 5 µm. The remaining reconstructions are in Appendix: Fig. A.5. **d** Super-resolution reconstruction with RCC drift correction. Scale bar: 5 µm. **e** Magnified view of the region of interest enclosed by a white rectangle in **c**, showing blurring from sample drift. Scale bar: 1 µm. **f** Magnified view of the region of interest enclosed by a white rectangle in **d**. Scale bar: 1 µm.

To quantify lateral drift, RCC was applied to the localisation data from STORM, splitting the data into several subsets, from which lateral drift was estimated [45, 46]. The drift was then quantified for one set of STORM data by taking the mean of the absolute drift values from all subsets to yield $\langle \bar{x} \rangle, \langle \bar{y} \rangle$ (Theory: 2.5, Methods: 3.7.4). This procedure was repeated for all three experimental repeats to obtain the final lateral drift quantification metric.

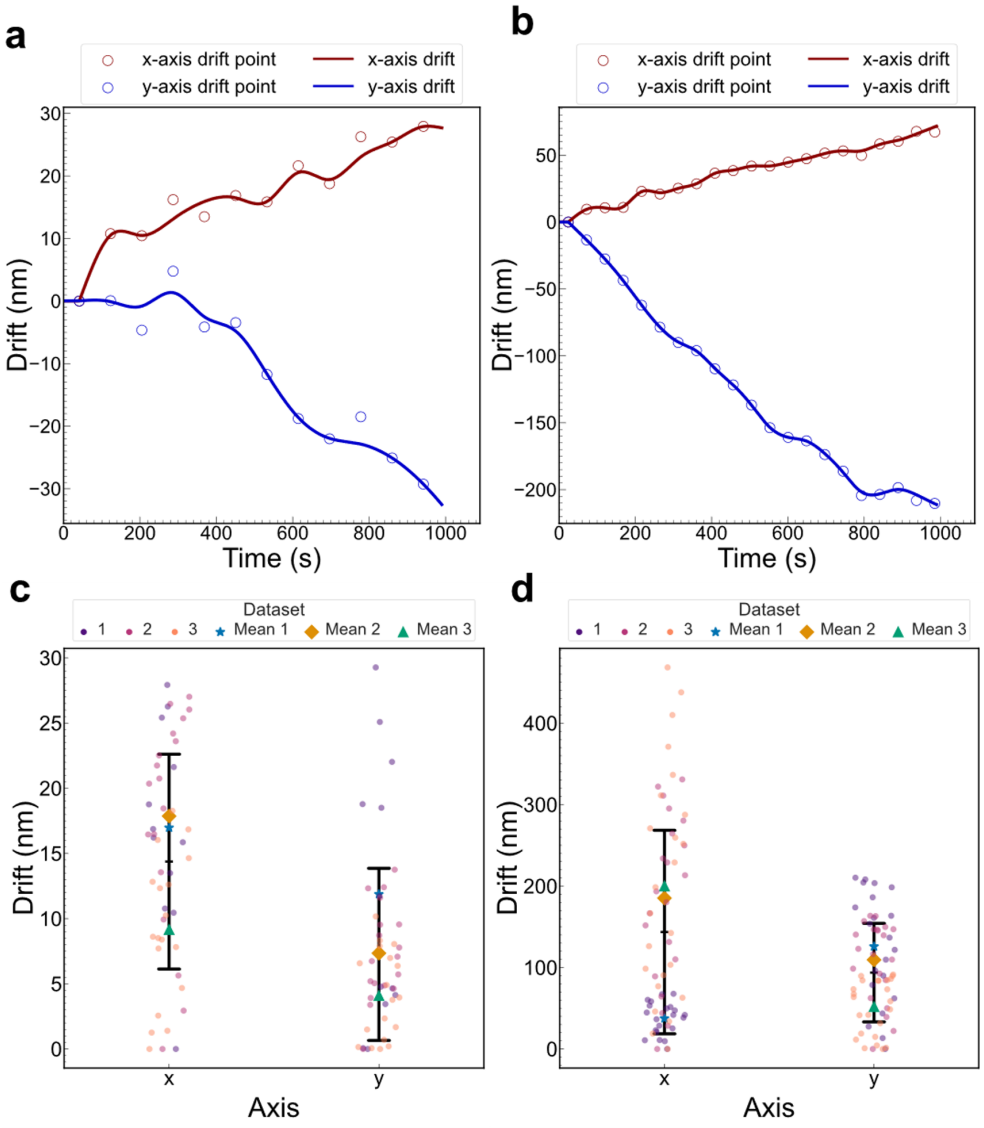

Fig. 4.9: **Quantitative comparison of lateral drift between the ROCS and commercial microscope. a** Drift trajectory from the first STORM image sequence of microtubules using the ROCS microscope. The drift trajectories of the two other image sequences are shown in Appendix: A.3.1. The scatter points represent the drift estimated from each image subset while the curves represent the drift trajectory. The localisation data were divided into 12 subsets. The mean sample drift was 17.0 ± 7.6 nm along the x-axis and 11.9 ± 9.9 nm along the y-axis. **b** Drift trajectory from the same biological structure as **b** but from the commercial microscope. The mean sample drift was 37.5 ± 19.4 nm along the x-axis and 125.8 ± 67.1 nm along the y-axis. The localisation data were divided into 21 subsets. **c** Dotplot of the estimated drift of image subsets from each STORM image sequence acquired with the ROCS microscope, as well as the mean drift from each STORM dataset. A blue star, orange diamond, and green triangle denote the mean drifts of datasets 1, 2, and 3 respectively. Each dot represents the drift from an image subset and is colour-coded depending on the dataset. The central bar is the mean across all repeats while the upper and lower bars represent one standard deviation. The mean drifts of datasets 2 and 3, in the order (x-drift, y-drift), were (17.9 nm, 7.3 nm) and (9.2 nm, 4.1 nm), respectively. The overall mean drift was 14.4 ± 8.2 nm along the x-axis and 7.3 ± 6.5 nm along the y-axis. **d** Same plot as **c** but for image sequences acquired with the commercial microscope. The mean drifts of datasets 2 and 3 were (185.2 nm, 109.4 nm) and (199.9 nm, 51.9 nm), respectively. The overall mean drift was 143.6 ± 124.0 nm along the x-axis and 93.7 ± 60.0 nm along the y-axis.

Large differences in sample drift between the ROCS microscope and commercial microscope were observed from the lateral drift quantification. For the ROCS, the drift from the example dataset was 17.0 ± 7.6 nm along the x-axis and 11.9 ± 9.9 nm along the y-axis (the remaining drift trajectories are in Appendix: A.3.1), while the overall drift was 14.4 ± 8.2 nm along the x-axis and 7.3 ± 6.5 nm along the y-axis (Fig. 4.9**a**, Fig. 4.9**c**). In contrast, the sample drift from the commercial microscope was higher with the example dataset exhibiting drift of 37.5 ± 19.4 nm along the x-axis and 125.8 ± 67.1 nm along the y-axis (Fig. 4.9**b**), and the measurements from all repeats exhibiting drift of 143.6 ± 124.0 nm along the x-axis and 93.7 ± 60.0 nm along the y-axis (Fig. 4.9**d**). This analysis corroborates the drift measurements from widefield imaging in that the ROCS microscope confers minimal sample drift that is unattainable with off-the-shelf commercial microscopes.

To further assess the effect of sample drift on the resolution performance of the ROCS microscope, the FRC resolutions before and after drift correction were compared. If sample drift was minimised to negligible levels, the FRC resolutions would be expected to be similar before and after drift correction while large differences in FRC resolutions would be expected if sample drift were high. Three independent experimental repeats were carried out with a representative example and the mean FRC resolution across the repeats shown in Fig. 4.10 and Table 4.1, respectively.

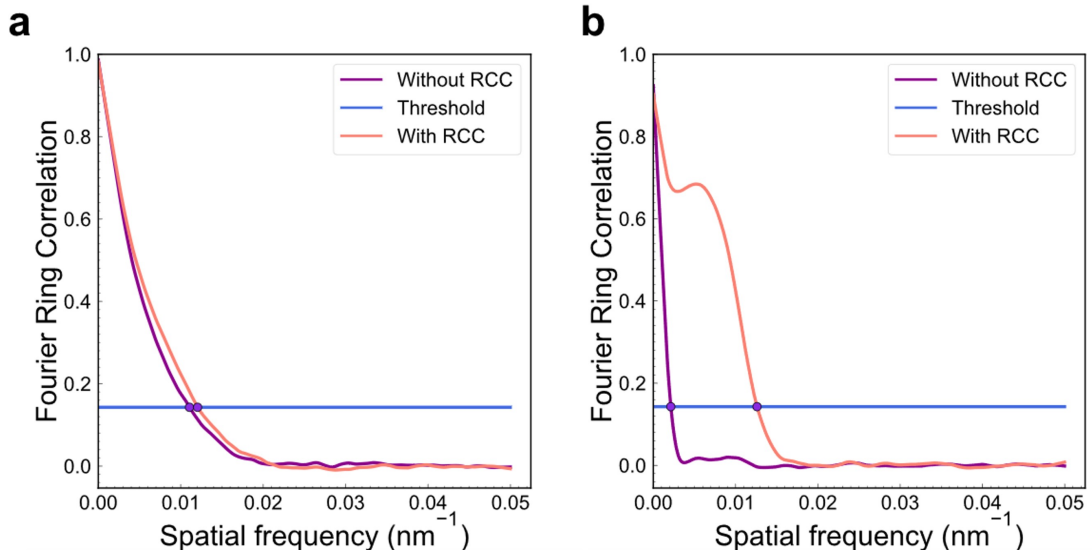

Fig. 4.10: **Comparisons of microtubule FRC resolutions before and drift correction from a representative example. a** Representative example of the FRC resolutions of a STORM image of microtubules acquired with the ROCS microscope. The FRC resolutions before and after RCC were 90.4 nm and 83.0 nm, respectively. **b** Representative example of the FRC resolutions of a STORM image of microtubules acquired with the commercial microscope. The FRC resolutions before and after RCC were 312.5 nm and 50.9 nm, respectively. A threshold of 1/7 (≈ 0.143) was used for all calculations.

Table 4.1: **Mean FRC resolutions of microtubule STORM images acquired with the ROCS and commercial microscopes before and after RCC.**

Microscope	Before/after RCC	Mean FRC resolution (nm)
ROCS	Before	92.6 ± 4.4
ROCS	After	81.9 ± 0.9
Commercial	Before	461.7 ± 107.4
Commercial	After	109.0 ± 41.1

As anticipated, the resolution of the STORM images from the ROCS microscope were similar before and after drift correction, with a difference of approximately 9 nm in the mean FRC resolution following RCC (Table 4.1). In contrast, the FRC resolution increased substantially following drift correction in the data acquired with the commercial microscope, with an approximately 4.2-fold increase in the mean FRC resolution, highlighting the consistent detrimental effect of sample drift on image resolution.

Notably, the measured drift from the ROCS microscope was below half the measured resolutions in all experimental repeats (Fig. 4.9**c**, Fig. 4.10**a**) which was not observed for the STORM images from the commercial microscope. Taken together, the FRC resolutions and the drift quantification highlight that the ROCS microscope can prevent

sample drift from degrading the resolution of STORM images resolutions—a capability that is unachievable in standard commercial microscopes without additional drift correction.

4.3.2 Evaluating sample drift from STORM imaging of NPCs

To further investigate the improvement in stability conferred by the ROCS microscope, STORM imaging of NPCs was carried out. Here, a U2OS cell line engineered to express endogenously the nuclear pore complex protein nucleoporin 96 (Nup96) fused to a SNAP-tag [50] was used, thereby permitting labelling with Alexa Fluor 647 (Methods: 3.4.5) followed by STORM imaging. The same experimental approach for STORM, single-molecule localisation, and drift quantification as the microtubule data was applied to the NPC data.

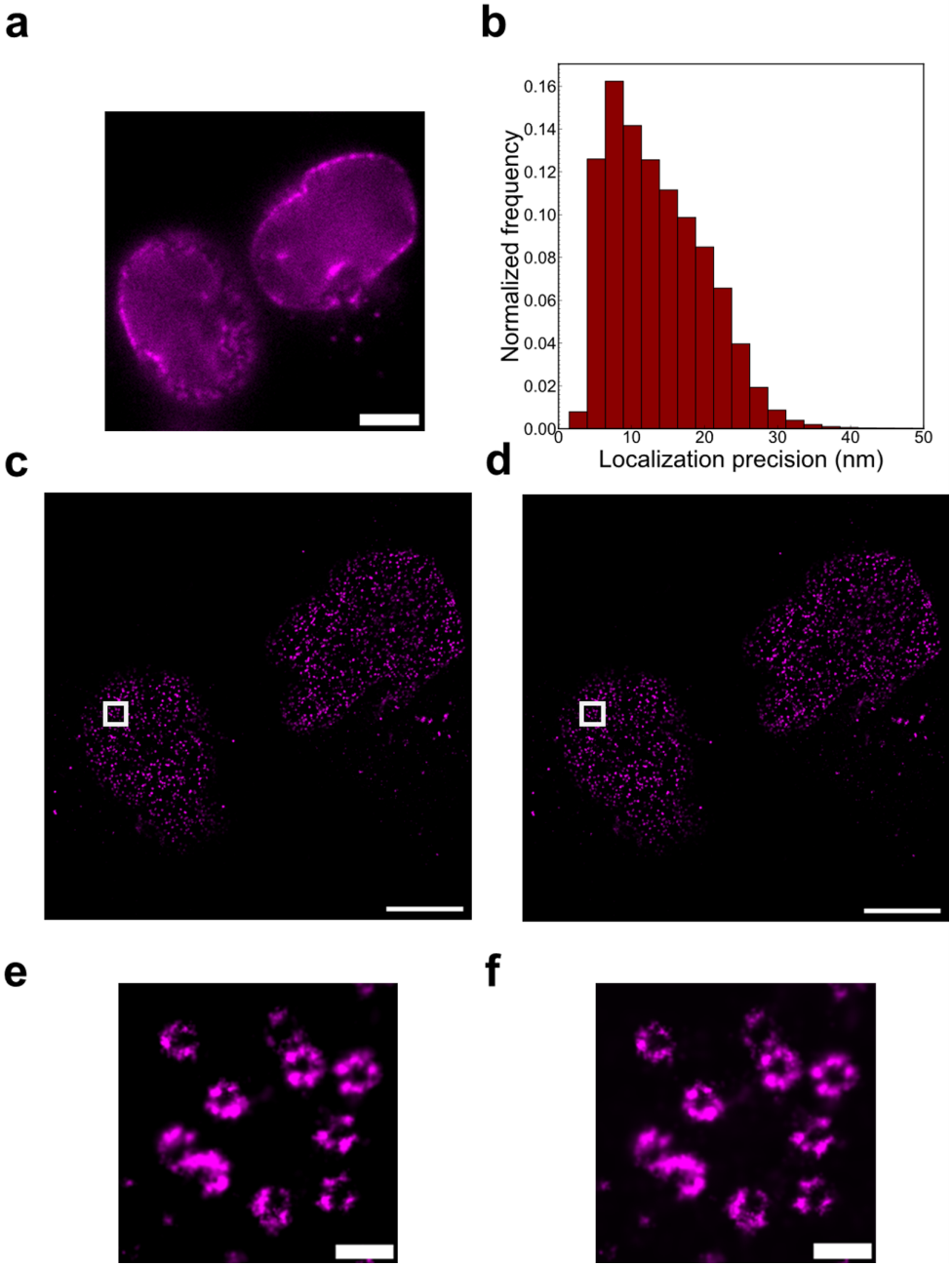

Fig. 4.11: **STORM imaging of Nup96-SNAP-Alexa Fluor 647 in U2OS cells using the ROCS microscope. a** Widefield image of two nuclei. Scale bar: 5 µm. **b** Localisation precision histogram of the single-molecule localisations. The mean localisation precision was 13.6 ± 6.6 nm. **c** Super-resolution reconstruction of two nuclei from the first STORM image sequence without RCC drift correction. Scale bar: 5 µm. The remaining reconstructions are in Appendix: Fig. A.4. **d** Super-resolution reconstruction of the same image sequence with RCC drift correction. Scale bar: 5 µm. **e** Magnified view of the region of interest enclosed by the white square in **c**. Scale bar: 0.2 µm. **f** Magnified view of the region of interest enclosed by the white square in **d**. Scale bar: 0.2 µm.

The qualitative assessment of STORM image quality from a representative image sequence of NPCs was similar to those from microtubule STORM imaging; the localisation precision of 13.6 ± 6.6 nm was indicative of reasonable single-molecule detection and

localisation (Fig. 4.11**b**), and little difference in the ring structures of NPCs was visible following drift correction (Fig. 4.11**e**, Fig. 4.11**f**, Appendix: Fig. A.4).

Again, the image sequences from the ROCS microscope were compared to the commercial microscope following the same experimental approach as previous.

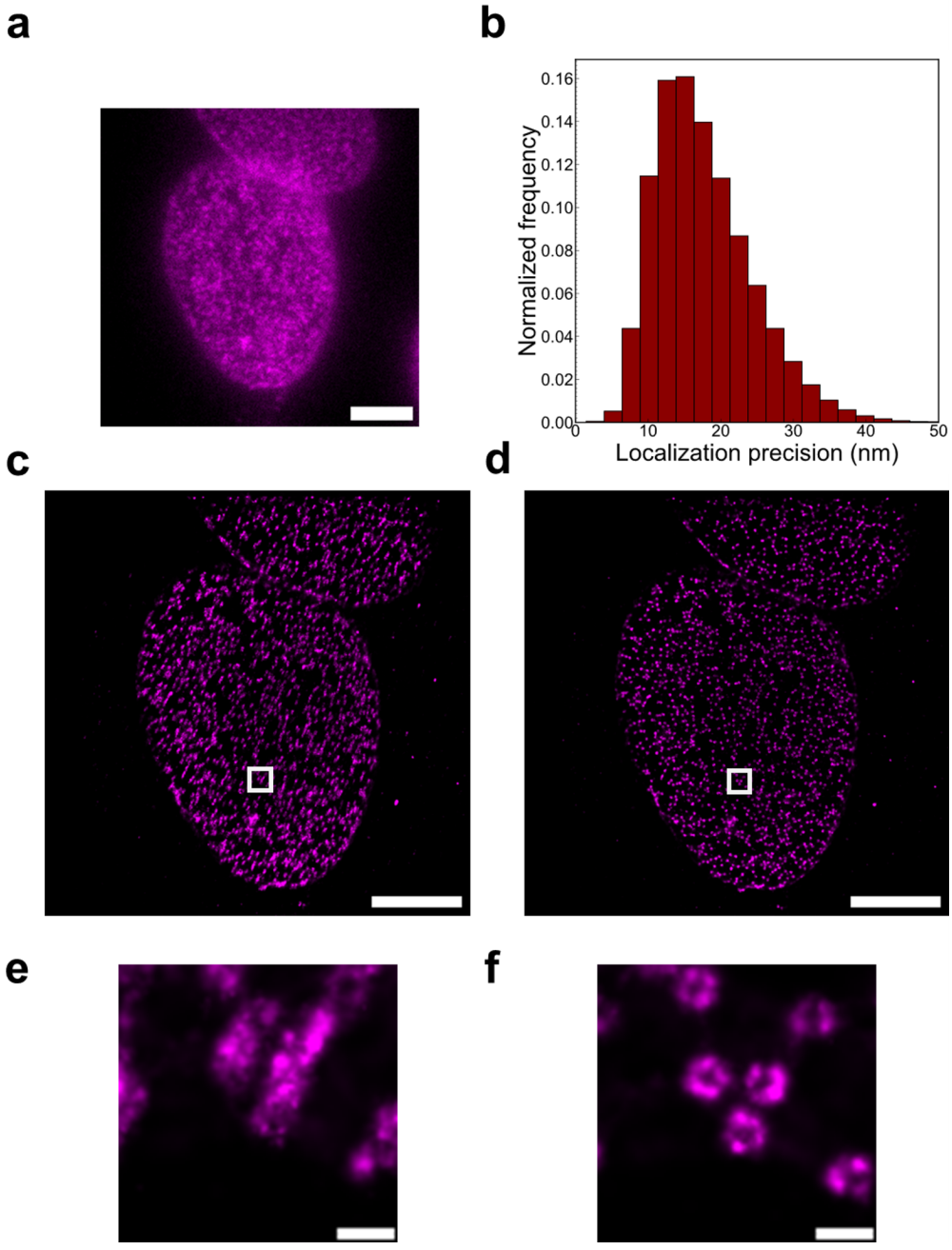

Fig. 4.12: **STORM imaging of Nup96-SNAP-Alexa Fluor 647 using the commercial Elyra PS.1 microscope. a** Widefield image of a nucleus. Scale bar: 5 µm. **b** Localisation precision histogram. The mean localisation precision was 17.7 ± 6.6 nm. **c** Super-resolution reconstruction from the first STORM image sequence without RCC. Scale bar: 5 µm. The remaining reconstructions are shown in Appendix: A.5. **d** Super-resolution reconstruction with RCC. Scale bar: 5 µm. **e** Magnified view of the region of interest enclosed by the white square in **c**. Scale bar: 0.2 µm. **f** Magnified view of the region of interest enclosed by the white square in **d**. Scale bar: 0.2 µm.

Similar to the qualitative assessment of microtubules, significant drift was visible in the STORM images acquired using the commercial microscope (Fig. 4.12**c**, Fig. 4.12**e**, Appendix: Fig. A.5), with the ring structures of NPCs indiscernible without RCC (Fig. 4.12**f**). The mean localisation precision of 17.7 ± 6.6 nm was also similar to the NPC data from the ROCS microscope (Fig. 4.12**b**, Fig. 4.11**b**), highlighting the similarity of performance for single-molecule localisation. Therefore, the differences in image quality could be attributed purely to the difference in stability between the two microscopes.

Quantification of the lateral drift from all experimental repeats of NPC STORM imaging corroborated the observations from the qualitative analysis (Fig. 4.13). For the ROCS, the drift from the example NPC dataset was 9.9 ± 6.1 nm along the x-axis and 10.3 ± 5.4 nm along the y-axis (the remaining drift trajectories are shown in Appendix: A.3.1), while the drift across all repeats was 6.8 ± 5.2 nm along the x-axis and 8.2 ± 5.2 nm along the y-axis (Fig. 4.13**a**, Fig. 4.13**c**). Similar to the microtubules, sample drift from the commercial microscope was higher with the example dataset and for all repeats. The drift for the example dataset was 53.4 ± 29.8 nm along the x-axis and 135.2 ± 65.7 nm along the y-axis while for all repeats, it was 89.3 ± 62.0 nm along the x-axis and 82.0 ± 59.6 nm along the y-axis (Fig. 4.13**b**, Fig. 4.13**d**). These measurements further illustrate the enhancement in stability offered by the ROCS microscope relative to commercial microscopes.

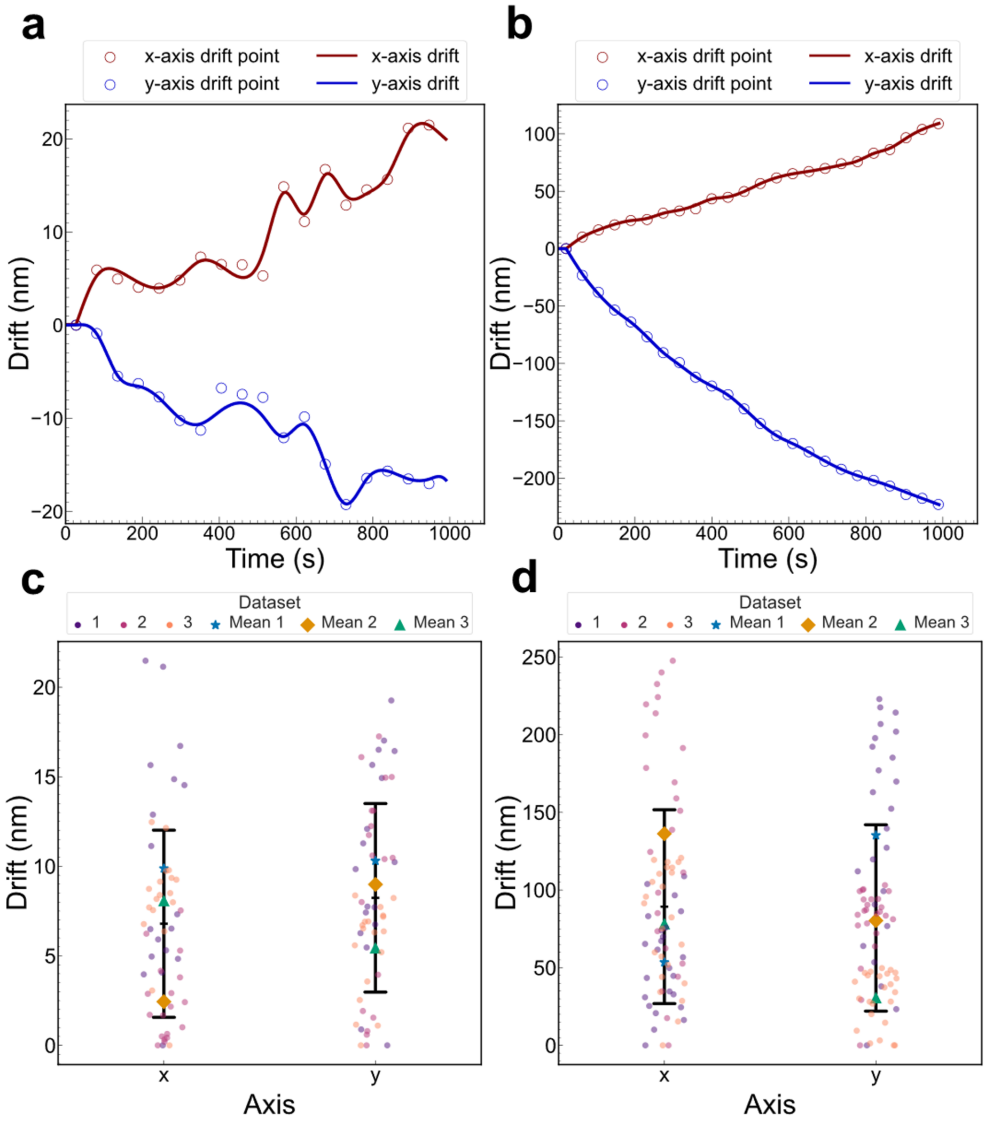

Fig. 4.13: **Quantitative comparison of lateral drift from NPC STORM imaging between the ROCS and commercial microscope. a** Drift trajectory from the first STORM image sequence of NPCs using the ROCS microscope. The remaining drift trajectories are shown in Appendix: A.3.1. The scatter points and curves are the same as in Fig. 4.9**a** and Fig. 4.9**b**. The localisation data was divided into 18 subsets for RCC. The mean sample drift for this image sequence was 9.9 ± 6.1 nm along the x-axis and 10.3 ± 5.4 nm along the y-axis. **b** Drift trajectory of the sample biological structure as **a** but imaged with the commercial microscope. The localisation data were divided into 24 subsets for RCC. The mean drift was 53.4 nm ± 29.8 nm along the x-axis and 135.2 ± 65.7 nm along the y-axis. **c** The same dotplot as Fig. 4.9**c** and Fig. 4.9**d** but for the NPC data from the ROCS microscope. The mean lateral drift of datasets 2 and 3, in the order (x-drift, y-drift) were (2.4 nm, 9.0 nm) and (8.1 nm, 5.4 nm). The overall drift was 6.8 ± 5.2 nm along the x-axis and 8.2 ± 5.2 nm along the y-axis. **d** Same as **c** but for the NPC data acquired with the commercial microscope. The mean lateral drifts of datasets 2 and 3 were (145.0 nm, 78.9 nm) and (78.1 nm, 30.5 nm). The overall mean drift across all repeats was 89.3 ± 62.0 nm along the x-axis and 82.0 ± 59.6 nm along the y-axis.

The same FRC resolution analysis was applied to the NPC localisation data where the resolutions were compared before and after RCC.

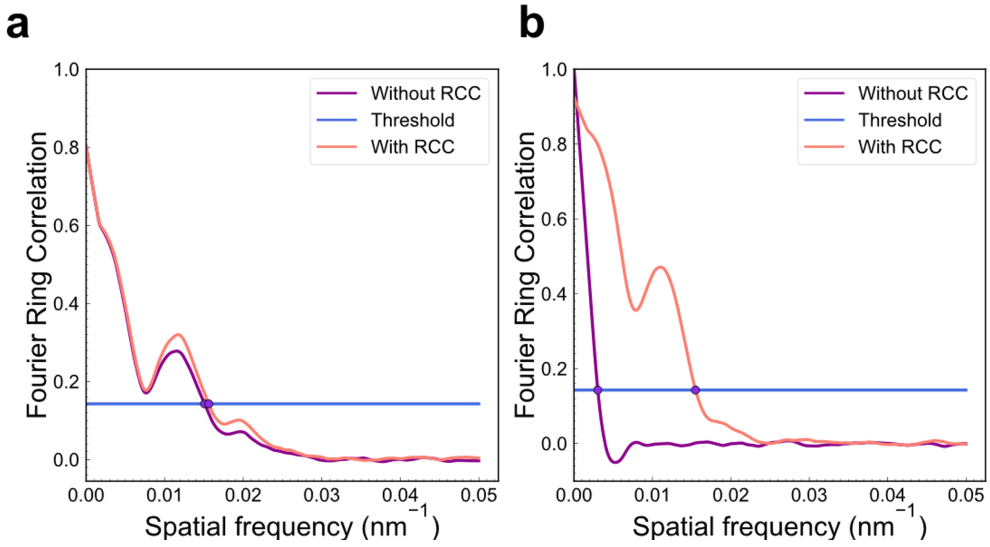

Fig. 4.14: **Comparisons of FRC resolutions of NPC data before and after drift correction from a representative example. a** A representative example of the FRC resolutions of NPC STORM images acquired with the ROCS microscope. The resolution was 66.4 nm before RCC and 64.1 nm after RCC. **b** A representative example of the FRC resolutions of NPC STORM images acquired with the commercial microscope. The resolution was 330.2 nm before RCC and 64.6 nm after RCC.

Table 4.2: **Mean FRC resolutions of NPC STORM images acquired with the ROCS and commercial microscopes before and after RCC.**

Microscope	Before/after RCC	Mean FRC resolution (nm)
ROCS	Before	65.2 ± 1.2
ROCS	After	62.2 ± 1.4
Commercial	Before	272.3 ± 54.8
Commercial	After	68.6 ± 20.7

As previously demonstrated with the FRC resolution analysis of microtubule data, RCC drift correction had little effect on the resolution of NPC STORM images acquired with the ROCS microscope, with a mean resolution improvement of 3 nm (Table 4.2). Meanwhile, the mean resolution increase from RCC for the NPC data from the commercial microscope was higher, with an increase of 203.7 nm (Table 4.2). It was also notable that, again, the sample drift measured using the ROCS microscope was less than half of the achievable FRC resolution while for the commercial microscope, the sample drift was higher than half the FRC resolution.

The drift measurements from STORM imaging of NPCs thus provide additional evidence that the novel ROCS microscope design offers a significant improvement in sample sta-

bility. Meanwhile, drift correction methods are mandatory to acquire meaningful biological information when using a commercial microscope, thereby increasing experimental complexity.

4.4 Discussion and Conclusions

In this chapter, the drift quantification of a novel ROCS microscope has demonstrated its exceptional mechanical stability, supporting the results from previous finite element analysis simulations [198]. In widefield imaging of fluorescent beads, the lateral and axial drift were both reduced to < 10 nm over two hours of image acquisition, thus virtually eliminating their detrimental effects (Fig. 4.1, Fig. 4.4). Imaging microtubules and NPCs also revealed that the ROCS microscope was capable of SMLM at a similar level of performance to a high-end commercial microscope but with the advantage of consistently achieving drift < 20 nm without the use of drift correction methods (Fig. 4.7, Fig. 4.8, Fig. 4.11, Fig. 4.12). Notably, there was little difference in the FRC resolution before and after drift correction for SMLM data acquired with the ROCS microscope (Fig. 4.10, Fig. 4.14) while the sample drift for all experimental repeats with the ROCS microscope was under half of the FRC resolution (Fig. 4.9, Fig. 4.13), highlighting that the drift was negated to such an an extent by the ROCS that it no longer has a detrimental effect on image fidelity.

In a comparison between the ROCS and microscopes built as conventional optical cage systems, the ROCS retains the advantages of optical cage systems, namely their compact design, ease of alignment, facile assembly of optomechanical components, and lower cost relative to commercial instruments. However, as mentioned previously, conventional optical cage systems are hypothesised to suffer from worse mechanical stability than the ROCS due to differences in the mounting of and connectivity of optomechanical components. While an experimental comparison between the microscope designs was not presented in this chapter, it is noteworthy that the ROCS microscope achieves better mechanical stability compared to several bench-top microscopes described in the literature that are constructed using conventional optical cage systems [203, 204]. In fact, the sample drift measurements from these examples exhibit a similar degree of drift to those from the commercial microscope in this chapter, thus underlining the poorer

mechanical stability of conventional optical cage systems compared to the ROCS and corroborating prior simulation results [198].

Because there were no experimental comparisons between microscope designs, the stability measurements of the ROCS microscope may benefit from a more systematic experimental analysis of the ROCS optomechanical components to quantify more precisely their contribution to negating drift. While there were previous vibrational mode analysis simulations comparing a right-angle kinematic mirror mount from the ROCS to the same component from a conventional optical cage system [198], it could be beneficial, for example, to quantify the drift following alteration of the ROCS optical layout such that one mirror mount was replaced with a conventional optical cage system mirror mount. The ROCS could be used as a benchmark for a mechanically stable system, allowing different optomechanical components to be tested in this manner, such as the sample stage and lens holders. With this approach, it may be possible to ascertain which optomechanical components contribute the most to sample drift, thereby guiding future development on improving microscope hardware stability, as well as assisting other researchers troubleshooting instruments that are exhibiting high levels of drift, particularly SMLM-capable instruments.

Finally, the SMLM imaging in this chapter focused purely on STORM imaging with Alexa Fluor 647—one of the best performing dyes for STORM [91]. Different fluorophores, which vary in their photophysical properties—particularly molar absorption coefficient and duty cycle—or different imaging modalities, such as PALM and DNA-PAINT, may require exposure times, excitation intensities, illumination wavelengths, or acquisition times that were not characterised with the ROCS microscope in this chapter. For example, several applications of PALM are reported in the literature where the acquisition time exceeds the ∼15-minute image acquisition using the ROCS microscope [21, 93, 205–207], likely necessary because of the lower photon counts of fluorescent proteins. Meanwhile, typical acquisition times for DNA-PAINT far exceed those used in this chapter, ranging from tens of minutes to several hours [208–210]. Even recent advancements in accelerating DNA-PAINT have typical acquisition times that exceed those in this chapter [211], and so the ROCS microscope may not always be capable of negating drift for an SMLM experiment to the extent demonstrated above. Never-

theless, the flexibility in tuning experimental parameters for SMLM—such as exposure time, reducing agent concentration for STORM, activation and excitation intensities for PALM, and imager strand length for DNA-PAINT—means that it may be possible to accommodate a range of imaging modalities using the ROCS and extend its ability to negate drift beyond STORM. Furthermore, even if the ROCS could not offer the extent of drift negation described herein for an imaging modality, it would be likely that the severity of drift would still be substantially below that of a commercial microscope or a microscope built with a conventional optical cage system, thereby facilitating downstream drift correction.

4.4.1 Conclusion

In summary, the ROCS microscope can decrease drift to negligible levels in standard fluorescence microscopy and STORM—a feature hitherto unattainable using commercial microscopes or conventional optical cage systems, thereby increasing the achievable localisation accuracy. In addition, negating drift was achieved without additional experimentation, software, or hardware, thereby decreasing experimental complexity by obviating the need for correcting drift during or after image acquisition. The ROCS design, therefore, simplifies the experimental workflow in SMLM, improving accessibility to SMLM for biological imaging, and providing a blueprint for more reliable and more reproducible SMLM.

5 Mirror-enhanced SMLM

5.1 Overview

Mirror-enhanced fluorescence describes the modulation of fluorescent signal by the presence of reflective layers. Previous literature has focused on the effects of metal interfaces on fluorophore properties [35, 36, 212], with some applications to cell imaging and nanometer axial distance quantification of fluorophores from surfaces [34, 38]. From these studies, it has been established that metal interfaces modulate fluorescence emission by modifying the radiative fluorescent decay rate, k_{r} and the non-radiative fluorescent decay rate, k_{nr}. These rates, in turn, affect the excited state fluorescence lifetime, τ, and the quantum yield, Φ, the degree of which depends on the distance from the surface, z, and the angle between the fluorophore emission dipole and the optical axis, θ. More specifically, the modified fluorescence lifetime is:

$$\frac{\tau(z,\theta)}{\tau_0} = \frac{k_{\mathrm{R},0} + k_{\mathrm{NR},0}}{k_{\mathrm{R}}(z,\theta) + k_{\mathrm{NR}}(z,\theta)} \,. \tag{5.1}$$

$\tau(z,\theta)$, $k_{\mathrm{R}}(z,\theta)$, and $k_{\mathrm{NR}}(z,\theta)$ are the fluorescent lifetime, radiative decay rate, and non-radiative decay rate, respectively, in the presence of a metal interface. τ_0, $k_{\mathrm{R},0}$, and $k_{\mathrm{NR},0}$ are equivalent but in the absence of a metal interface. It is also assumed that the orientations of fluorophore dipoles are isotropically distributed, and so only the distance from the surface, z affects the fluorescent lifetime enhancement.

At short distances, the fluorescence lifetime is shortened due to the enhanced non-radiative decay rate, k_{NR}, which can be attributed to energy transfer from the fluorophore to the metal, while at greater distances, interference effects from the mirror reflection of the fluorophore result in oscillations of the apparent fluorescent lifetime [213], and so the fluorescent lifetime and quantum yield will be higher for certain ranges of distances from the metallic surface, resulting in fluorescence enhancement. The degree of enhancement and the distances where the enhancement is maximised can be modulated by altering the thickness of the reflective layers, as well as their material

composition. Herein, a reflective surface consisting of silicon nitride, silver, and germanium was used (Methods: 3.9), where the silicon nitride provided a biocompatible surface for cell culture, the silver enabled fluorescent enhancement, and the germanium was used to aid the deposition of a smooth silver layer [214].

In the context of SMLM, the higher quantum yield and fluorescent lifetime is predicted to increase the number of photons collected, thereby increasing the localisation precision and resolution. Indeed, a prior implementation of mirror-enhanced SMLM demonstrated a maximum enhancement of approximately two-fold [40, 215]. Theoretically, such an improvement would lead to a 1.4-fold increase in the localisation precision since $\sigma_{xy} \propto \frac{1}{\sqrt{N}}$, where N is the number of photons. While evidence of resolution improvements was presented in theses studies, there has been no further work to develop or reproduce these results. Moreover, the localisation accuracy and resolution of previously presented SMLM data were ultimately limited by the use of antibodies, which introduce linkage errors of 10–20 nm. There is also potential to combine mirror-enhanced fluorescence with computational methods to increase further the resolution, for example by using SRDTrans [81]—the denoising algorithm for which a characterisation and evaluation is presented in Chapter 7.

The aim of this chapter, therefore, is to re-evaluate mirror-enhanced SMLM as a tool for resolution enhancement more comprehensively, as well as evaluate its effectiveness in combination with SRDTrans. The ROCS microscope described in Chapter 4 was used for all STORM imaging.

5.2 Verification of Mirror-enhanced Fluorescence

The mirror-coated glass slides were designed with the same materials and thickness as Heil *et al.* 2018, i.e. with 10 nm silicon nitride, 50 nm silver, and 2 nm germanium, and were purchased from Nanjing Bote Electro-Optics Co., Ltd. Following the approach of Chapter 4, the mirror-enhancement effect was first evaluated on widefield epifluorescent images of 100 nm fluorescent beads which were acquired similarly to Methods: 3.5.1 and Methods: 3.9 but with an excitation wavelength of 640 nm instead of 488 nm. In total, three independent widefield images in each category were acquired for comparison.

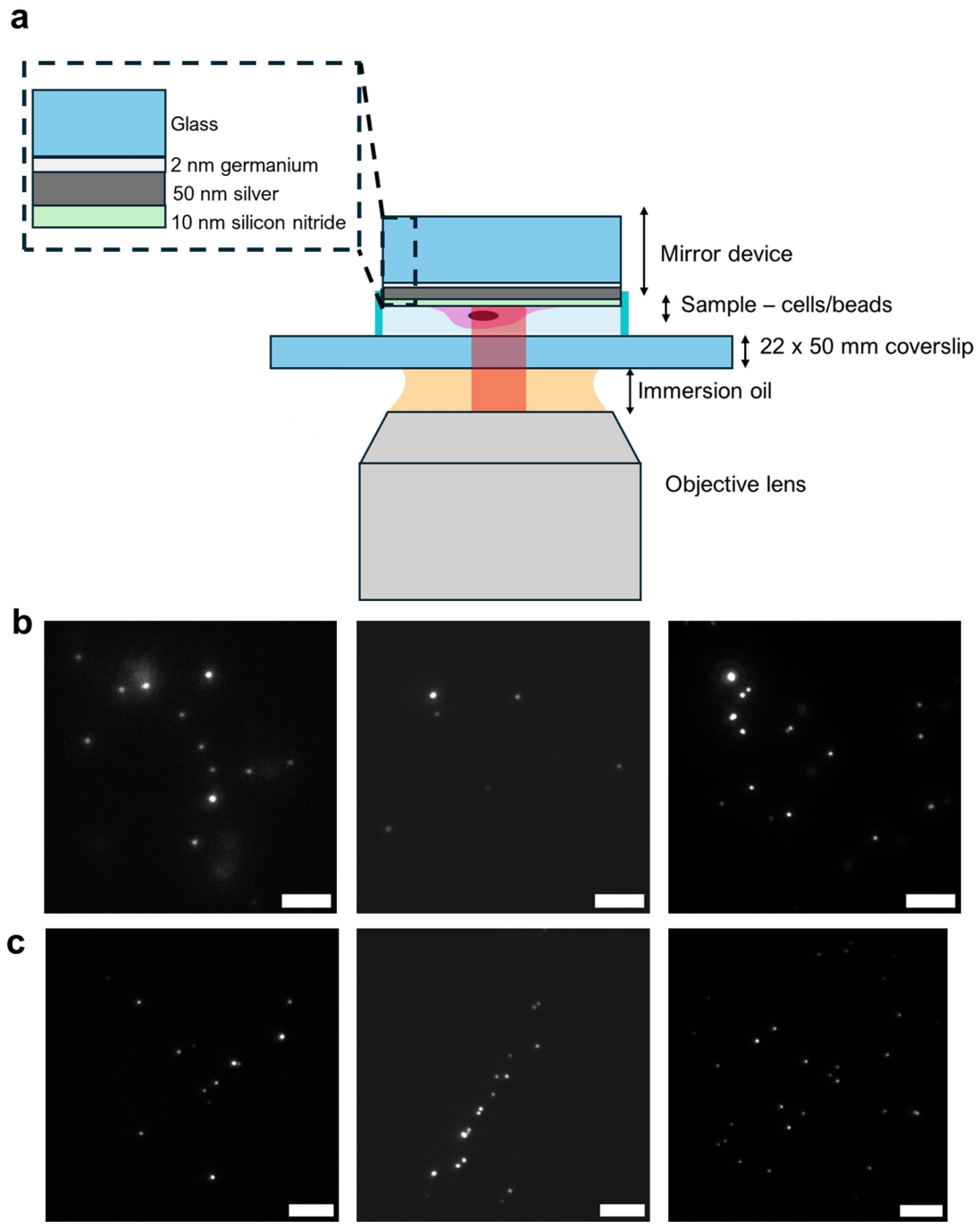

Fig. 5.1: **Schematic of mirror-enhanced imaging and comparison of widefield images from epifluorescent bead imaging with and without mirror-enhanced fluorescence**. Scale bars: 5 µm. **a** Schematic of the mirror-enhanced fluorescence experimental setup. The illumination light is shown in red. **b** Widefield image of the beads with mirror-enhancement using an excitation wavelength of 640 nm. The first, second, and third repeats are shown on the left, middle, and right, respectively. **c** Widefield image of the beads without mirror-enhancement. The order is the same as **a** and the grayscale range of the image has been adjusted to be identical to **a**. Each pair of images from each repeat have been adjusted to have the same grayscale range.

To evaluate the effects of mirror-enhancement on the photophysical properties of single-molecules, single-molecule localisation was carried out for each bead under identical

imaging conditions (Theory: 2.3, Methods: 3.7.1). From this procedure, the intensities, background fluorescence, and localisation precisions of the beads (I_0, b, and σ_{xy} from Theory: Eqs. 2.10, 2.11, 2.12, and 2.24) with and without mirror-enhancement were compared.

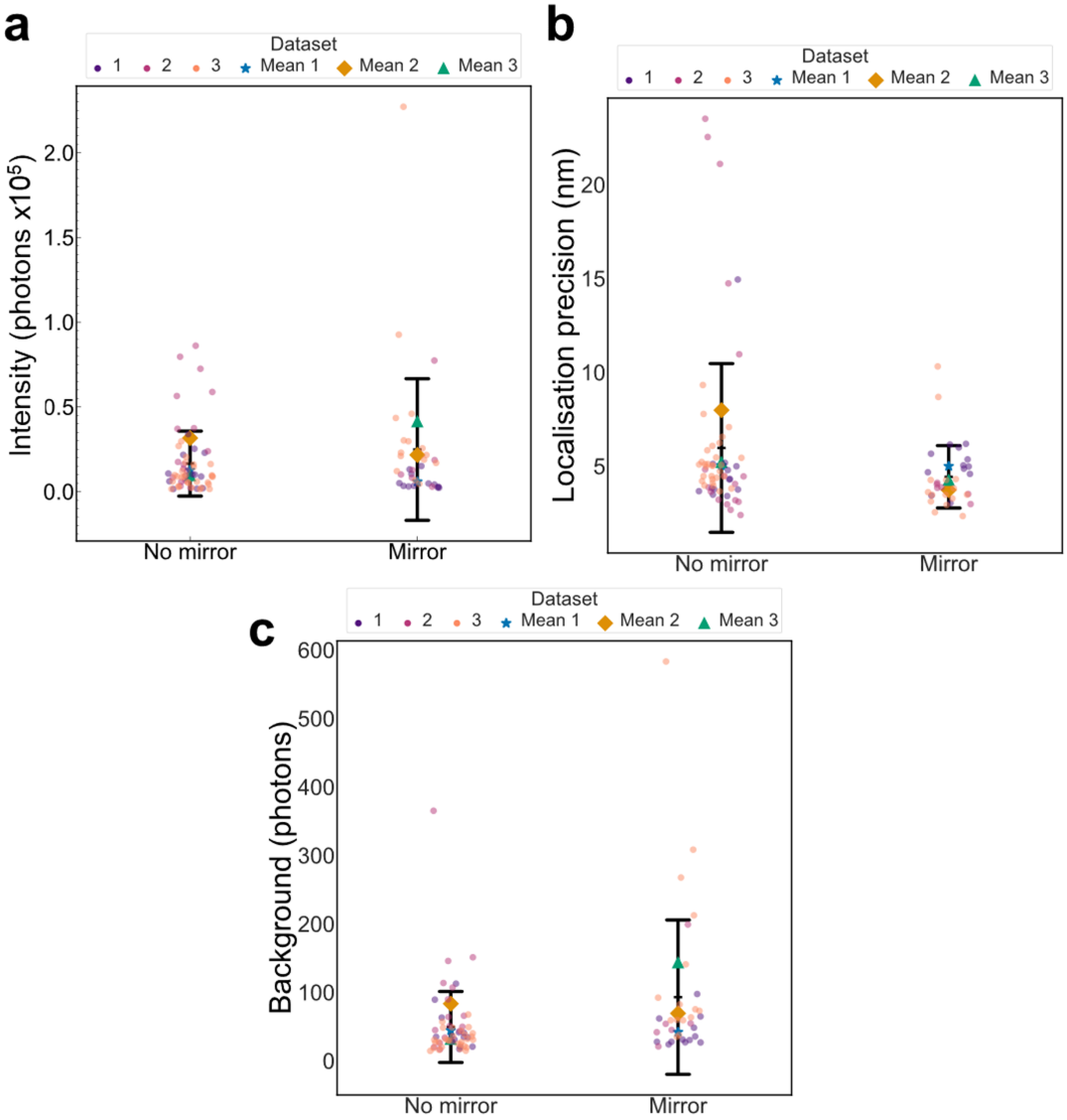

Fig. 5.2: **Comparison of photophysical properties from epifluorescent bead imaging with and without mirror-enhanced fluorescence.a** Dotplot comparing the bead intensities (I_0) estimated from single-molecule localisation. The intensities have been scaled down by 100000 for ease of representation. A blue star, orange diamond, and green triangle denote the mean intensity of image 1, 2, and 3, respectively. The dots represent the intensity of a bead and are colour-coded depending on the dataset. The central bar is the mean of all beads from all images while the upper and lower bars represent one standard deviation. The mean intensities of images 1, 2, and 3 without mirror-enhancement were: 12640 photons, 31610 photons, and 9440 photons, respectively. The overall mean intensity was 17900 ± 19170 photons. With mirror-enhancement, the mean intensities were: 5840 photons, 21660 photons, and 41310 photons, while the overall mean intensity was 22940 ± 41780 photons. **b** Dotplot comparing the localisation precisions. The mean localisation precisions without mirror-enhancement were: 5.0 nm, 8.0 nm, and 5.2 nm, and the overall mean localisation precision was: 6.1 ± 4.5 nm. With mirror-enhancement, the localisation precision was: 5.0 nm, 3.7 nm, and 4.3 nm, while the overall mean localisation precision was 4.3 ± 1.7 nm. **c** Dotplot comparing the backgrounds. Without mirror-enhancement, the mean backgrounds were: 44 photons, 83 photons, 32 photons. The overall mean background was 53 ± 52 photons. With mirror-enhancement, the mean backgrounds were: 42 photons, 69 photons, and 143 photons, and the overall mean background was 85 ± 113 photons.

From the comparative analysis, the beads imaged with the mirror-coated slides appeared

brighter than those without mirror-enhancement (Fig. 5.1**a, c, e** & Fig. 5.1**b, d, f**). The mean intensity of the beads across three repeats was slightly higher with mirror enhancement than without (22940 ± 41780 photons compared to 17900 ± 19170 photons, Fig. 5.2**a**), albeit with more variance. The higher variance can likely be attributed to the distance between the beads and reflective layer not being known. It is likely that there was experiment-experiment variation in the z-distance, resulting in differing degrees of fluorescence enhancement and, thereby, increasing the variability.

The background fluorescence was also slightly higher when using mirror-enhancement, with a mean of 85 ± 113 photons compared to 53 ± 52 photons (Fig. 5.2**c**). Nevertheless, the increase in background for the mirror slides was not detrimental to the improvement in localisation precision that arose from the increase in intensity. Indeed, the mean localisation precision with mirror enhancement was 4.3 ± 1.7 nm while the mean localisation precision without mirror enhancement was 6.1 ± 4.5 nm (Fig. 5.2**b**), demonstrating that the mirror-enhancement effect was observable with these slides.

5.2.1 Widefield Imaging with Mirror-enhanced Fluorescence

To verify further the presence of mirror-enhanced fluorescence, nuclear pore complexes were labelled with Alexa Fluor 647, as described in Methods: 3.4.5, resulting in fluorescent emission only from the nuclei. The nuclei from epifluorescent images were segmented using the implementation of Otsu's method included in the scikit-image Python package [133, 181]. The signal-to-noise ratio (SNR) was subsequently quantified according to [216]:

$$\mathrm{SNR} = \frac{\overline{\mathrm{Im}(x,y)}_S - \overline{\mathrm{Im}(x,y)}_N}{\sigma_N} \,, \tag{5.2}$$

where $\overline{\mathrm{Im}(x,y)}_S$ and $\overline{\mathrm{Im}(x,y)}_N$ are the mean intensities for the images corresponding to the nucleus (signal) and the background (noise), respectively. σ_N is the standard deviation of the background.

Again, the SNRs of three images of nuclei without mirror-enhancement were compared to three widefield images of nuclei with mirror-enhancement. The results of this comparison are shown below.

Table 5.1: **Comparison of signal-to-noise ratios between mirror-enhanced fluorescent imaging and standard fluorescent imaging from epifluorescent images of nuclei.** The signal-to-noise ratio was calculated using Eq. 5.2 where the intensity of the nucleus was taken as the signal and the background intensity was taken as the noise. The mean and standard deviation were then calculated from three repeats.

Mean SNR without a mirror	Mean SNR with a mirror
4.7 ± 0.7	8.1 ± 0.7

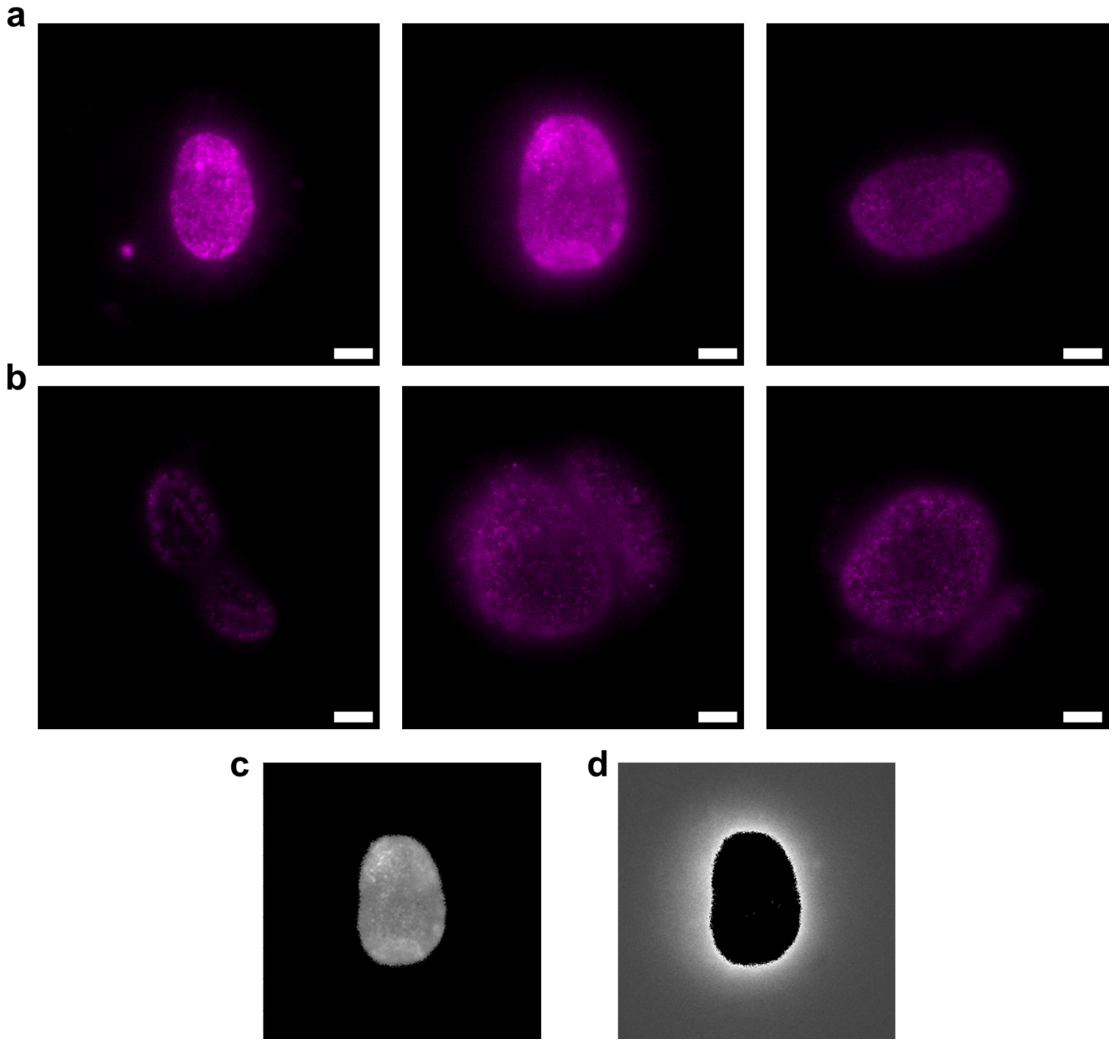

Fig. 5.3: **Epifluorescent images of nuclei in U2OS cells labelled with Alexa Fluor 647 with and without mirror-enhancement.** All nuclei have been labelled with Alexa Fluor 647. Three independent repeats were carried out in which there was one cell imaged per repeat. **a** Epifluorescent images of nuclei with mirror enhancement. The scale bar is 5 µm. The grayscale range has been adjusted such that all images have the same grayscale range as the furthest left image. **b** Epifluorescent images of nuclei without mirror enhancement. The scale bar is 5 µm. The grayscale range has been adjusted so that all images have the same grayscale range as the furthest left image in **a**. **c** Example of the segmentation process. The mask corresponding to the segmented nucleus from the middle image of **a** is shown. **d** The background excluding the segmented nucleus produced by the segmentation process from the middle image of **a**.

Qualitatively, the images of nuclei with mirror-enhancement (Fig. 5.3**a**) appear to have greater intensity compared to those without (Fig. 5.3**b**). Indeed, the mean SNR of the

three repeats using the mirror-coated slides was almost 2-fold higher with a value of 8.1 ± 0.9 compared to a mean SNR of 4.7 ± 0.9 without the mirror coating.

This analysis demonstrated a greater mirror enhancement effect for widefield imaging compared to that using fluorescent beads (Fig. 5.2)—an observation that is possibly attributed to the difference in quantum yield (see Discussion, section 5.5 for more details). As such, it is likely that improved STORM imaging is achievable with these mirror-coated slides.

5.3 Mirror-enhanced STORM Imaging

Following the demonstration of the mirror-enhancement effect on diffraction-limited fluorescence microscopy, mirror-enhanced STORM imaging with epi-illumination of U2OS cells stably expressing Nup96-SNAP was carried out. The cells were grown on the silicon nitride layer of the mirror-coated slides and the NPCs were labelled according to Methods: 3.4.5 and Methods: 3.9. The STORM image sequence was acquired as described in Methods: 3.6.1 and single-molecule localisation was carried out as described in Theory: 2.3 and Methods: 3.7.1. In total, three image sequences of mirror-enhanced STORM imaging of NPCs were acquired. For comparison, three STORM image sequences of NPCs on ordinary glass coverslips were also acquired. Image acquisitions were carried out within a similar timespan to ensure the age of reagents did not affect the data quality, allowing for a fairer comparison.

Since the structure of NPCs is well-defined (Introduction: 1.4.2), structural differences—which reflect differences in resolution—between NPCs with and without mirror-enhancement may be discernible by visual comparison, depending on the extent of resolution enhancement. An example of such a comparison for the first image sequence is shown below (see Appendix: Fig. A.6 for the STORM images of dataset 2 and Fig. 5.6 for the third dataset).

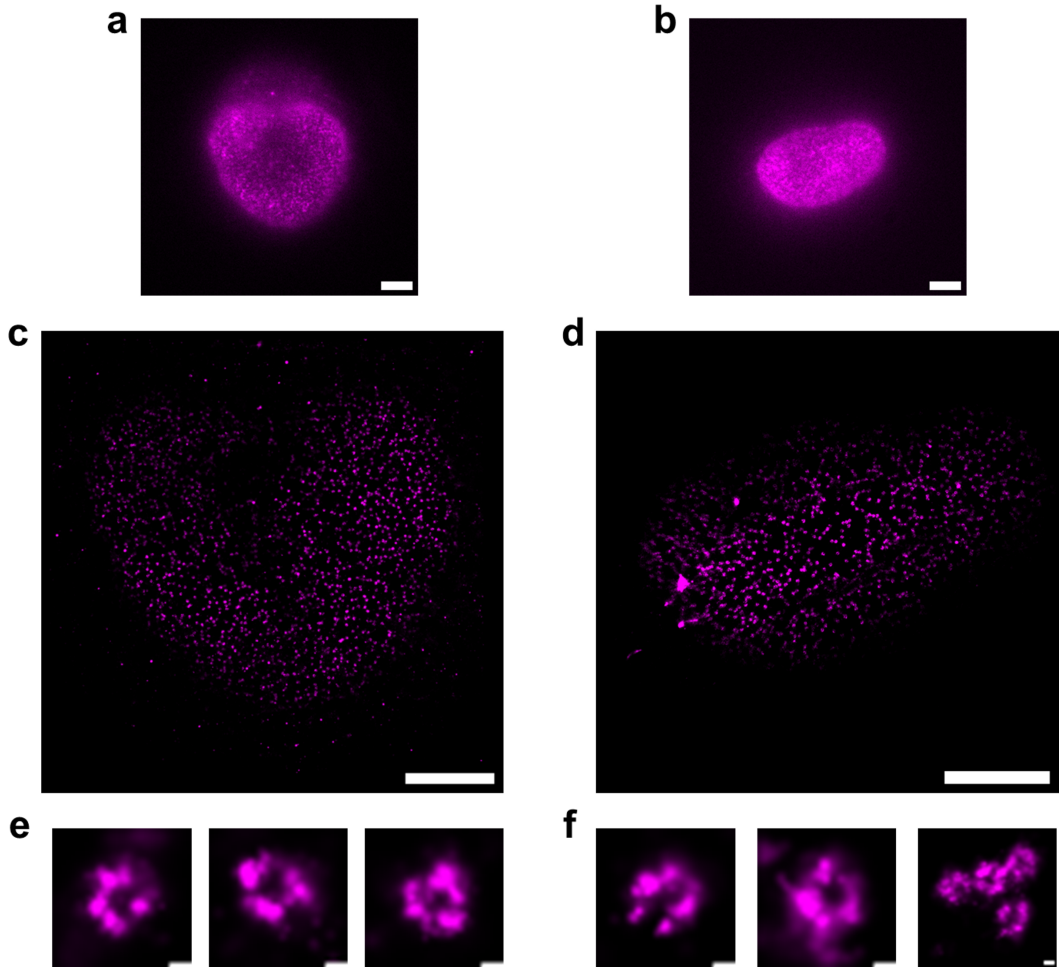

Fig. 5.4: **Comparison of NPC structures between mirror-enhanced STORM imaging and conventional STORM imaging.** Data from the first dataset is shown in this figure. **a** Widefield images of a nucleus without mirror enhancement. The scale bar is 5 µm. **b** Widefield image of a nucleus with mirror enhancement. The scale bar is 5 µm. **c** Super-resolution image of **a** following conventional STORM imaging. The scale bar is 5 µm. **d** Super-resolution image of **b** following mirror-enhanced STORM imaging. The scale bar is 5 µm. **e** Three representative examples of NPCs from **c**, i.e. with conventional STORM imaging. The scale bar is 50 nm. **f** Three representative examples of NPCs from **d**, i.e. with mirror-enhanced STORM. The scale bar is 50 nm.

From the visual comparison, little difference in NPC structure was discernible between imaging with conventional STORM or mirror-enhanced STORM for the first dataset (Fig. 5.4**c**, Fig. 5.4**e**, Fig. 5.4**d**, Fig. 5.4**f**). Therefore, it was unclear whether mirror-enhancement had a measurable impact on the resolution for this dataset. As such, a more comprehensive, quantitative analysis was carried out on the photophysical parameters of the single-molecule localisation data. The weighted mean intensity, background, and localisation precision for each dataset were calculated and compared.

Because the number of single-molecules detected in each STORM image sequence differed, the arithmetic mean of each photophysical parameter across the three different

datasets would not be accurate representation of the overall mean. To address this, the weighted means (μ) and standard deviations (σ) for each parameter (j) were calculated and tabulated below using the following formulae.

$$\mu_j = \frac{\sum_{i=1}^{N} n_i \bar{x}_{j,i}}{\sum_{i=1}^{N} n_i} \tag{5.3}$$

$$\sigma_j = \sqrt{\frac{\sum_{i=1}^{N} (\bar{x}_{j,i} - \mu_j)^2}{\sum_{i=1}^{N} n_i}} \tag{5.4}$$

Here, $\bar{x}_{j,i}$ and n_i are the arithmetic mean for the jth parameter and sample size, respectively, for the ith dataset, with a total number of N datasets.

Table 5.2: **Weighted means of the single-molecule photophysical parameters from comparing mirror-enhanced STORM and conventional STORM.** The weighted means were calculated for each parameter using Eq. 5.3 and the standard deviations were calculated using Eq. 5.4

Experiment	Weighted mean intensities (photons)	Weighted mean background (photons)	Weighted mean localisation precisions (nm)
No mirror	1195 ± 137	61 ± 12	15.1 ± 1.9
Mirror	3735 ± 1498	113 ± 22	13.4 ± 0.5

The Fourier ring correlation resolution was also calculated with a custom routine [177] according to Theory: 2.4 and Methods: 3.7.3. Unlike the FRC calculations described in Chapter 4.3.1, the two datasets were generated by splitting the localisations by whether they were detected in an odd-numbered frame or even-numbered frame.

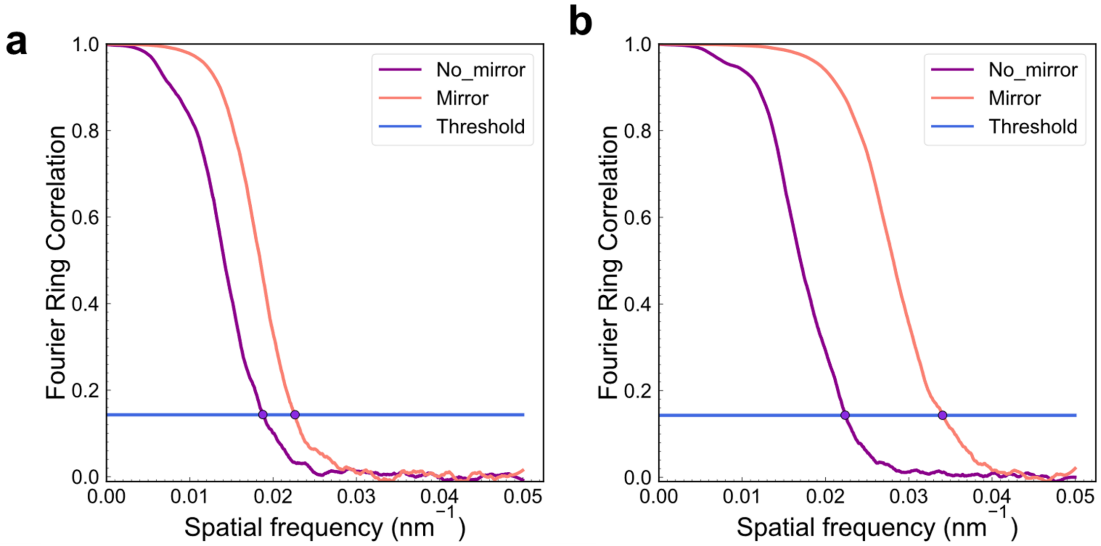

Fig. 5.5: **Two representative examples of the NPC FRC resolution from conventional STORM and mirror-enhanced STORM.** A threshold of 1/7 (≈ 0.143) was used. **a** FRC curve of the super-resolution reconstructions of the first NPC dataset, comparing the resolutions with and without mirror-enhancement. The resolution without the mirror was 53.3 nm while the resolution with the mirror was 44.2 nm. **b** FRC curves comparing the resolutions of the third NPC dataset. The resolution without mirror enhancement was 44.7 nm while the resolution with mirror enhancement was 29.4 nm.

Table 5.3: **Mean FRC resolutions of NPC STORM images acquired with and without mirror enhancement**

Mean FRC resolution without a mirror (nm)	Mean FRC resolution with a mirror (nm)
48.0 ± 4.0	39.7 ± 9.0

The analysis of the photophysical parameters of single-molecules from STORM imaging (Fig. 5.2) displayed a similar pattern to that from fluorescent beads (Fig. 5.2**a**, 5.2**b**, 5.2**c**). Both the background and intensity were higher with mirror-enhancement than without. The mean background for all datasets was 61 ± 12 photons without the mirror compared to 113 ± 22 photons with the mirror (Table 5.2). The mean intensity was 1195 ± 137 photons without the mirror compared to 3735 ± 1498 photons with the mirror (Table 5.2). Meanwhile, the localisation precision was slightly higher when mirror-enhancement was implemented—with a mean of 13.4 ± 0.5 nm with the mirror compared to 15.1 ± 1.9 nm without (Table 5.2)—the exception being the third dataset where the data without mirror-enhancement had a higher localisation precision than with mirror-enhancement. Overall, the measurement of photophysical properties showed that fluorescence enhancement is present in STORM imaging and is not restricted to

widefield images.

The FRC resolution measurements also showed some evidence for the presence of the mirror-enhancement effect. In two out of three datasets (Fig. 5.5**a**, Fig. 5.5**b**), the FRC resolution was higher with mirror-enhancement than without. Moreover, the mean FRC resolution (Table 5.3) of all three datasets was higher for mirror-enhanced STORM (39.7 $\pm$ 9.0 nm) than without (48.0 $\pm$ 4.0 nm). Furthermore, the resolution quantification for the first dataset showed a $\sim$ 9 nm difference in resolution with and without mirror-enhancement, and so may explain why little structural difference was observed in the qualitative assessment in Fig. 5.4 (see Discussion for more details).

Conversely, from the FRC resolution quantification, it would be expected to observe more structural differences for the third dataset (Fig. 5.5**b**) given the larger difference in resolution ($\sim$ 15 nm).

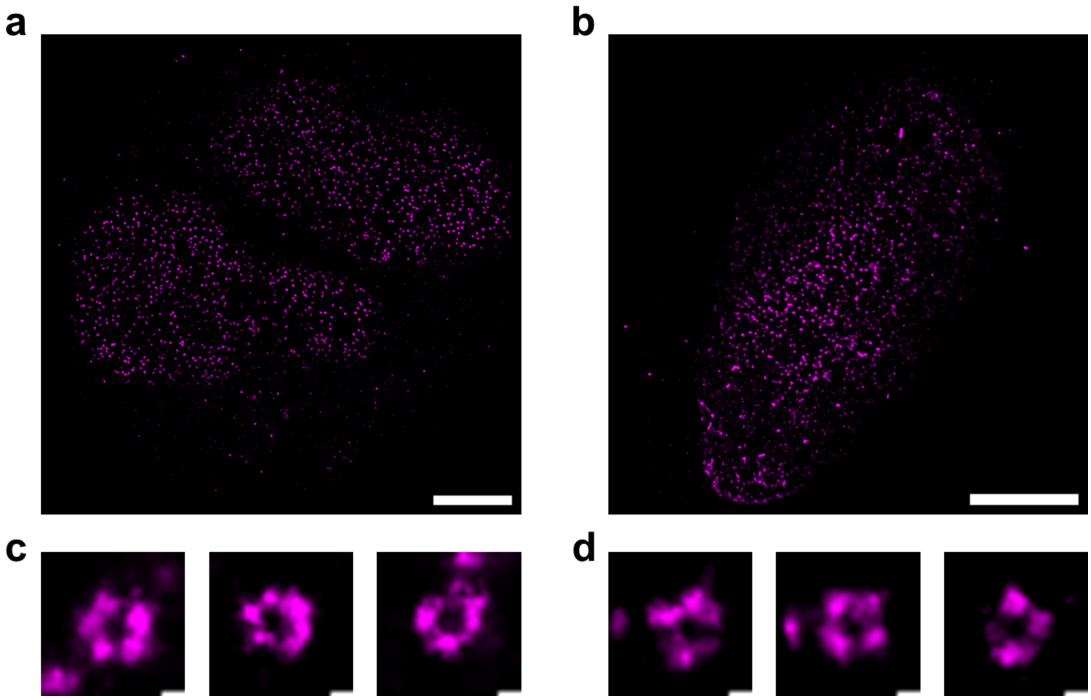

Fig. 5.6: **Comparison of NPC structures from the third dataset between mirror-enhanced STORM and conventional STORM. a** Super-resolution reconstruction of NPCs from conventional STORM imaging. Scale bar: 5 µm. **b** Super-resolution reconstruction of NPCs from mirror-enhanced STORM imaging. Scale bar: 5 µm. **c** Three representative examples of NPC structures from **a** (conventional STORM). Scale bar: 50 nm. **d** Three representative examples of nuclear pore complexes from **b** (mirror-enhanced STORM). Scale bar: 50 nm.

As predicted by the FRC resolution, some improvement in NPC structure resolution was visible for dataset 3; the lobes of the NPCs from mirror-enhanced STORM were more distinct compared to those from conventional STORM which appeared more as continuous circles (Fig. 5.6**d**, Fig. 5.6**c**). Nonetheless, as also observed in the first dataset (Fig. 5.4), the NPC structures did not appear as eight-fold symmetric rings. This observation is likely attributed to the incomplete labelling of the NPCs—an experimental limitation that has been observed in other instances of NPC STORM imaging with Nup96-SNAP-AF647 [93].

Despite the difference in FRC resolution with and without mirror-enhancement for the third dataset, both STORM images had similar localisation precisions—12.1 nm without the mirror compared to 12.9 nm. Therefore, the resolution difference for this pair was likely purely due to stochastic differences in labelling density. The mirror-enhancement effect, however, likely still contributed to the improved resolution relative to the first and second datasets from conventional STORM imaging, given that the measured localisation precision was slightly higher.

5.4 Combining mirror-enhancement with denoising

As discussed in Theory: 2.4, the resolution in SMLM is limited by the localisation precision and labelling density. Mirror-enhanced fluorescence can improve the former but not the latter. Consequently, methods that improve labelling density can be combined with mirror-enhanced fluorescence to increase the resolution in SMLM beyond what is achievable from improving the localisation precision or labelling density in isolation.

To increase the number of detected molecules, a denoising algorithm, SRDTrans, was used [81]. Details of the algorithm are described in Theory: 2.7 and a detailed characterisation and evaluation of the algorithm is given in Chapter 7. Briefly, the algorithm is an unsupervised transformer network which can be trained on an SMLM image sequence to learn parameters for denoising. These parameters can then be used for inference which entails denoising the same SMLM image sequence that the algorithm was trained with, or other SMLM image sequences. By denoising the image sequence, the labelling density can be improved through detection of single-molecule signals that may normally be too weak to be detected.

Here, SRDTrans was trained on the third dataset of mirror-enhanced STORM imaging (Fig. 5.6), as described in Methods: 3.10.1, and inference was carried out on the same dataset. This dataset was chosen because it featured the highest FRC resolution relative to the NPC data from conventional STORM imaging and mirror-enhanced STORM imaging. For the denoised image sequence, single-molecule localisation was carried out followed by FRC resolution evaluation.

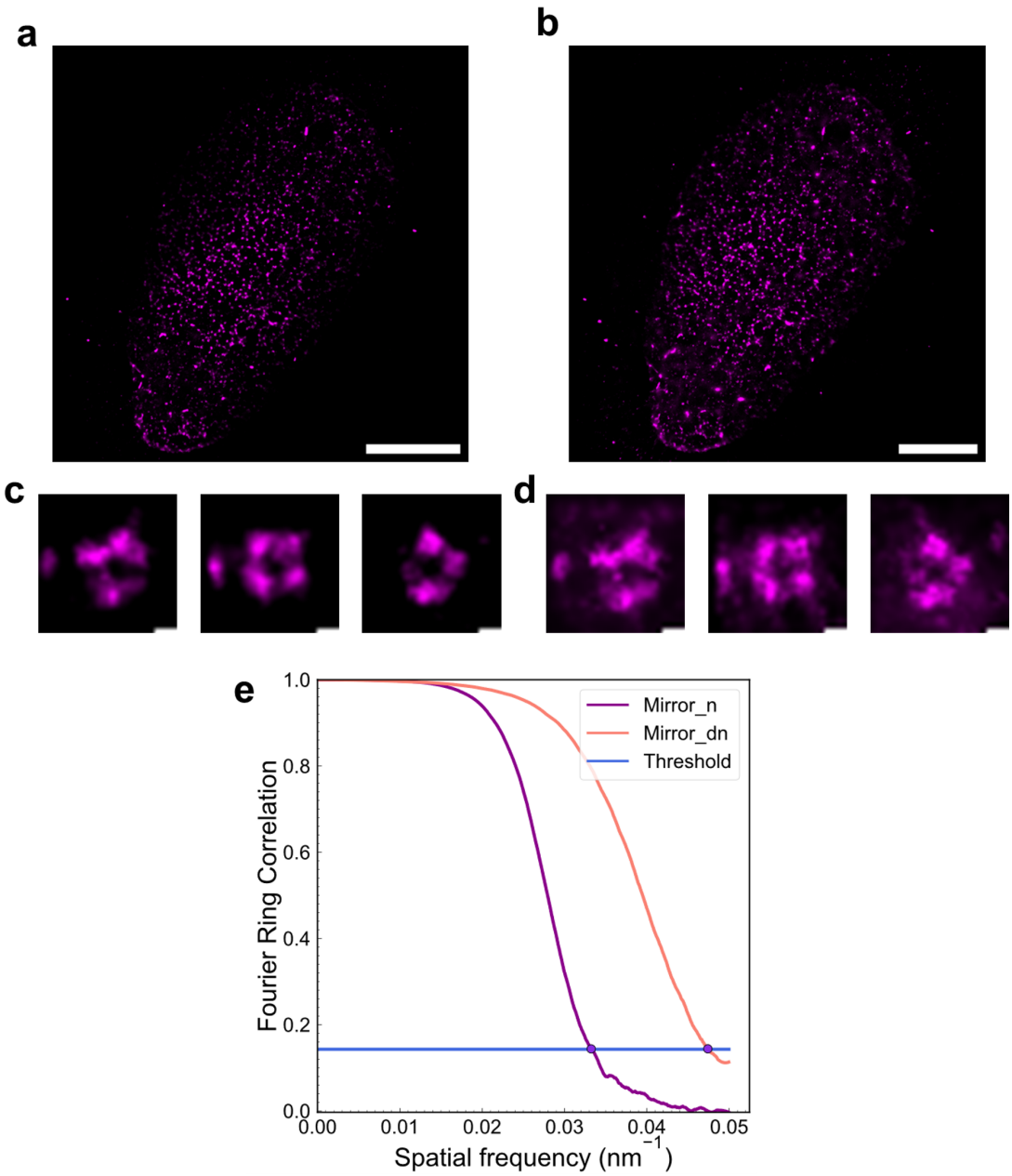

Fig. 5.7: **Comparison of NPC structures from the third dataset of mirror-enhanced STORM with and without computational denoising.** **a** Super-resolution reconstruction of NPCs from mirror-enhanced STORM imaging in combination without denoising using SRDTrans. **b** Reconstruction of the same data in **a** following denoising using SRDTrans. **c** Three representative NPC structures from **a**. The examples are the same regions of interests as those in Fig. 5.6**d**. The scale bar is 50 nm. **d** Three representative NPC structures from **b**, using the same regions of interests as **c**. **e** FRC resolution of the super-resolution image in **a** compared to that in Fig.**b**. "Mirror_n" denotes the NPC data from mirror-enhanced STORM without denoising while "Mirror_dn" denotes the denoised NPC data from mirror-enhanced STORM. The resolution without denoising was 29.4 nm. The resolution with denoising was 21.1 nm. A threshold of 0.143 was used.

Application of the denoising algorithm resulted in a slight resolution improvement, with a resolution of 21.1 nm compared to 29.4 nm without denoising (Fig. 5.7**c**). Some small improvements in the NPC structures were also observed (Fig. 5.7**b**), with some

of the lobes appearing to have higher labelling density compared to the structures with mirror-enhancement alone (Fig. 5.6**d**), while still remaining distinct, as opposed to the structures from conventional STORM which appear more as continuous rings (Fig. 5.6**c**). As an example, the furthest right NPC structure in Fig. 5.7**b** had slightly higher density in the centre-left lobe compared to the same structure in 5.7**d**. However, the structural differences were relatively slight, as reflective of the small FRC resolution difference (Fig. 5.7**c**). Overall, these results demonstrate that mirror-enhanced fluorescence provides a photonic platform that can be combined with other computational methods that increase resolution.

5.5 Discussion and Conclusions

In this chapter, the use of mirror-enhanced fluorescence has been characterised for epifluorescent imaging of beads, fluorescently labelled nuclei, and STORM imaging of NPCs. The epifluorescent imaging of fluorescent beads demonstrated that mirror-coated slides increase both the intensity and background of fluorescent beads, with the increase in intensity having a greater impact on the localisation precision, ultimately improving the localisation from 6.1 $\pm$ 4.5 nm with conventional epifluorescent imaging, to 4.3 $\pm$ 1.7 nm (Fig. 5.2). The widefield images of nuclei corroborated these results with a $\sim$ 2-fold improvement in signal-to-noise ratios when using mirror-coated slides (Table 5.1, Fig. 5.4). Finally, mirror-enhanced STORM images of NPCs displayed some improvements in localisation precision and FRC resolution, with increases of $\sim$ 1.7 nm and $\sim$ 9 nm, respectively (Fig. 5.2, Fig. 5.5, Fig. 5.6). Combining mirror-enhanced fluorescence with denoising resulted in a further resolution increase of $\sim$ 8 nm (Fig. 5.7).

In the comparison of mirror-enhancement between epifluorescent imaging of fluorescent beads and epifluorescent imaging of nuclei, as well as STORM, the recorded intensities of Alexa Fluor 647 molecules were increased to a greater extent by mirror-enhancement than those on the fluorescent beads. For example, the mean intensity increased from 17900 $\pm$ 19170 photons without mirror-enhancement to 22940 $\pm$ 41780 photons with mirror-enhancement for bead imaging (Fig. 5.2**a**), whereas the mean intensity increased from 1195 $\pm$ 137 photons without mirror-enhancement to 3735 $\pm$ 1498 with mirror-enhancement for STORM imaging (Table 5.2). The widefield images—

which also used Alexa Fluor 647—showed a similar increase in signal-to-noise ratio with mirror-enhancement (Table 5.1, Fig. 5.3). This discrepancy in the extent of fluorescence enhancement was likely due to differences in the intrinsic quantum yields between the fluorophores. It has been previously reported the extent of quantum yield enhancement depends on the intrinsic quantum yield [212, 215]; fluorophores with lower intrinsic quantum yield display greater fluorescent enhancement, as evidenced in a comparison of Alexa Fluor 488 (quantum yield = 0.92 [217]), Alexa Fluor 532 (quantum yield = 0.61 [217]), and Alexa Fluor 647 (quantum yield = 0.33 [217]) by Heil, 2020 [215] in which Alexa Fluor 647 displayed the greatest degree of fluorescent enhancement. While the quantum yield of the red-emitting dye conjugated to fluorescent beads is unknown, it is unlikely to be Alexa Fluor 647 given the differences in excitation and emission maxima—λ_{EX} = 660 nm and λ_{EM} = 680 nm for the beads [218] while λ_{EX} = 650 nm and λ_{EM} = 655 nm for Alexa Fluor 647 [91]. Thus, it is possible that differences in quantum yield was responsible for the difference in fluorescent enhancement between bead imaging and STORM imaging.

There were several differences in the mirror-enhanced STORM results presented in this chapter compared to the implementation of mirror-enhanced STORM by Heil *et al.* 2018 [40]. First, Heil *et al.* 2018 observed lower background fluorescence with mirror-enhanced STORM relative to conventional STORM, contrasting the results in this chapter where higher background was observed with mirror-enhanced STORM (Fig. 5.2). This discrepancy may be explained by the difference in excitation intensities in the comparisons of imaging modalities. For the implementation of mirror-enhanced STORM by Heil *et al.* 2018, the excitation power was lowered to 50% ($\approx$ 5 kW/cm^2) while for conventional STORM, the excitation power was 100% ($\approx$ 10 kW/cm^2) [215]. In comparison, the same excitation power (60% $\approx$ 2.4 kW/cm^2) was used for conventional STORM and mirror-enhanced STORM in this work. Since higher excitation intensities increase background fluorescence [219], it is likely that the differences in background fluorescence between conventional and mirror-enhanced STORM can be attributed to this difference in excitation power.

Another notable difference was the higher localisation precisions recorded by Heil *et al.* 2018 for both conventional STORM and mirror-enhanced STORM; therein, mean

localisation precisions of $\sim$ 9 nm were recorded for STORM with epifluorescent illumination, $\sim$ 8.5 nm for STORM with total internal reflection fluorescence (TIRF), and $\sim$ 7.5 nm for mirror-enhanced STORM [215]. This inconsistency can likely be explained by the higher excitation power and the differing emission filters in the imaging paths of the microscopes. As previously mentioned, the excitation power was higher in the original implementation of mirror-enhanced STORM ($\sim$ 5 kW/cm^2 compared to $\sim$ 2.4 kW/cm^2). Because higher localisation precisions are correlated with higher excitation intensities [219], the disagreement in localisation precision may be partly explained by differing excitation intensities. In addition, the emission filter used by Heil *et al.* 2018 was a Chroma ET700/75m. This filter has a 66.8% collection efficiency ([220, 221]) for Alexa Fluor 647 compared to the Chroma ET690/50m emission filter used in the ROCS microscope (Methods: 3.1) which has a 55.8% collection efficiency ([220, 222]) for the same dye, resulting in a $\sim$ 20% higher collection efficiency in the original implementation of mirror-enhanced STORM. Therefore, it is likely that the combination of higher excitation intensity and higher collection efficiency contribute to the discrepancy in localisation precisions between this work and that of Heil *et al.* 2018. It is notable, however, that despite the lower localisation precisions in this chapter, the increase in mean localisation precision from mirror-enhanced fluorescence presented in this chapter (Fig. 5.2) was comparable to that in the original implementation (1.7 nm increase in this work, $\sim$ 1.5 nm increase in Heil *et al.* 2018), demonstrating that the impact of mirror-enhancement was similar for both studies.

Despite the higher localisation precisions in the original implementation, the FRC resolutions in the original implementation (57 nm for epifluorescence, 49 nm for TIRF) were lower than the resolutions from conventional STORM imaging (48 $\pm$ 4.6 nm, Fig. 5.5). Meanwhile, the FRC resolution for mirror-enhanced STORM (37 nm) was higher than datasets 1 and 2 in this work (44.2 nm and 45.6 nm, respectively) but lower than dataset 3 (29.4 nm). The lower resolution from conventional STORM reported by Heil *et al.* 2018 was likely due to the immunolabelling of NPCs with primary and secondary antibodies which can add up to 15 nm of linkage error [223, 224]. In contrast, the smaller size of the SNAP-tag used in this chapter adds negligible linkage error [18]. The detrimental effect of linkage error is exemplified in Chapter 7, wherein FRC resolutions

of 41.7 nm and 39.7 nm are presented for NPC structures acquired with conventional STORM (Chapter 7: Fig. 7.6**a**, Fig. 7.6**b**). Both values are comparable to the FRC resolution of 37 nm from mirror-enhanced STORM presented in Heil *et al.* 2018, thus highlighting that further resolution improvement is possible with careful selection of the fluorescent labelling method, and that the higher localisation precisions in the original implementation likely had little impact on the discrepancy in FRC resolutions.

Nevertheless, the FRC resolution from mirror-enhanced STORM implemented by Heil *et al.* 2018 was still higher than two out of three datasets in this chapter, even with higher linkage error. Given the similarity in the increases in localisation precision from mirror-enhancement, and the lower resolutions in conventional STORM, the discrepancy in FRC resolutions is unlikely due to differences in the degree of mirror-enhancement, or to the higher localisation precisions. Rather, a potential explanation may be the difference in sample preparation methodologies between this chapter and the original implementation. For the benchmarking of mirror-enhanced STORM in Heil *et al.* 2018, nuclear envelopes were isolated from *Xenopus laevis* oocytes and attached to coverslips as described in refs. [225, 226]. This extraction method was used to ensure that NPCs were situated at $\sim$ 50 nm from the reflective surface, maximising fluorescence enhancement. In contrast, the NPCs in this chapter were labelled in whole cells that had been fixed and permeabilised. Therefore, the distance between NPCs and the reflective surface—and thus, the extent of fluorescence enhancement—was unknown. As such, it is possible that greater fluorescence enhancement was achieved by Heil *et al.* 2018, resulting in higher FRC resolutions.

A higher labelling efficiency may also be achievable with purified nuclear envelopes compared to labelling via fixation and permeabilisation (Methods: 3.4.5). Considering that NPCs are situated on the nuclear envelope [99], a fluorescent label would be hypothesised to have more direct access to its binding target when using purified nuclear envelopes, whereas labelling NPCs in whole cells would require the fluorescent label to diffuse through channels in the plasma membrane that are formed through permeabilisation. Given that the labelling efficiency of Nup96-SNAP-AF647 has been previously characterised to be 58% [93], it would, therefore, be beneficial to evaluate and compare the labelling efficiency of NPCs from purified nuclear envelopes to assess whether the

difference in labelling contributed to the difference in FRC resolutions. Any comparative analysis of the NPC FRC resolutions, however, is ultimately limited by the lack of experimental repeats in the FRC measurements from Heil *et al* 2018. More experimental evidence would be required for a more rigorous assessment of the effects of linkage error and labelling method on the FRC resolution of mirror-enhanced STORM.

Finally, the mirror-enhanced STORM imaging presented in this chapter could be improved substantially if the degree of fluorescent enhancement were characterised. As previously mentioned, the distance between the NPCs and the reflective surface was unknown. Previous literature and Eq. 5.1 have established how the modulation of fluorescence lifetime and fluorescent enhancement depends on this distance [35, 36]. Such considerations were circumvented in Heil *et al.* 2018 by using purified nuclear envelopes, purified microtubules, and membrane proteins, all of which would be situated at distances that maximise fluorescence enhancement once attached to a coverslip. However, the use of purified organelles is uncommon in SMLM, meaning that the challenges of imaging intracellular structures in whole cells using mirror-enhanced fluorescence have not been adequately addressed. Instead, the approach described in ref. [38] could be used, wherein fluorescence lifetimes were measured with varying thicknesses of the dielectric coating, meaning that fluorescent lifetime measurements of the sample can be used as a read-out for the distance between the fluorophore and reflective layer. This method could allow for better tunability of the mirror-fluorophore distance during image acquisition, thereby maximising the benefits of fluorescence enhancement.

5.5.1 Conclusions

Taken together, the characterisation and application of mirror-enhanced STORM in this chapter—despite differences in the mirror slide dimensions, background fluorescence, and localisation precisions—showed a similar overall outcome to the original work, with the advantage of imaging of whole cells, as well as improvements in the localisation precisions and FRC resolutions of NPCs that can be attributed to the presence of a reflective layer. Mirror-enhanced STORM was also successfully combined with computational denoising, thus incorporating the resolution improvements of both technologies. The results in this chapter, therefore, demonstrate that using reflective surfaces in STORM is a feasible

and reproducible photonic technology with which to increase the resolution of SMLM beyond that achievable with conventional imaging.

6 Comparing Approaches to Fluorescent Labelling of Intracellular Proteins Using Nanobodies

6.1 Overview

Fluorescent labelling with nanobodies overcomes many of the disadvantages associated with other fluorescent labelling methods commonly used in STORM and SMLM (Introduction: 1.2.2); nanobodies (single-domain antibodies) allow endogenous proteins to be labelled—unlike using fluorescent proteins—and they circumvent the large linkage error associated with using antibodies for fluorescent labelling, thereby increasing the localisation accuracy. However, fluorescent labelling with nanobodies is a less mature technology compared to labelling with antibodies, and so best practices are not as well-established, limiting their wider usage. To address these limitations, evaluations of live-cell labelling methods using nanobodies for STORM are presented in this chapter. Comparisons of labelling with nanobodies that differ in the location of the reactive cysteine residue used for dye conjugation are also presented.

The anti-vimentin nanobodies, VB3 and VB6, were chosen for the comparison of live-cell labelling methods. Previous literature had described their use for fluorescent labelling for diffraction-limited microscopy [105], as well as validated their binding to vimentin using western blotting and biolayer interferometry. Prior to the results presented in this chapter, the DNA sequences encoding VB3 and VB6 had been cloned into pOPINE plasmids containing the sequence for the SNAP-tag (Methods: 3.3). These plasmids were used for mammalian cell transfection (Methods: 3.4.3), thereby inducing endogenous expression of VB3-SNAP and VB6-SNAP and allowing for fluorescent labelling of the SNAP-tag. The same sequences were also cloned into pOPINVHH plasmids by Dr. Siva Ramadurai (The Rosalind Franklin Institute) for protein expression and purification (Methods: 3.3.4, Methods: 3.3.5). The pOPINVHH plasmids had been engineered such that the nanobody contained an extra cysteine residue and a polyhistidine tag at the C-terminus, thereby allowing for dye conjugation and affinity chromatography,

respectively.

To compare fluorescent labelling of nanobodies with different locations of their reactive cysteine residues, an anti-GFP nanobody was used to label U2OS cells stably expressing Nup96-GFP. Prior to this chapter, the anti-GFP nanobody was cloned into a pOPIN-VHH plasmid by Dr. Siva Ramadurai for protein expression, protein purification, and dye conjugation as described above.

While there is literature that describes the use of nanobodies for STORM [59, 61, 63, 107], there is little information aimed at comparing and evaluating different labelling methodologies. As such, the aim of this chapter is to compare the outcomes of STORM imaging of nanobody-labelled vimentin with different fluorescent labelling methods, as well as the outcomes of STORM imaging using different mutants of the anti-GFP nanobody. By performing this comparison, it is hoped that the results will inform on best practices for the development of nanobody labelling protocols.

6.2 STORM imaging of vimentin using purified nanobodies

To compare different labelling methods, the outcome of STORM imaging using conventional cell fixation, permeabilisation, and immunolabelling with nanobodies was assessed. Here, vimentin in HeLa cells was labelled with purified VB3-Alexa Fluor 647 according to Methods: 3.4.8. STORM imaging was carried out using the ROCS microscope from Chapter 4 as described in Methods: 3.6.1. Single-molecule localisation was carried out as in Theory: 2.3 and Methods: 3.7.1, and a qualitative assessment of the super-resolution image was carried out.

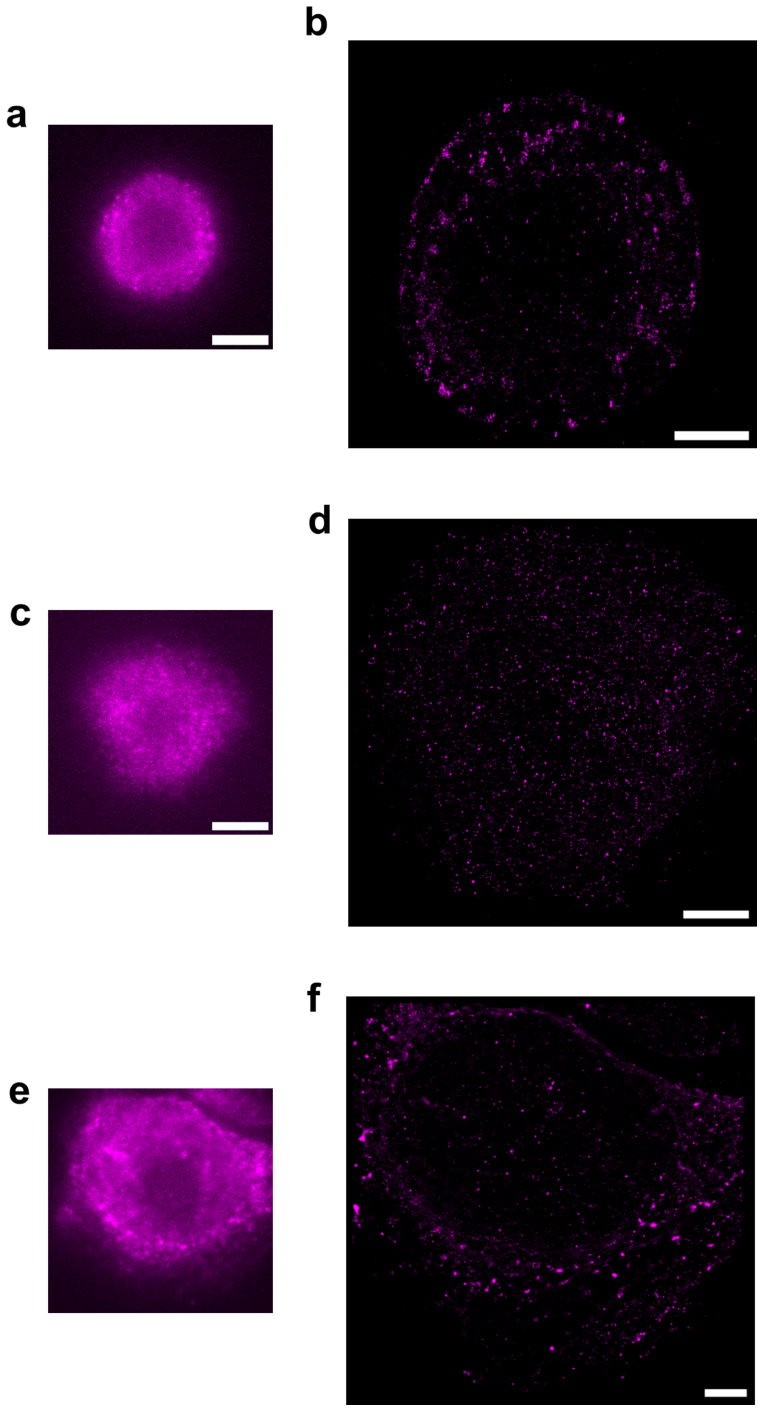

Fig. 6.1: **STORM imaging of vimentin in HeLa cells labelled with anti-vimentin nanobodies conjugated to AF647 using conventional cell fixation and permeabilisation.** Widefield image scale bars: 10 µm. STORM reconstruction scale bars: 5 µm. **a**–**b** Widefield image (**a**) and STORM reconstruction **b** following imaging of vimentin labelled with VB3-AF647. **c**–**d** Widefield image (**c**) and reconstruction (**d**) with vimentin labelled with VB3-AF647 at twice the concentration of **a** and **b**. **e**–**f** Widefield image **e** and reconstruction **f** of vimentin labelled with a different anti-vimentin nanobody, VB6, conjugated to AF647.

Unexpectedly, vimentin filaments could not be visualised from either the widefield image (Fig. 6.1**a**) or the STORM reconstruction (Fig. 6.1**b**). Such an outcome was

not observed in previous literature describing STORM imaging of vimentin [107, 227], indicating that some optimisation of the labelling protocol was required. Given the inability to visualise vimentin filaments in the STORM reconstructions, quantitative analyses using the FRC resolution were not carried out as in previous chapters.

To improve the labelling, the concentration of VB3-AF647 was doubled from 1:200 to 1:100. Since the labelling density in the super-resolution image in Fig. 6.1**b** appeared sparse, it may have been possible that the nanobody concentration was too low to achieve a sufficient labelling density to visualise vimentin.

Again, the expected filamentous structures of vimentin were not observed following nanobody labelling (Fig. 6.1**c**, Fig. 6.1**d**), despite using a higher concentration, suggesting that VB3 may not have been binding to vimentin, or that the structure of vimentin was disrupted by the fixation and permeabilisation protocol. Different modifications to the labelling protocol, such as a higher concentration of bovine serum albumin for blocking and a lower concentration of Triton-X100 for permeabilisation, were made. However, there was little change in the experimental outcome (not shown), with all STORM reconstructions resembling those in Fig. 6.1**b** and Fig. 6.1**d**.

To assess whether the binding of VB3 to vimentin was contributing to the poor labelling, the labelling procedure (Methods: 3.4.8) was repeated with VB6 conjugated to Alexa Fluor 647 (VB6-AF647). If improved labelling is observed, it can be inferred that VB3 had insufficient binding affinity for vimentin and the fixation and permeabilisation does not contribute to the outcomes in Figs. 6.1**b** and 6.1**d**.

Both the outcome from widefield imaging and STORM imaging were similar to that with VB3 (Fig. 6.1**e**, Fig. 6.1**f**). Therefore, it was likely that either both nanobodies do not exhibit sufficient binding to vimentin or that fixation and permeabilisation was affecting the ability of the nanobodies to label vimentin.

6.3 STORM imaging of vimentin labelled in live cells with nanobody-SNAP fusion proteins

The potential detrimental impact of cell fixation and permeabilisation was assessed by using live-cell labelling methods. The first method to be tested involved transfection of HeLa cells using a pOPINE plasmid encoding VB3 or VB6 fused to a SNAP-tag. Here, cells would endogenously express VB3-SNAP or VB6-SNAP, allowing labelling of the SNAP-tag using the same method as that used for nuclear pore complexes (Methods: 3.4.5) but with a lower Triton-X100 concentration of 0.1%. While this method does involve fixation and permeabilisation, these steps occur after nanobody-vimentin binding, reducing the risk of disrupting the epitopes to which the nanobodies bind.

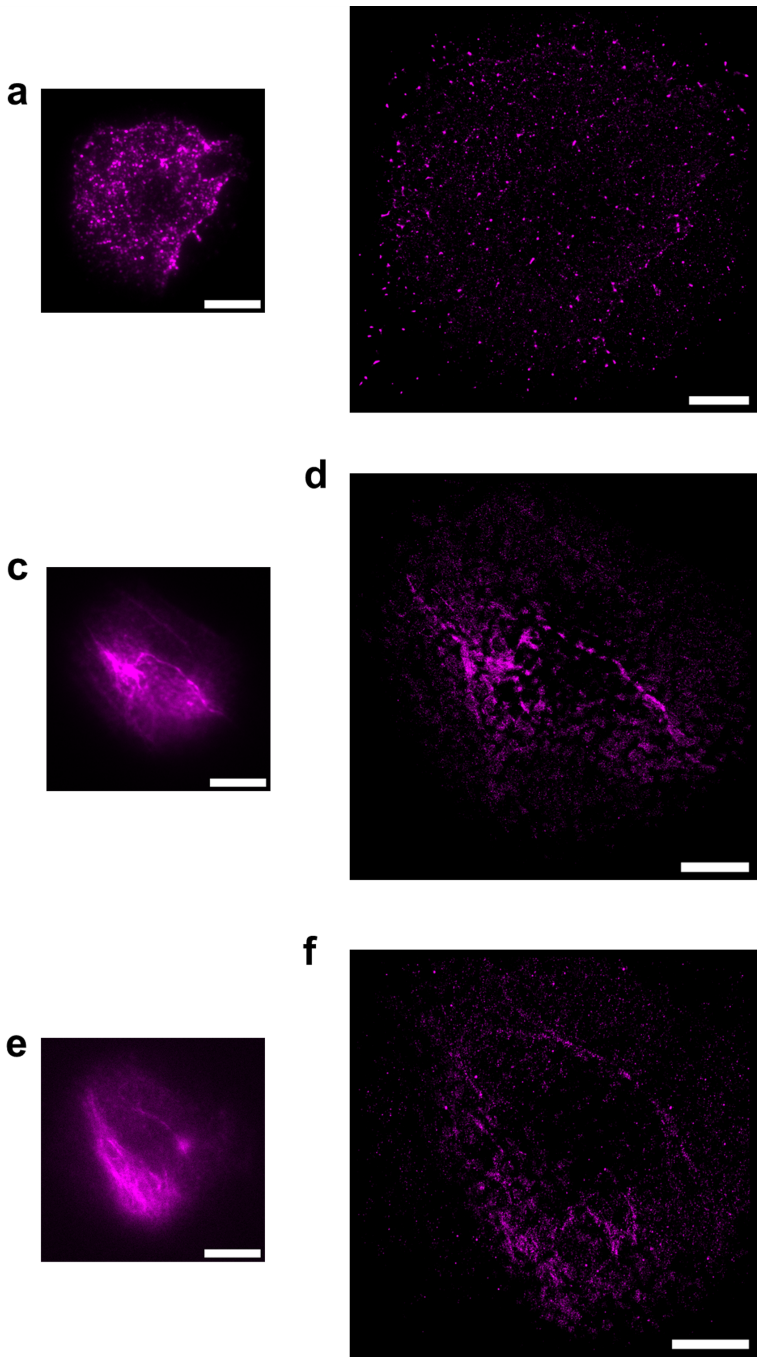

Fig. 6.2: **STORM imaging of vimentin following transfection with VB3-SNAP or VB6-SNAP and fluorescent labelling with AF647.** Scale bars: 10 µm for widefield images, 5 µm for STORM reconstructions. **a**–**b** Widefield image (**a**) and STORM reconstruction **b** of a HeLa cell following transfection with VB3-SNAP and labelling with AF647. **c**–**d** Widefield image (**c**) and reconstruction (**d**) of a cell following transfection with VB6-SNAP and labelling with AF647. **e**–**f** Widefield image **e** and reconstruction **f** following transfection with VB6-SNAP and labelling with an AF647 concentration lowered from 1 µM to 0.4 µM.

With the VB3-SNAP variant, little improvement was visible. No filaments were visible in either the widefield image (Fig. 6.2**a**) or the STORM reconstruction (Fig. 6.2**b**), and the fluorophores are scattered throughout the inside of the cell. In contrast, some

improvement was observed from VB6-SNAP. Vimentin filaments were visible in the widefield image (Fig. 6.2**c**) and traces of the filaments were visible in the STORM reconstruction (Fig. 6.2**d**). However, there was high background noise in the STORM reconstruction, thereby degrading the super-resolution image quality. The filaments also exhibited discontinuities which may be indicative of artifacts induced by fixation and permeabilisation [98], or insufficient labelling density. Nevertheless, since the VB6 nanobody displayed more promising results, subsequent evaluations of STORM imaging outcomes were focused on the VB6 nanobody.

To reduce background noise, the labelling procedure was repeated with VB6-SNAP using a lower fluorophore concentration of 0.4 µM (original concentration: 1 µM). However, even with a lower fluorophore concentration, there was little difference in the outcome of STORM imaging. While the filaments were visible in the widefield image (Fig. 6.2**e**), the background noise from unspecifically bound fluorophores was still high in the STORM reconstruction (Fig. 6.2**f**), and so varying the fluorophore concentration was unlikely to impact the imaging outcome.

6.4 STORM imaging of vimentin labelled in live cells with streptolysin-O

The results thus far have demonstrated that fluorescent labelling in live cells followed by fixation and permeabilisation better preserve the structure of vimentin compared to methods involving fixation and permeabilisation prior to labelling. It was, therefore, hypothesised that nanobody labelling using streptolysin-O (SLO) would improve labelling efficiency. SLO is a pore-forming protein from *Streptococcus pyogenes* that can be used to deliver nanobodies into live cells (Methods: 3.4.7). This technique is less disruptive to cells compared to fixation and permeabilisation since the stretolysin-O can be washed off, allowing the plasma membrane to reseal. While cell fixation was still necessary for STORM imaging, permeabilisation was avoided by using SLO for labelling.

Prior work to determine the optimal SLO concentration and cell confluency for nanobody labelling with SLO had been carried out by Dr. Siva Ramadurai. From this, confocal microscopy images of vimentin labelled with VB6-AF647 (Fig. 6.3**a**) had been acquired

(SP8 Lightning confocal microscope, Leica Microsystems Ltd.), demonstrating the feasibility of using SLO for vimentin labelling. The SLO labelling method was then repeated for STORM. The cell line was also changed to U2OS cells from HeLa cells since it was reasoned that the flatter shape of U2OS cells may reduce the background noise present above and below the focal plane.

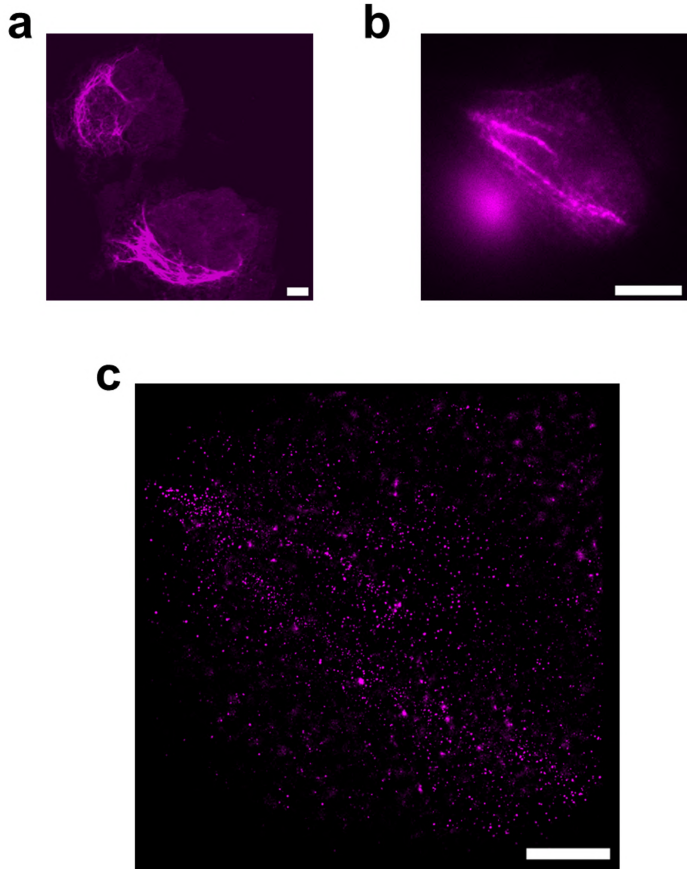

Fig. 6.3: **STORM imaging of vimentin following VB6-AF647 labelling using Streptolysin-O. a** Confocal image of live HeLa cells following VB6-AF647 delivery using SLO. The image was acquired by Dr. Siva Ramadurai (The Rosalind Franklin Institute) using a SP8 Lightning confocal microscope (Leica Microsystems Ltd.) and is reused with permission. Scale bar: 5 µm. **b** Widefield image of fixed U2OS cells using the same labelling method as **a**. Scale bar: 10 µm. **c** Super-resolution reconstruction following STORM of the image in **b**.

Intact vimentin filaments were visible in both the widefield image and the confocal image (Fig. 6.3**a**, Fig. 6.3**b**), supporting the observation that fixation and permeabilisation were detrimental to nanobody labelling. While the confocal image appeared sharper, this difference can likely be attributed to the increased contrast from the optical sectioning capability of a confocal microscope—a feature that is not present in epifluorescent imaging. Despite vimentin being visible in the diffraction-limited images, the super-resolution image from STORM (Fig. 6.3**c**) still displayed similar problems to previous results; the outline of the filaments was visible but lacked continuity, and visualisation of

the filaments was obfuscated by background noise from unspecifically bound nanobodies. Again, it is possible that the fixation procedure was disrupting the structure of vimentin, or the labelling density was too low.

6.5 STORM imaging of vimentin with mutated nanobodies

From the super-resolution images of vimentin labelled using VB6-SNAP and VB6-AF647 with SLO (Fig. 5.4**d**, Fig. 5.5**c**), the noise from unspecifically bound nanobodies was high and the filaments exhibited poor continuity. Thus, it was hypothesised that the labelling density from labelling vimentin with VB6 was too low to achieve high resolution STORM images.

To increase nanobody labelling density, it was reasoned that changing the location of the active cysteine residue used for conjugation to the maleimide derivative of AF647 may be beneficial. Using a different residue for dye conjugation may result in improved presentation of the dye in relation to the interaction between the nanobody and vimentin. In other words, certain mutations might result in the dye being enclosed within the core of the nanobody, worsening photoswitching, while other mutations might result in the dye being more solvent-exposed, allowing for better photoswitching. Using mutagenesis to alter nanobody binding outcomes has been utilised previously by Pleiner *et al.* 2015 for anti-nucleoporin nanobodies where particular mutants improved the signal-to-noise ratio in confocal imaging. Following a similar approach, two mutants each of VB3 and VB6 were generated. One mutant has a reactive cysteine at the N-terminus (termed NtCys) while the other has the 7th position serine mutated into a cysteine residue (S7C). The VB3 and VB6 constructs used thus far have a reactive cysteine residue at the C-terminus (termed CtCys)

Here, the different nanobody mutants were generated by PCR with primers that encoded the relevant mutation. The PCR products were then ligated into the pOPINVHH vector, expressed in *E. coli*, and purified as previously described (Methods: 3.3, Methods: 3.3.4, Methods: 3.3.5). Following conjugation to AF647, VB3-AF647 was used to label vimentin in live U2OS cells using SLO. The cells were then fixed and imaged using a ZEISS Elyra PS.1 Microscope (Methods: 3.6.3). While most previous results have fo-

cused on VB6, mutating VB6 resulted in precipitation during protein purification, and so VB3 was used instead.

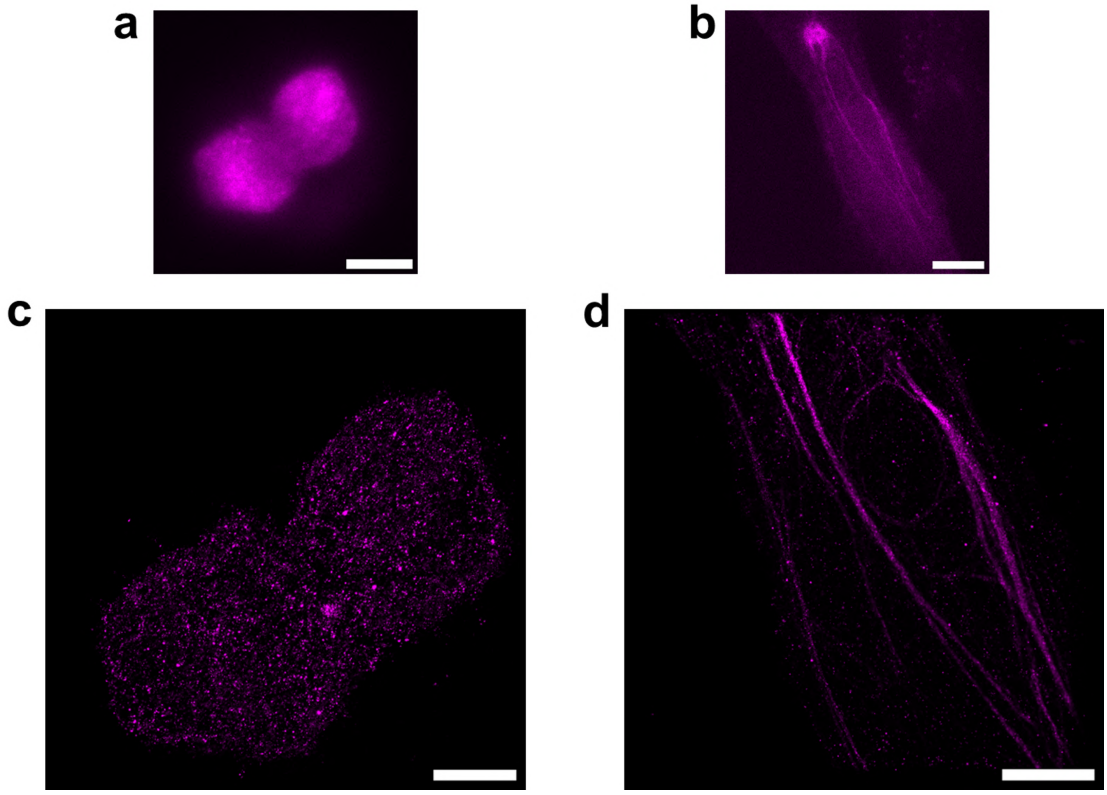

Fig. 6.4: **STORM imaging of vimentin with different VB3 mutants.** Scale bars: 10 µm for **a** and **b**, 5 µm for **c** and **d**. **a** Widefield image of a U2OS cell labelled with VB3-NtCys. **b** Widefield image of a U2OS cell labelled with VB3-S7C. **c** Super-resolution reconstruction following STORM of the image in **a**. **d** Super-resolution reconstructions following STORM of the image in **b**.

Vimentin filaments were not observed when cells were labelled with the VB3-NtCys mutant (Fig. 6.4**a**, Fig. 6.4**c**) but showed improved resolution on labelling with the VB3-S7C mutant (Fig. 6.4**b**, Fig. 6.4**d**). Notably, the STORM reconstruction in Fig. 6.4**d** from VB3-S7C labelling displayed the highest image quality out of the different labelling methods presented, with vimentin filaments clearly visible. These results, therefore, demonstrate that nanobody labelling density can be improved by altering the location of the active cysteine residue. Live-cell labelling methods were also shown to preserve native structures better with stark differences in imaging outcomes compared to traditional cell fixation and permeabilisation.

6.6 STORM imaging of NPCs with nanobody mutants

To investigate further STORM imaging outcomes with different nanobody mutants, STORM imaging of U2OS cells stably expressing Nup96-GFP was carried out. Here, two anti-GFP nanobodies with different mutations were used: one with an additional cysteine residue introduced at the N-terminus (NtCys) and the other with an additional cysteine residue introduced at the C-terminus (CtCys). These cysteine residues were then used for conjugation to a maleimide derivative of Alexa Fluor 647. Neither of these mutations in anti-vimentin nanobodies had resulted in successful labelling of vimentin. The cells were labelled with nanobody-dye conjugates according to Methods: 3.4.6 and STORM was carried out as previously.

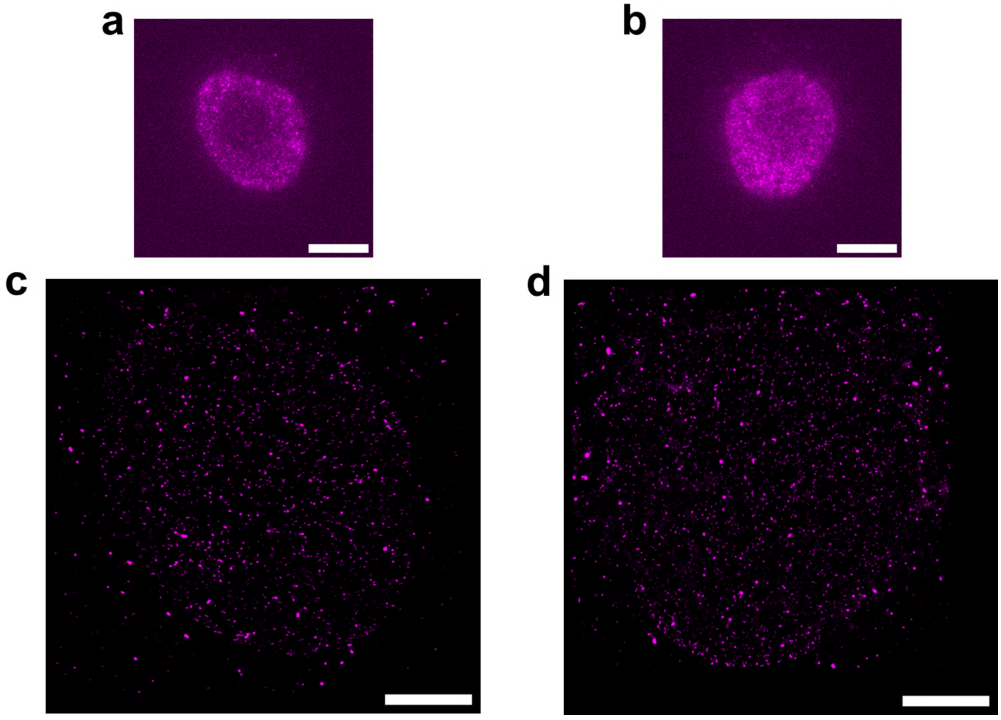

Fig. 6.5: **STORM imaging of U2OS cells stably expressing Nup96-GFP with different anti-GFP nanobody mutants conjugated to AF647.** Scale bars: 10 µm for **a** and **b**, 5 µm for **c** and **d**. **a** Widefield image of a nucleus in U2OS cells following labelling with the NtCys-anti-GFP nanobody. **b** Widefield image of a nucleus in U2OS cells following labelling with CtCys-anti-GFP nanobody. The grayscale range of the image has been adjusted such that it was identical to **a**. **c** Super-resolution reconstruction following STORM of the image in **a**. **d** Super-resolution reconstruction of the image in **b**.

From the widefield images of Nup96-GFP labelled with different anti-GFP nanobody mutants (Fig. 6.5**a**, Fig. 6.5**b**), higher contrast was observed for the anti-GFP nanobody that had a C-terminal reactive cysteine. However, neither mutant displayed resolvable NPC ring structures (Fig. 6.5**c**, Fig. 6.5**d**) as observed in Chapter 4 and Chapter 5,

suggesting that the nanobody mutants did not have sufficient affinity to achieve the labelling densities required for STORM, or that the ability of the dye to photoswitch was inadequate.

Despite attempts to improve the labelling density, such as by using higher nanobody concentrations, the outcome of STORM imaging did not change from that presented in Fig. 6.5. As such, an alternative approach to examine differences in labelling between the mutants was adopted. Here, photoswitching parameters were investigated from the STORM image sequences, namely the duty cycle (Theory: Eq. 2.3), photoswitching time, number of photoswitching cycles, photons per photoswitching cycle, and total photons. Single-molecules from the first 10000 frames ($\sim$ 300 s) that exceeded an intensity threshold were selected for analysis (Methods: 3.8.1). In total, three image sequences each of the NtCys mutant, CtCys mutant, and a positive control were analysed. The positive control was U2OS cells stably expressing Nup96-SNAP that had been labelled with Alexa Fluor 647 and had visible NPC structures following STORM (these data are the same as those presented in Chapter 7, Fig. 7.7).

Similar to the analyses in Chapter 5 and Table 5.2, the weighted means of each photoswitching parameter are tabulated below:

Table 6.1: **Weighted means for each experimental repeat and for all photoswitching parameters of different anti-GFP nanobodies.** The weighted means and weighted standard deviations were calculated using Eq. 5.3 and Eq. 5.4, respectively.

Mutant	Weighted mean duty cycle	Weighted mean photo-switching time (s)	Weighted mean number of cycles	Weighted mean photons per cycle	Weighted mean total photons
NtCys	0.00049 ± 0.00015	222 ± 65	9 ± 3	5810 ± 653	60197 ± 22450
CtCys	0.00044 ± 0.00003	516 ± 157	11 ± 0	4835 ± 197	59375 ± 188
Control	0.00077 ± 0.00023	444 ± 239	17 ± 3	6905 ± 131	123582 ± 25331

From this analysis, the single-molecules in the control image sequence had, on average, a higher number of cycles, more photons per cycle, and more emitted photons (Table 6.1). The number of photons is critical to ensuring that single-molecules are localised accurately. Therefore, it was likely that placing the reactive cysteine residue at either the

N-terminus or C-terminus had a negative effect on the ability of the dye to photoswitch and thus, on its ability to be localised accurately. The binding affinities between these two nanobodies and Nup96-GFP may also be worse than that between Nup96-SNAP and the dye, decreasing the labelling density and resolution of NPCs.

6.7 Discussion and conclusions

In this chapter, the outcomes of STORM with different fluorescent labelling methods using nanobodies have been presented. The outcomes of STORM using nanobodies that differ in the location of the dye-reactive cysteine residue have also been presented. From labelling vimentin with VB3 and VB6, classic cell fixation and permeabilisation did not yield the expected filamentous structure in either widefield images or super-resolution STORM reconstructions (Fig. 6.1). Live-cell labelling via transfection with VB6-SNAP or via delivery of nanobodies using SLO offered minor improvements in visualising vimentin, with filamentous structures visible in widefield images but not in STORM images (Fig. 6.2, Fig. 6.3). Finally, fluorescent labelling combining SLO delivery with the VB3 mutant, S7C, resulted in clear visualisation of vimentin filaments in widefield images and STORM (Fig. 6.3).

From labelling Nup96-GFP with anti-GFP nanobodies, it was observed that nanobodies containing an extra N-terminal dye-reactive cysteine or extra C-terminal dye-reactive cysteine did not produce the expected ring structures of NPCs from STORM (Fig. 6.5). Furthermore, the measured photoswitching parameters were worse than those obtained from fluorescent labelling with Nup96-SNAP and SNAP-reactable AF647 (Table 6.1).

The observation that carrying out fluorescent labelling prior to fixation and permeabilisation improves visualisation of vimentin corroborates results from previous literature that highlight the detrimental effects of fixation on cellular morphology and nanostructure [228–230]. However, all imaging work in this chapter, nevertheless, used fixed cells due to the ROCS microscope lacking live-cell imaging capability. The scope of this chapter could, therefore, be expanded through installation of a stage top incubator for the ROCS microscope and assessing whether the same outcomes could be observed in live cells. Such a modification may negate some of the advantages in stability conferred

by the ROCS microscope—due to the instability of sample stages—but would allow for a more accurate assessment of labelling outcomes. An additional challenge would be the compatibility of AF647 with live-cell STORM. The reducing environment in a cell may not be conducive to optimal photoswitching, and so different dyes—potentially those that spontaneously blink [231–233]—may be necessary for an accurate assessment of labelling outcomes in live cells.

The scope of this chapter could also be further expanded by assessing photoswitching and STORM outcomes with different nanobody mutants and with more fluorophores. Recent literature has indicated that nanobodies conjugated to AF647 display worse photoswitching behaviour [234]—an observation corroborated by the results in Table 6.1. In contrast, the same study indicated that conjugating nanobodies to Janelia Fluor 635b restored adequate photoswitching for high-resolution STORM. Thus, it would be of interest to the wider SMLM community to investigate the photoswitching of nanobodies that are conjugated to different dyes commonly used for STORM by repeating the experimental approach used to generate the results in Table 6.1 (Methods: 3.8.1). It would also be of interest to examine the degree by which photoswitching can be modulated by altering the location of the dye-reactive amino acid residue using the same experimental approach. Finally, the biochemical mechanisms for the worsened photoswitching of nanobodies conjugated to Alexa Fluor 647 remain unclear. Further interrogation of this would likely entail measurements of binding affinities, investigation of resistance to the reducing conditions of the STORM buffer, and potentially structural studies of nanobodies bound to their epitopes. Overall, the information gained by expanding this aspect of the work would provide useful guidance to laboratories aiming to develop fluorescent labelling methods using nanobodies for both research and biotechnological applications.

The evaluation of STORM imaging of vimentin and Nup96-GFP may have benefitted from prior assessment of binding affinity using biophysical techniques such as biolayer interferometry [235]. While differences in the appearance of vimentin filaments were visible from using different labelling methodologies (Fig. 6.1, Fig. 6.2, Fig. 6.3), it was challenging to assess the degree to which these observations may have been attributable to differences in binding affinities. In particular, assessing the affinities of nanobodies

that differ in the location of the dye-reactive cysteine residue may give biochemical insights into the variation in photoswitching performance and the variation in labelling density. For example, if nanobodies with different mutations exhibited the same affinity, it may be possible that the dye is poorly exposed to the reducing agent in the buffer and, thus, does not photoswitch adequately. In contrast, if varying affinities are observed, it may be possible that the dye interferes with nanobody-epitope binding.

6.7.1 Conclusions

Overall, the assessment of using nanobodies for classic cell fixation and permeabilisation, and for live-cell labelling revealed that fixation and permeabilisation disrupted the structure of biological targets, thus rendering them unobservable. In contrast, live-cell labelling displayed much improved preservation of the biological sample. Additionally, it was revealed that altering the location of the dye-reactive amino acid residue could afect the outcome of STORM, as well as the photoswitching behaviour of the conjugated dye. These results provide guidance to those seeking to optimise the usage of nanobodies to label biological structures for STORM—information which is lacking in current literature—and also provide a starting point for more detailed biochemical investigations into mechanisms that would explain the worsened photoswitching for particular mutants or dyes.

7 Evaluating Denoising in SMLM

7.1 Overview

The signal-to-noise ratio (SNR) in SMLM is critical to the reliability and accuracy of localising single-molecules—the process from which a super-resolution image is reconstructed and biological information is extracted. Problems with SNR are exacerbated in imaging modalities that necessitate lower excitation intensities or use fluorophores with lower photon counts, such as live-cell imaging or PALM with fluorescent proteins. While SNR can be improved by modifying experimental protocols, it is often challenging to know *a priori* the experimental parameters that will produce the optimal SNR. Denoising algorithms are, therefore, an attractive solution to improve SNR and localisation accuracy without time-consuming modifications to experimental protocols.

To avoid confusion with measures of SNR commonly used in image processing, the term "SNR" is not used henceforth in this work for assessments of super-resolution images. Because super-resolution images are formed from the pointillistic accumulation of fluorophore positions, their characteristics differ from diffraction-limited images which record the intensity of fluorescent signals. As such, traditional SNR metrics developed for diffraction-limited images are avoided. Instead, for qualitative assessments, the visibility of structural features is used to assess the effects of denoising on super-resolution image quality. The image quality is deemed sufficient when structural features are not obfuscated by noise. "Noise", in turn, is defined as any image feature that obfuscates visualisation of the sample structure, including autofluorescence, unspecifically bound fluorophores, background fluorescence, shot noise, EMCCD amplification noise, and read noise [65, 67, 98, 236, 237]. For quantitative assessments, metrics developed specifically for SMLM, such as the Fourier Ring correlation (Theory: 2.4), are used.

Deep learning methods are a promising approach to tackle denoising since they, in theory, should be able to learn the characteristics of noise in an image without prior assumptions. SRDTrans is one of few deep learning denoising methods that have been

described for SMLM [81]. However, as described in Introduction: 1.2.3, the broader applicability of this algorithm is limited by its lack of evaluation on different biological samples—particularly where the sample structure is unknown *a priori*—and by its lack of evaluation on common types of noise in SMLM. Further, the ability of the algorithm to generalise to different microscopes, which is a key feature of deep learning, was uncharacterised.

In this chapter the results of a systematic characterisation and evaluation of the denoising capability of SRDTrans (previously used for denoising in Chapter 5) are presented. Three different biological samples were used to investigate the generalisability to different structures, namely microtubules (Introduction: 1.4.1), nuclear pore complexes (NPCs, Introduction: 1.4.2), and the ACE-2 receptor (Introduction: 1.4.4), representing a stereotypic 1D structure, a stereotypic 2D structure, and an unstructured sample, respectively. Generalisability across the different samples, different types of noise, and different microscopes was investigated, as well as the effect of denoising on the estimated photophysical parameters of single molecules. Finally, further applications to address some of the limitations of the algorithm are presented.

7.2 Evaluating model training methods

An important consideration in deep learning is the extent of sample space covered by the training data [84]. Biases in the selection of training data can introduce artefacts and skew experimental outcomes during inference. As such, establishing best practices for model training is critical to the effectiveness of a deep learning model.

Given that only microtubules were used to train SRDTrans in its original implementation [81], the best practices for model training using other biological samples were not obvious. Therefore, different denoising parameters were obtained by training SRDTrans on different datasets (Methods: 3.10.1); here, the datasets included a publicly available SMLM image sequence of microtubules acquired originally by the developers of SRDTrans [238], a synthetic SMLM image sequence generated using ThunderSTORM, and an image sequence of microtubules acquired with the ROCS microscope. Model inference was carried out on a STORM image sequence of microtubules immunolabelled with

Alexa Fluor 647 that had been acquired with the ROCS microscope (Methods: 3.4.4, 3.6.1), producing a denoised image sequence. The first frame—which was reprensentative of subsequent frames—of this denoised image sequence was used to assess for image artefacts that would have resulted from denoising.

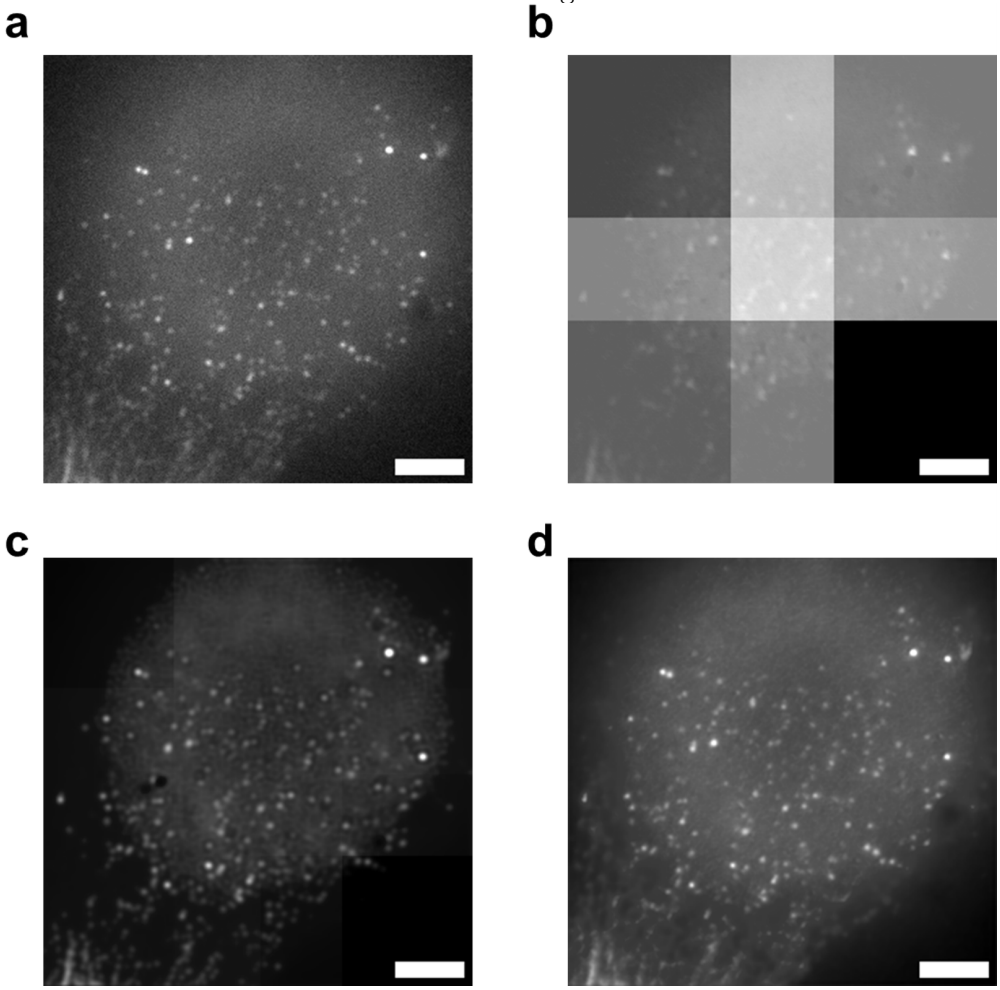

Fig. 7.1: **Assessing the presence of image artefacts from denoising microtubule SMLM data using SRDTrans trained with different datasets.** The scale bars are 5 µm in all images. A STORM image sequence of microtubules immunolabelled with Alexa Fluor 647 was used for evaluation. **a** First frame of the original STORM image sequence, i.e. without denoising. **b** First frame of the denoised STORM image sequence in which the denoising parameters were obtained by training SRDTrans on an image sequence of microtubules made publicly available by Li *et al.* 2023. **c** First frame of the denoised STORM image sequence where the denoising parameters were from training SRDTrans on a synthetic SMLM image sequence. **d** First frame of denoised data wherein model inference was carried out on the same image sequence with which SRDTrans was trained.

Obvious checkerboard artefacts were visible when using the microtubule data provided by Li *et al.* 2023 for training (Fig. 7.1**b**). Such artefacts are well-documented for deconvolution operations that are common in neural networks and vision transformers [239], typically arising from uneven overlap of the areas from which successive deconvolutions are carried out. The same artefacts were visible, albeit less apparent, when using denois-

ing parameters trained with synthetic SMLM data (Fig. 7.1**c**). Both examples imply that neither the SMLM data from Li *et al.* 2023 nor synthetic data capture accurately the noise in the images acquired by the ROCS microscope. In contrast, training SRD-Trans on the microtubule STORM image sequence acquired with the ROCS microscope and carrying out model inference on the same dataset produced an artefact-free image sequence (Fig. 7.1**d**).

To investigate further best practices for model training, the denoising parameters obtained by training on a STORM image sequence of microtubules acquired with the ROCS microscope were used for inference on NPCs in U2OS cells labelled with Alexa Fluor 647 and ACE-2 receptor in Calu-3 cells labelled with ATTO 488. The NPCs were labelled as described in Methods: 3.4.5. The ACE-2-SNAP fusion protein was introduced into Calu-3 cells via transfection using a pOPINE plasmid (Methods: 3.4.3) and was labelled with ATTO 488 according to Methods: 3.4.9. For denoising ACE-2-SNAP-ATTO 488, the model trained from microtubule data was also compared to a model trained on an image sequence of ACE-2-SNAP-ATTO 488.

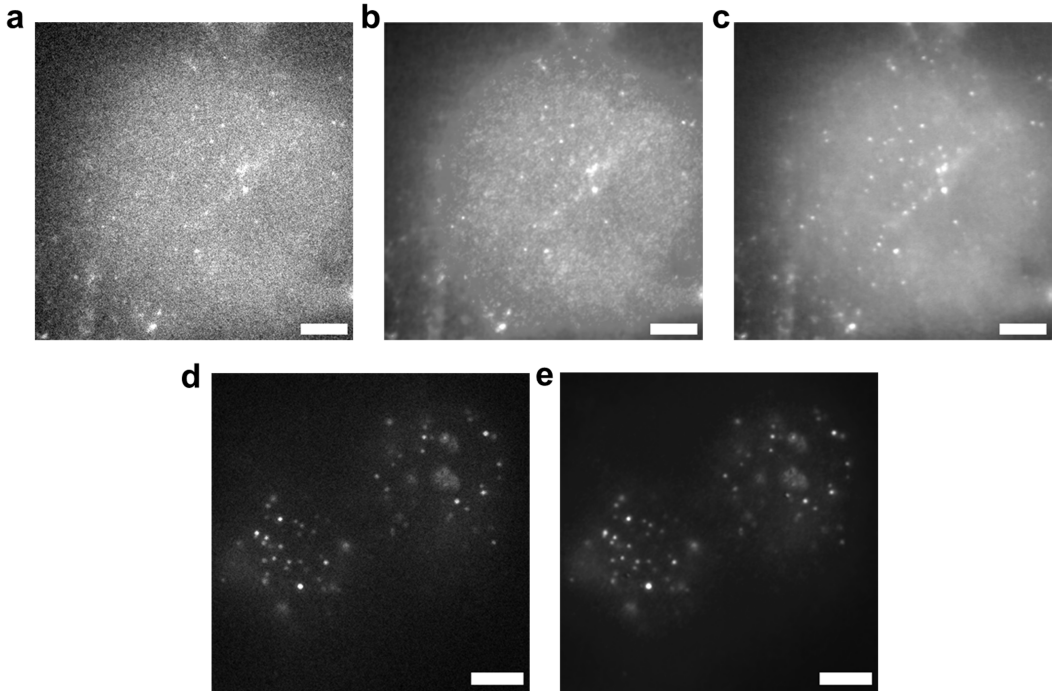

Fig. 7.2: **Assessing for image artefacts from denoising NPC SMLM data and ACE-2 SMLM data using SRDTrans.** The scale bars are 5 µm in all images. The ACE-2 receptors are labelled with ATTO488 while the NPCs are labelled with AF647. **a** First frame of the ACE-2 image sequence without denoising. **b** First frame of the denoised ACE-2 image sequence using STORM image sequence of microtubules to train SRDTrans. **c** First frame of the denoised ACE-2 image sequence where an ACE-2 STORM image sequence was used for training. This image and the images in **a** and **b** have been adjusted to have the same grayscale range. **d** First frame of the NPC image sequence without denoising. **e** First frame of the denoised NPC image sequence using a microtubule STORM image sequence for training. This image and the image in **d** have been adjusted to have the same grayscale range.

From the first frame of the ACE-2 image sequence (Fig. 7.2**b**), despite using a different biological sample for training, denoising using a model trained on the microtubule image sequence did not produce the artefacts observed in Fig. 7.1**b** and Fig. 7.1**c**, likely because both image sequences were acquired from the same microscope. As expected from the microtubule denoising results in Fig. 7.1**d**, training SRDTrans on the ACE-2 image sequence and carrying out inference on the same dataset also did not produce any artefacts. Interestingly, using the same dataset for training and inference resulted in higher contrast of single molecules compared to inference using a model that had been trained on the microtubule data (Fig. 7.2**b**, Fig. 7.2**c**). However, little difference in contrast was observable for the NPC data that had been denoised using a model trained with the microtubule data (Fig. 7.2**d**, Fig. 7.2**e**). The difference in outcomes between the ACE-2 denoised data and NPC denoised data was likely due to the dissimilarity in fluorophore properties between ATTO 488 and Alexa Fluor 647; the photon count

and molar absorption coefficient, ϵ, are both lower for ATTO 488 [91], worsening the contrast. Therefore, though model training using only the microtubule data produced images free from the artefacts in Fig. 7.1**b** and Fig. 7.1**c**, higher contrast was observed when model inference was carried out on a STORM image sequence that had the same fluorophore as the STORM image sequence used for training.

7.3 Evaluating denoising on microtubules

Having outlined methods to train SRDTrans without producing artefacts during the learning process, denoising was evaluated on microtubule image sequences. Here, microtubules were immunolabelled with a primary anti-α-tubulin antibody and a secondary antibody conjugated to Alexa Fluor 647 (Methods: 3.4.4). STORM imaging and single-molecule localisation was carried out as described in Methods: 3.6.1, Theory: 2.3, and Methods: 3.7.1. The denoising parameters were obtained by training SRDTrans on the first microtubule image sequence as presented in Fig. 7.1**a** according to Methods: 3.10.1. Similar to Chapter 4: Fig. 4.7, a qualitative assessment was first carried out on the super-resolution images of microtubules. If denoising were successful, more details of the filaments would be expected to be observed—for example, improved filament continuity or less background from unspecifically bound fluorophores. Conversely, no additional details would be expected to be observed if denoising were ineffective. This assessment was carried out for three independent image sequences from which a representative example is shown in Fig. 7.3. The reconstructions of the remaining images are shown in Appendix: Fig. A.7.

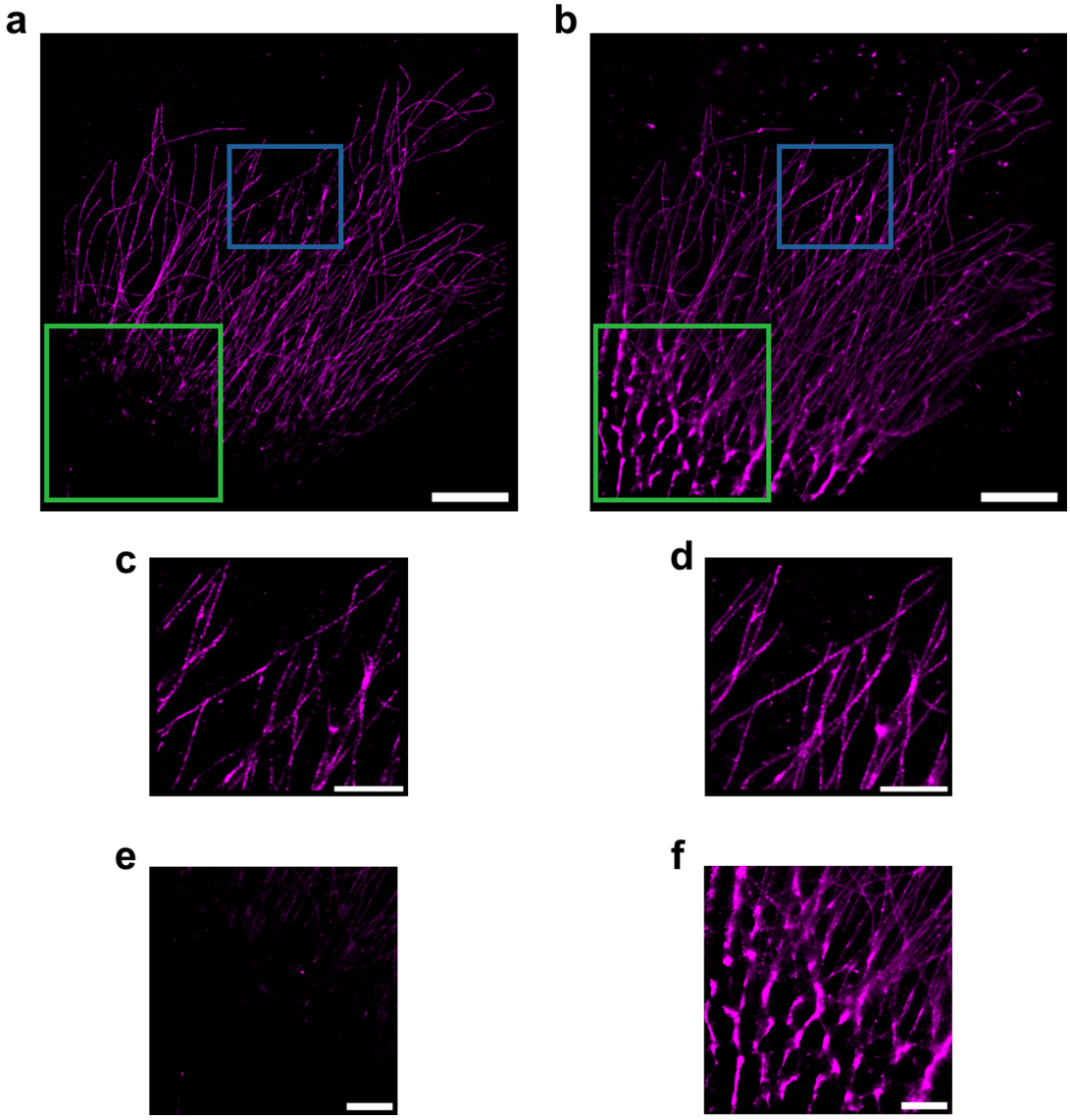

Fig. 7.3: **Assessment of denoising from STORM imaging of immunolabelled ∝-Tubulin immunolabelled with dye-conjugated antibodies. a** Super-resolution reconstruction of microtubules without denoising. Scale bar: 5 µm. **b** Super-resolution reconstruction microtubules following denoising with SRDTrans. Scale bar: 5 µm. Here, training and inference was carried out on the same image sequence. **c** Magnified view of the blue inset from **a**. Scale bar: 2 µm. **d** Magnified view of the blue inset from the denoised image in **b**. Scale bar: 2 µm. **e** Magnified view of the green inset in the bottom-left corner of **a**. Scale bar: 2 µm. **f** Magnified view of the green insert in the bottom-left corner of **b**. Scale bar: 2 µm.

From the example in Fig. 7.3, a greater number of single-molecules were detected following denoising, with approximately 1.1×10^6 localisations compared to 2.2×10^6 before denoising. As a result, filament continuity increased following denoising. The inset in Fig. 7.3**a** features filaments that are particularly discontinuous, as observable in the magnified view (Fig. 7.3**c**). Following denoising, the filaments in the same region of interest generally appeared more complete (Fig. 7.3**d**). However, denoising also resulted in more detected localisations in the bottom-left corner of the super-resolution image

(Fig. 7.3**b**, 7.3**f**). These localisations likely arose from out-of-focus fluorescence at the edge of the field of illumination (Fig. 7.1**a**). The laser intensity at the edge of the field of illumination may have been too low to induce a complete transition to the dark state for all fluorophores at the beginning of image acquisition, as observable in the first frame in Fig. 7.1**d**, resulting in poor photoswitching. The lower intensity at the edge of the field of illumination also means that the edge fluorophores would have insufficient intensity to be detected during localisation of an ordinary STORM image sequence (Fig. 7.3**e**) but are detectable following denoising due to improved single-molecule detection.

With the observation that denoising with SRDTrans improved single-molecule detection of microtubule structures, it would be expected for the Fourier ring correlation (FRC) resolution to increase concomitantly following denoising. To test this hypothesis, the FRC resolutions before and after denoising were evaluated for all repeats according to Methods: 3.7.3 and Theory: 2.4. A custom routine was used to calculate the FRC resolution, and the localisation data were split into two halves depending on whether the molecule was detected in an odd-numbered or even-numbered frame.

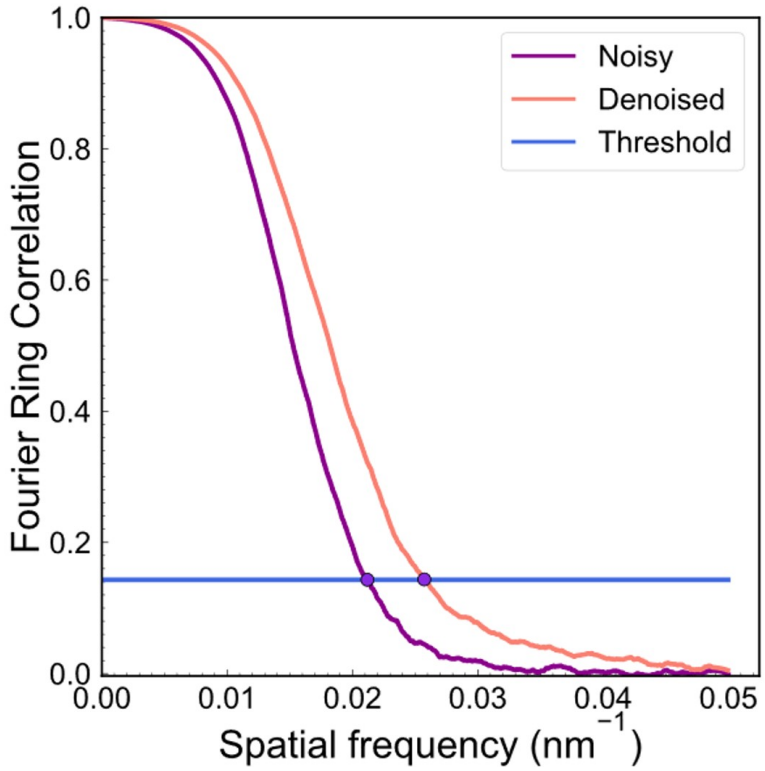

Fig. 7.4: **A representative example comparing the microtubule FRC resolution before and after denoising.** The resolution threshold was ≈ 0.143. the resolution before denoising was: 47.2 nm and the resolutions following denoising was 38.9 nm.

Table 7.1: **Mean FRC resolutions of microtubule STORM images before and after denoising.**

Before/after denoising	Mean FRC resolution (nm)
Before	50.2 ± 5.0
After	41.1 ± 2.4

As expected, denoising with SRDTrans resulted in resolution improvements for all datasets, increasing the mean FRC resolution from 50.2 ± 5.0 nm before denoising to 41.1 ± 2.4 nm after denoising (Table 7.1). Overall, the assessment of denoising on microtubule data demonstrate that SRDTrans can detect single molecules bound to the structure of interest that would otherwise be undetected due to noise, resulting in higher resolution. Nevertheless, there are potential trade-offs with respect to imaging artefacts. If fluorescence from unbound fluorophores or from fluorophores not transferred to a dark state were present, the denoising process may worsen the quality of the super-resolution image (Fig. 7.3**b**). Therefore, while it would be expected for this denoising method to improve single-molecule detection and hence, the resolution, of other SMLM biological

data, it may not be suitable depending on the type of noise that is prominent.

7.4 Evaluating denoising on nuclear pore complexes

Having characterised and evaluated the effectiveness of SRDTrans for denoising microtubule data, the same procedure was applied to three STORM image sequences of NPCs that expressed the Nup96-SNAP fusion protein labelled with Alexa Fluor 647. Here, SRDTrans was trained on the first STORM image sequence of microtubules labelled with Alexa Fluor 647, i.e. the same image sequence presented in Fig. 7.1**a**. The denoising parameters were used to carry out inference on STORM image sequences of NPCs, producing denoised image sequences. Again, an initial qualitative assessment of the NPC ring structures was carried out. A representative example from the second dataset is shown in Fig. 7.5, with reconstructions from the remaining datasets shown in Appendix: Fig. A.7.

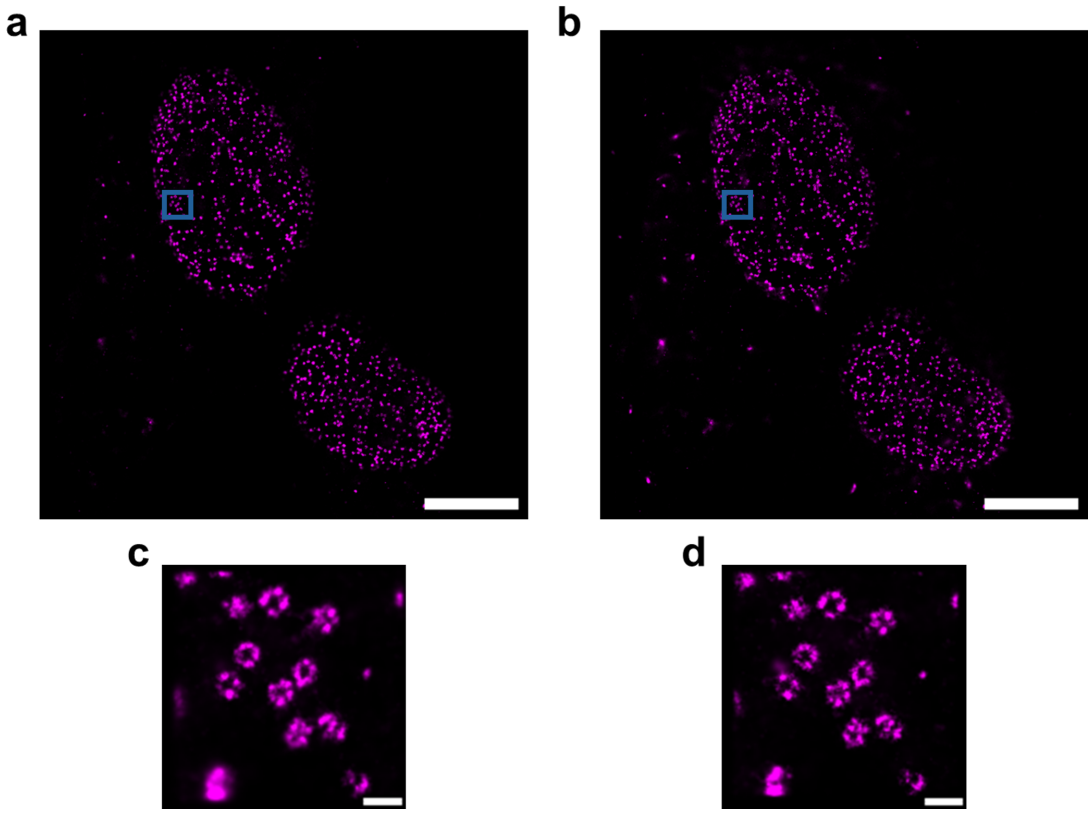

Fig. 7.5: **Assessment of denoising from STORM imaging of NPCs labelled with Alexa Fluor 647. a** Super-resolution reconstruction of NPCs without denoising. Scale bar: 5 µm. **b** Super-resolution reconstruction of NPCs following denoising. SRDTrans was trained using an image sequence of microtubules that had been labelled with Alexa Fluor 647. **c** Magnified view of the blue, square inset in **a**. The scale bar is 200 nm. **d** Magnified view of the blue, square inset in **b**. The scale bar is 200 nm.

Similar to the super-resolution images of microtubule data (Fig. 7.3), there was an increase in the number of detected single-molecules following denoising, with 2×10^6 localisations compared to 1×10^6 before denoising. However, visual differences in super-resolution image quality were less apparent following denoising (Fig. 7.3**a**, Fig. 7.3**b**, Appendix: Fig. A.7). For example, the lobes of the NPCs appeared slightly more distinct following denoising but no obvious changes in their completeness were observable (Fig. 7.5**b**, Fig. 7.5**d**). To provide a quantitative analysis, the FRC resolutions before and after denoising were also calculated using the same procedure as described above for the FRC resolution calculations of microtubules.

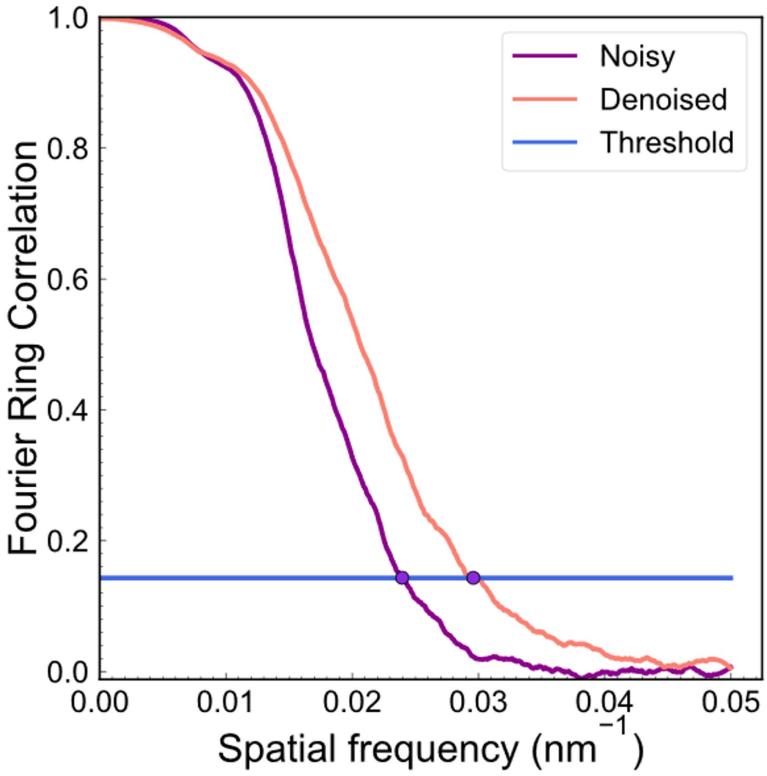

Fig. 7.6: **Comparison of NPC FRC resolution before and after denoising from a representative example.** The resolution before denoising was 41.7 nm while the resolutions following denoising was: 33.8 nm.

Table 7.2: **Mean FRC resolutions of NPC STORM images before and after denoising.**

Before/after denoising	Mean FRC resolution (nm)
Before	42.2 ± 2.8
After	31.1 ± 2.6

The FRC resolution measurements from the NPCs corroborated those from the microtubules; applying denoising improved the mean FRC resolution (Table 7.2) from 42.2 ± 2.8 nm to 31.1 ± 2.6 nm. However, similar to the FRC resolution measurements for mirror-enhanced STORM (Chapter 5: Table 5.2), the differences in FRC resolution before and after denoising were likely too small to produce substantial differences in the appearance of NPCs.

7.4.1 Resolution evaluation with rolling FRC

Since the NPC super-resolution images exhibited more heterogeneity compared to those from microtubules, the rolling FRC (rFRC) algorithm [153] was applied to the super-

resolution reconstructions of NPCs to gain more localised insights into the resolution enhancement from denoising. Unlike the FRC resolution measurements presented thus far, which calculate the correlation using the entirety of two super-resolution half-images, the rFRC method calculates the correlation using a small window (64 pixels x 64 pixels in this work), resulting in an FRC resolution value for the central pixel of the window. Sliding the window across the entirety of both super-resolution half-images then results in a per-pixel FRC resolution, thereby providing more localised resolution information.

The output of the rFRC algorithm is a heatmap that displays areas of high or low resolution, demarcating areas of the super-resolution image on which to focus biological inference. However, using this heatmap for a quantitative resolution comparison is challenging. First, the colours of the heatmap can be changed by modifying the grayscale range of the image. Second, using the heatmap to extract regions of interest increases the risk of selection bias. Therefore, to compare the effect of denoising, the same region of interest of NPCs was analysed before and after denoising to allow for a fair comparison of the local resolution. To extract quantitative insights, the mean rFRC resolutions for the regions of interest were calculated by taking the mean rFRC resolution value across all non-zero pixels within a region of interest. Similar to the previous FRC calculations, the localisation data were split into two half-images depending on whether the molecules were detected in an odd-numbered frame or even-numbered frame. The results of this analysis are shown in Fig. 7.7.

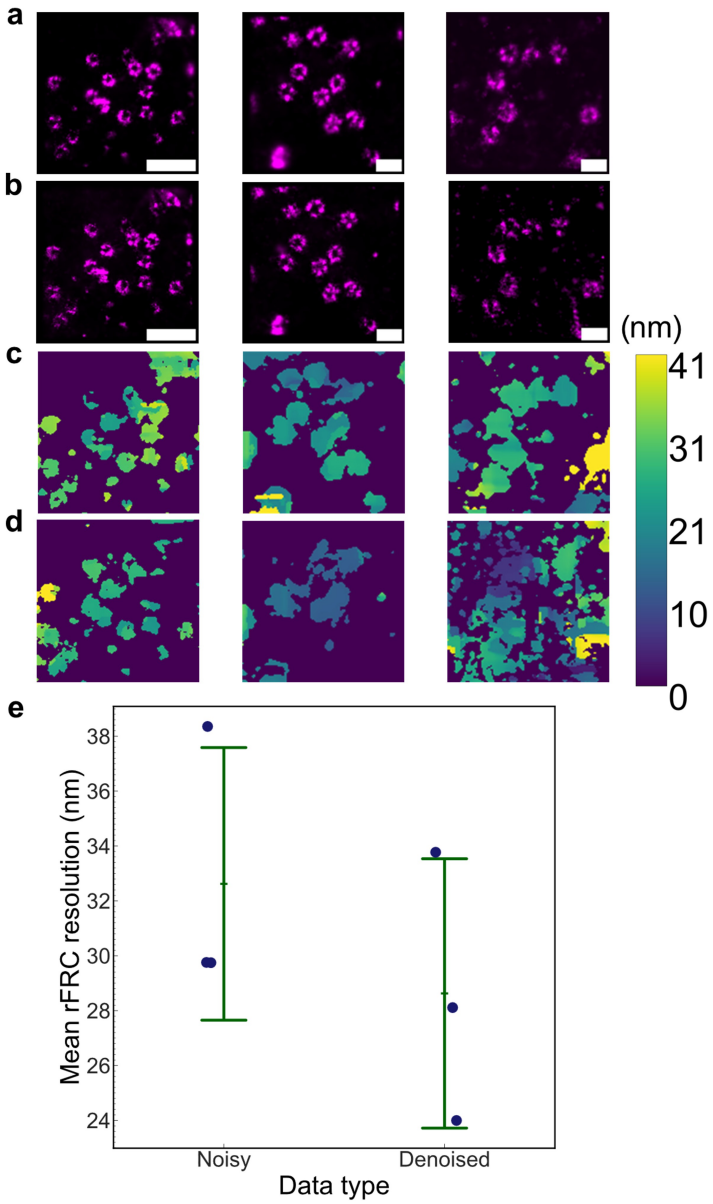

Fig. 7.7: **Comparison of NPC FRC resolutions before and after denoising, using the rolling FRC algorithm**. All scale bars are 200 nm in length. **a** Regions of interest from all datasets without denoising in order of left to right: dataset 1, dataset 2, and dataset 3. **b** Regions of interest from all datasets with denoising in the same order as **a**. **c** Heatmaps output by the rolling FRC algorithm of all datasets without denoising in the same order as **a**. **d** Heatmaps of all datasets following denoising in the same order as **a**. **e** Dotplot of the mean rFRC resolution. The mean rFRC resolutions of datasets 1, 2, and 3 before denoising were: 29.8 nm, 29.7 nm, and 38.3 nm, respectively. The mean rFRC resolutions in the same order, following denoising, were: 28.1 nm, 24.0 nm, and 33.8 nm, respectively. The overall mean rFRC resolution without denoising was 32.6 ± 5.0 nm, and the overall mean rFRC resolution following denoising was 28.6 ± 4.9 nm.

Application of the rFRC algorithm resulted in more detailed insights on the effect of denoising on the NPC structures themselves. In concordance with the results from the global FRC resolution analysis (Table 7.2), the resolution of the NPCs increased from a mean of 32.6 ± 5.0 nm to 28.6 ± 4.9 nm following denoising. This resolution

increase was smaller than that from the global FRC measurements and may explain the observation that only subtle structural differences were visible following denoising. Nevertheless, some structural differences were visible in the third dataset (Fig. 7.7**a**, Fig. 7.7**b**, furthest right), with more distinct lobes following denoising, thus reflecting some resolution improvement.

7.5 Denoising with ACE-2 receptor

Having characterised and evaluated the effectiveness of denoising for microtubules and NPCs—two samples with well-characterised molecular organisation—further evaluation was carried out on the ACE-2 receptor labelled with ATTO 488, an example of a sample without a well-defined molecular organisation. STORM of ACE-2 receptor labelled with ATTO 488 was originally carried out as part of two-colour STORM to investigate the internalisation of SARS-CoV-2 spike protein (see Chapter 8 for details). As part of this investigation, the ACE-2 receptor was imaged with STORM following incubation with the spike protein for three different durations: 5 minutes, 15 minutes, and 30 minutes. In this chapter, the three image sequences acquired at each of these timepoints are treated as independent repeats with the 5-minute, 15-minute, and 30-minute timepoints termed the first, second, and third image sequences, respectively.

For denoising, SRDTrans was trained on the first image sequence of ACE-2-ATTO 488 (Fig. 7.2**a**) according to Methods: 3.10.1 to obtain denoising parameters which were then used for inference on all datasets. Denoising was analysed as previously with a qualitative assessment followed by a quantitative assessment. The super-resolution images of the first dataset are shown in Fig. 7.8 with the remaining images shown in Appendix: Fig. A.8.

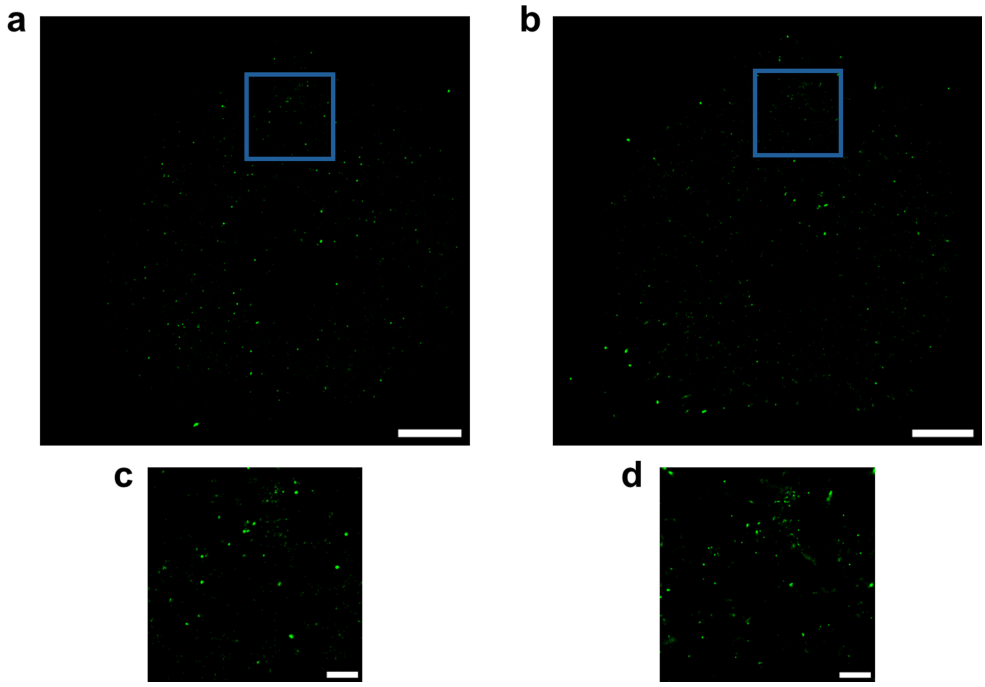

Fig. 7.8: **Assessment of denoising from STORM imaging of ACE-2 receptors labelled with ATTO 488. a** Super-resolution reconstruction of ACE-2 receptors without denoising. Scale bar: 5 µm. **b** Super-resolution reconstruction of ACE-2 receptors after denoising. Scale bar: 5 µm. **c** Magnified view of the area enclosed by the blue, square inset in **a**. Scale bar: 1 µm. **d** Magnified view of the area enclosed by the inset in **b**. Scale bar: 1 µm.

A notable difference following denoising, also observed for microtubules and NPCs, was the increase in the number of localisations (Fig. 7.8**a**, Fig. 7.8**b**). In the original data, 22090 localisations were recorded while in the denoised data, 102055 localisations were recorded. Such an increase was also apparent in the insets highlighted in Fig. 7.8, where 1391 localisations were recorded for the data without denoising while 4560 localisations were recorded following denoising. However, because no ground truth structure is available for ACE-2, it was difficult to determine whether the increase in localisations corresponded to more detections of labelled ACE-2 receptor, or to more detections of ATTO 488 that were not bound to ACE-2-SNAP.

For the quantitative assessment of denoising ACE-2 receptors, unlike the measurements for microtubules and NPCs, the two half-images were generated by splitting the localisation data at the midpoint instead of by odd and even frames. The latter splitting method resulted in two half-images that exhibited FRC values that exceeded the resolution threshold, even at high spatial frequency values, thereby preventing the calculation of an FRC resolution and necessitating the use of a different splitting method.

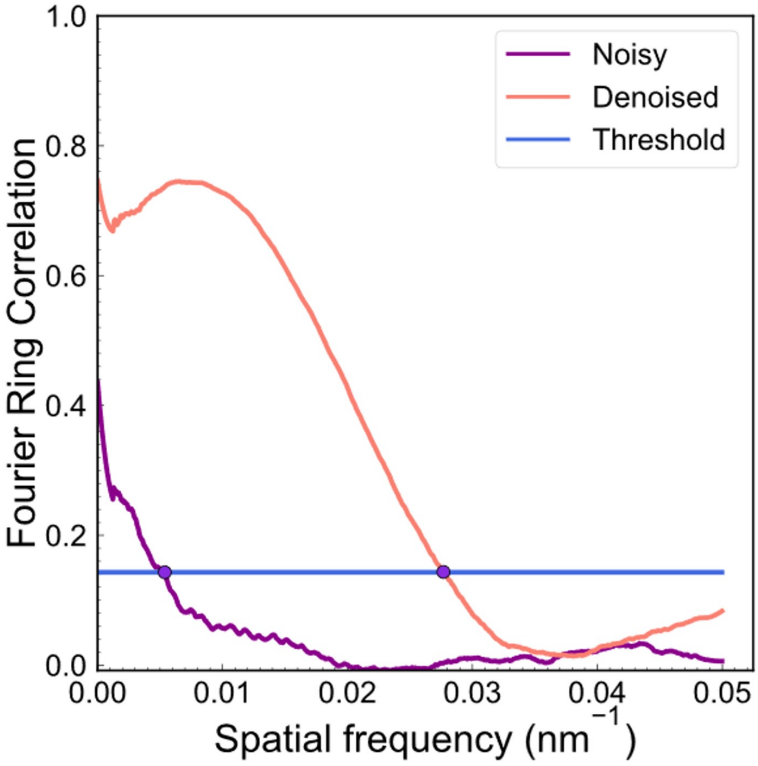

Fig. 7.9: **Comparison of ACE-2 FRC resolutions before and after denoising from a representative example.** The resolution threshold was ≈ 0.143. Unlike Figs. 7.4, 7.6, and 7.7, the localisation data was split at its midpoint rather than by odd-numbered frames and even-numbered frames. The resolution before denoising was 186.0 nm while the resolution following denoising was 36.1 nm.

Table 7.3: **Mean FRC resolutions of ACE-2 STORM images before and after denoising.**

Before/after denoising	Mean FRC resolution (nm)
Before	193.2 ± 140.6
After	38.3 ± 11.7

While a substantial increase in the FRC resolution was recorded in the first dataset (Fig. 7.9), and the mean FRC resolution increased from 193.2 ± 140.6 nm to 39.3 ± 11.7 nm following denoising (Table 7.3), the usefulness of the FRC resolution as a metric for evaluating denoising was unclear. For microtubules and NPCs, the resolution increase from denoising correlated well to the visibility of new information, such as improved filament continuity or better separation between the corners of NPCs. For ACE-2 receptors, however, the benefits of the resolution increase from denoising were more difficult to discern. Rather than relying on a single evaluation metric, metrics that focus on image fidelity or an investigation of a biologically driven research question would

likely be required for further insights into the effects of denoising on ACE-2 receptors (see Discussion for further details). Such an investigation is presented in Chapter 8.

7.6 Assessing denoising with a commercial microscope

The evaluation of SRDTrans has demonstrated its broad utility across different biological samples. However, another key aspect of generalisability is its ability to denoise image sequences acquired with different optical configurations. To a degree, generalisability to different microscopes has already been demonstrated since the microscope in this work has different optical components to the microscope used by Li *et al.* 2023. More specifically, the microscopes use different cameras and will, therefore, have different noise characteristics. Nevertheless, both cameras are sCMOS cameras, and so an evaluation of denoising using a microscope with an EMCCD camera would be beneficial to assess if deep learning artefacts would arise from using this type of camera, particularly because EMCCD cameras are widely used for SMLM and because their noise characteristics differ from sCMOS cameras [67, 236].

To evaluate denoising across different optical configurations, SMLM of microtubules and NPCs was carried out on a ZEISS Elyra PS.1 microscope—the same microscope used for drift quantification in Chapter 4. The microtubules and NPCs were labelled as previously described (Methods: 3.4.4, Methods: 3.4.5) and STORM imaging was carried out as described in Methods: 3.6.3. The denoising was carried out by obtaining denoising parameters from training SRDTrans on the first image sequence of microtubules acquired with the ROCS microscope according to Methods: 3.10.1. In other words, the image sequence that produced the super-resolution image in Fig. 7.3**a**.

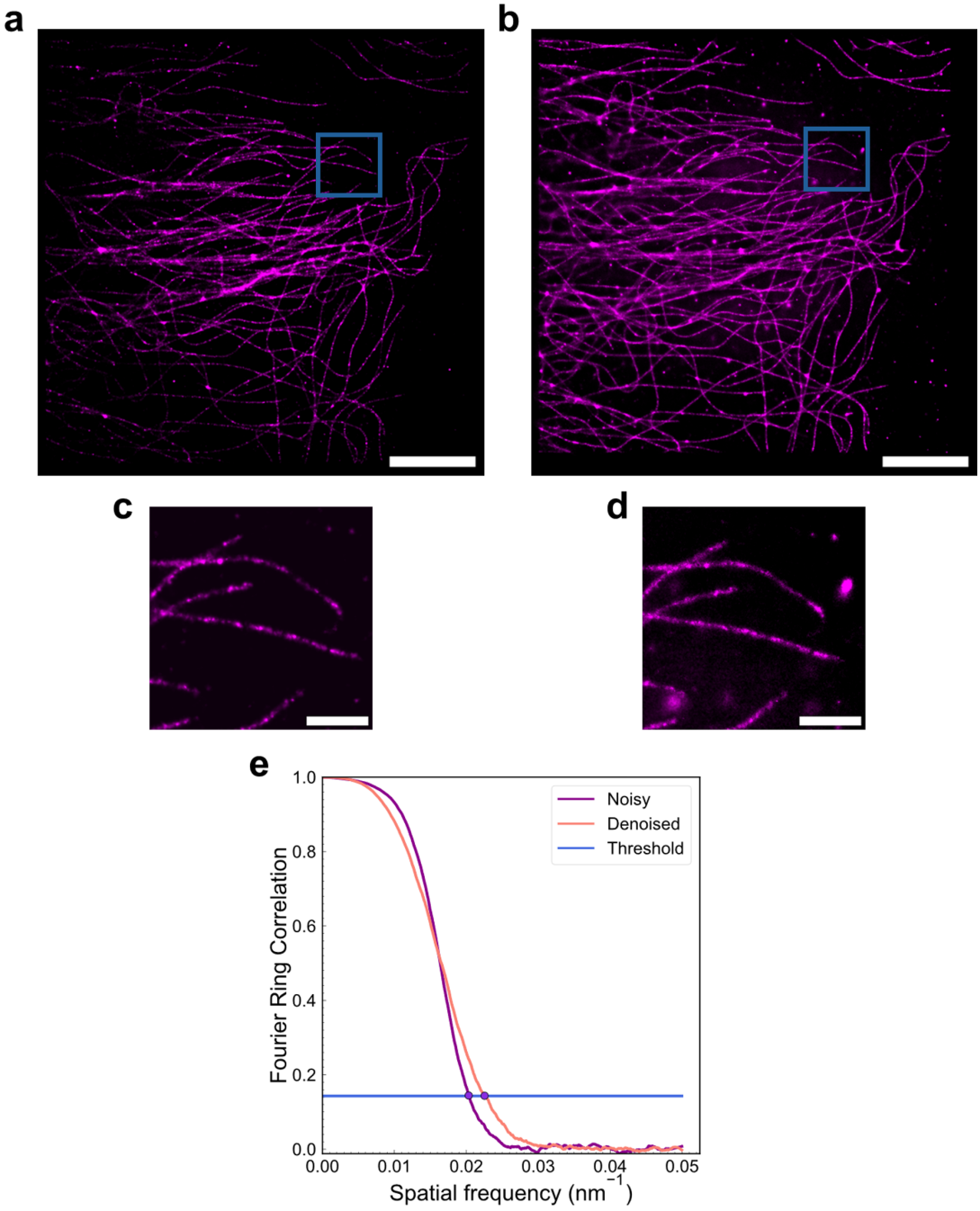

Fig. 7.10: **Assessment of denoising from STORM imaging of AF647-labelled microtubules using the commercial microscope. a** Super-resolution reconstruction of microtubules without denoising. Scale bar: 5 µm. **b** Super-resolution reconstruction of microtubules following denoising. Scale bar: 5 µm. **c** Magnified view of the area enclosed by the inset in **a**. The scale bar is 1 µm. **d** Magnified view of the area enclosed by the inset in **d**. The scale bar is 1 µm. **e** FRC curve comparing the resolutions before and after denoising. The resolution before denoising was 49.2 nm and the resolution after denoising was 44.4 nm.

The denoised results from STORM imaging of microtubules using the commercial microscope (Fig. 7.10) were similar to those obtained from the ROCS microscope (Fig. 7.3); the filament continuity improved (Fig. 7.10**c**, Fig. 7.10**d**) while the FRC resolution improved from 49.2 nm to 44.4 nm following denoising. This resolution increase

was lower than those observed with the ROCS microscope (Fig. 7.4) but nonetheless resulted in an observable difference in STORM image quality.

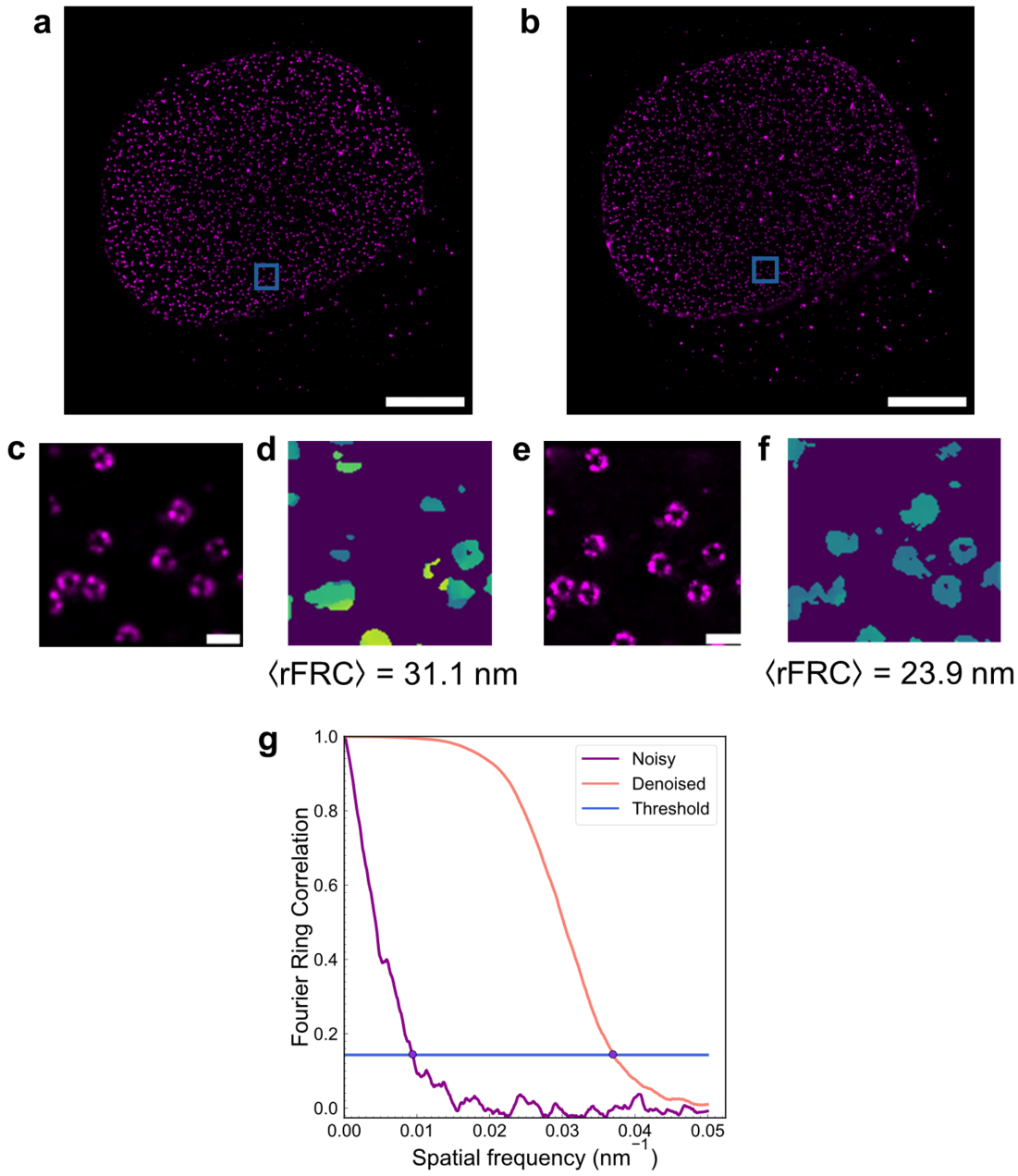

Fig. 7.11: **Assessment of denoising from STORM imaging of AF647-labelled NPCs using the commercial microscope.** **a** Reconstruction of NPCs without denoising. Scale bar: 5 µm. **b** Reconstruction of NPCs after denoising. Scale bar: 5 µm. **c** Magnified view of the area enclosed by the inset in **a**. Scale bar: 200 nm. **d** Heatmap of the region of interest in **c** output by the rolling FRC algorithm that was used in Fig. 7.7. The mean rFRC value across all non-zero pixels was 31.1 nm **e** Magnified view of the inset in **b**. Scale bar: 200 nm. **f** Heatmap of the region of interest in **e** output by the rolling FRC algorithm. The mean rFRC across all non-zero pixels was 23.9 nm. **g** FRC curves comparing the resolution across the entirety of the super-resolution images before and after denoising. The resolution before denoising was 106.3 nm and the resolution after denoising was 27.1 nm.

The results from STORM imaging of NPCs using the commercial microscope had a

higher resolution increase following denoising to those acquired with the ROCS microscope (Fig. 7.5, Fig. 7.6) with the resolution increasing from 106.3 nm to 27.1 nm (Fig. 7.11**g**). However, the low resolution recorded without denoising (106.3 nm) was likely attributed to the heterogeneity of resolution of NPCs, as previously highlighted (see 7.4.1). The same rFRC algorithm used to generate the results in Fig. 7.7 was, therefore, applied to the same region of interest before and denoising (Fig. 7.11**d**, Fig. 7.11**f**). From this analysis, more realistic resolution values of 31.1 nm before denoising and 23.9 nm after denoising were obtained.

The effect of the resolution increase was observable in the improved image quality and more distinctive ring structures from the denoised super-resolution reconstruction (Fig. 7.11**c**, Fig. 7.11**e**). Taken together, the results from denoising NPCs and microtubule image sequences acquired using the commercial microscope demonstrated that SRDTrans can also produce deep-learning-artefact-free, denoised data when using an EMCCD camera, despite the different noise characteristics of EMCCD cameras and despite the training data being acquired with a different camera type. Therefore, SRDTrans would be expected to be applicable to image sequences acquired with any standard SMLM imaging optical configuration even if the model were trained with data that had been obtained with a different camera.

7.7 Assessing denoising on different types of noise

The assessment of SRDTrans thus far has focused on its ability to generalise denoising to different biological samples and different experimental configurations. An aspect of SRDTrans that has not yet been examined in detail is its ability to denoise different types of noise. As described in Introduction: 1.2.3, noise in SMLM is heterogenous. Therefore, an evaluation of SRDTrans would not be complete without investigating different sources of noise. Here, the nanobody-labelled vimentin from Chapter 6 is used as an example of a super-resolution image where the quality has been degraded by noise from unspecifically bound flurophores. Meanwhile, NPCs acquired with low-power STORM are used as an example of where shot noise and camera noise hinder single-molecule localisation.

7.7.1 Denoising of nanobody-labelled vimentin

From the STORM imaging of vimentin labelled with anti-vimentin nanobodies described in Chapter 6, non-homogenous background fluorescence in the super-resolution image—likely corresponding to unspecifically bound fluorophores—was prominent. While the poor contrast was detrimental to the development of nanobody labelling methods in that chapter, the noise incurred by unspecifically bound fluorophores means that this dataset is a good example for evaluating the ability of SRDTrans to remove noise from unspecifically bound fluorophores. This type of noise presents problems particularly for downstream spatial analysis methods, such as cluster analysis, since more false positive localisations are detected, thereby increasing the likelihood of extracting inaccurate spatial patterns [240].

Vimentin in U2OS cells was labelled with the anti-vimentin nanobody, VB3 (Chapter 6: 6.4), by Dr. Siva Ramadurai (The Rosalind Franklin Institute) using Streptolysin-O as described in Methods: 3.4.7. The nanobody was conjugated to Alexa Fluor 647 by mutating its 7th position serine residue to a cysteine residue that could react with a maleimide derivative of Alexa Fluor 647. STORM imaging was performed with a Zeiss Elyra PS.1 microscope (Methods: 3.6.3) and single-molecule localisation was carried out as previous (Theory: 2.3, Methods: 3.7.1). SRDTrans was trained using the image sequence obtained from STORM imaging of vimentin and model inference was carried out on the same image sequence. The denoising evaluation was carried out as described for microtubules, NPCs, and ACE-2 receptors. However, only one dataset was evaluated, owing to the challenges in vimentin labelling described in Chapter 6. For the FRC evaluation, the two half-images were generated by splitting based on whether the localisation was recorded in an odd-numbered frame or even-numbered frame.

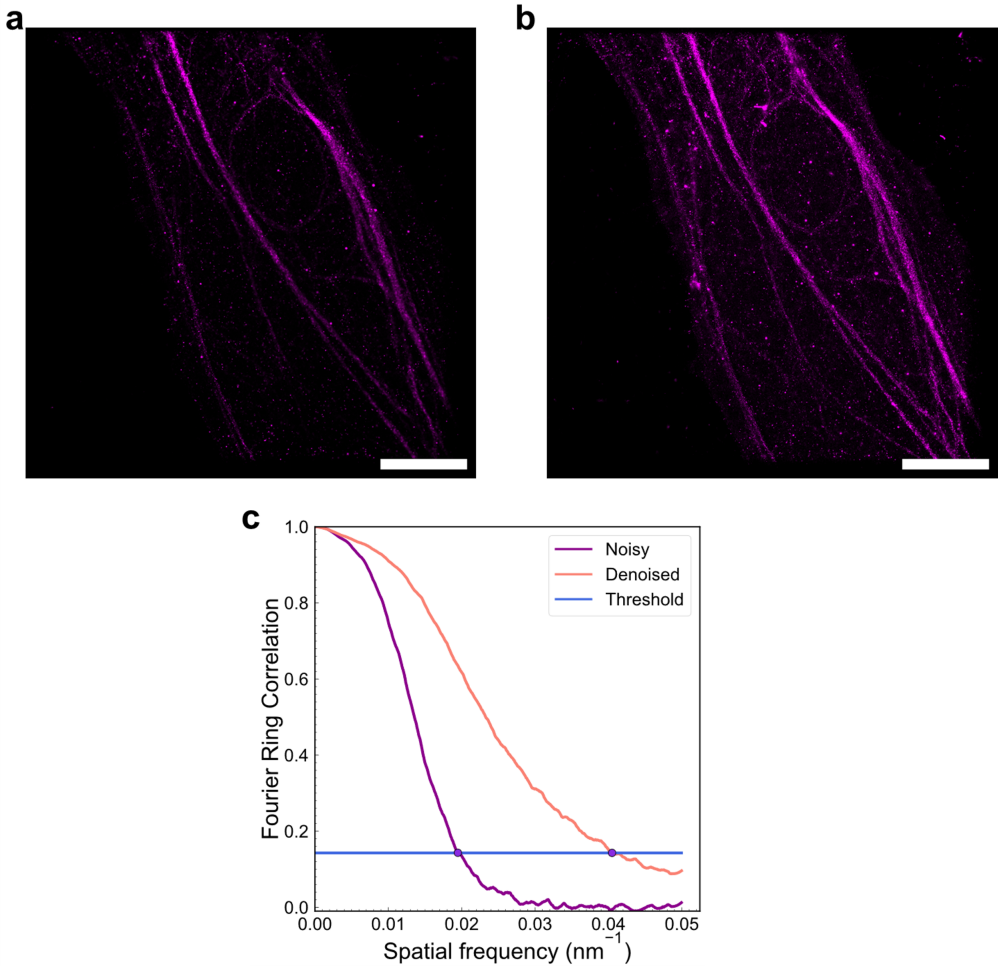

Fig. 7.12: **Assessment of denoising noise from unspecifically bound fluorophores evaluated from STORM imaging of vimentin labelled with VB3 conjugated to Alexa Fluor 647.** Scale bars: 5 µm. **a** Super-resolution reconstruction of vimentin without denoising. **b** Super-resolution reconstruction after denoising. The image has been adjusted to have the same grayscale range as **a**. **c** FRC curve comparing the resolutions before and after denoising. The threshold was ≈ 0.143. The resolution before denoising was 51.3 nm and the resolution after denoising was 24.7 nm.

As expected from previous evaluations, the FRC resolution improved following denoising, increasing from 51.3 nm without denoising to 24.7 nm (Fig. 7.12**c**). Similar to denoising microtubules (Fig. 7.3), the vimentin filaments were more prominent and better-defined following denoising (Fig. 7.12**a**, Fig. 7.12**b**). However, compared to the result without denoising, more noise from unspecifically bound fluorophores was present, suggesting that denoising with SRDTrans had little effect on this type of noise. While the image quality in this dataset was sufficient to observe the vimentin filaments, it would be unlikely for denoising to provide many benefits if the noise from unspecifically bound fluorophores were worse. In such cases, the biological structure would likely remain obscured by noise.

7.7.2 Denoising NPCs acquired with low-power STORM

Denoising the STORM image sequence of vimentin revealed that SRDTrans is less effective at removing noise originating from unspecifically bound fluorophores. It is, therefore, likely better suited when the dominant form of noise is camera-based or shot noise. To test this hypothesis, STORM imaging was carried out on NPCs labelled with Alexa Fluor 647 using a low power density to reduce the intensity of fluorescence emission. Here, the power density was 0.8 kW/cm^2 which was at least half of the typical power density used for STORM throughout this work (Methods: 3.6.1). Under these conditions, noise originating from the camera and shot noise are expected to be the primary form of noise, thereby allowing for the assessment of the effectiveness of SRDTrans at removing shot noise and noise intrinsic to cameras. The denoising evaluation was carried out as previously with vimentin.

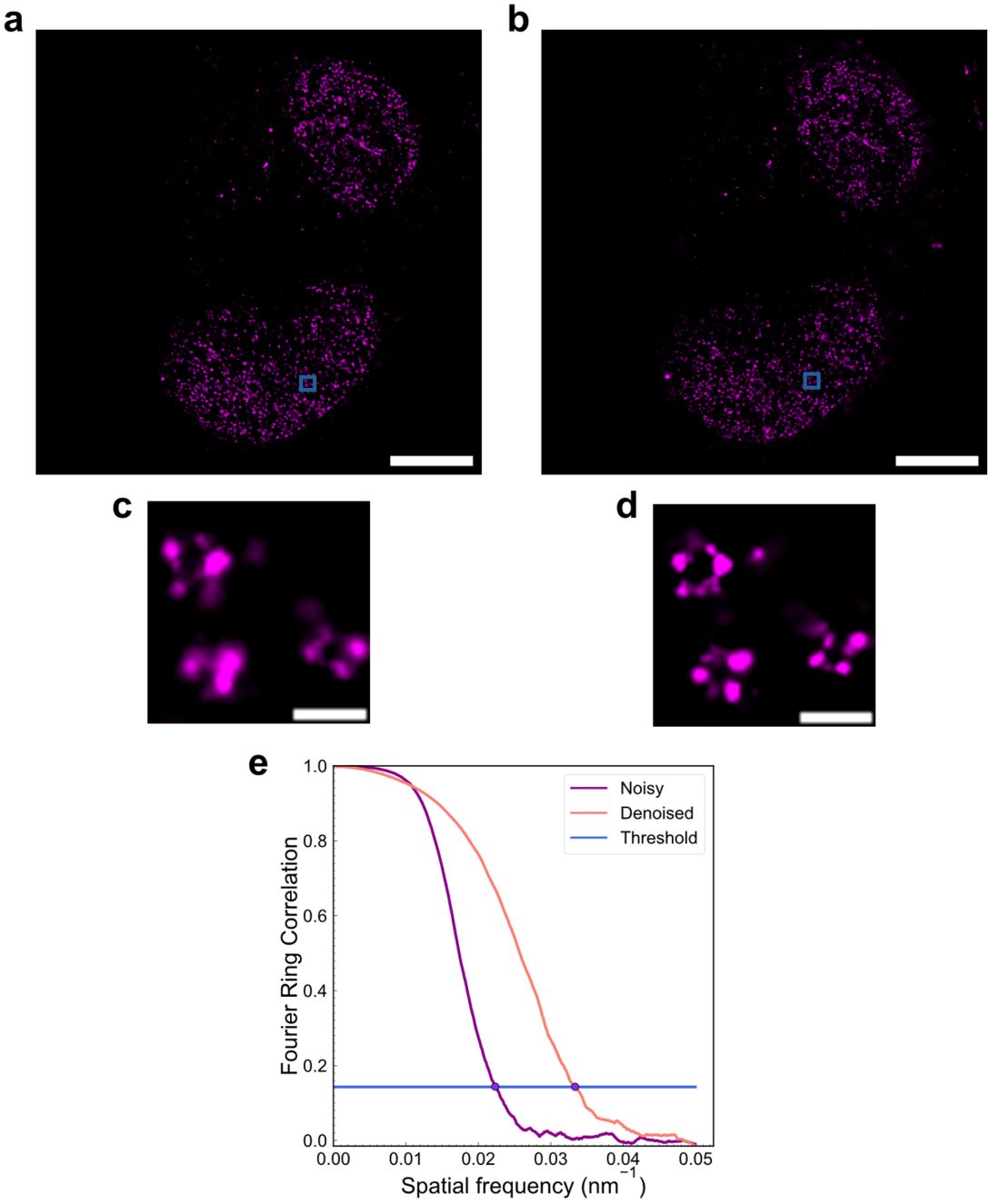

Fig. 7.13: **Assessment of denoising camera-based noise and shot noise evaluated from STORM imaging of nuclear pore complexes using low power. a** Super-resolution reconstruction of NPCs from low-power STORM imaging without denoising. Scale bar: 5 µm. **b** Super-resolution reconstruction of NPCs from low-power STORM imaging following denoising. Scale bar: 5 µm. The grayscale range of the image has been adjusted such that it is the same as **a**. **c** Magnified view of the area marked by the blue inset in **a**. Scale bar: 200 nm. **d** Magnified view of the area marked by the blue inset in **b**. The grayscale range of the image has been adjusted to be the same as **c**. Scale bar: 200 nm. **e** FRC curve comparing resolutions before and after denoising. The threshold was 0.143. The resolution before denoising was 44.8 nm while the resolution following denoising was 30.0 nm.

An improvement in the image quality of NPCs was observed following denoising (Fig. 7.13**c**, Fig. 7.13**d**). While the image quality was lower than those acquired from STORM

using the standard power density (Fig. 7.5, Fig. 7.7), there was, nevertheless, a substantial increase in the clarity and resolution of the NPC ring structures following denoising. Similar to other datasets, the FRC resolution also improved after denoising, increasing from 44.8 nm to 30.0 nm. Taken together, the denoising evaluation from low-power STORM imaging and vimentin STORM imaging demonstrated that SRDTrans is best adapted for conditions where camera noise and shot noise are dominant. If noise from unspecifically bound fluorophores or background fluorescence is dominant, then SRDTrans is unlikely to offer meaningful improvements.

7.8 Comparison of single-molecule photophysical parameters

During the assessment of the generalisability and effectiveness of denoising for different biological samples, microscopes, and types of noise, differences in the estimated photophysical parameters of single-molecules, such as the intensity and background, were not examined. These parameters can be used for applications such as estimations of single-molecule axial positions and estimations of single-molecule orientations [241, 242], and so assessing whether denoising modulates these parameters may be beneficial for the wider SMLM community.

Conducting a fair comparison of single-molecule properties from the localisation data as previously (Chapter 5, Fig. 5.4) was challenging due to the increase in the number of detected single-molecules following denoising. Ideally, for paired data, the photophysical parameters of the same molecule would be compared before and after denoising. Such a procedure is possible in ThunderSTORM but would require the manual selection of hundreds of thousands of localisations. Therefore, the photophysical properties of single-molecules was analysed using a custom-written Python script which used the same coordinates from local maxima detection for both the original and denoised image sequence, thereby ensuring the same single-molecule in both datasets was compared. The implementation details are described in Methods: 3.10.2. Briefly, the custom script used the same algorithm as ThunderSTORM (Theory: 2.3) but used a difference-of-Gaussians filter and calculated the localisation precision by determining the Cramér-Rao

lower bound for the xy-coordinates, $\hat{\theta}_x, \hat{\theta}_y$ (Theory: 2.4, Eqs. 2.21, 2.22, 2.23).

The photophysical parameters of the single-molecules were analysed for all repeats of the microtubule and NPC localisation data presented previously (Fig. 7.3, Table 7.1, Fig. 7.5, Table 7.2). Here, weighted means and standard deviations for each photophysical parameter were calculated—using Eq. 5.3 and Eq. 5.4—and tabulated in Table 7.4.

Table 7.4: **Weighted means of the estimated photophysical parameters of single-molecule from comparing STORM image sequences with and without denoising.** The weighted means were calculated for each parameter using Eq. 5.3 and the standard deviations were calculated using Eq. 5.4.

Sample	Weighted mean intensities (photons)	Weighted mean background (photons)	Weighted mean localisation precisions (nm)
Microtubules, denoised	928 ± 390	109 ± 115	14.7 ± 0.5
Microtubules, noisy	968 ± 427	110 ± 114	13.7 ± 0.5
NPCs, denoised	559 ± 54	38 ± 8	24.1 ± 1.8
NPCs, noisy	601 ± 50	38 ± 8	20.2 ± 0.3

For the microtubule image sequences, there were small differences in the intensity, background fluorescence, and localisation precision of single molecules following denoising. The mean intensity decreased from 968 ± 427 photons to 928 ± 390 photons (Table 7.4). The background fluorescence was similar with a mean of 110 ± 114 photons before denoising and a mean of 109 ± 115 photons following denoising (Table 7.4). Finally, the localisation precision decreased from a mean of 13.7 ± 0.5 nm to 14.7 ± 0.5 nm following denoising (Table 7.4).

The analysis of photophysical parameters from NPC image sequences produced similar results to that from the microtubules. The mean intensity of single molecules was slightly lower following denoising, with a value of 559 ± 54 photons compared to 601 ± 50 photons before denoising (Table 7.4). The mean background was unchanged following denoising (Table 7.4), as observed for the microtubule data, while the localisation precision was also lower following denoising for the NPC data, with a decrease from 20.2 ± 0.3 nm to 24.1 ± 1.8 nm. Overall, the results from comparing the photophysical parameters demonstrated that denoising decreased the intensity and localisation precision of single-molecules, likely because of smoothing of the intensity profile following denoising (see Discussion for further details).

7.9 Further applications: tuning loss functions

A limitation of SRDTrans previously highlighted is its inability to discriminate between fluorescence originating from fluorophores attached to the structure of interest and fluorescence originating from unspecifically bound fluorophores or fluorophores from outside the field of illumination that have not transitioned to a stable dark state. This limitation was observed in the first denoised image sequence of microtubules (Fig. 7.3) where more single molecules were visible in the corner, contributing to noise. Likewise, noise from unspecifically bound fluorophores was still prominent following denoising for the vimentin image sequences (Fig. 7.12).

To address these limitations, two new loss functions were implemented for SRDTrans. The details of these loss functions are described in Theory: 2.7 and Methods: 3.10.1. Briefly, the new loss functions aid the minimisation of the total loss function when the pixel-to-pixel temporal intensity difference is high, and when there is high temporal variance in the brightest regions of an image frame. The intended effect of these loss functions is to assist training of the denoising model if fluorophores display appropriate photoswitching behaviour and penalise the model if not, ultimately aiming to reduce from unspecifically bound fluorophores since these are more likely to aggregate and exhibit abnormal photoswitching.

The denoising of SRDTrans with the new loss functions was evaluated on the first dataset of microtubules and the vimentin dataset. In both cases, training and inference was carried out using the same image sequence. Single-molecule localisation was carried out on the denoised image sequences as previously and the super-resolution reconstructions were compared to those that had been denoised without the additional loss functions.

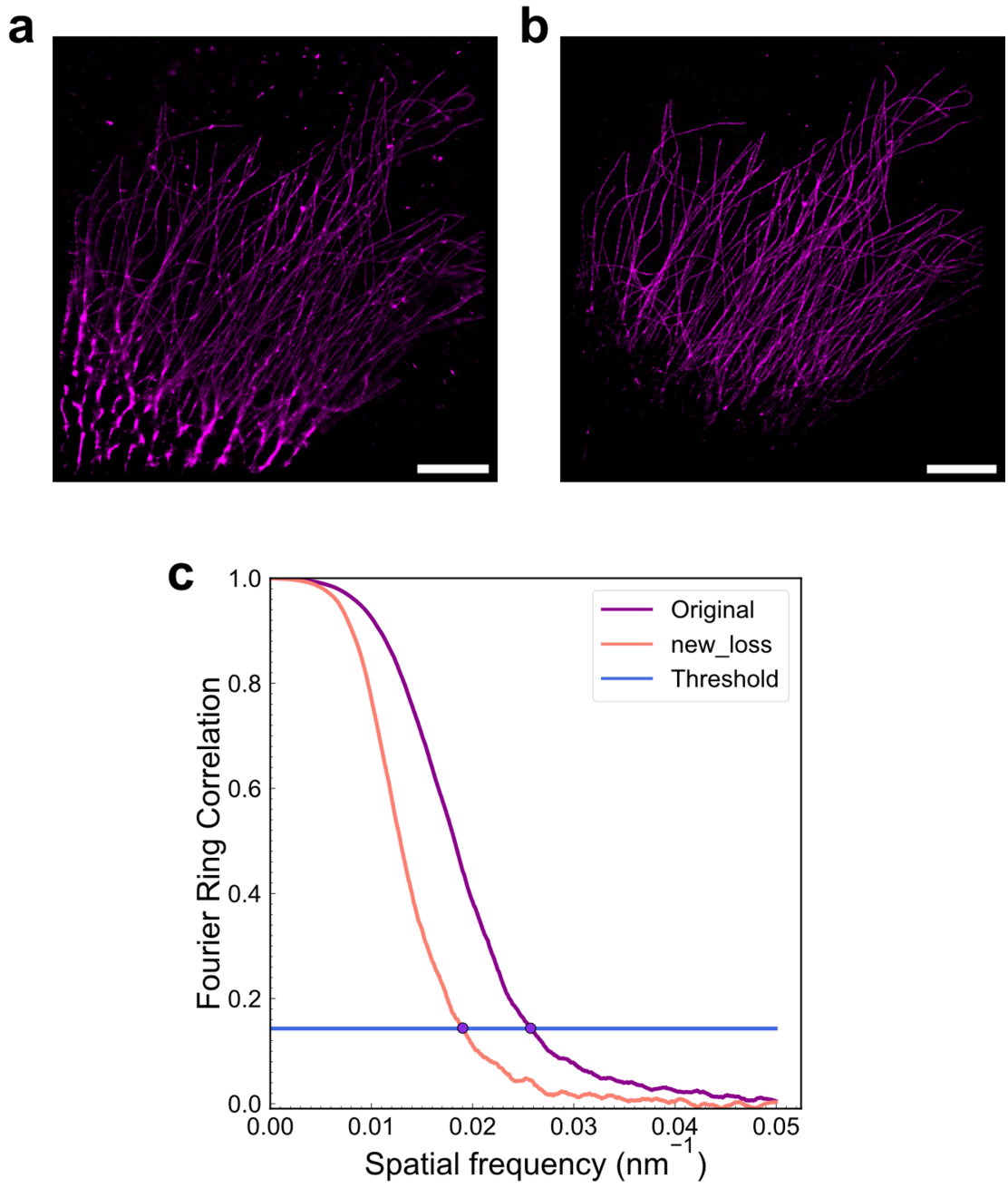

Fig. 7.14: **Assessment of denoising the first microtubule image sequence after training SRDTrans with new loss functions**. **a** Super-resolution reconstruction of the first image sequence of microtubules after denoising without the addition of new loss functions. Scale bar: 5 µm. **b** Super-resolution reconstruction of the same dataset after denoising with the new loss functions. Scale bar: 5 µm. **c** FRC curves comparing the resolution without and with the new loss functions. Here, "Original" denotes denoised localisation data without the new loss functions, i.e. those presented in Fig. 7.3**b**. "new_loss" denotes denoised localisation data after addition of the new loss functions. The resolution without the new loss functions was 38.9 nm while the resolution with the new loss functions was 52.6 nm.

Comparing the reconstruction from denoising with the new loss functions to the previous denoised reconstruction in Fig. 7.3, less background is present around the edges of the

image (Fig. 7.14**a**), demonstrating that the new loss functions can remove noise when it exhibits different photoswitching behaviour. However, the new loss functions also decreased the FRC resolution (Fig. 7.14**c**). Without the new loss functions, the FRC resolution was 38.9 nm but with the new loss functions, the FRC resolution was 52.6 nm. Notably, the FRC resolution was worse than the microtubule data without denoising (Fig. 7.4). While the filaments still exhibited better continuity than the reconstruction without denoising, the filaments towards the left and right edges of the image have worse continuity than either the reconstruction without denoising or the reconstruction with denoising.

Denoising with the new loss functions was then applied to vimentin image sequences. The results are shown in Fig. 7.15.

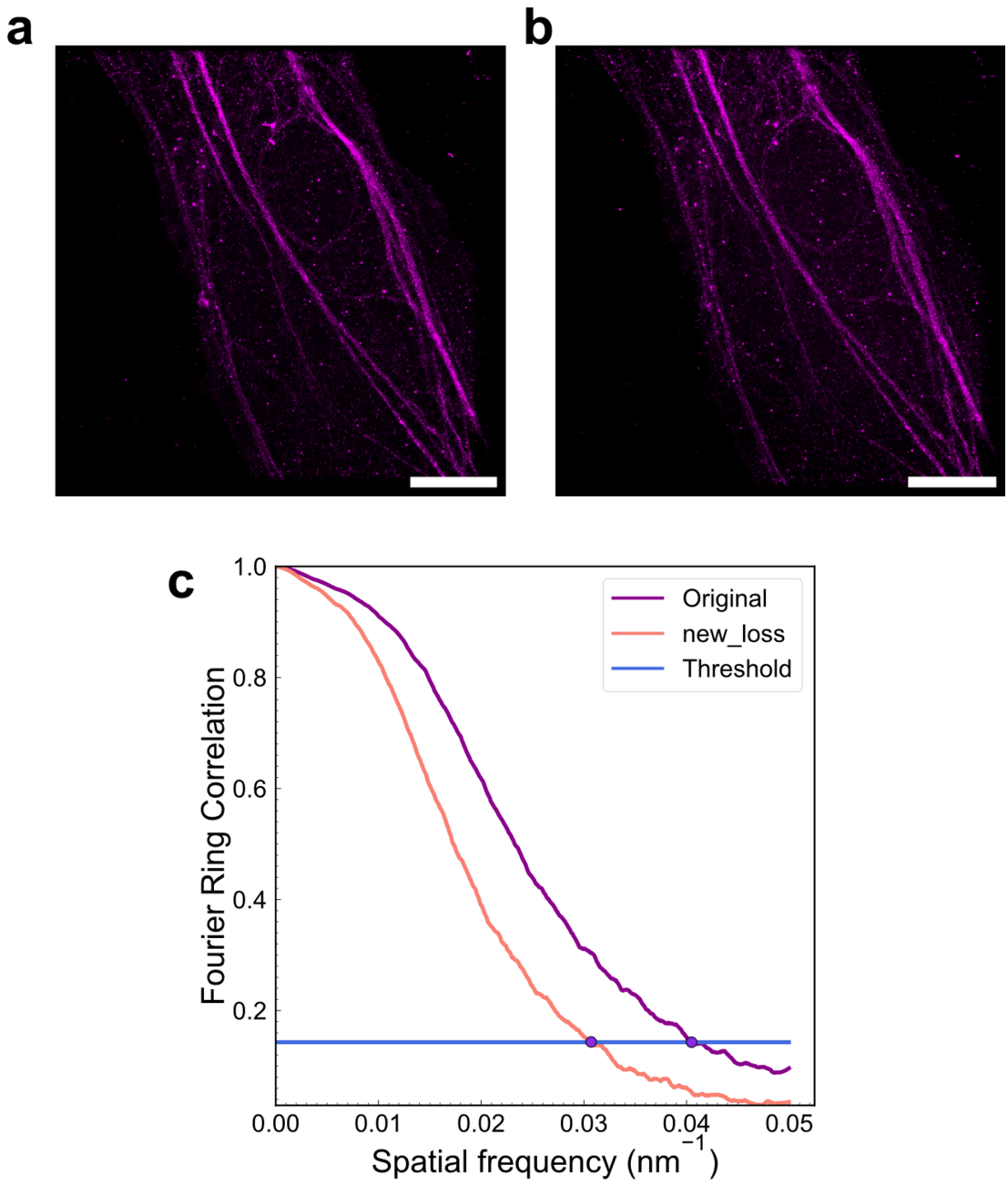

Fig. 7.15: **Assessment of denoising the vimentin image sequence after training SRDTrans with new loss functions. a** Super-resolution reconstruction of nanobody-labelled vimentin after denoising with the new loss functions. Scale bar: 5 µm. **b** FRC curves comparing the resolution with and without the new loss functions. The legend labels are the same as those in Fig. 7.14**c**, where the denoised localisation data without the new loss functions are those presented in Fig. 7.12**c**. The resolution without the new loss functions was 24.7 nm and the resolution with the new loss functions was 32.6 nm.

With the new loss functions, little difference was observable for the super-resolution image of the nanobody-labelled vimentin (Fig. 7.15**a**). Unlike the microtubule image sequence, the noise from the unspecifically bound fluorophores likely exhibited similar photoswitching behaviour to fluorophores that were bound to the vimentin, and so

the new loss functions were less effective at discriminating between fluorescence that corresponded to noise or signal. Similar to denoising the microtubule image sequences with the new loss functions (Fig. 7.14), the FRC resolution was worse with the new loss functions, decreasing from 24.7 nm to 32.6 nm (Fig. 7.15**b**).

Taken together, adding these new loss functions to SRDTrans may have aided with removing noise from fluorescence which differed in its photoswitching behaviour, such as out-of-focus fluorophores or fluorophores towards the edges of the field of illumination. However, the new loss functions did not adequately address noise from unspecifically bound fluorophores and also degraded the attainable resolution.

7.10 Discussion and conclusions

The denoising performance for SRDTrans has been characterised in this chapter, providing a more comprehensive and transparent evaluation to that of the original work. The denoising model obtained from training SRDTrans can be generalised to biological samples that are structurally different from the data used for training (Fig. 7.2), as well as to image sequences obtained with a camera with different noise characteristics (Fig. 7.10, Fig. 7.11). However, the model was likely more effective when the training data had similar contrast to the test data (Fig. 7.1). Experimentally, this observation means that the image sequence used for training ought to have a fluorophore with similar brightness to the image sequence used for denoising, as well as similar image acquisition parameters. Apart from model generalisation, the effect of denoising on super-resolution images was also characterised in this chapter for microtubules, NPCs, and ACE-2 receptors (Fig. 7.3, Fig. 7.5, Fig. 7.8). It was observed that denoising effectively increases the *in silico* labelling density through improved detection of single-molecules—an observation not noted in the original work—thereby increasing the localisation accuracy and attainable resolution (Table 7.1, Table 7.2, Fig. 7.7). Further characterisation of SRDTrans revealed that it performed best when the predominant sources of noise in the image sequence were camera-based noise and shot noise but performed poorly if the predominant source of noise originated from unspecifically bound fluorophores (Fig. 7.12, Fig. 7.13). Finally, adding new loss functions to the model assisted with the removal of noise from out-of-focus fluorophores but was unable to address noise from unspecifically

bound fluorophores (Fig. 7.14, Fig. 7.15).

A notable observation from comparing the estimated photophysical parameters before and after denoising was that the localisation precision was consistently lower for the denoised localisation data (Table 7.4). A possible explanation for this could be that SRDTrans smooths images slightly as a consequence of denoising—an effect that is most prominent upon comparison of the non-denoised images in Fig. 7.1**a** and Fig. 7.2**d** to their denoised counterparts in Fig. 7.1**d** and Fig. 7.2**e**. This smoothing would cause the maximum fluorescence intensity for a single-molecule to be decreased, thereby resulting in a lower estimate for the intensity, $\hat{\theta}_I$, which was also observed in the comparison of estimated photophysical parameters in Table 7.4. The lower intensity would then result in lower localisation precision for the same single-molecule in a denoised image sequence. It should be noted, however, that despite lower localisation precisions following denoising, the FRC resolution was consistently shown to improve from denoising (Table 7.1, Table 7.2). Therefore, the resolution enhancement from improved single-molecule detection is greater than the loss in resolution from the lower localisation precision. Nonetheless, caution ought to be applied if the estimated intensities and localisation precisions from denoised localisation data are applied to postprocessing analyses, as they may give different results to using non-denoised localisation data.

The removal of noise originating from unspecifically bound fluorophores was challenging for SRDTrans. This observation can be attributed to the fluorescence emission profiles of unspecifically bound fluorophores being similar to those from fluorophores bound to the sample. Even with the new loss functions (Theory: 2.7), substantial differences were only observed in Fig. 7.14 because the noisy fluorophores at the edge of the image were out of focus. Such a result means that caution must be taken when applying SRDTrans to spatial analysis methods that use localisation data, as denoising is likely to retain or increase detections of single-molecules that are not bound to the sample. As such, it is unlikely that improvements in the accuracy of spatial statistics would be observed even after applying denoising. Going forward, in the absence of a deep learning algorithm that can denoise unspecifically bound fluorophores in SMLM image sequences, preprocessing and postprocessing approaches may be preferable. These methods include straightforward procedures such as changing the intensity threshold for single-molecule

detection, merging molecules, and filtering localisations by intensity, background, PSF size, or localisation precision. More sophisticated methods such as using DBSCAN in ThunderSTORM to remove unspecific background localisations [135, 243] may also be beneficial for removing noise from unspecifically bound fluorophores.

One of the challenges for SRDTrans in this chapter was unambiguously determining whether the increased number of localisations detected from the ACE-2 image sequences corresponded to fluorophores bound to the structure of interest, or whether it corresponded to unspecifically bound fluorophores. Such concerns were not present for microtubule and NPC localisations due to visible differences in the reconstruction before and after denoising (Fig. 7.3, Fig. 7.7). However, since the ACE-2 receptors lack a clearly defined spatial organisation, the same analysis approach could not be applied. In this respect, the use of FRC resolutions for evaluating denoising was not very informative for the ACE-2 receptor (Fig. 7.9, Table 7.3). For example, the FRC curve for the ACE-2 receptor presented in Fig. 7.9 exhibited an unusual shape relative to those in Chapter 4, Figs. 4.8 and 4.12—all of which used the same method to split the localisation data. Extending this logic further, it is likely that using FRC resolutions may be unhelpful when the sample does not have a well-defined organisation. Instead, the evaluation of denoised ACE-2 receptor localisation could be expanded and improved by including methods that map and quantify image artefacts. Two such methods are NanoJ-SQUIRREL and HAWKMAN, both of which are capable of identifying areas where image fidelity has degraded [244, 245]. Applying these methods may have provided more informative insights on the impact of SRDTrans on image fidelity.

The scope of this chapter could be expanded by testing SRDTrans on low-SNR SMLM modalities. While some results presented in this work did use ATTO 488 (Fig. 7.2**a**–**c**, Fig. 7.8)—a dye emitting fewer photons than AF647 [91]—the typical photon counts of fluorescent proteins used in PALM are even lower than that of ATTO 488 [246]. DNA-PAINT can also suffer from low SNR due to the high background arising from free diffusion of fluorophores conjugated to the imager strand [247]. It would, thus, be of interest to evaluate denoising on images sequences acquired from PALM or DNA-PAINT. The results from this would allow for a more comprehensive evaluation of the denoising capability of SRDTrans, thereby better informing other users of SMLM on

the benefits and limits of SRDTrans.

Finally, it would be beneficial if the evaluation of denoising were expanded to other algorithms beyond SRDTrans. Two advantages of SRDTrans are its use of a vision transformer architecture and its development specifically for SMLM image sequences, both of which may be responsible for its effectiveness at denoising SMLM data (Fig. 7.3–Fig. 7.7, Fig, 7.13). However, it is challenging to assess accurately the benefits that these two factors confer since denoising algorithm evaluations as comprehensive as that presented herein are lacking in the literature—despite the rapid development of denoising algorithms for fluorescence microscopy [74, 75, 248, 249]. It would, therefore, be beneficial to benchmark SRDTrans against other deep learning denoising methods using the approach described in this chapter, particularly for algorithms that use convolution neural networks since they are hypothesised to perform worse than vision transformers [86, 87]. Such an evaluation would inform the SMLM community on selecting the best denoising method for achieving deeper biological insights, as well as inform developers of denoising algorithms on the advantages and disadvantages of different deep learning architectures and strategies.

7.10.1 Conclusions

Overall, a comprehensive evaluation of SRDTrans has revealed that it was effective at denoising SMLM image sequences from different biological samples and imaging configurations if the predominant types of noise are shot noise or camera-based. In other words, if the noise was mainly shot noise, read noise, and or amplification noise. The effect of denoising was to improve detection of fluorophores in the image sequences, thereby increasing the labelling density and resolution. The results in this chapter represent a substantial extension to the original work describing SRDTrans, thus informing users of SMLM on the benefits and drawbacks of using SRDTrans for denoising. The results also demonstrate the ability of vision transformer architectures to denoise SMLM image sequences—information which could be helpful for future development of denoising algorithms.

8 Biological Imaging Applications—STORM of ACE-2 receptor and SARS-CoV-2 spike protein

8.1 Overview

STORM is a powerful method to investigate the cellular organisation of proteins due to its ability to acquire spatial information at resolutions in the tens of nanometers, facilitating the application of spatial statistics methods to attain quantitative insights into cellular processes. Here, the internalisation of SARS-CoV-2 spike protein is used as the biological system of interest (Introduction: 1.4.4)—a process yet to be examined in detail with SMLM. In this chapter, results from colocalisation analysis and cluster analysis (Theory: 2.6, Theory: 2.6.1) from two-colour STORM of ACE-2 receptor and SARS-CoV-2 spike protein are presented. Such an experimental approach also serves as a method with which to evaluate whether denoising using SRDTrans (Chapter 7) distorts experimental results when investigating biological systems.

Prior to the work presented in this chapter, SARS-CoV-2 spike protein had been expressed, purified, and conjugated to a maleimide derivative of Alexa Fluor 647 by Dr. Siva Ramadurai (The Rosalind Franklin Institute) according to Methods: 3.3.4, 3.3.5, 3.3.6. Separately, the DNA sequence encoding ACE-2 was cloned into pOPINE plasmids containing the sequence for the SNAP-tag (Methods: 3.3). The plasmid was used to transfect Calu-3 lung cells (Methods: 3.4.3), to express the ACE-2-SNAP fusion protein which was then labelled with ATTO 488.

SARS-CoV-2 spike protein was incubated with Calu-3 cells for 5 minutes, 15 minutes, or 30 minutes before cell fixation and two-colour STORM. A negative control was also implemented where no spike protein was added. The localisation data from two-colour STORM were analysed with a similar approach to Malkusch *et al.* 2012 (Theory: 2.6), allowing co-localised molecules to be identified. Cluster analysis using HDBSCAN and principal component analysis (PCA) was then carried out (Theory:

2.6.1). The aim of these analyses was to compare differences in the clustering and spatial organisation of ACE-2 following addition of the spike protein at different time points. These analyses also present a methodological improvement to popular clustering methods through the use of HDBSCAN instead of DBSCAN [243, 250]; DBSCAN requires two hyperparameters—the cluster size and cluster radius—while HDBSCAN requires only the cluster size, thus simplifying analysis workflows.

By analysing the spatial organisation of a pathogen-host interaction at resolutions below the diffraction limit, it is hoped that the results will facilitate the elucidation of the mechanisms of pathogenesis. Furthermore, it is hoped that the analytical approach presented in this chapter will serve as a template for the acquisition of quantitative insights from SMLM experiments.

8.2 Two-colour STORM of ACE-2 and SARS-CoV-2 spike protein

For multicolour STORM, channel registration must be carried out to correct for chromatic aberrations (Fig. 8.1**a**, Fig. 8.1**b**). As such, 100 nm diameter fluorescent beads were imaged with excitation wavelengths of 488 nm and 640 nm—corresponding to the excitation wavelengths of ATTO 488 and AF647, respectively. The beads were localised (Theory: 2.3, Methods: 3.7.1) and channel registration was performed using the subpixel xy-localisations according to Theory: 2.6 and Methods: 3.8.2. The channel registration error was taken to be the median nearest neighbour distance from the bead localisations of one channel to another. This procedure was repeated prior to STORM for each timepoint.

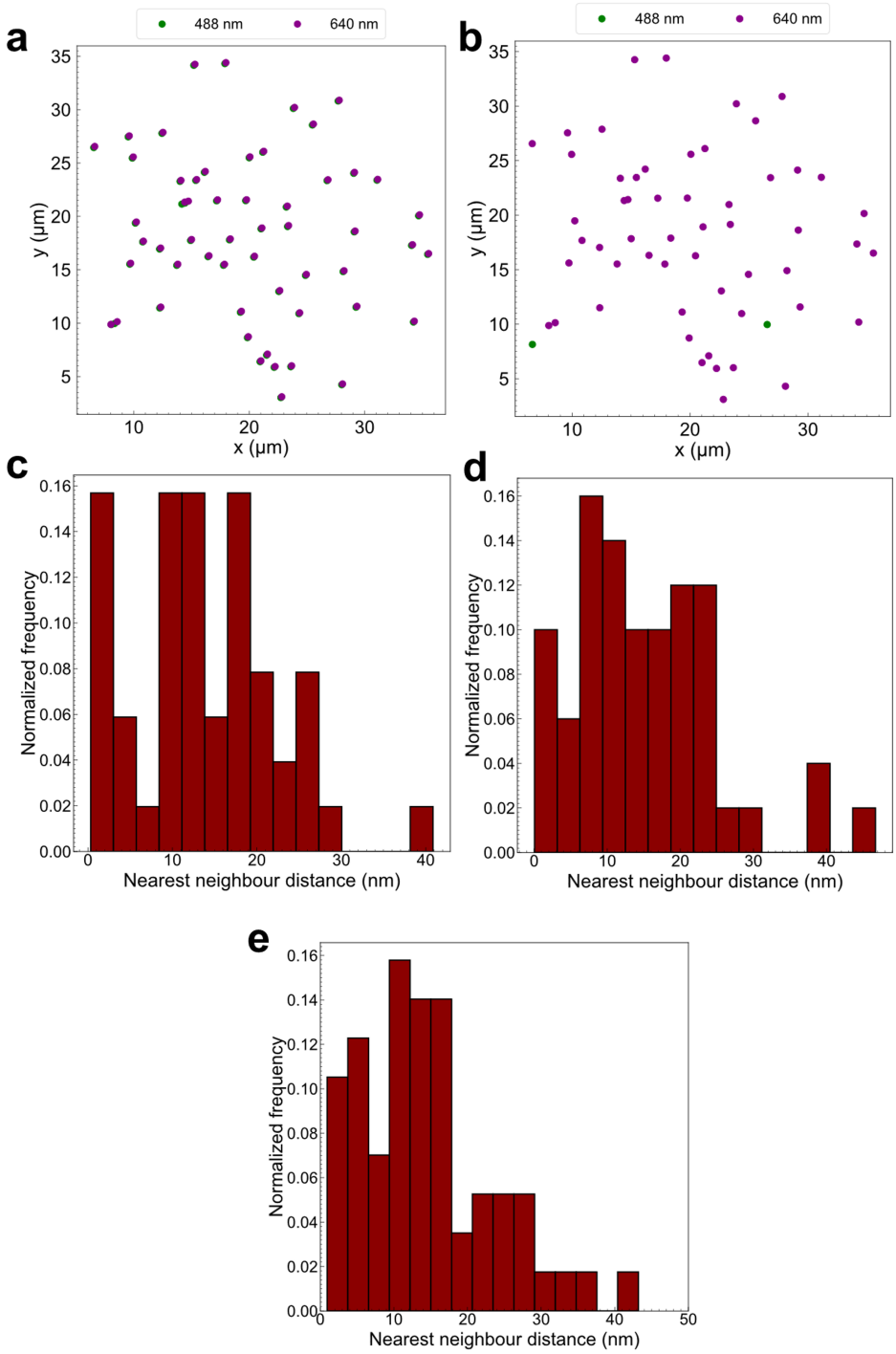

Fig. 8.1: **Channel registration procedure for two-colour STORM of ACE-2-SNAP and SARS-CoV-2 spike protein, as well as the associated registration errors. a** Scatterplot of bead localisations before channel registration. Green circles mark localisations from imaging with 488 nm while magenta circles mark localisations from imaging with 640 nm. **b** Scatterplot of bead localisations following channel registration. **c** Histogram of nearest neighbour distances from the 5 minutes timepoint of ACE-2 and spike protein. The registration error was 13.5 nm. **d** Histogram of nearest neighbour distances from the 15 minutes timepoint. The channel registration error was 14.6 nm. **e** Histogram of nearest neighbour distances from the 30 minutes timepoint. The registration error was 13.8 nm.

The registration errors were 13.5 nm, 14.6 nm, and 13.8 nm for the 5 minutes, 15 minutes, and 30 minutes timepoints, respectively (Fig. 8.1**c**–**e**), all of which were within

typical localisation precision values, demonstrating that channel registration would not have a measurable impact on the results from two-colour STORM.

For two-colour STORM, the ACE-2-SNAP fusion protein was labelled with ATTO 488 according to Methods: 3.4.9. STORM imaging was then carried out according to Methods: 3.6.2 for each timepoint. Widefield images of the 5-minute timepoint are shown in Fig. 8.2 along with the corresponding localisations before and after channel registration.

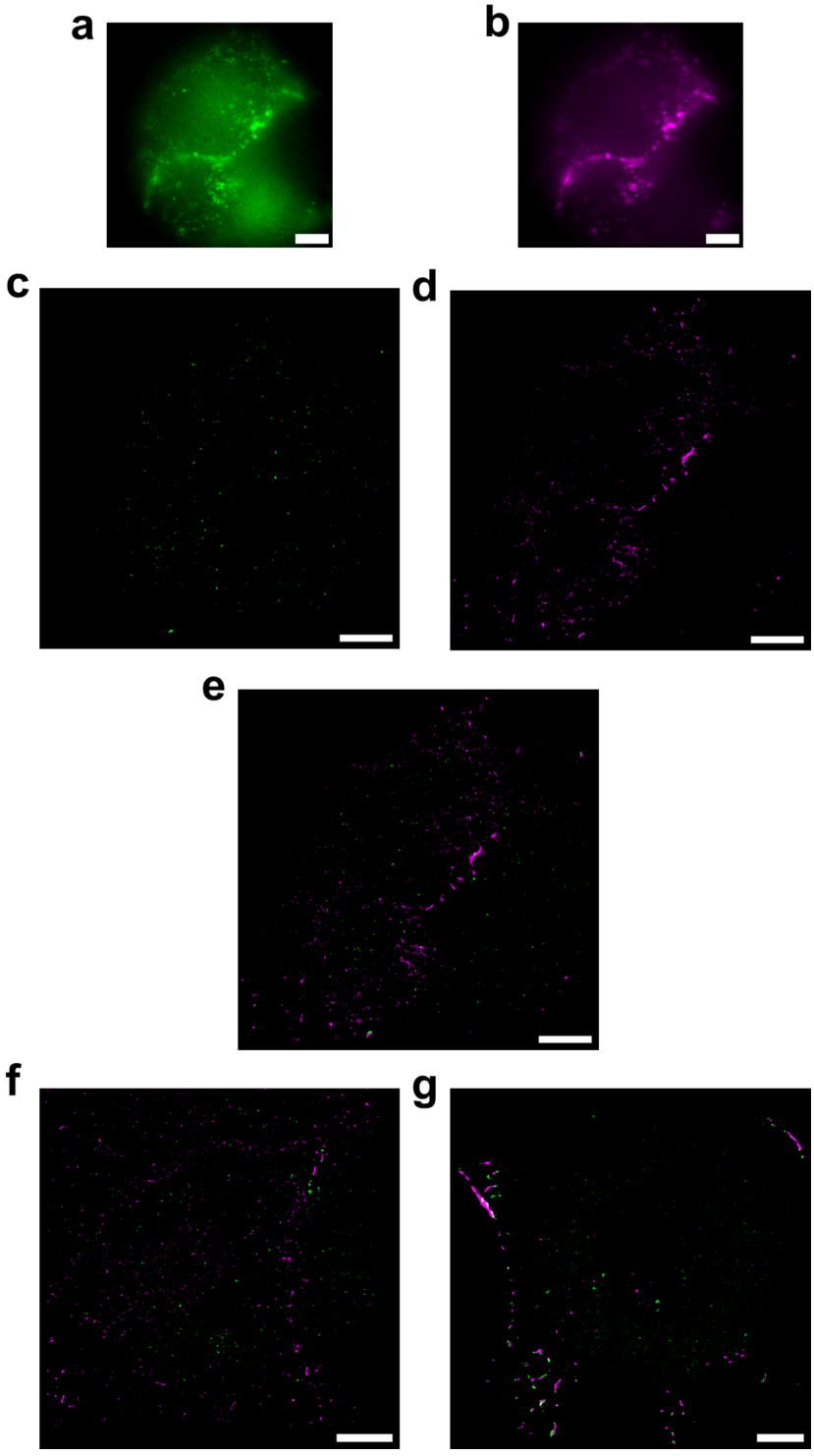

Fig. 8.2: **Super-resolution images following two-colour STORM of ACE-2-ATTO 488 and SARS-CoV-2 spike-AF647.** Scale bars: 5 µm. **a** Example widefield image of a Calu-3 cell with ACE-2-SNAP labelled with ATTO 488 at the 5-minute timepoint. **b** Example widefield image of the spike protein labelled with AF647 after incubating with Calu-3 cells for 5 minutes. **c** Super-resolution reconstruction of **a** following STORM and prior to channel registration. **d** Super-resolution reconstruction of **b** following STORM. **e** Merged image of **c** and **d** following channel registration. **f** Merged image of the ACE-2 localisations and spike protein localisations from the 15-minute incubation timepoint. **g** Merged image of the ACE-2 localisations and spike protein localisations from the 30-minute incubation timepoint.

From the widefield images (Fig. 8.2**a**, Fig. 8.2**b**), fluorescence from both channels can

be observed in similar locations, implying spatial correlation between ACE-2 and the spike protein. The STORM reconstructions corroborate this observation, with spatial overlap visible between the localisations of both channels (Fig. 8.2**e**). Similar outcomes were also observed for ACE-2 and spike protein at other timepoints (Fig. 8.2**f**, Fig. 8.2**g**).

8.2.1 Colocalisation analysis and cluster analysis of ACE-2 receptor and spike

To gain quantitative insights into the interactions and spatial organisation of the ACE-2 receptor and spike protein, colocalisation analysis and cluster analysis were carried out for the localisation data of both channels. The localisation data acquired at each timepoint were analysed to assess for differences in spatial organisation during the internalisation of the virus.

First, the presence of clusters was verified with Ripley's H-function [160] (Theory: Eq. 2.41, Methods: 3.8.3)—a normalised variant of Ripley's K-function. STORM of a negative control (Appendix: Fig. A.9) where Calu-3 cells were transfected with pOPINE-ACE-2-SNAP and labelled with ATTO 488 without the addition of spike protein was also carried out. Using Ripley's H-function, positive values would indicate clustering while negative values would indicate dispersion. A maximum radius of observation of 1500 nm was used but only the first 500 nm were plotted below for clarity.

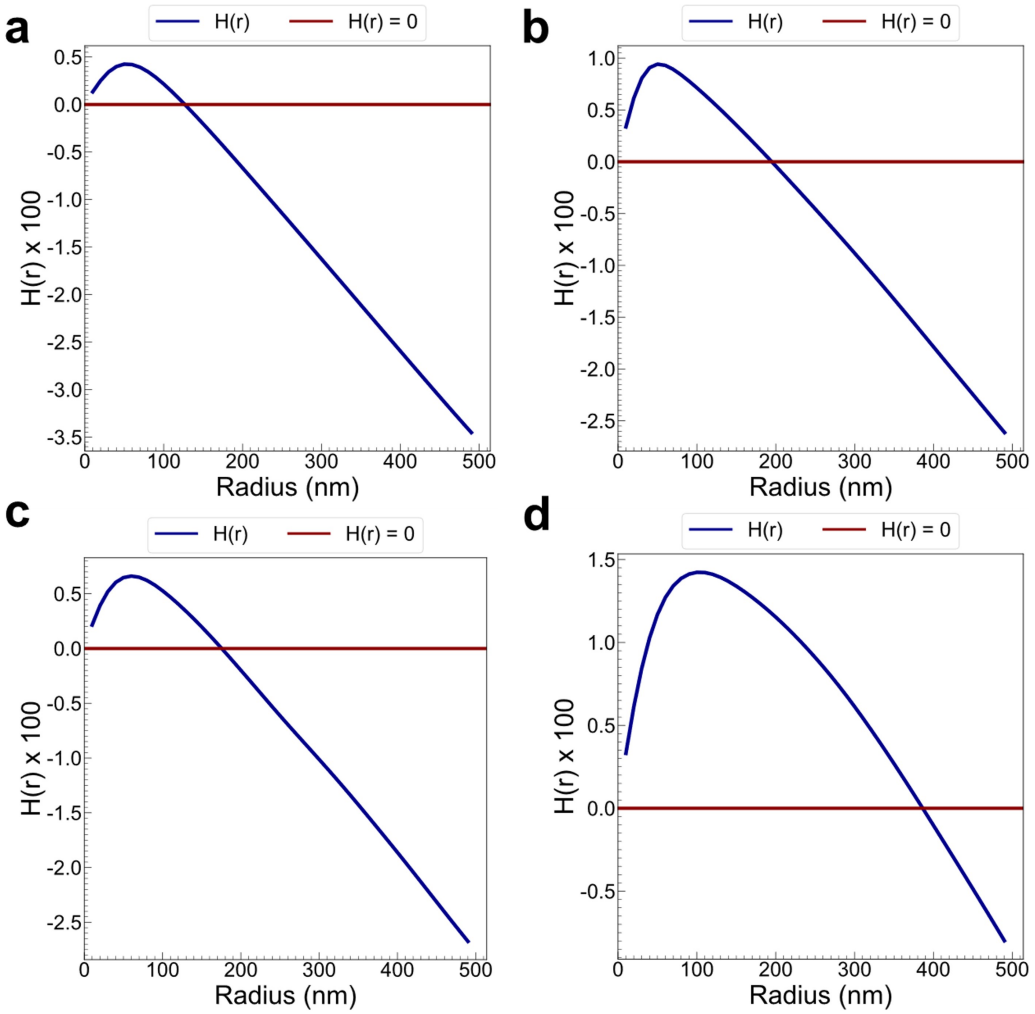

Fig. 8.3: **Assessing for the presence of clusters of ACE-2 receptor and SARS-CoV-2 spike protein using Ripley's H-function.** Ripley's H-function was calculated using Eq. 2.41 with a maximum radius of observation of 1500 nm. Only the first 500 nm were plotted for clarity. All values for the H-function have been scaled down by a factor of 100 for visual clarity. The blue lines denote the calculated H-function values while the red horizontal lines denote where the H-function equals zero. **a** Plot of the calculated H-function for the negative control, i.e. where no spike protein was added. The radius at which the maximum was located was $\sim$ 50 nm. **b** Plot of the calculated H-function for the 5-minute spike protein incubation. The radius at which the maximum was located was $\sim$ 50 nm. **c** Plot of the calculated H-function for the 15-minute spike protein incubation. The radius corresponding to the maximum was 60 nm. **d** Plot of the calculated H-function for the 30-minute spike protein incubation. The radius corresponding to the maximum was 100 nm.

At all timepoints, clusters were detectable within a typical radial range of 0–150 nm—with the exception of Fig. 8.3**d**—as indicated by the range of radii over which the H-function was positive (Fig. 8.3**a**–**c**). Using these results, the maximum search radius for colocalisation analysis was set to 120 nm.

Colocalisation analysis was carried out as described in Theory: 2.6 and Methods: 3.8.2, resulting in a coordinate-based colocalisation (CBC) value for all localisations that

ranged from -1 (channels anti-correlated) through 0 (channels not correlated, unlikely to be colocalised) to +1 (channels correlated, likely to be colocalised). Localisations with a CBC higher than 0.4 were retained for cluster analysis, following the example from Clus-DoC [250]. Here, clusters were identified using hierarchical density-based spatial clustering of applications with noise (HDBSCAN) described in Theory: 2.6.1 and Methods: 3.8.3. A minimum cluster size of 4 localisations was used since it has been established that the ACE-2 receptor interacts with a trimeric spike protein [110].

Following cluster identification, the cluster area, radius, circularity, density, and the number of ACE-2 receptors in each cluster were calculated. With these descriptors, dimensionality reduction via principal component analysis (PCA) was carried out using two principal components (Theory: 2.6.1, Methods: 3.8.3). The aim of PCA was to examine whether the cluster parameters differed with varying spike protein incubation times. By plotting the first principal component against the second component, it would be expected for cluster data from different timepoints to be localised to distinct locations on the plot. In contrast, if the cluster parameters were similar, the data would be expected to localise at similar locations. The loadings of each principal component also provide information on which cluster parameters are correlated. The results from PCA for the control and 5 minutes timepoint are shown below along with the proportion of explained variance from using two principal components.

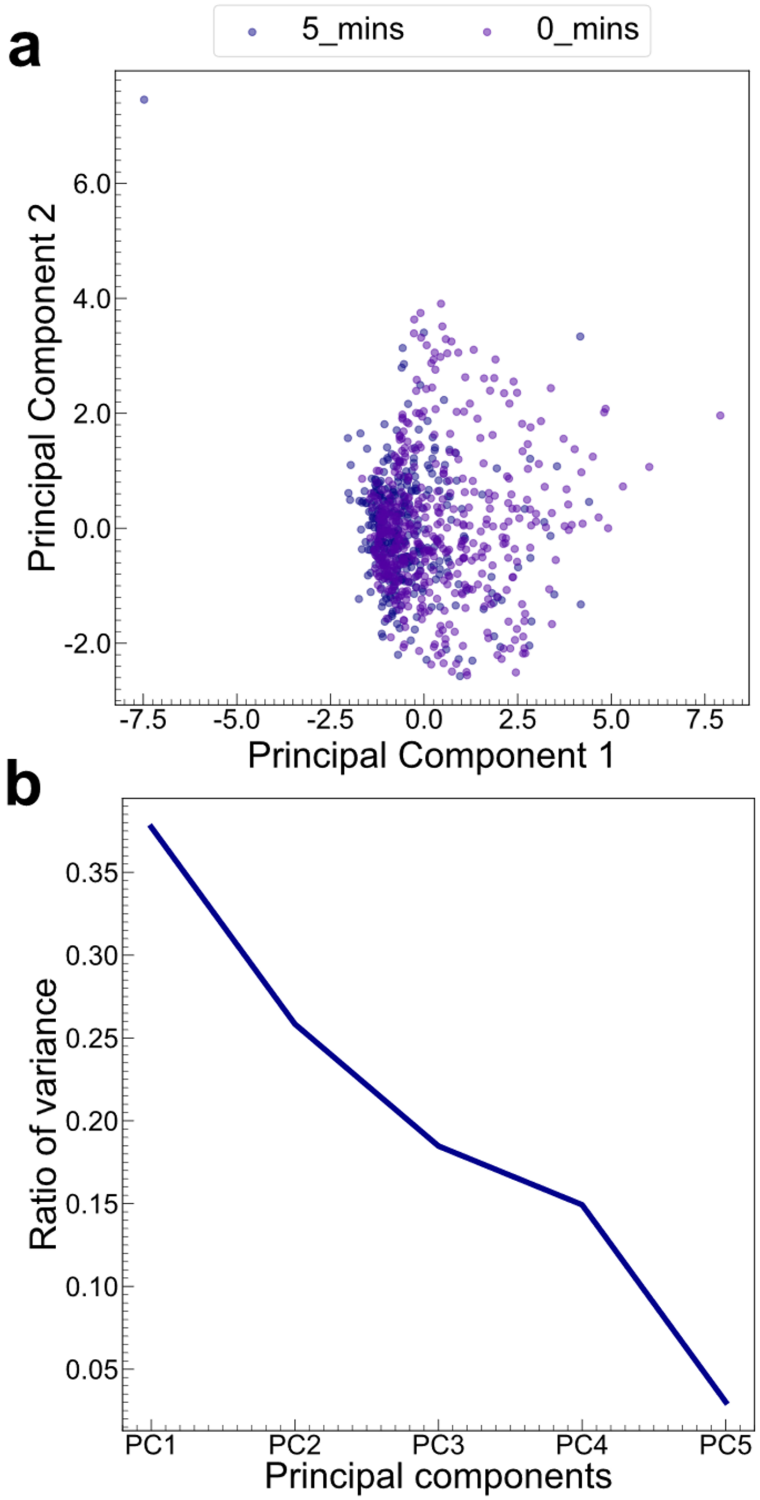

Fig. 8.4: **Principal component analysis of cluster parameters of the negative control ("0_mins") and ACE-2 and spike with a 5-minute incubation time ("5_mins"). a** 2D scatterplot of the cluster data following dimensionality reduction to two principal components. Each scatter point represents a cluster of localisations identified by HDBSCAN where the five cluster descriptors have been reduced to two principal components. The cluster data from the 5-minute incubation timepoint are coloured violet while the cluster data from the negative control are coloured purple. **b** Plot of the explainable variance from each principal component. Using two principal components results in a total explainable variance of $\sim 64.5\%$.

The loadings for principal component 1 (PC1) and principal component 2 (PC2) are as

follows:

$$\text{PC1} = 0.86A + 0.94r - 0.29C + 0.28N - 0.33D\,, \tag{8.1}$$

$$\text{PC2} = 0.26A - 0.09r + 0.82C + 0.70N + 0.28D\,. \tag{8.2}$$

Here, A, r, C, N, D are the five cluster descriptors and denote the area, radius, circularity, number of ACE-2 receptors, and density, respectively. The results from the loadings imply that cluster area and cluster radius are strongly correlated for PC1 while the number of ACE-2 receptors is weakly correlated and the cluster circularity and density are weakly anti-correlated. For PC2, the circularity and number of ACE-2 receptors are strongly correlated while the area and density are weakly correlated, and the radius is weakly anticorrelated.

There was a degree of overlap between the cluster data of the negative control and 5-minute timepoint (Fig. 8.4**a**). However, the data of the control were slightly more spread out along the positive directions of both principal components. From the loadings described in Eq. 8.1 and Eq. 8.2, some of the clusters from the negative control had larger areas and radii, as well as higher circularity and more ACE-2 receptors. As such, it may be possible that the addition of spike protein initiated the accumulation and sequestering of ACE-2 receptors.

To further assess this hypothesis, the PCA was repeated but with the 15-minute and 30-minute timepoints included.

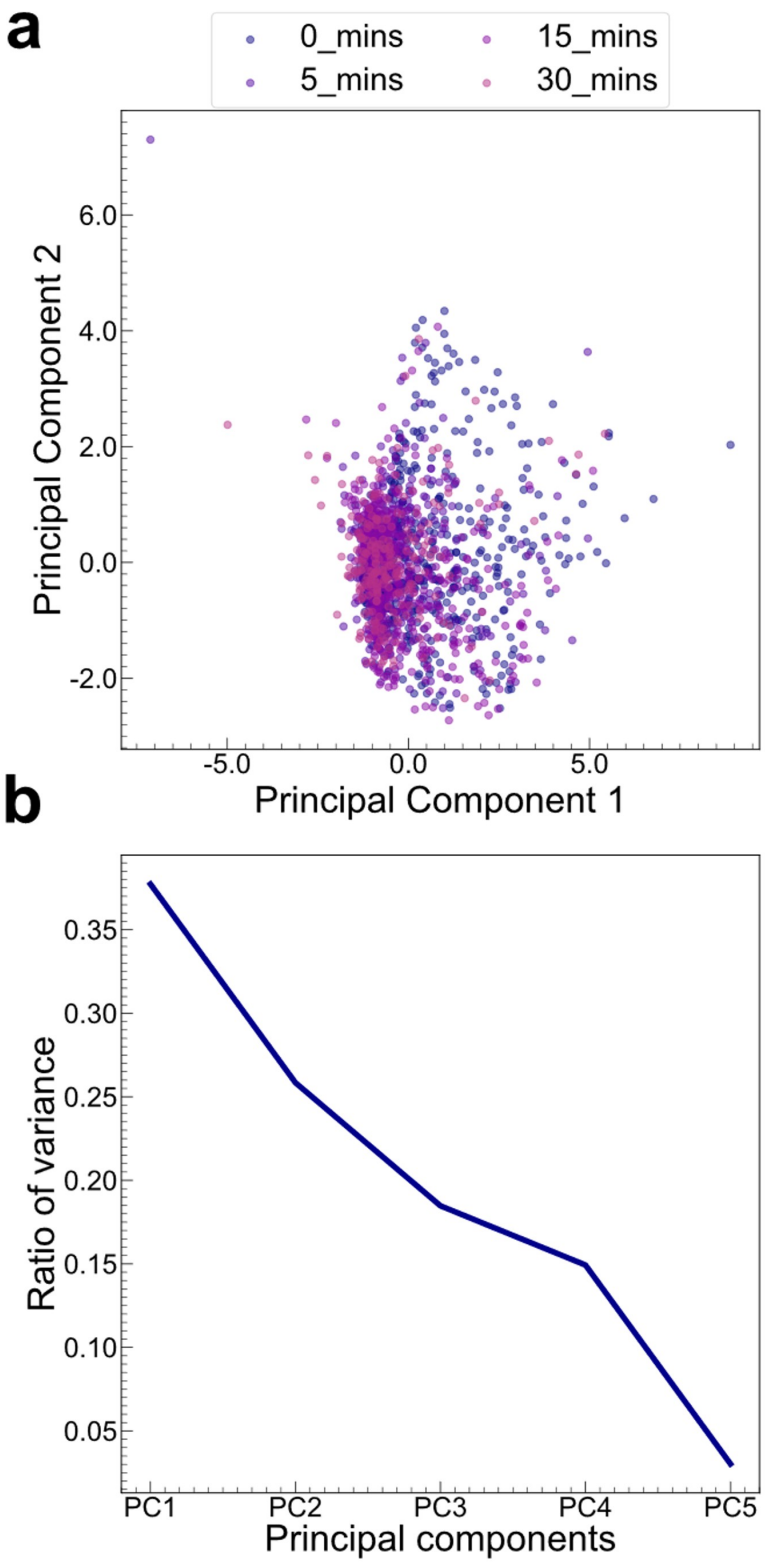

Fig. 8.5: **Principal component analysis of ACE-2 and SARS-CoV-2 spike protein clusters wherein the spike protein has been incubated for 5 minutes, 15 minutes, or 30 minutes. a** 2D scatterplot of the cluster data from all timepoints following dimensionality reduction to two principal components. "0_mins" denotes the negative control where no spike protein was added. **b** Line plot of the explained variance for each principal component. With two principal components, the proportion of explained variance was $\sim 63.5\%$.

The loadings of the principal components used in Fig. 8.5**a** were as follows:

$$\text{PC1} = 0.87A + 0.93r - 0.22C + 0.31N - 0.35D\,, \tag{8.3}$$

$$\text{PC2} = 0.24A - 0.14r + 0.83C + 0.66N + 0.29D\,. \tag{8.4}$$

The loadings of the principal components were similar to Fig. 8.4**a**, again suggesting that cluster area and radius were correlated and that variation in these descriptors was the primary driver for cluster-to-cluster variation. Cluster circularity and the number of ACE-2 receptors were also correlated for PC2, implying that these two variables also drove cluster-to-cluster variation.

There was overlap between the control and all timepoints (Fig. 8.5**a**), suggesting that ACE-2 and spike protein formed similar clusters irrespective of the incubation duration. It is possible that 15-minute and 30-minute incubation times were too long relative to viral internalisation timescales, meaning that most ACE-2-spike interactions—and subsequent internalisation—may have happened in the first five minutes (see Discussion for further details). Therefore, longer incubations may not have meaningfully altered the characteristics of the clusters.

8.3 Cluster analysis with denoised ACE-2 localisation data

An aspect of denoising using SRDTrans that was not adequately addressed in Chapter 7 was whether its increased capability to detect localisations would affect the results from an investigation focused on a biological system. To assess this, PCA was repeated using the localisations from denoised ACE-2 image sequences. The image sequences of ACE-2-SNAP ATTO 488 were denoised as described in Chapter 7, section 7.5, and the colocalisation analysis and cluster analysis were carried out as previously. To compare the effects of denoising, pairwise comparisons of the cluster data at each timepoint were carried out, e.g. the ACE-2 localisations from the 5-minute timepoint were compared to the denoised localisations from the same timepoint. If denoising affected the cluster data, it would be expected that the scatterpoints from a 2D principal component plot would localise to different locations. Conversely, if denoising had little effect, a degree of overlap would be expected.

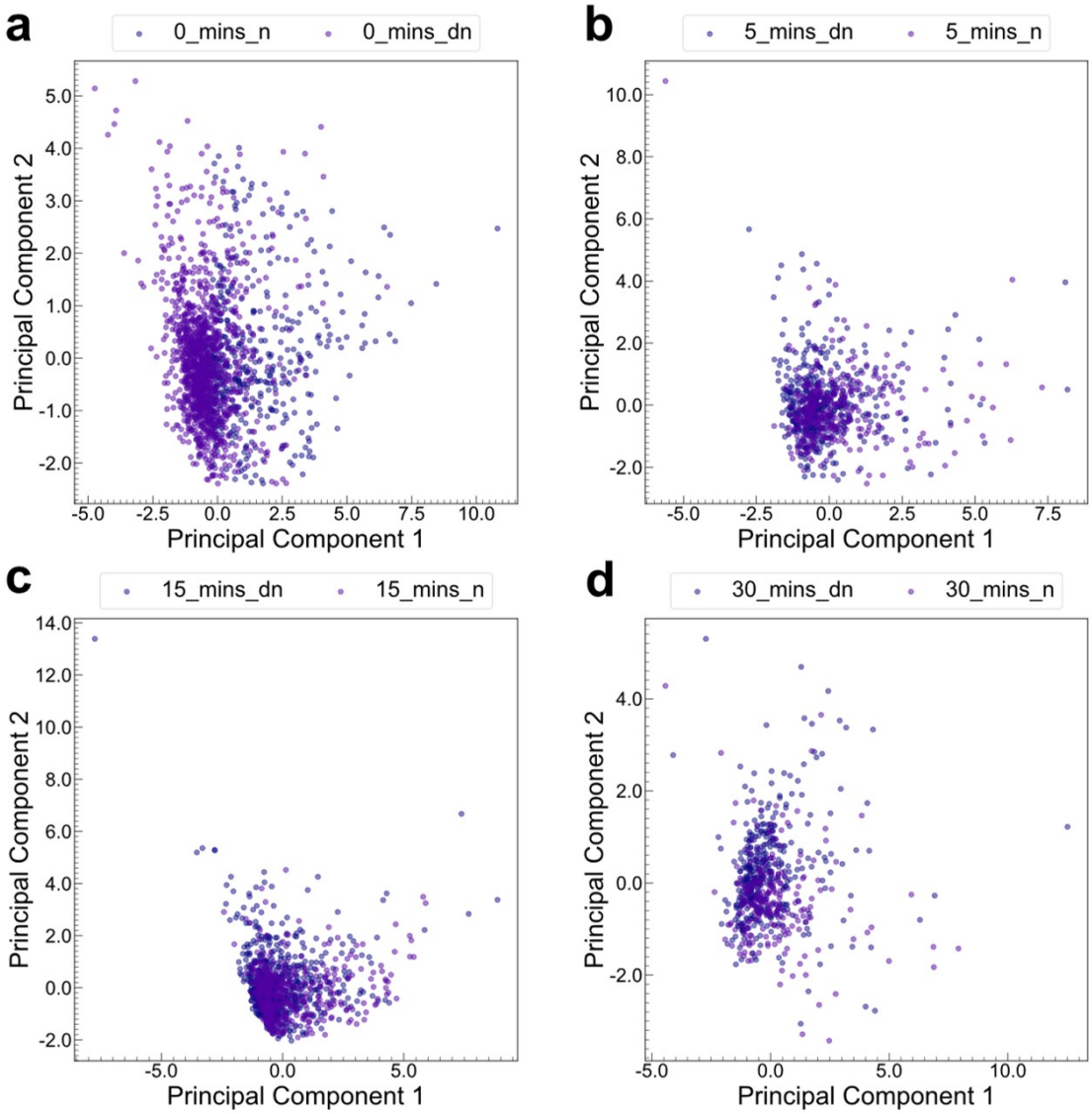

Fig. 8.6: **Comparison of PCA of ACE-2 and spike cluster data before and after denoising.** Similar to Fig 8.4 and Fig. 8.5, the cluster descriptors have undergone dimensionality reduction to two principal components using PCA. **a** 2D scatterplot of the cluster data from the negative control before and after denoising. **b** 2D scatterplot of the cluster data from the 5-minute timepoint. **c** 2D scatterplot of the cluster data from the 15-minute timepoint. **d** 2D scatterplot of the cluster data from the 30-minute timepoint.

At all timepoints and the negative control, there was overlap between the cluster data after denoising (Fig. 8.6**a**–**d**), indicating the cluster characteristics were similar to those before denoising. Therefore, it was likely that denoising did not substantially alter the outcome of cluster analysis of ACE-2 and spike protein, meaning that, for this work, similar conclusions would be derived from a biologically driven investigation regardless of whether denoised localisation data was used or not. However, application of denoising to a wider range of biological data would be required for a more robust assessment.

8.4 Discussion and conclusions

In this chapter, colocalisation and cluster analysis have been carried out for two-colour STORM following incubation of the SARS-CoV-2 spike protein at timepoints of 5 minutes, 15 minutes, and 30 minutes (Fig. 8.1, Fig. 8.3). PCA was carried out for cluster data originating from these timepoints, as well as for a negative control where no spike protein was added (Fig. 8.4, Fig. 8.5). This analysis revealed differences in cluster characteristics between the negative control and the 5 minute timepoint but no changes in cluster characteristics across additional timepoints was observed. Finally, the outcomes of cluster analysis were also compared to cluster data originating from localisation data that had been denoised using the approach described in Chapter 7. Similar outcomes were observed between cluster data with and without denoising, implying that applying SRDTrans would not alter the biological conclusions from postprocessing analyses of SMLM data.

Apart from the analysis of biological data, the cluster analysis method presented in this chapter offered some improvements to current methodologies for cluster analysis. For example, DBSCAN is a popular algorithm for cluster analysis in SMLM [157, 250, 251]. However, it requires two parameters—a neighbourhood radius (ϵ) and a minimum number of points per cluster. The former parameter complicates analysis since the appropriate cluster size cannot be known *a priori*. Instead, ϵ is often estimated through heuristics that differ from experiment to experiment; as an example, refs. [252–255] all use different methods to estimate ϵ. The use of DBSCAN is, thus, prone to introducing subjectivity and bias into the results of cluster analysis [161]. In contrast, HDBSCAN, the clustering algorithm used in this work, requires only the minimum number of points per cluster—a parameter which, in the case of ACE-2 and SARS-CoV-2 spike protein, is more readily estimated from biophysical studies described in the literature [115]. Despite these advantages, HDBSCAN is rarely mentioned in the context of SMLM cluster analysis, with most literature focusing on DBSCAN [95, 157, 240]. Therefore, the results in this chapter demonstrate the feasibility of using HDBSCAN for less subjective and more reproducible cluster analysis.

A notable observation in this chapter was that addition of SARS-CoV-2 spike protein

resulted in a decrease in cluster size and fewer ACE-2 receptors per cluster (Fig. 8.4). Such an observation contrasts those recorded in refs. [256, 257] where it was shown that addition of spike protein increased the cluster sizes of ACE-2 receptor, thereby concentrating the spike protein to facilitate cell-cell fusion and pathogenesis. However, a comparison between these findings and this chapter is challenging because only diffraction-limited microscopy was used in refs. [256, 257]. It may be possible that the large clusters detected in the negative control simply corresponded to the normal organisation of ACE-2 receptors—which may not have been detectable with diffraction-limited techniques—and that the clusters detected after adding the spike protein correspond to the concentrating of ACE-2 receptor and spike observed in refs. [256, 257]. It may also be possible that the ACE-2 receptor clusters in the negative control were a consequence of transfection-induced overexpression. As such, the negative control presented in this chapter may be improved by labelling endogenously expressed ACE-2 receptor in Calu-3 cells and carrying out cluster analysis to characterise the receptor organisation prior to infection. Finally, it is possible that the detected clusters do not correspond to true molecular clusters since the same fluorophore can undergo multiple photoswitching events [161]. Therefore, the accuracy of the cluster analysis, and the conclusions derived from them, may be improving through the use of algorithms that can correct for repeat localisations from the same molecule [258].

Another observation in this chapter was that the cluster characteristics were similar at all timepoints (Fig. 8.6). A possible explanation for this was that the timepoints did not accurately capture the timecourse of infection. For example, a previous investigation into the dynamics of SARS-CoV-2 infection using single-particle tracking found that viral binding and internalisation took place over the course of $\sim$ 2–3 minutes [259, 260]. Similarly, a separate study found that spike protein was detected in cells within five minutes [113]. The timepoints in this chapter, therefore, were unlikely to capture the internalisation of the virus and instead, were more likely to capture the continual entry of the SARS-CoV-2 spike protein into cells, resulting in similar clusters at all timepoints. To examine viral internalisation more accurately, shorter time intervals ought to have been used, an example of which could be 0 minutes–5 minutes with 1-minute intervals. Such a modification would allow for the acquisition of more accurate cluster data at

different stages of infection and internalisation.

The two-colour STORM and postprocessing methodology presented in this chapter could be expanded to a more detailed investigation of SARS-CoV-2 infection and internalisation. For example, other proteins involved in endocytosis—such as microtubules, dynamin, and clathrin—could be imaged with the spike protein in a two-colour STORM experiment. Applying the same analysis approach in this chapter could give quantitative insights into the spatial organisation of these proteins during infection, providing more detail into the mechanisms of SARS-CoV-2 infection. In addition, the biological model for viral infection could be improved through the use of virus-like particles or pseudoviruses [261, 262]. Both are designed to mimic the ability of live viruses to enter and infect host cells but are unable to replicate. Using this infection model better resembles the real biology of SARS-CoV-2 infection and internalisation compared to using purified spike protein. Therefore, repeating the two-colour STORM imaging and analysis presented in this chapter with this infection model could lead to more accurate and more meaningful quantitative insights into the spatial organisation of viral and host proteins during infection.

8.4.1 Conclusions

This chapter has presented an investigation into the internalisation of SARS-CoV-2 spike protein using two-colour STORM, colocalisation analysis, and cluster analysis. The cluster analysis approach presented advantages over current cluster analysis approaches through its use of HDBSCAN over DBSCAN. Similar cluster analysis results were observed from localisation data with and without denoising, demonstrating that SRD-Trans is unlikely to affect the overall outcome of postprocessing analyses. Meanwhile, two-colour STORM of ACE-2 receptor and SARS-CoV-2 spike protein revealed that the clusters of ACE-2 receptor—formed before the addition of spike protein—decreased in size following incubation with SARS-CoV-2 spike protein, possibly indicative of a spike-protein-induced sequestering and concentration of ACE-2 receptor. However, little difference in cluster characteristics was observed across the investigated infection timepoints of 5 minutes, 15 minutes, and 30 minutes. Therefore, further studies with earlier timepoints and with more biologically representative infection models are re-

quired for more accurate insights into the spatial organisation of ACE-2 receptor and SARS-CoV-2 during infection and internalisation.

9 Summary, Conclusions, and Future Directions

SMLM is a powerful technique with which to examine biological systems, delivering insights into the *in situ* spatial arrangement, organisation, and function of proteins at resolutions beyond that of conventional fluorescence microscopy methods. However, the application of SMLM to the life sciences still faces numerous challenges, as outlined in Introduction: 1.3 under aims 1–4. The research presented in this thesis has examined aspects of some of these challenges and attempted to address them.

The first aim of this thesis was to address the detrimental effect of sample drift in SMLM. Because current methods of drift correction introduce additional experimental complexity, hampering reproducibility and accessibility, a novel ROCS microscope design capable of negating drift purely through its mechanical construction was developed, as presented in Chapter 4. A systematic quantification of the lateral and axial drift was carried out for conventional widefield microscopy of sub-diffraction-limited fluorescent beads, demonstrating that the ROCS microscope exhibited negligible mechanical drift. Drift quantification from STORM of microtubules and NPCs revealed that the extent of the lateral drift of the ROCS was similar to the mean localisation precision of single-molecules. Furthermore, applying drift correction did not substantially alter the resolution of super-resolution images—a feature unachievable even when using a high-end commercial microscope—thus providing evidence that the ROCS was capable of negating drift in SMLM such that drift correction was unnecessary. Further work could focus on characterising the drift from PALM and DNA-PAINT image sequences, acquired with the ROCS microscope, to provide guidance to more users of SMLM.

The second aim of this thesis was to extend prior work on mirror-enhanced SMLM [40, 215] and implement further resolution enhancements. In Chapter 5, the resolution increase from mirror-enhanced STORM corroborated the results from previous literature, with higher localisation precision and resolution achieved using a reflective layer compared to conventional STORM. The results in Chapter 5 also presented some improvements compared to the original work. For example, the use of a fluorescent labelling

method with lower linkage error improved the resolution of NPCs compared to the original implementation. Further, the feasibility of mirror-enhanced STORM for imaging intracellular proteins in whole cells—absent in the original work—was demonstrated. In addition to adding a reflective surface, the application of SRDTrans, a denoising algorithm, resulted in further resolution improvement, highlighting the viability of using reflective surfaces as a photonic platform for increasing the resolution in SMLM. However, a key challenge that was identified was quantifying the degree of fluorescent enhancement and tuning this to maximise photon collection in SMLM. Further developments should focus on methods to quantify the degree of fluorescent enhancement when applying SMLM to intracellular proteins which would allow for greater control of image acquisition and for mirror-enhanced fluorescence to be exploited fully for resolution improvement.

The third aim was to assess the labelling efficiency of tagging intracellular proteins with nanobodies in live-cells and to compare the outcomes to those from conventional cell fixation and permeabilisation. The results in Chapter 6 demonstrated that vimentin could not be labelled with dye-conjugated nanobodies when cell fixation and permeabilisation occurred prior to the addition of nanobodies, with the expected filamentous structures unobservable in widefield or STORM images. In contrast, delivering nanobodies either by transfection with DNA encoding the nanobodies, or by introducing the nanobodies into cells via Streptolysin-O-induced membrane pores resulted in visualisation of the expected filamentous structures. Improvements to STORM of vimentin were observed by mutating the nanobodies such that the serine residue in the 7th position was mutated to a dye-reactive cysteine. Further investigations of nanobody mutants with different positions of the dye-reactive cysteine showed that Alexa Fluor 647 conjugated to a cysteine residue inserted at the N-terminus or C-terminus exhibited diminished photoswitching compared to Alexa Fluor 647 conjugated to a SNAP-tag. The experimental evidence in this chapter provides useful guidance to researchers looking to exploit fully the unique capabilities of fluorescent labelling with nanobodies for SMLM. Subsequent work from this chapter could focus on expanding the evaluation of STORM imaging outcomes and photoswitching from nanobodies with different dyes and with different dye-reactive cysteine locations.

The fourth aim was to extend previous work on SRDTrans [81]—a deep learning denoising algorithm—to provide a more comprehensive and systematic evaluation of its denoising capabilities. While a novel deep learning architecture (the vision transformer) for denoising was presented in the original work, there was insufficient guidance on best practices for training and applying the algorithm, insufficient evaluation of its ability to denoise different types of noise, and insufficient evidence of the generalisability of the algorithm to different biological samples and different microscopes. In Chapter 7, a substantial extension to the original work was presented, wherein best practices for training the denoising algorithm were established. Through a systematic evaluation of denoising image sequences of microtubules, NPCs, and ACE-2 receptors, it was demonstrated that denoising increases the number of detected molecules in SMLM, increasing the resolution. Further investigations revealed that SRDTrans exhibits excellent denoising when camera-based noise (shot noise, read noise, and amplification noise) is dominant but exhibits worse performance if noise from unspecifically bound fluorophores is high. Denoised localisation data also ought to be used with caution if estimations of single-molecule fluorescence intensity, background intensity, or localisation precision are critical for quantitative analyses since the denoising process changes these values relative to their equivalents without denoising. Further work arising from this chapter would address whether the vision transformer architecture presents improved denoising relative to other deep learning architectures. Such an evaluation would provide useful guidance to users of SMLM and researchers aiming to develop novel denoising algorithms for SMLM.

Finally, the fifth aim was to apply the various methodological developments to a range of biological samples. Nuclear pore complexes and microtubules were the primary focus for benchmarking. However, work was also focused on gaining insights into the spatial organisation of ACE-2 receptor and SARS-CoV-2 spike protein during infection and internalisation. In Chapter 8, results were presented from colocalisation analysis and cluster analysis from two-colour STORM localisations of the ACE-2 receptor and SARS-CoV-2 spike protein that had been acquired with the ROCS microscope. The cluster statistics revealed that cluster size and the number of ACE-2 receptors per cluster decrease upon addition of spike protein, and that cluster characteristics remained similar

at the 5-minute, 15-minute, and 30-minute infection timepoints. Further work into viral internalisation should focus on using the same experimental approach at more granular timepoints—for example, 1.5 minutes, 3 minutes, and 4.5 minutes—to capture more accurately the course of infection and internalisation. The work in this chapter may also benefit from the implementation of virus-like particles or pseudoviruses to provide a more realistic infection model.

Overall, the experimental work in this thesis has provided novel technology and new insights into aspects of SMLM that are expected to benefit current SMLM users, as well as provide useful guidance to researchers aiming to improve and develop methods in SMLM.

10 References

1. Abbe, E. Beiträge zur Theorie des Mikroskops und der mikroskopischen Wahrnehmung. (German) [Contributions to the Theory of Microscopes and Microscopic Perception]. *Archiv für Mikroskopische Anatomie* **9,** 413–468 (1873).

2. Galbraith, C. G. & Galbraith, J. A. Super-resolution microscopy at a glance. *Journal of Cell Science* **124,** 1607–1611 (2011).

3. Balzarotti, F., Eilers, Y., Gwosch, K. C., Gynnå, A. H., Westphal, V., Stefani, F. D., Elf, J. & Hell, S. W. Nanometer resolution imaging and tracking of fluorescent molecules with minimal photon fluxes. *Science* **355,** 606–612 (2017).

4. Schermelleh, L., Ferrand, A., Huser, T., Eggeling, C., Sauer, M., Biehlmaier, O. & Drummen, G. P. C. Super-resolution microscopy demystified. *Nature Cell Biology* **21,** 72–84 (2019).

5. Sigal, Y. M., Zhou, R. & Zhuang, X. Visualizing and discovering cellular structures with super-resolution microscopy. *Science* **361,** 880–887 (2018).

6. Chojnacki, J., Staudt, T., Glass, B., Bingen, P., Engelhardt, J., Anders, M., Schneider, J., Müller, B., Hell, S. W. & Kräusslich, H.-G. Maturation-Dependent HIV-1 Surface Protein Redistribution Revealed by Fluorescence Nanoscopy. *Science* **338,** 524–528 (2012).

7. Dani, A., Huang, B., Bergan, J., Dulac, C. & Zhuang, X. Superresolution Imaging of Chemical Synapses in the Brain. *Neuron* **68,** 843–856 (2010).

8. Nixon-Abell, J., Obara, C. J., Weigel, A. V., Li, D., Legant, W. R., Xu, C. S., Pasolli, H. A., Harvey, K., Hess, H. F., Betzig, E., Blackstone, C. & Lippincott-Schwartz, J. Increased spatiotemporal resolution reveals highly dynamic dense tubular matrices in the peripheral ER. *Science* **354,** aaf3928 (2016).

9. Gustafsson, M. G. L. Surpassing the lateral resolution limit by a factor of two using structured illumination microscopy. *Journal of Microscopy* **198,** 82–87 (2000).

10. Schermelleh, L., Carlton, P. M., Haase, S., Shao, L., Winoto, L., Kner, P., Burke, B., Cardoso, M. C., Agard, D. A., Gustafsson, M. G. L., Leonhardt, H. & Sedat, J. W. Subdiffraction Multicolor Imaging of the Nuclear Periphery with 3D Structured Illumination Microscopy. *Science* **320,** 1332–1336 (2008).

11. Wu, Y. & Shroff, H. Faster, sharper, and deeper: structured illumination microscopy for biological imaging. *Nature Methods* **15,** 1011–1019 (2018).

12. Tillberg, P. W., Chen, F., Piatkevich, K. D., Zhao, Y., Yu, C.-C. (, English, B. P., Gao, L., Martorell, A., Suk, H.-J., Yoshida, F., DeGennaro, E. M., Roossien, D. H., Gong, G., Seneviratne, U., Tannenbaum, S. R., Desimone, R., Cai, D. & Boyden, E. S. Protein-retention expansion microscopy of cells and tissues labeled using standard fluorescent proteins and antibodies. *Nature Biotechnology* **34,** 987–992 (2016).

13. Chang, J.-B., Chen, F., Yoon, Y.-G., Jung, E. E., Babcock, H., Kang, J. S., Asano, S., Suk, H.-J., Pak, N., Tillberg, P. W., Wassie, A. T., Cai, D. & Boyden, E. S. Iterative expansion microscopy. *Nature Methods* **14,** 593–599 (2017).

14. Hell, S. W. Far-Field Optical Nanoscopy. *Science* **316,** 1153–1158 (2007).

15. Hell, S. W., Jakobs, S. & Kastrup, L. Imaging and writing at the nanoscale with focused visible light through saturable optical transitions. *Applied Physics A* **77,** 859–860 (2003).

16. Hofmann, M., Eggeling, C., Jakobs, S. & Hell, S. W. Breaking the diffraction barrier in fluorescence microscopy at low light intensities by using reversibly photoswitchable proteins. *Proceedings of the National Academy of Sciences* **102,** 17565–17569 (2005).

17. Hell, S. W. & Wichmann, J. Breaking the diffraction resolution limit by stimulated emission: stimulated-emission-depletion fluorescence microscopy. *Optics Letters* **19,** 780–782 (1994).

18. Lelek, M., Gyparaki, M. T., Beliu, G., Schueder, F., Griffié, J., Manley, S., Jungmann, R., Sauer, M., Lakadamyali, M. & Zimmer, C. Single-molecule localization microscopy. *Nature Reviews Methods Primers* **1,** 1–27 (2021).

19. Rust, M. J., Bates, M. & Zhuang, X. Sub-diffraction-limit imaging by stochastic optical reconstruction microscopy (STORM). *Nature Methods* **3,** 793–796 (2006).

20. Heilemann, M., van de Linde, S., Schüttpelz, M., Kasper, R., Seefeldt, B., Mukherjee, A., Tinnefeld, P. & Sauer, M. Subdiffraction-Resolution Fluorescence Imaging with Conventional Fluorescent Probes. *Angewandte Chemie International Edition* **47,** 6172–6176 (2008).

21. Betzig, E., Patterson, G. H., Sougrat, R., Lindwasser, O. W., Olenych, S., Bonifacino, J. S., Davidson, M. W., Lippincott-Schwartz, J. & Hess, H. F. Imaging Intracellular Fluorescent Proteins at Nanometer Resolution. *Science* **313,** 1642–1645 (2006).

22. Hess, S. T., Girirajan, T. P. K. & Mason, M. D. Ultra-High Resolution Imaging by Fluorescence Photoactivation Localization Microscopy. *Biophysical Journal* **91,** 4258–4272 (2006).

23. Jungmann, R., Steinhauer, C., Scheible, M., Kuzyk, A., Tinnefeld, P. & Simmel, F. C. Single-Molecule Kinetics and Super-Resolution Microscopy by Fluorescence Imaging of Transient Binding on DNA Origami. *Nano Letters* **10,** 4756–4761 (2010).

24. van de Linde, S., Löschberger, A., Klein, T., Heidbreder, M., Wolter, S., Heilemann, M. & Sauer, M. Direct stochastic optical reconstruction microscopy with standard fluorescent probes. *Nature Protocols* **6,** 991–1009 (2011).

25. Sage, D., Kirshner, H., Pengo, T., Stuurman, N., Min, J., Manley, S. & Unser, M. Quantitative evaluation of software packages for single-molecule localization microscopy. *Nature Methods* **12,** 717–724 (2015).

26. Sage, D., Pham, T.-A., Babcock, H., Lukes, T., Pengo, T., Chao, J., Velmurugan, R., Herbert, A., Agrawal, A., Colabrese, S., Wheeler, A., Archetti, A., Rieger, B., Ober, R., Hagen, G. M., Sibarita, J.-B., Ries, J., Henriques, R., Unser, M. & Holden, S. Super-resolution fight club: assessment of 2D and 3D single-molecule localization microscopy software. *Nature Methods* **16,** 387–395 (2019).

27. Heo, M., Nord, A. L., Chamousset, D., van Rijn, E., Beaumont, H. J. E. & Pedaci, F. Impact of fluorescent protein fusions on the bacterial flagellar motor. *Scientific Reports* **7,** 12583 (2017).

28. Schneider, K. L., Wollman, A. J. M., Nyström, T. & Shashkova, S. Comparison of endogenously expressed fluorescent protein fusions behaviour for protein quality control and cellular ageing research. *Scientific Reports* **11,** 12819 (2021).

29. Huang, B., Bates, M. & Zhuang, X. Super-Resolution Fluorescence Microscopy. *Annual Review of Biochemistry* **78,** 993–1016 (2009).

30. Liu, S., Hoess, P. & Ries, J. Super-Resolution Microscopy for Structural Cell Biology. *Annual Review of Biophysics* **51,** 301–326 (2022).

31. Cnossen, J., Hinsdale, T., Thorsen, R. Ø., Siemons, M., Schueder, F., Jungmann, R., Smith, C. S., Rieger, B. & Stallinga, S. Localization microscopy at doubled precision with patterned illumination. *Nature Methods* **17,** 59–63 (2020).

32. Salerno, M., Bazzurro, V., Angeli, E., Bianchini, P., Roushenas, M., Pakravanan, K. & Diaspro, A. MINFLUX Nanoscopy: A "Brilliant" Technique Promising Major Breakthrough. *Microscopy Research and Technique* **88,** 1264–1272 (2025).

33. Prakash, K. At the molecular resolution with MINFLUX? *Philosophical Transactions of the Royal Society A: Mathematical, Physical and Engineering Sciences* **380,** 20200145 (2022).

34. Moal, E. L., Fort, E., Lévêque-Fort, S., Cordelières, F. P., Fontaine-Aupart, M.-P. & Ricolleau, C. Enhanced Fluorescence Cell Imaging with Metal-Coated Slides. *Biophysical Journal* **92,** 2150–2161 (2007).

35. Drexhage, K. H. Influence of a dielectric interface on fluorescence decay time. *Journal of Luminescence* **1-2,** 693–701 (1970).

36. Chance, R. R., Prock, A. & Silbey, R. Lifetime of an excited molecule near a metal mirror: Energy transfer in the Eu^{3+}/silver system. *The Journal of Chemical Physics* **60,** 2184–2185 (1974).

37. Chance, R. R., Prock, A. & Silbey, R. in *Advances in Chemical Physics* 1–65 (John Wiley & Sons, Ltd, Hoboken, NJ, USA, 1978).

38. Karedla, N., Chizhik, A. I., Gregor, I., Chizhik, A. M., Schulz, O. & Enderlein, J. Single-Molecule Metal-Induced Energy Transfer (smMIET): Resolving Nanometer Distances at the Single-Molecule Level. *ChemPhysChem* **15,** 705–711 (2014).

39. Karedla, N., Chizhik, A. M., Stein, S. C., Ruhlandt, D., Gregor, I., Chizhik, A. I. & Enderlein, J. Three-dimensional single-molecule localization with nanometer accuracy using Metal-Induced Energy Transfer (MIET) imaging. *The Journal of Chemical Physics* **148,** 204201 (2018).

40. Heil, H. S., Schreiber, B., Götz, R., Emmerling, M., Dabauvalle, M.-C., Krohne, G., Höfling, S., Kamp, M., Sauer, M. & Heinze, K. G. Sharpening emitter localization in front of a tuned mirror. *Light: Science & Applications* **7,** 99 (2018).

41. Fazekas, F. J., Shaw, T. R., Kim, S., Bogucki, R. A. & Veatch, S. L. A mean shift algorithm for drift correction in localization microscopy. *Biophysical Reports* **1,** 100008 (2021).

42. Carter, A. R., King, G. M., Ulrich, T. A., Halsey, W., Alchenberger, D. & Perkins, T. T. Stabilization of an optical microscope to 0.1 nm in three dimensions. *Applied Optics* **46,** 421–427 (2007).

43. McGorty, R., Kamiyama, D. & Huang, B. Active microscope stabilization in three dimensions using image correlation. *Optical Nanoscopy* **2,** 3 (2013).

44. Lee, S. H., Baday, M., Tjioe, M., Simonson, P. D., Zhang, R., Cai, E. & Selvin, P. R. Using fixed fiduciary markers for stage drift correction. *Optics Express* **20,** 12177–12183 (2012).

45. Mlodzianoski, M. J., Schreiner, J. M., Callahan, S. P., Smolková, K., Dlasková, A., Šantorová, J., Ježek, P. & Bewersdorf, J. Sample drift correction in 3D fluorescence photoactivation localization microscopy. *Optics Express* **19,** 15009–15019 (2011).

46. Wang, Y., Schnitzbauer, J., Hu, Z., Li, X., Cheng, Y., Huang, Z.-L. & Huang, B. Localization events-based sample drift correction for localization microscopy with redundant cross-correlation algorithm. *Optics Express* **22,** 15982–15991 (2014).

47. Fan, X., Gensch, T., Büldt, G., Zhang, Y., Musha, Z., Zhang, W., Roncarati, R. & Huang, R. Three dimensional drift control at nano-scale in single molecule localization microscopy. *Optics Express* **28,** 32750–32763 (2020).

48. Nieuwenhuizen, R. P. J., Lidke, K. A., Bates, M., Puig, D. L., Grünwald, D., Stallinga, S. & Rieger, B. Measuring image resolution in optical nanoscopy. *Nature Methods* **10,** 557–562 (2013).

49. Los, G. V., Encell, L. P., McDougall, M. G., Hartzell, D. D., Karassina, N., Zimprich, C., Wood, M. G., Learish, R., Ohana, R. F., Urh, M., Simpson, D., Mendez, J., Zimmerman, K., Otto, P., Vidugiris, G., Zhu, J., Darzins, A., Klaubert, D. H., Bulleit, R. F. & Wood, K. V. HaloTag: A Novel Protein Labeling Technology for Cell Imaging and Protein Analysis. *ACS Chemical Biology* **3,** 373–382 (2008).

50. Cole, N. B. Site-Specific Protein Labeling with SNAP-Tags. *Current protocols in protein science* **73,** 30.1.1–30.1.16 (2013).

51. Bates, M., Huang, B., Dempsey, G. T. & Zhuang, X. Multicolor Super-Resolution Imaging with Photo-Switchable Fluorescent Probes. *Science* **317,** 1749–1753 (2007).

52. Huang, B., Wang, W., Bates, M. & Zhuang, X. Three-Dimensional Super-Resolution Imaging by Stochastic Optical Reconstruction Microscopy. *Science* **319,** 810–813 (2008).

53. Snapp, E. Design and Use of Fluorescent Fusion Proteins in Cell Biology. *Current Protocols in Cell Biology* **27,** 21.4.1–21.4.13 (2005).

54. Thorn, K. Genetically encoded fluorescent tags. *Molecular Biology of the Cell* **28,** 848–857 (2017).

55. Couchman, J. R. Commercial Antibodies: The Good, Bad, and Really Ugly. *Journal of Histochemistry & Cytochemistry* **57,** 7–8 (2009).

56. Kalyuzhny, A. E. The Dark Side of the Immunohistochemical Moon: Industry. *Journal of Histochemistry & Cytochemistry* **57,** 1099–1101 (2009).

57. Hamers-Casterman, C., Atarhouch, T., Muyldermans, S., Robinson, G., Hammers, C., Songa, E. B., Bendahman, N. & Hammers, R. Naturally occurring antibodies devoid of light chains. *Nature* **363,** 446–448 (1993).

58. Muyldermans, S. Nanobodies: Natural Single-Domain Antibodies. *Annual Review of Biochemistry* **82,** 775–797 (2013).

59. Ries, J., Kaplan, C., Platonova, E., Eghlidi, H. & Ewers, H. A simple, versatile method for GFP-based super-resolution microscopy via nanobodies. *Nature Methods* **9,** 582–584 (2012).

60. Carrington, G., Tomlinson, D. & Peckham, M. Exploiting nanobodies and Affimers for superresolution imaging in light microscopy. *Molecular Biology of the Cell* **30,** 2737–2740 (2019).

61. Platonova, E., Winterflood, C. M., Junemann, A., Albrecht, D., Faix, J. & Ewers, H. Single-molecule microscopy of molecules tagged with GFP or RFP derivatives in mammalian cells using nanobody binders. *Methods* **88,** 89–97 (2015).

62. Mikhaylova, M., Cloin, B. M. C., Finan, K., van den Berg, R., Teeuw, J., Kijanka, M. M., Sokolowski, M., Katrukha, E. A., Maidorn, M., Opazo, F., Moutel, S., Vantard, M., Perez, F., van Bergen en Henegouwen, P. M. P., Hoogenraad, C. C., Ewers, H. & Kapitein, L. C. Resolving bundled microtubules using anti-tubulin nanobodies. *Nature Communications* **6,** 7933 (2015).

63. Pleiner, T., Bates, M., Trakhanov, S., Lee, C.-T., Schliep, J. E., Chug, H., Böhning, M., Stark, H., Urlaub, H. & Görlich, D. Nanobodies: site-specific labeling for super-resolution imaging, rapid epitope-mapping and native protein complex isolation. *eLife* **4,** e11349 (2015).

64. Hess, S. T., Gould, T. J., Gunewardene, M., Bewersdorf, J. & Mason, M. D. Ultra-High Resolution Imaging of Biomolecules by Fluorescence Photoactivation Localization Microscopy (FPALM). *Methods in molecular biology* **544,** 483–522 (2009).

65. Lee, K., Choi, S., Yang, C., Wu, H.-C. & Yu, J. Autofluorescence generation and elimination: a lesson from glutaraldehyde. *Chemical Communications* **49,** 3028–3030 (2013).

66. van Wee, R., Filius, M. & Joo, C. Completing the canvas: advances and challenges for DNA-PAINT super-resolution imaging. *Trends in biochemical sciences* **46,** 918–930 (2021).

67. Huang, F., Hartwich, T. M. P., Rivera-Molina, F. E., Lin, Y., Duim, W. C., Long, J. J., Uchil, P. D., Myers, J. R., Baird, M. A., Mothes, W., Davidson, M. W., Toomre, D. & Bewersdorf, J. Video-rate nanoscopy enabled by sCMOS camera-specific single-molecule localization algorithms. *Nature methods* **10,** 653–658 (2013).

68. Meiniel, W., Olivo-Marin, J.-C. & Angelini, E. D. Denoising of Microscopy Images: A Review of the State-of-the-Art, and a New Sparsity-Based Method. *IEEE Transactions on Image Processing* **27,** 3842–3856 (2018).

69. Laissue, P. P., Alghamdi, R. A., Tomancak, P., Reynaud, E. G. & Shroff, H. Assessing phototoxicity in live fluorescence imaging. *Nature Methods* **14,** 657–661 (2017).

70. Belthangady, C. & Royer, L. A. Applications, promises, and pitfalls of deep learning for fluorescence image reconstruction. *Nature Methods* **16,** 1215–1225 (2019).

71. Baddeley, D. & Bewersdorf, J. Biological Insight from Super-Resolution Microscopy: What We Can Learn from Localization-Based Images. *Annual Review of Biochemistry* **87,** 965–989 (2018).

72. Feng, Q., Song, Q., Yan, M., Huang, Z. L. & Wang, Z. MSDenoiser: Muti-step adaptive denoising framework for super-resolution image from single molecule localization microscopy. *Frontiers in Physics* **10** (2022).

73. Prince, S. J. D. *Understanding Deep Learning* (The MIT Press, Cambridge, MA, USA, 2025).

74. Weigert, M., Schmidt, U., Boothe, T., Müller, A., Dibrov, A., Jain, A., Wilhelm, B., Schmidt, D., Broaddus, C., Culley, S., Rocha-Martins, M., Segovia-Miranda, F., Norden, C., Henriques, R., Zerial, M., Solimena, M., Rink, J., Tomancak, P., Royer, L., Jug, F. & Myers, E. W. Content-aware image restoration: pushing the limits of fluorescence microscopy. *Nature Methods* **15,** 1090–1097 (2018).

75. Chen, J., Sasaki, H., Lai, H., Su, Y., Liu, J., Wu, Y., Zhovmer, A., Combs, C. A., Rey-Suarez, I., Chang, H.-Y., Huang, C. C., Li, X., Guo, M., Nizambad, S., Upadhyaya, A., Lee, S.-J. J., Lucas, L. A. G. & Shroff, H. Three-dimensional residual channel attention networks denoise and sharpen fluorescence microscopy image volumes. *Nature Methods* **18,** 678–687 (2021).

76. Wang, Z., Xie, Y. & Ji, S. Global voxel transformer networks for augmented microscopy. *Nature Machine Intelligence* **3,** 161–171 (2021).

77. Lehtinen, J., Munkberg, J., Hasselgren, J., Laine, S., Karras, T., Aittala, M. & Aila, T. *Noise2Noise: Learning Image Restoration without Clean Data* in *Proceedings of the 35th International Conference on Machine Learning* (PMLR, Stockholm, Sweden, 2018), 2965–2974.

78. Li, X., Zhang, G., Wu, J., Zhang, Y., Zhao, Z., Lin, X., Qiao, H., Xie, H., Wang, H., Fang, L. & Dai, Q. Reinforcing neuron extraction and spike inference in calcium imaging using deep self-supervised denoising. *Nature Methods* **18,** 1395–1400 (2021).

79. Krull, A., Buchholz, T.-O. & Jug, F. *Noise2Void - Learning Denoising From Single Noisy Images* in *2019 IEEE/CVF Conference on Computer Vision and Pattern Recognition* (IEEE, Long Beach, CA, USA, 2019), 2124–2132.

80. Huang, T., Li, S., Jia, X., Lu, H. & Liu, J. *Neighbor2Neighbor: Self-Supervised Denoising from Single Noisy Images* in *2021 IEEE/CVF Conference on Computer Vision and Pattern Recognition* (IEEE, Nashville, TN, USA, 2021), 14776–14785.

81. Li, X., Hu, X., Chen, X., Fan, J., Zhao, Z., Wu, J., Wang, H. & Dai, Q. Spatial redundancy transformer for self-supervised fluorescence image denoising. *Nature Computational Science* **3,** 1067–1080 (2023).

82. Ouyang, W., Aristov, A., Lelek, M., Hao, X. & Zimmer, C. Deep learning massively accelerates super-resolution localization microscopy. *Nature Biotechnology* **36,** 460–468 (2018).

83. Nehme, E., Weiss, L. E., Michaeli, T. & Shechtman, Y. Deep-STORM: super-resolution single-molecule microscopy by deep learning. *Optica* **5,** 458–464 (2018).

84. Möckl, L., Roy, A. R. & Moerner, W. E. Deep learning in single-molecule microscopy: fundamentals, caveats, and recent developments. *Biomedical Optics Express* **11,** 1633–1661 (2020).

85. Speiser, A., Müller, L.-R., Hoess, P., Matti, U., Obara, C. J., Legant, W. R., Kreshuk, A., Macke, J. H., Ries, J. & Turaga, S. C. Deep learning enables fast and dense single-molecule localization with high accuracy. *Nature methods* **18,** 1082–1090 (2021).

86. Luo, W., Li, Y., Urtasun, R. & Zemel, R. *Understanding the Effective Receptive Field in Deep Convolutional Neural Networks* in *Advances in Neural Information Processing Systems* **29** (Curran Associates, Inc., Barcelona, Spain, 2016).

87. Rahaman, N., Baratin, A., Arpit, D., Draxler, F., Lin, M., Hamprecht, F., Bengio, Y. & Courville, A. *On the Spectral Bias of Neural Networks* in *Proceedings of the 36th International Conference on Machine Learning* (PMLR, Long Beach, CA, USA, 2019), 5301–5310.

88. Chen, J., Lu, Y., Yu, Q., Luo, X., Adeli, E., Wang, Y., Lu, L., Yuille, A. L. & Zhou, Y. TransUNet: Transformers Make Strong Encoders for Medical Image Segmentation. *arXiv,* 2102.04306 (2021).

89. Zhou, H.-Y., Guo, J., Zhang, Y., Han, X., Yu, L., Wang, L. & Yu, Y. nnFormer: Volumetric Medical Image Segmentation via a 3D Transformer. *IEEE Transactions on Image Processing* **32,** 4036–4045 (2023).

90. Hatamizadeh, A., Tang, Y., Nath, V., Yang, D., Myronenko, A., Landman, B., Roth, H. & Xu, D. *UNETR: Transformers for 3D Medical Image Segmentation* in *Proceedings of the IEEE/CVF Winter Conference on Applications of Computer Vision* (IEEE, Lake Placid, NY, USA, 2021).

91. Dempsey, G. T., Vaughan, J. C., Chen, K. H., Bates, M. & Zhuang, X. Evaluation of fluorophores for optimal performance in localization-based super-resolution imaging. *Nature methods* **8,** 1027–1036 (2011).

92. Wegel, E., Göhler, A., Lagerholm, B. C., Wainman, A., Uphoff, S., Kaufmann, R. & Dobbie, I. M. Imaging cellular structures in super-resolution with SIM, STED and Localisation Microscopy: A practical comparison. *Scientific Reports* **6,** 27290 (2016).

93. Thevathasan, J. V., Kahnwald, M., Cieśliński, K., Hoess, P., Peneti, S. K., Reitberger, M., Heid, D., Kasuba, K. C., Hoerner, S. J., Li, Y., Wu, Y.-L., Mund, M., Matti, U., Pereira, P. M., Henriques, R., Nijmeijer, B., Kueblbeck, M., Sabinina, V. J., Ellenberg, J. & Ries, J. Nuclear pores as versatile reference standards for quantitative superresolution microscopy. *Nature Methods* **16,** 1045–1053 (2019).

94. Mund, M. & Ries, J. How good are my data? Reference standards in superresolution microscopy. *Molecular Biology of the Cell* **31,** 2093–2096 (2020).

95. Nieves, D. J., Pike, J. A., Levet, F., Williamson, D. J., Baragilly, M., Oloketuyi, S., de Marco, A., Griffié, J., Sage, D., Cohen, E. A. K., Sibarita, J.-B., Heilemann, M. & Owen, D. M. A framework for evaluating the performance of SMLM cluster analysis algorithms. *Nature Methods* **20,** 259–267 (2023).

96. Ledbetter, M. C. & Porter, K. R. A "MICROTUBULE" IN PLANT CELL FINE STRUCTURE. *The Journal of Cell Biology* **19,** 239–250 (1963).

97. Wade, R. H. On and Around Microtubules: An Overview. *Molecular Biotechnology* **43,** 177–191 (2009).

98. Whelan, D. R. & Bell, T. D. M. Image artifacts in Single Molecule Localization Microscopy: why optimization of sample preparation protocols matters. *Scientific Reports* **5,** 7924 (2015).

99. Kabachinski, G. & Schwartz, T. U. The nuclear pore complex – structure and function at a glance. *Journal of Cell Science* **128,** 423–429 (2015).

100. von Appen, A., Kosinski, J., Sparks, L., Ori, A., DiGuilio, A. L., Vollmer, B., Mackmull, M.-T., Banterle, N., Parca, L., Kastritis, P., Buczak, K., Mosalaganti, S., Hagen, W., Andres-Pons, A., Lemke, E. A., Bork, P., Antonin, W., Glavy, J. S., Bui, K. H. & Beck, M. In situ structural analysis of the human nuclear pore complex. *Nature* **526,** 140–143 (2015).

101. Hoelz, A., Debler, E. W. & Blobel, G. The Structure of the Nuclear Pore Complex. *Annual Review of Biochemistry* **80,** 613–643 (2011).

102. Szymborska, A., de Marco, A., Daigle, N., Cordes, V. C., Briggs, J. A. G. & Ellenberg, J. Nuclear Pore Scaffold Structure Analyzed by Super-Resolution Microscopy and Particle Averaging. *Science* **341,** 655–658 (2013).

103. Arrindell, J. & Desnues, B. Vimentin: from a cytoskeletal protein to a critical modulator of immune response and a target for infection. *Frontiers in Immunology* **14** (2023).

104. Danielsson, F., Peterson, M. K., Caldeira Araújo, H., Lautenschläger, F. & Gad, A. K. B. Vimentin Diversity in Health and Disease. *Cells* **7,** 147 (2018).

105. Maier, J., Traenkle, B. & Rothbauer, U. Real-time analysis of epithelial-mesenchymal transition using fluorescent single-domain antibodies. *Scientific Reports* **5,** 13402 (2015).

106. Ridge, K. M., Eriksson, J. E., Pekny, M. & Goldman, R. D. Roles of vimentin in health and disease. *Genes & Development* **36,** 391–407 (2022).

107. Virant, D., Traenkle, B., Maier, J., Kaiser, P. D., Bodenhöfer, M., Schmees, C., Vojnovic, I., Pisak-Lukáts, B., Endesfelder, U. & Rothbauer, U. A peptide tag-specific nanobody enables high-quality labeling for dSTORM imaging. *Nature Communications* **9,** 930 (2018).

108. Nunes Vicente, F., Lelek, M., Tinevez, J.-Y., Tran, Q. D., Pehau-Arnaudet, G., Zimmer, C., Etienne-Manneville, S., Giannone, G. & Leduc, C. Molecular organization and mechanics of single vimentin filaments revealed by super-resolution imaging. *Science Advances* **8,** eabm2696 (2022).

109. Mercer, J., Schelhaas, M. & Helenius, A. Virus Entry by Endocytosis. *Annual Review of Biochemistry* **79,** 803–833 (2010).

110. Jackson, C. B., Farzan, M., Chen, B. & Choe, H. Mechanisms of SARS-CoV-2 entry into cells. *Nature Reviews Molecular Cell Biology* **23,** 3–20 (2022).

111. Hoffmann, M., Kleine-Weber, H., Schroeder, S., Krüger, N., Herrler, T., Erichsen, S., Schiergens, T. S., Herrler, G., Wu, N.-H., Nitsche, A., Müller, M. A., Drosten, C. & Pöhlmann, S. SARS-CoV-2 Cell Entry Depends on ACE2 and TMPRSS2 and Is Blocked by a Clinically Proven Protease Inhibitor. *Cell* **181,** 271–280.e8 (2020).

112. Qu, B., Miskey, C., Gömer, A., Kleinert, R. D. V., Ibanez, S. C., Eberle, R., Ebenig, A., Postmus, D., Nocke, M. K., Herrmann, M., Itotia, T. K., Herrmann, S. T., Heinen, N., Höck, S., Hastert, F. D., von Rhein, C., Schürmann, C., Li, X., van Zandbergen, G., Widera, M., Ciesek, S., Schnierle, B. S., Tarr, A. W., Steinmann, E., Goffinet, C., Pfaender, S., Locker, J. K., Mühlebach, M. D., Todt, D. & Brown, R. J. P. TMPRSS2-mediated SARS-CoV-2 uptake boosts innate immune activation, enhances cytopathology, and drives convergent virus evolution. *Proceedings of the National Academy of Sciences of the United States of America* **121,** e2407437121 (2024).

113. Bayati, A., Kumar, R., Francis, V. & McPherson, P. S. SARS-CoV-2 infects cells after viral entry via clathrin-mediated endocytosis. *Journal of Biological Chemistry* **296,** 100306 (2021).

114. Zhao, M.-M., Yang, W.-L., Yang, F.-Y., Zhang, L., Huang, W.-J., Hou, W., Fan, C.-F., Jin, R.-H., Feng, Y.-M., Wang, Y.-C. & Yang, J.-K. Cathepsin L plays a key role in SARS-CoV-2 infection in humans and humanized mice and is a promising target for new drug development. *Signal Transduction and Targeted Therapy* **6,** 134 (2021).

115. Asor, R., Olerinyova, A., Burnap, S. A., Kushwah, M. S., Soltermann, F., Rudden, L. S., Hensen, M., Vasiljevic, S., Brun, J., Hill, M., Chang, L., Dejnirattisai, W., Supasa, P., Mongkolsapaya, J., Zhou, D., Stuart, D. I., Screaton, G. R., Degiacomi, M. T., Zitzmann, N., Benesch, J. L. P., Struwe, W. B. & Kukura, P. Oligomerization-driven avidity correlates with SARS-CoV-2 cellular binding and inhibition. *Proceedings of the National Academy of Sciences of the United States of America* **121,** e2403260121 (2024).

116. Valeur, B. & Berberan-Santos, M. N. *Molecular Fluorescence: Principles and Applications* 2nd Edition (John Wiley & Sons, Incorporated, Weinheim, Germany, 2013).

117. van de Linde, S. & Sauer, M. How to switch a fluorophore: from undesired blinking to controlled photoswitching. *Chemical Society Reviews* **43,** 1076–1087 (2014).

118. Heilemann, M., van de Linde, S., Mukherjee, A. & Sauer, M. Super-Resolution Imaging with Small Organic Fluorophores. *Angewandte Chemie International Edition* **48,** 6903–6908 (2009).

119. Dempsey, G. T., Bates, M., Kowtoniuk, W. E., Liu, D. R., Tsien, R. Y. & Zhuang, X. Photoswitching Mechanism of Cyanine Dyes. *Journal of the American Chemical Society* **131,** 18192–18193 (2009).

120. Herdly, L., Tinning, P. W., Geiser, A., Taylor, H., Gould, G. W. & van de Linde, S. Benchmarking Thiolate-Driven Photoswitching of Cyanine Dyes. *The Journal of Physical Chemistry B* **127,** 732–741 (2023).

121. Diekmann, R., Kahnwald, M., Schoenit, A., Deschamps, J., Matti, U. & Ries, J. Optimizing imaging speed and excitation intensity for single-molecule localization microscopy. *Nature Methods* **17,** 909–912 (2020).

122. Hecht, E. *Optics, Global Edition* 5th Edition (Pearson Education, Limited, Harlow, UK, 2016).

123. Lipson, A., Lipson, S. G. & Lipson, H. *Optical Physics* 4th Edition (Cambridge University Press, Cambridge, UK, 2010).

124. Shannon, C. Communication in the Presence of Noise. *Proceedings of the IRE* **37,** 10–21 (1949).

125. Kubitscheck, U. *Fluorescence Microscopy : From Principles to Biological Applications* 2nd Edition (John Wiley & Sons, Incorporated, Weinheim, Germany, 2017).

126. Zhang, B., Zerubia, J. & Olivo-Marin, J.-C. Gaussian approximations of fluorescence microscope point-spread function models. *Applied Optics* **46,** 1819–1829 (2007).

127. Smith, C. S., Joseph, N., Rieger, B. & Lidke, K. A. Fast, single-molecule localization that achieves theoretically minimum uncertainty. *Nature Methods* **7,** 373–375 (2010).

128. Mortensen, K. I., Churchman, L. S., Spudich, J. A. & Flyvbjerg, H. Optimized localization analysis for single-molecule tracking and super-resolution microscopy. *Nature Methods* **7,** 377–381 (2010).

129. Stallinga, S. & Rieger, B. Accuracy of the Gaussian Point Spread Function model in 2D localization microscopy. *Optics Express* **18,** 24461–24476 (2010).

130. Török, P., Higdon, P. D. & Wilson, T. Theory for confocal and conventional microscopes imaging small dielectric scatterers. *Journal of Modern Optics* **45,** 1681–1698 (1998).

131. Miora, R. H. D., Rohwer, E., Kielhorn, M., Sheppard, C., Bosman, G. & Heintzmann, R. Calculating point spread functions: methods, pitfalls, and solutions. *Optics Express* **32,** 27278–27302 (2024).

132. Price-Whelan, A. M. *et al.* The Astropy Project: Sustaining and Growing a Community-oriented Open-source Project and the Latest Major Release (v5.0) of the Core Package. *The Astrophysical Journal* **935,** 167 (2022).

133. van der Walt, S., Schönberger, J. L., Nunez-Iglesias, J., Boulogne, F., Warner, J. D., Yager, N., Gouillart, E. & Yu, T. scikit-image: image processing in Python. *PeerJ* **2,** e453 (2014).

134. Schindelin, J., Arganda-Carreras, I., Frise, E., Kaynig, V., Longair, M., Pietzsch, T., Preibisch, S., Rueden, C., Saalfeld, S., Schmid, B., Tinevez, J.-Y., White, D. J., Hartenstein, V., Eliceiri, K., Tomancak, P. & Cardona, A. Fiji: an open-source platform for biological-image analysis. *Nature Methods* **9,** 676–682 (2012).

135. Ovesný, M., Křížek, P., Borkovec, J., Švindrych, Z. & Hagen, G. M. ThunderSTORM: a comprehensive ImageJ plug-in for PALM and STORM data analysis and super-resolution imaging. *Bioinformatics* **30,** 2389–2390 (2014).

136. Huang, F., Schwartz, S. L., Byars, J. M. & Lidke, K. A. Simultaneous multiple-emitter fitting for single molecule super-resolution imaging. *Biomedical Optics Express* **2,** 1377–1393 (2011).

137. Ober, R. J., Ram, S. & Ward, E. S. Localization Accuracy in Single-Molecule Microscopy. *Biophysical Journal* **86,** 1185–1200 (2004).

138. Wasserman, L. *All of Statistics: A Concise Course in Statistical Inference* (Springer, New York, NY, 2004).

139. Abraham, A. V., Ram, S., Chao, J., Ward, E. S. & Ober, R. J. Quantitative study of single molecule location estimation techniques. *Optics express* **17,** 23352 (2009).

140. Chao, J., Ward, E. S. & Ober, R. J. Fisher information theory for parameter estimation in single molecule microscopy: tutorial. *Journal of the Optical Society of America A* **33,** B36–B57 (2016).

141. Huang, Z.-L., Zhu, H., Long, F., Ma, H., Qin, L., Liu, Y., Ding, J., Zhang, Z., Luo, Q. & Zeng, S. Localization-based super-resolution microscopy with an sCMOS camera. *Optics Express* **19,** 19156–19168 (2011).

142. O'Neill, R. Algorithm AS 47: Function Minimization Using a Simplex Procedure. *Journal of the Royal Statistical Society. Series C (Applied Statistics)* **20,** 338–345 (1971).

143. Press, W. H., Teukolsky, S. A., Vetterling, W. T. & Flannery, B. P. *Numerical Recipes The Art of Scientific Computing* 3rd Edition (Cambridge University Press, Cambridge, United Kingdom, 2007).

144. Laurence, T. A. & Chromy, B. A. Efficient maximum likelihood estimator fitting of histograms. *Nature Methods* **7,** 338–339 (2010).

145. Kay, S. M. *Fundamentals of statistical signal processing: estimation theory* (Prentice-Hall, Inc., Upper Saddle River, NJ, USA, 1993).

146. Thompson, R. E., Larson, D. R. & Webb, W. W. Precise Nanometer Localization Analysis for Individual Fluorescent Probes. *Biophysical Journal* **82,** 2775–2783 (2002).

147. van de Linde, S., Wolter, S., Heilemann, M. & Sauer, M. The effect of photoswitching kinetics and labeling densities on super-resolution fluorescence imaging. *Journal of Biotechnology* **149,** 260–266 (2010).

148. van Heel, M. Similarity measures between images. *Ultramicroscopy* **21,** 95–100 (1987).

149. Scheres, S. H. W. & Chen, S. Prevention of overfitting in cryo-EM structure determination. *Nature Methods* **9,** 853–854 (2012).

150. Rosenthal, P. B. & Henderson, R. Optimal Determination of Particle Orientation, Absolute Hand, and Contrast Loss in Single-particle Electron Cryomicroscopy. *Journal of Molecular Biology* **333,** 721–745 (2003).

151. Saxton, W. O. & Baumeister, W. The correlation averaging of a regularly arranged bacterial cell envelope protein. *Journal of Microscopy* **127,** 127–138 (1982).

152. van Heel, M. & Schatz, M. Fourier shell correlation threshold criteria. *Journal of Structural Biology* **151,** 250–262 (2005).

153. Zhao, W., Huang, X., Yang, J., Qu, L., Qiu, G., Zhao, Y., Wang, X., Su, D., Ding, X., Mao, H., Jiu, Y., Hu, Y., Tan, J., Zhao, S., Pan, L., Chen, L. & Li, H. Quantitatively mapping local quality of super-resolution microscopy by rolling Fourier ring correlation. *Light: Science & Applications* **12,** 298 (2023).

154. Ries, J. SMAP: a modular super-resolution microscopy analysis platform for SMLM data. *Nature Methods* **17,** 870–872 (2020).

155. Malkusch, S., Endesfelder, U., Mondry, J., Gelléri, M., Verveer, P. J. & Heilemann, M. Coordinate-based colocalization analysis of single-molecule localization microscopy data. *Histochemistry and Cell Biology* **137,** 1–10 (2012).

156. Erdelyi, M., Rees, E., Metcalf, D., Schierle, G. S. K., Dudas, L., Sinko, J., Knight, A. E. & Kaminski, C. F. Correcting chromatic offset in multicolor super-resolution localization microscopy. *Optics Express* **21,** 10978–10988 (2013).

157. Nieves, D. J. & Owen, D. M. Analysis methods for interrogating spatial organisation of single molecule localisation microscopy data. *The International Journal of Biochemistry & Cell Biology* **123,** 105749 (2020).

158. dos Santos, Á., Gough, R. E., Wang, L. & Toseland, C. P. *Measuring Nuclear Organization of Proteins with STORM Imaging and Cluster Analysis* in *Chromosome Architecture: Methods and Protocols* (ed Leake, M. C.) (Springer US, New York, NY, USA, 2022), 293–309.

159. Ripley, B. D. Modelling Spatial Patterns. *Journal of the Royal Statistical Society: Series B (Methodological)* **39,** 172–192 (1977).

160. Kiskowski, M. A., Hancock, J. F. & Kenworthy, A. K. On the Use of Ripley's K-Function and Its Derivatives to Analyze Domain Size. *Biophysical Journal* **97,** 1095–1103 (2009).

161. Khater, I. M., Nabi, I. R. & Hamarneh, G. A Review of Super-Resolution Single-Molecule Localization Microscopy Cluster Analysis and Quantification Methods. *Patterns* **1,** 100038 (2020).

162. Campello, R. J. G. B., Moulavi, D. & Sander, J. *Density-Based Clustering Based on Hierarchical Density Estimates* in *The 17th Pacific-Asia Conference on Knowl-*

edge Discovery and Data Mining (eds Pei, J., Tseng, V. S., Cao, L., Motoda, H. & Xu, G.) (Springer, Gold Coast, QLD, Australia, 2013), 160–172.

163. Barber, C. B., Dobkin, D. P. & Huhdanpaa, H. The quickhull algorithm for convex hulls. *ACM Transactions on Mathematical Software* **22,** 469–483 (1996).

164. Merchant, F. A. & Castleman, K. *Microscope Image Processing* 2nd Edition (Academic Press, Cambridge, MA, USA, 2022).

165. Jolliffe, I. T. & Cadima, J. Principal component analysis: a review and recent developments. *Philosophical Transactions of the Royal Society A: Mathematical, Physical and Engineering Sciences* **374,** 20150202 (2016).

166. Greenacre, M., Groenen, P. J. F., Hastie, T., D'Enza, A. I., Markos, A. & Tuzhilina, E. Principal component analysis. *Nature Reviews Methods Primers* **2,** 100 (2022).

167. Vaswani, A., Shazeer, N., Parmar, N., Uszkoreit, J., Jones, L., Gomez, A. N., Kaiser, Ł. u. & Polosukhin, I. *Attention is All you Need* in *31st Conference on Neural Information Processing Systems* **30** (Curran Associates, Inc., Long Beach, CA, USA, 2017).

168. Liu, Z., Lin, Y., Cao, Y., Hu, H., Wei, Y., Zhang, Z., Lin, S. & Guo, B. *Swin Transformer: Hierarchical Vision Transformer using Shifted Windows* in *2021 IEEE/CVF International Conference on Computer Vision* (Nashville, TN, USA, 2021), 9992–10002.

169. Deisenroth, M. P., Faisal, A. A. & Ong, C. S. *Mathematics for Machine Learning* (Cambridge University Press, Cambridge, UK, 2020).

170. Edelstein, A., Amodaj, N., Hoover, K., Vale, R. & Stuurman, N. Computer Control of Microscopes Using μManager. *Current Protocols in Molecular Biology* **92,** 14.20.1–14.20.17 (2010).

171. Berrow, N. S., Alderton, D., Sainsbury, S., Nettleship, J., Assenberg, R., Rahman, N., Stuart, D. I. & Owens, R. J. A versatile ligation-independent cloning method suitable for high-throughput expression screening applications. *Nucleic Acids Research* **35,** e45 (2007).

172. Eyssen, L. E., Ramadurai, S., Abdelkarim, S., Buckle, I., Cornish, K., Lin, H., Jones, A., Stephens, G. & Owens, R. From Llama to Nanobody: A Streamlined Workflow for the Generation of Functionalised VHHs. *Bio-protocol* **14,** e4962 (2025).

173. Jimenez, A., Friedl, K. & Leterrier, C. About samples, giving examples: Optimized Single Molecule Localization Microscopy. *Methods* **174,** 100–114 (2020).

174. Abdel Ghani, E. M., Weis, S., Walev, I., Kehoe, M., Bhakdi, S. & Palmer, M. Streptolysin O: Inhibition of the Conformational Change during Membrane Binding of the Monomer Prevents Oligomerization and Pore Formation. *Biochemistry* **38,** 15204–15211 (1999).

175. Substoontorn, P. Autofocus Manual. https://micro-manager.org/Autofocus_manual. 2007.

176. Izeddin, I., Boulanger, J., Racine, V., Specht, C. G., Kechkar, A., Nair, D., Triller, A., Choquet, D., Dahan, M. & Sibarita, J. B. Wavelet analysis for single molecule localization microscopy. *Optics Express* **20,** 2081–2095 (2012).

177. Tang, M. frc-comp-analysis. *Github repository.* https://github.com/Matthewt303/frc-comp-analysis. 2025.

178. Bittel, A. M., Nickerson, A., Saldivar, I. S., Dolman, N. J., Nan, X. & Gibbs, S. L. Methodology for Quantitative Characterization of Fluorophore Photoswitching to Predict Superresolution Microscopy Image Quality. *Scientific Reports* **6,** 29687 (2016).

179. Tang, M. photophysical-analysis. *Github repository.* https://github.com/Matthewt303/photophysical-analysis. 2026.

180. Tang, M. SMLM-cluster-analysis. *Github repository.* https://github.com/Matthewt303/SMLM-cluster-analysis. 2026.

181. Otsu, N. A Threshold Selection Method from Gray-Level Histograms. *IEEE Transactions on Systems, Man, and Cybernetics* **9,** 62–66 (1979).

182. Kingma, D. P. & Ba, J. *Adam: A Method for Stochastic Optimization* in *International Conference on Learning Representations (ICLR)* (San Diego, CA, USA, 2015).

183. Tang, M. dn-photophys-analysis. *Github repository* https://github.com/Matthewt303/dn-photophys-analysis. 2026.

184. Harris, C. R., Millman, K. J., van der Walt, S. J., Gommers, R., Virtanen, P., Cournapeau, D., Wieser, E., Taylor, J., Berg, S., Smith, N. J., Kern, R., Picus, M., Hoyer, S., van Kerkwijk, M. H., Brett, M., Haldane, A., del Río, J. F., Wiebe, M., Peterson, P., Gérard-Marchant, P., Sheppard, K., Reddy, T., Weckesser, W., Abbasi, H., Gohlke, C. & Oliphant, T. E. Array programming with NumPy. *Nature* **585,** 357–362 (2020).

185. Hunter, J. D. Matplotlib: A 2D Graphics Environment. *Computing in Science & Engineering* **9,** 90–95 (2007).

186. OpenCV Team. Open Source Computer Vision Library. *Github repository.* https://github.com/opencv/opencv. 2025.

187. Virtanen, P., Gommers, R., Oliphant, T. E., Haberland, M., Reddy, T., Cournapeau, D., Burovski, E., Peterson, P., Weckesser, W., Bright, J., van der Walt, S. J., Brett, M., Wilson, J., Millman, K. J., Mayorov, N., Nelson, A. R. J., Jones, E., Kern, R., Larson, E., Carey, C. J., Polat, İ., Feng, Y., Moore, E. W., VanderPlas, J., Laxalde, D., Perktold, J., Cimrman, R., Henriksen, I., Quintero, E. A., Harris, C. R., Archibald, A. M., Ribeiro, A. H., Pedregosa, F. & van Mulbregt, P. SciPy 1.0: fundamental algorithms for scientific computing in Python. *Nature Methods* **17,** 261–272 (2020).

188. Pedregosa, F., Varoquaux, G., Gramfort, A., Michel, V., Thirion, B., Grisel, O., Blondel, M., Prettenhofer, P., Weiss, R., Dubourg, V., Vanderplas, J., v Passos, A., Cournapeau, D., Brucher, M., Perrot, M. & Duchesnay, É. Scikit-learn: Machine Learning in Python. *Journal of Machine Learning Research* **12,** 2825–2830 (2011).

189. Waskom, M. L. seaborn: statistical data visualization. *Journal of Open Source Software* **6,** 3021 (2021).

190. Lam, S. K., Pitrou, A. & Seibert, S. *Numba: a LLVM-based Python JIT compiler* in *Proceedings of the Second Workshop on the LLVM Compiler Infrastructure in HPC* (ACM, Austin, TX, USA, 2015), 1–6.

191. McKinney, W. *Data Structures for Statistical Computing in Python* in *Proceedings of the 9th Python in Science Conference* (SciPy Proceedings, Austin, TX, USA, 2010), 56–61.

192. Gohlke, C. Tifffile. *Github repository.* https://github.com/cgohlke/tifffile. 2025.

193. Richardson, N., Cook, I., Crane, N., Dunnington, D., François, R., Keane, J., Mecum, B., Moldovan-Grünfeld, D., Ooms, J., Wujciak-Jens, J. & Apache Arrow. *arrow: Integration to 'Apache' 'Arrow'* (2025).

194. Ingram, S. RipleyK. *Github repository.* https://github.com/SamPIngram/RipleyK. 2025.

195. Paszke, A., Gross, S., Massa, F., Lerer, A., Bradbury, J., Chanan, G., Killeen, T., Lin, Z., Gimelshein, N., Antiga, L., Desmaison, A., Köpf, A., Yang, E., DeVito, Z., Raison, M., Tejani, A., Chilamkurthy, S., Steiner, B., Fang, L., Bai, J. & Chintala, S. *PyTorch: An Imperative Style, High-Performance Deep Learning Library* 2019.

196. Wightman, R. PyTorch Image Models. *Github repository.* https://github.com/huggingface/pytorch-image-models. 2019.

197. Rogozhnikov, A. *Einops: Clear and Reliable Tensor Manipulations with Einstein-like Notation* in *International Conference on Learning Representations* (Online, 2022).

198. Qiu, H., Tang, M. C., Roberts, S. K., Li, G., Su, R., Martin-Fernandez, M. L., Clarke, D. T., Liu, S., Liu, X. & Wang, L. Reinforced optical cage systems enable drift-free single-molecule localization microscopy. *Communications Engineering* (2025).

199. Chahar, A. S. & Pal, P. Study on various properties of reinforced concrete – A review. *Materials Today: Proceedings. International Conference on Advances in Construction Materials and Structures* **65,** 597–602 (2022).

200. Hemami, H. A General Framework for Rigid Body Dynamics, Stability, and Control. *Journal of Dynamic Systems, Measurement, and Control* **124,** 241–251 (2002).

201. Zehrer, A. C., Martin-Villalba, A., Diederich, B. & Ewers, H. An open-source, high resolution, automated fluorescence microscope. *eLife* **12** (2024).

202. Xu, J., Ma, H. & Liu, Y. Stochastic Optical Reconstruction Microscopy (STORM). *Current Protocols in Cytometry* **81,** 12.46.1–12.46.27 (2017).

203. Ma, H., Fu, R., Xu, J. & Liu, Y. A simple and cost-effective setup for super-resolution localization microscopy. *Scientific Reports* **7,** 1542 (2017).

204. Alsamsam, M. N., Kopūstas, A., Jurevičiūtė, M. & Tutkus, M. The miEye: Benchtop super-resolution microscope with cost-effective equipment. *HardwareX* **12,** e00368 (2022).

205. Shroff, H., Galbraith, C. G., Galbraith, J. A., White, H., Gillette, J., Olenych, S., Davidson, M. W. & Betzig, E. Dual-color superresolution imaging of genetically expressed probes within individual adhesion complexes. *Proceedings of the National Academy of Sciences* **104,** 20308–20313 (2007).

206. Brown, T. A., Tkachuk, A. N., Shtengel, G., Kopek, B. G., Bogenhagen, D. F., Hess, H. F. & Clayton, D. A. Superresolution Fluorescence Imaging of Mitochondrial Nucleoids Reveals Their Spatial Range, Limits, and Membrane Interaction. *Molecular and Cellular Biology* **31,** 4994–5010 (2011).

207. Sengupta, P., Jovanovic-Talisman, T., Skoko, D., Renz, M., Veatch, S. L. & Lippincott-Schwartz, J. Probing protein heterogeneity in the plasma membrane using PALM and pair correlation analysis. *Nature Methods* **8,** 969–975 (2011).

208. Schnitzbauer, J., Strauss, M. T., Schlichthaerle, T., Schueder, F. & Jungmann, R. Super-resolution microscopy with DNA-PAINT. *Nature Protocols* **12,** 1198–1228 (2017).

209. Lee, J., Park, S., Kang, W. & Hohng, S. Accelerated super-resolution imaging with FRET-PAINT. *Molecular Brain* **10,** 63 (2017).

210. Piantanida, L., S. Li, I. T. & L. Hughes, W. Advancements in DNA-PAINT: applications and challenges in biological imaging and nanoscale metrology. *Nanoscale* **17,** 14016–14034 (2025).

211. Strauss, S. & Jungmann, R. Up to 100-fold speedup and multiplexing in optimized DNA-PAINT. *Nature methods* **17,** 789–791 (2020).

212. Bauch, M., Toma, K., Toma, M., Zhang, Q. & Dostalek, J. Plasmon-Enhanced Fluorescence Biosensors: a Review. *Plasmonics* **9,** 781–799 (2014).

213. Chance, R. R., Prock, A. & Silbey, R. Lifetime of an emitting molecule near a partially reflecting surface. *The Journal of Chemical Physics* **60,** 2744–2748 (1974).

214. Logeeswaran VJ, Kobayashi, N. P., Islam, M. S., Wu, W., Chaturvedi, P., Fang, N. X., Wang, S. Y. & Williams, R. S. Ultrasmooth Silver Thin Films Deposited with a Germanium Nucleation Layer. *Nano Letters* **9,** 178–182 (2009).

215. Heil, H. S. *Sharpening Super-Resolution by Single Molecule Localization Microscopy in Front of a Tuned Mirror.* PhD thesis (Bayerische Julius-Maximilians-Universitaet Wuerzburg, Germany, 2020).

216. Kriukova, E., LaRochelle, E., Pfefer, T. J., Kanniyappan, U., Gioux, S., Pogue, B., Ntziachristos, V. & Gorpas, D. Impact of signal-to-noise ratio and contrast definition on the sensitivity assessment and benchmarking of fluorescence molecular imaging systems. *Journal of Biomedical Optics* **30,** S13703 (2024).

217. Thermo Fisher Scientific Inc. Fluorescence quantum yields (QY) and lifetimes (τ) for Alexa Fluor dyes—Table 1.5 - UK https://www.thermofisher.com/uk/en/home/references/molecular-probes-the-handbook/tables/fluorescence-quantum-yields-and-lifetimes-for-alexa-fluor-dyes.html. 2015.

218. Thermo Fisher Scientific Inc. Fluorescence Microscopy Accessories and Reference Standards—Section 23.1 - UK https://www.thermofisher.com/uk/en/home/references/molecular-probes-the-handbook/tools-for-fluorescence-applications-including-reference-standards-and-optical-filters/fluorescence-microscopy-reference-standards-and-antifade-reagents.html. 2015.

219. Lin, Y., Long, J. J., Huang, F., Duim, W. C., Kirschbaum, S., Zhang, Y., Schroeder, L. K., Rebane, A. A., Velasco, M. G. M., Virrueta, A., Moonan, D. W., Jiao, J., Hernandez, S. Y., Zhang, Y. & Bewersdorf, J. Quantifying and Optimizing Single-Molecule Switching Nanoscopy at High Speeds. *PLOS ONE* **10,** e0128135 (2015).

220. Lambert, T. J. FPbase: a community-editable fluorescent protein database. *Nature Methods* **16,** 277–278 (2019).

221. FPbase. FPbase Fluorescence Spectra Viewer for Chroma ET700/75m and Alexa Fluor 647. https://www.fpbase.org/spectra/?s=306,307,345&showY=0&

showX=1&showGrid=0&areaFill=1&logScale=0&scaleEC=0&scaleQY=0&shareTooltip=1&palette=wavelength&xMin=400&xMax=750.

222. FPbase. FPbase Fluorescence Spectra Viewer for Chroma ET690/50m and Alexa Fluor 647. https://www.fpbase.org/spectra/?s=306,307,715&showY=0&showX=1&showGrid=0&areaFill=1&logScale=0&scaleEC=0&scaleQY=0&shareTooltip=1&palette=wavelength&xMin=400&xMax=750.

223. Sahl, S. J., Hell, S. W. & Jakobs, S. Fluorescence nanoscopy in cell biology. *Nature Reviews Molecular Cell Biology* **18,** 685–701 (2017).

224. Früh, S. M., Matti, U., Spycher, P. R., Rubini, M., Lickert, S., Schlichthaerle, T., Jungmann, R., Vogel, V., Ries, J. & Schoen, I. Site-Specifically-Labeled Antibodies for Super-Resolution Microscopy Reveal In Situ Linkage Errors. *ACS Nano* **15,** 12161–12170 (2021).

225. Krohne, G., Franke, W. W. & Scheer, U. The major polypeptides of the nuclear pore complex. *Experimental Cell Research* **116,** 85–102 (1978).

226. Löschberger, A., van de Linde, S., Dabauvalle, M.-C., Rieger, B., Heilemann, M., Krohne, G. & Sauer, M. Super-resolution imaging visualizes the eightfold symmetry of gp210 proteins around the nuclear pore complex and resolves the central channel with nanometer resolution. *Journal of Cell Science* **125,** 570–575 (2012).

227. Leduc, C., Salles, A., Shorte, S. L. & Etienne-Manneville, S. Imaging Intermediate Filaments and Microtubules with 2-dimensional Direct Stochastic Optical Reconstruction Microscopy. *Journal of Visualized Experiments : JoVE,* 57087 (2018).

228. Li, Y., Almassalha, L. M., Chandler, J. E., Zhou, X., Stypula-Cyrus, Y. E., Hujsak, K. A., Roth, E. W., Bleher, R., Subramanian, H., Szleifer, I., Dravid, V. P. & Backman, V. The effects of chemical fixation on the cellular nanostructure. *Experimental Cell Research* **358,** 253–259 (2017).

229. Meade, A. D., Clarke, C., Draux, F., Sockalingum, G. D., Manfait, M., Lyng, F. M. & Byrne, H. J. Studies of chemical fixation effects in human cell lines using Raman microspectroscopy. *Analytical and Bioanalytical Chemistry* **396,** 1781–1791 (2010).

230. Hobro, A. J. & Smith, N. I. An evaluation of fixation methods: Spatial and compositional cellular changes observed by Raman imaging. *Vibrational Spectroscopy* **91,** 31–45 (2017).

231. Uno, S., Kamiya, M., Yoshihara, T., Sugawara, K., Okabe, K., Tarhan, M. C., Fujita, H., Funatsu, T., Okada, Y., Tobita, S. & Urano, Y. A spontaneously blinking fluorophore based on intramolecular spirocyclization for live-cell super-resolution imaging. *Nature Chemistry* **6,** 681–689 (2014).

232. Tyson, J., Hu, K., Zheng, S., Kidd, P., Dadina, N., Chu, L., Toomre, D., Bewersdorf, J. & Schepartz, A. Extremely Bright, Near-IR Emitting Spontaneously Blinking Fluorophores Enable Ratiometric Multicolor Nanoscopy in Live Cells. *ACS Central Science* **7,** 1419–1426 (2021).

233. Holland, K. L., Plutkis, S. E., Daugird, T. A., Sau, A., Grimm, J. B., English, B. P., Zheng, Q., Dave, S., Rahman, F., Xie, L., Dong, P., Tkachuk, A. N., Brown, T. A., Singer, R. H., Liu, Z., Galbraith, C. G., Musser, S. M., Legant, W. R. & Lavis, L. D. A series of spontaneously blinking dyes for super-resolution microscopy. *bioRxiv,* 2024.02.23.581625 (2024).

234. Basak, S., Inamdar, K., Pollak, Y. G., Albert, L., Jans, D. C., Jakobs, S., Enderlein, J., Tsukanov, R. & Opazo, F. Self-blinking dye restores efficient use of nanobodies in single-molecule localization microscopy. *bioRxiv* (2025).

235. Bates, T. A., Gurmessa, S. K., Weinstein, J. B., Trank-Greene, M., Wrynla, X. H., Anastas, A., Anley, T. W., Hinchliff, A., Shinde, U., Burke, J. E. & Tafesse, F. G. Biolayer interferometry for measuring the kinetics of protein–protein interactions and nanobody binding. *Nature Protocols* **20,** 861–883 (2025).

236. Saurabh, S., Maji, S. & Bruchez, M. P. Evaluation of sCMOS cameras for detection and localization of single Cy5 molecules. *Optics Express* **20,** 7338–7349 (2012).

237. Beier, H. T. & Ibey, B. L. Experimental Comparison of the High-Speed Imaging Performance of an EM-CCD and sCMOS Camera in a Dynamic Live-Cell Imaging Test Case. *PLOS ONE* **9,** e84614 (2014).

238. Li, X., Hu, X. & Chen, X. SRDTrans dataset: experimentally obtained SMLM data. *Zenodo Dataset.* 10.5281/zenodo.7813185. 2023.

239. Odena, A., Dumoulin, V. & Olah, C. Deconvolution and Checkerboard Artifacts. *Distill* **1,** e3 (2016).

240. Panconi, L., Owen, D. M. & Griffié, J. Cluster analysis for localisation-based data sets: dos and don'ts when quantifying protein aggregates. *Frontiers in Bioinformatics* **3** (2023).

241. Szalai, A. M., Siarry, B., Lukin, J., Williamson, D. J., Unsain, N., Cáceres, A., Pilo-Pais, M., Acuna, G., Refojo, D., Owen, D. M., Simoncelli, S. & Stefani, F. D. Three-dimensional total-internal reflection fluorescence nanoscopy with nanometric axial resolution by photometric localization of single molecules. *Nature Communications* **12,** 517 (2021).

242. Thorsen, R. Ø., Hulleman, C. N., Rieger, B. & Stallinga, S. Photon efficient orientation estimation using polarization modulation in single-molecule localization microscopy. *Biomedical Optics Express* **13,** 2835–2858 (2022).

243. Ester, M., Kriegel, H.-P., Sander, J. & Xu, X. *A density-based algorithm for discovering clusters in large spatial databases with noise* in *Proceedings of the Second International Conference on Knowledge Discovery and Data Mining* (AAAI Press, Portland, OR, USA, 1996), 226–231.

244. Culley, S., Albrecht, D., Jacobs, C., Pereira, P. M., Leterrier, C., Mercer, J. & Henriques, R. Quantitative mapping and minimization of super-resolution optical imaging artifacts. *Nature Methods* **15,** 263–266 (2018).

245. Marsh, R. J., Costello, I., Gorey, M.-A., Ma, D., Huang, F., Gautel, M., Parsons, M. & Cox, S. Sub-diffraction error mapping for localisation microscopy images. *Nature Communications* **12,** 5611 (2021).

246. Wang, S., Moffitt, J. R., Dempsey, G. T., Xie, X. S. & Zhuang, X. Characterization and development of photoactivatable fluorescent proteins for single-molecule–based superresolution imaging. *Proceedings of the National Academy of Sciences* **111,** 8452–8457 (2014).

247. Chung, K. K., Zhang, Z., Kidd, P., Zhang, Y., Williams, N. D., Rollins, B., Yang, Y., Lin, C., Baddeley, D. & Bewersdorf, J. Fluorogenic DNA-PAINT for faster, low-background super-resolution imaging. *Nature methods* **19,** 554–559 (2022).

248. Wang, Y., Pinkard, H., Khwaja, E., Zhou, S., Waller, L. & Huang, B. Image denoising for fluorescence microscopy by self-supervised transfer learning. *bioRxiv,* 2021.02.01.429188 (2021).

249. Liu, J., Teng, Q., Ma, Q. & Jiang, J. FM2S: Towards Spatially-Correlated Noise Modeling in Zero-Shot Fluorescence Microscopy Image Denoising. *arXiv,* 2412.10031 (2025).

250. Pageon, S. V., Nicovich, P. R., Mollazade, M., Tabarin, T. & Gaus, K. ClusDoC: a combined cluster detection and colocalization analysis for single-molecule localization microscopy data. *Molecular Biology of the Cell* **27,** 3627–3636 (2016).

251. Malkusch, S. & Heilemann, M. Extracting quantitative information from single-molecule super-resolution imaging data with LAMA – LocAlization Microscopy Analyzer. *Scientific Reports* **6,** 34486 (2016).

252. Roberts, S. K., Hirsch, M., McStea, A., Zanetti-Domingues, L. C., Clarke, D. T., Claus, J., Parker, P. J., Wang, L. & Martin-Fernandez, M. L. Cluster Analysis of Endogenous HER2 and HER3 Receptors in SKBR3 Cells. *Bio-protocol* **8,** e3096 (2018).

253. Harwardt, M.-L. I. E., Schröder, M. S., Li, Y., Malkusch, S., Freund, P., Gupta, S., Janjic, N., Strauss, S., Jungmann, R., Dietz, M. S. & Heilemann, M. Single-Molecule Super-Resolution Microscopy Reveals Heteromeric Complexes of MET and EGFR upon Ligand Activation. *International Journal of Molecular Sciences* **21,** 2803 (2020).

254. Marenda, M., Lazarova, E., van de Linde, S., Gilbert, N. & Michieletto, D. Parameter-free molecular super-structures quantification in single-molecule localization microscopy. *Journal of Cell Biology* **220,** e202010003 (2021).

255. dos Santos, Á., Rollins, D. E., Hari-Gupta, Y., McArthur, H., Du, M., Ru, S. Y. Z., Pidlisna, K., Stranger, A., Lorgat, F., Lambert, D., Brown, I., Howland, K., Aaron, J., Wang, L., Ellis, P. J. I., Chew, T.-L., Martin-Fernandez, M. L., Pyne, A. L. B. & Toseland, C. P. Autophagy receptor NDP52 alters DNA conformation to modulate RNA polymerase II transcription. *Nature Communications* **14,** 2855 (2023).

256. Sanders, D. W., Jumper, C. C., Ackerman, P. J., Bracha, D., Donlic, A., Kim, H., Kenney, D., Castello-Serrano, I., Suzuki, S., Tamura, T., Tavares, A. H., Saeed, M., Holehouse, A. S., Ploss, A., Levental, I., Douam, F., Padera, R. F., Levy, B. D. & Brangwynne, C. P. SARS-CoV-2 requires cholesterol for viral entry and pathological syncytia formation. *eLife* **10,** e65962 (2021).

257. Zhang, Q., Tang, W., Stancanelli, E., Jung, E., Syed, Z., Pagadala, V., Saidi, L., Chen, C. Z., Gao, P., Xu, M., Pavlinov, I., Li, B., Huang, W., Chen, L., Liu, J., Xie, H., Zheng, W. & Ye, Y. Host heparan sulfate promotes ACE2 super-cluster assembly and enhances SARS-CoV-2-associated syncytium formation. *Nature Communications* **14,** 5777 (2023).

258. Bohrer, C. H., Yang, X., Thakur, S., Weng, X., Tenner, B., McQuillen, R., Ross, B., Wooten, M., Chen, X., Zhang, J., Roberts, E., Lakadamyali, M. & Xiao, J. A pairwise distance distribution correction (DDC) algorithm to eliminate blinking-caused artifacts in SMLM. *Nature Methods* **18,** 669–677 (2021).

259. Zhang, Y., Zhang, X., Li, Z., Zhao, W., Yang, H., Zhao, S., Tang, D., Zhang, Q., Li, Z., Liu, H., Li, H., Li, B., Lappalainen, P., Xu, T., Cui, Z. & Jiu, Y. Single particle tracking reveals SARS-CoV-2 regulating and utilizing dynamic filopodia for viral invasion. *Science Bulletin* **68,** 2210–2224 (2023).

260. Atemin, A., Ivanova, A., Peppel, W., Stamatov, R., Gallegos, R., Durden, H., Uzunova, S., Vershinin, M. D., Saffarian, S. & Stoynov, S. S. Kinetic Landscape of Single Virus-like Particles Highlights the Efficacy of SARS-CoV-2 Internalization. *Viruses* **16,** 1341 (2024).

261. Nooraei, S., Bahrulolum, H., Hoseini, Z. S., Katalani, C., Hajizade, A., Easton, A. J. & Ahmadian, G. Virus-like particles: preparation, immunogenicity and their roles as nanovaccines and drug nanocarriers. *Journal of Nanobiotechnology* **19,** 59 (2021).

262. Thimmiraju, S. R., Kimata, J. T. & Pollet, J. Pseudoviruses, a safer toolbox for vaccine development against enveloped viruses. *Expert Review of Vaccines* **23,** 174–185 (2024).

263. Goodman, J. W. *Introduction to Fourier Optics* 4th Edition (W.H. Freeman and Company, New York, NY, USA, 2017).

264. Riley, K. F., Hobson, M. P. & Bence, S. J. *Mathematical Methods for Physics and Engineering: A Comprehensive Guide* 3rd Edition (Cambridge University Press, Cambridge, United Kingdom, 2006).

265. Strauss, M. T. Picasso-server: a community-based, open-source processing framework for super-resolution data. *Communications Biology* **5,** 930 (2022).

A Appendix

A.1 Selected Mathematical Definitions

In Chapter 2: Theory, several mathematical operations and functions are stated without definitions. This section aims to lay out clear definitions for some of these.

A.1.1 2D Convolution

The convolution between two continuously valued functions, $f(x, y)$ and, $g(x, y)$ is given by [263]:

$$f(x, y) \ * \ g(x, y) = \int_{-\infty}^{\infty} \int_{-\infty}^{\infty} f(s_1, s_2) g(x - s_1, y - s_2) ds_1 ds_2 \, . \tag{A.1}$$

Here, s_1 and s_2 are dummy variables that shift the function $g(-x, -y)$.

For a digital image, $\mathrm{Im}(x, y)$, a discrete summation with a convolution matrix, $K(x, y)$, is used instead of an integral: [164]

$$\mathrm{Im}(x, y) \ * \ K(x, y) = \sum_{i=-m}^{m} \sum_{j=-n}^{n} \mathrm{Im}(m, n) K(x - m, y - n) \, . \tag{A.2}$$

i and j are equivalent to s_1 and s_2 in Eq. A.1, and are defined along $-m \leq i \leq m$ and $-n \leq j \leq n$, respectively.

A.1.2 The error function

The error function is used to calculate the definite integral of a Gaussian function and is defined as: [264]

$$\mathrm{erf}(x) = \frac{2}{\sqrt{\pi}} \int_0^x \exp(-t^2) dt \, . \tag{A.3}$$

A.1.3 Derivation of Equation 2.23

The equation described in Theory: 2.23 is a more useful way to calculate the Fisher information matrix compared to Eq. 2.22 since the partial derivatives with respect to $\boldsymbol{\theta}$ are described in the literature [127, 265]. A derivation of Eq. 2.23 from Eq. 2.22 is given here.

The Fisher information matrix, restated from Eq. 2.22, is given as:

$$\mathbf{I}_{ij}(\boldsymbol{\theta}) = \mathrm{E}\left[\frac{\partial \ln\left[\mathcal{L}(\mathrm{Im}(x,y) \mid \boldsymbol{\theta})\right]}{\partial \boldsymbol{\theta}_i} \cdot \frac{\partial \ln\left[\mathcal{L}(\mathrm{Im}(x,y) \mid \boldsymbol{\theta})\right]}{\partial \boldsymbol{\theta}_j}\right],\ i,j \in \{1,2,\dots n\}\,. \tag{A.4}$$

The log-likelihood, $\ln\left[\mathcal{L}(\mathrm{Im}(x,y) \mid \boldsymbol{\theta})\right]$, with minor modifications from Eq. 2.20 is given as:

$$\ln\left[\mathcal{L}(\mathrm{Im}(x,y) \mid \boldsymbol{\theta})\right] = \sum_{x,y\,\in\,\mathrm{Im}} \mathrm{Im}(x,y) \ln\left[\mathrm{PSF}(x,y,\boldsymbol{\theta})\right] - \mathrm{PSF}(x,y,\boldsymbol{\theta}). \tag{A.5}$$

The modification from $\mathrm{PSF}(x,y|\boldsymbol{\theta})$ to $\mathrm{PSF}(x,y,\boldsymbol{\theta})$ reflects the use of values of $\boldsymbol{\theta}$ wherein best estimates have already been determined through maximimum likelihood estimation.

The partial derivative of Eq. A.5 with respect to $\boldsymbol{\theta}_i$ is given by:

$$\frac{\partial \ln\left[\mathcal{L}(\mathrm{Im} \mid \boldsymbol{\theta})\right]}{\partial \boldsymbol{\theta}_i} = \sum \frac{\partial \mathrm{PSF}}{\partial \boldsymbol{\theta}_i}\left(\frac{\mathrm{Im}}{\mathrm{PSF}} - 1\right), \tag{A.6}$$

with explicit dependence on $x, y, \boldsymbol{\theta}$ removed for clarity. Similarly, the partial derivative with respect to $\boldsymbol{\theta}_j$ is given by:

$$\frac{\partial \ln\left[\mathcal{L}(\mathrm{Im} \mid \boldsymbol{\theta})\right]}{\partial \boldsymbol{\theta}_j} = \sum \frac{\partial \mathrm{PSF}}{\partial \boldsymbol{\theta}_j}\left(\frac{\mathrm{Im}}{\mathrm{PSF}} - 1\right). \tag{A.7}$$

Substituting Eq. A.6 and Eq. A.7 into Eq. A.4 leads to:

$$\mathbf{I}_{ij}(\boldsymbol{\theta}) = \mathrm{E}\left[\sum \left(\frac{\mathrm{Im}^2}{\mathrm{PSF}^2} - 2\frac{\mathrm{Im}}{\mathrm{PSF}} + 1\right)\frac{\partial \mathrm{PSF}}{\partial \boldsymbol{\theta}_i}\frac{\partial \mathrm{PSF}}{\partial \boldsymbol{\theta}_j}\right]. \tag{A.8}$$

From Eq. A.8, a factor of $\frac{1}{\mathrm{PSF}^2}$ can be pulled out from the term in round brackets, followed by factoring, leading to:

$$\mathbf{I}_{ij}(\boldsymbol{\theta}) = \mathrm{E}\left[\sum (\mathrm{Im} - \mathrm{PSF})^2 \frac{1}{\mathrm{PSF}^2}\frac{\partial \mathrm{PSF}}{\partial \boldsymbol{\theta}_i}\frac{\partial \mathrm{PSF}}{\partial \boldsymbol{\theta}_j}\right]. \tag{A.9}$$

Using the fact that the PSF is the expected value of the Poissonian model of photon

detection (Theory: 2.15), and that the variance for a Poisson distribution is defined as:

$$\mathrm{Var}(\mathrm{Im}) = \mathrm{E}[(\mathrm{Im} - \mathrm{PSF})^2] = \mathrm{PSF}\,, \tag{A.10}$$

the Fisher information matrix can be written as:

$$\mathbf{I}_{ij}(\boldsymbol{\theta}) = \sum_{x,y\,\in\,\mathrm{Im}} \frac{1}{\mathrm{PSF}(x,y,\boldsymbol{\theta})} \frac{\partial\,\mathrm{PSF}(x,y,\boldsymbol{\theta})}{\partial \boldsymbol{\theta}_i} \frac{\partial\,\mathrm{PSF}(x,y,\boldsymbol{\theta})}{\partial \boldsymbol{\theta}_j}\,. \tag{A.11}$$

With the dependence of PSF on $x, y, \boldsymbol{\theta}$ added back in, this equation is the same as that of Theory: Eq. 2.23.

A.1.4 2D Fourier transform

The 2D Fourier transform, $F(u,v)$ of a 2D function, $f(x,y)$, is given by: [263]

$$F(u,v) = \int_{-\infty}^{\infty}\int_{-\infty}^{\infty} f(x,y)\exp\left[-2\pi i(ux+vy)\right]dxdy\,. \tag{A.12}$$

For the discrete 2D Fourier transform, which is used for the Fourier transforms of images in this work, u and v are defined along $0 \leq u \leq M-1$ and $0 \leq v \leq N-1$, respectively. The formula is given as: [143]

$$F(u,v) = \sum_{x=0}^{M-1}\sum_{y=0}^{N-1} f(x,y)\exp\left[-2\pi i\left(\frac{ux}{M}+\frac{vy}{N}\right)\right]. \tag{A.13}$$

A.2 Supplementary information for Chapter 3

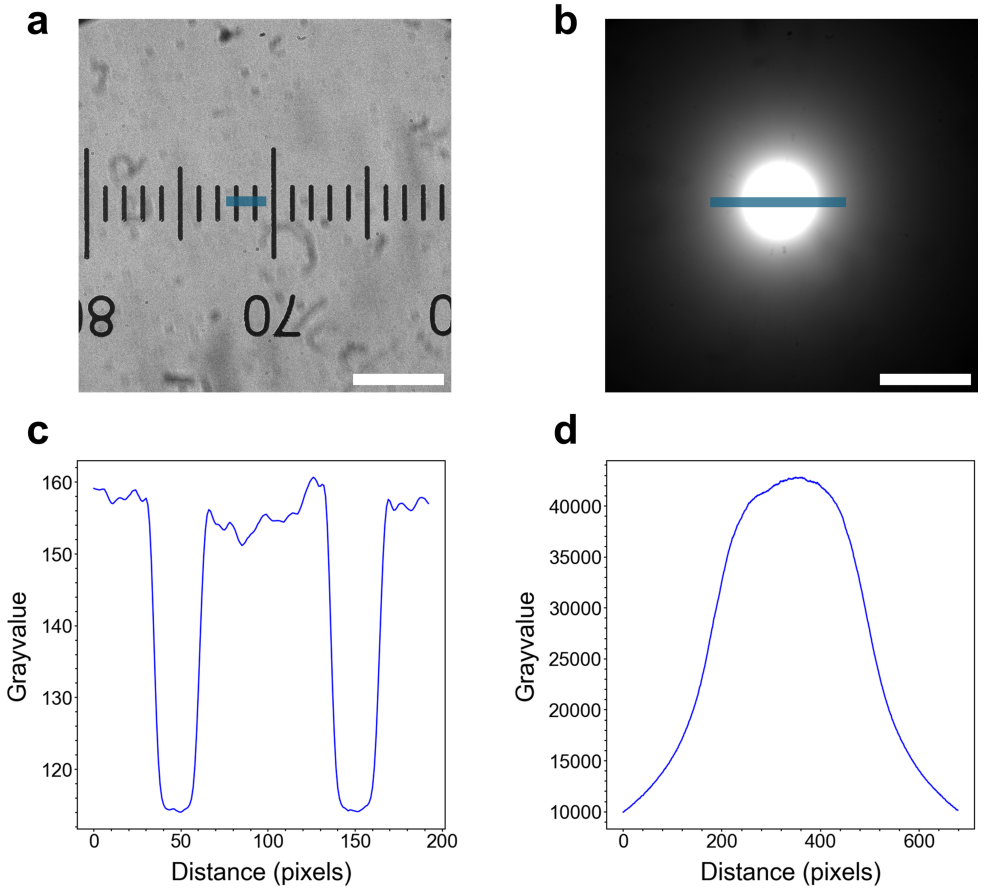

Fig. A.1: **ROCS microscope measurements of the FOI and pixel resolution. a** Brightfield image of a patterned microscope slide (Psyer Optics, S8) where the length between two graticules is 10 µm. A blue line denotes the area over which the pixel resolution was measured. The length of the scale bar is 200 pixels. **b** Widefield image of the FOI using a camera exposure time of 3 ms and a power density of 20 W/cm^2. The blue line denotes the area over which the FOI was measured. Scale bar: 200 pixels. **c** Plot of intensity against distance for the blue line shown in **a**. Zero on the x-axis denotes the furthest left of the line. **d** Plot of intensity against the distance for the FOI shown in **b**. Zero on the x-axis denotes the furthest left of the line.

A.3 Supplementary information for Chapter 4

This section contains figures that were too lengthy for Chapter 4. The information provided here does not change the conclusions of the chapter.

A.3.1 Additional drift trajectory plots

The remaining drift trajectory plots for the two remaining STORM experimental repeats are shown here. For microtubules:

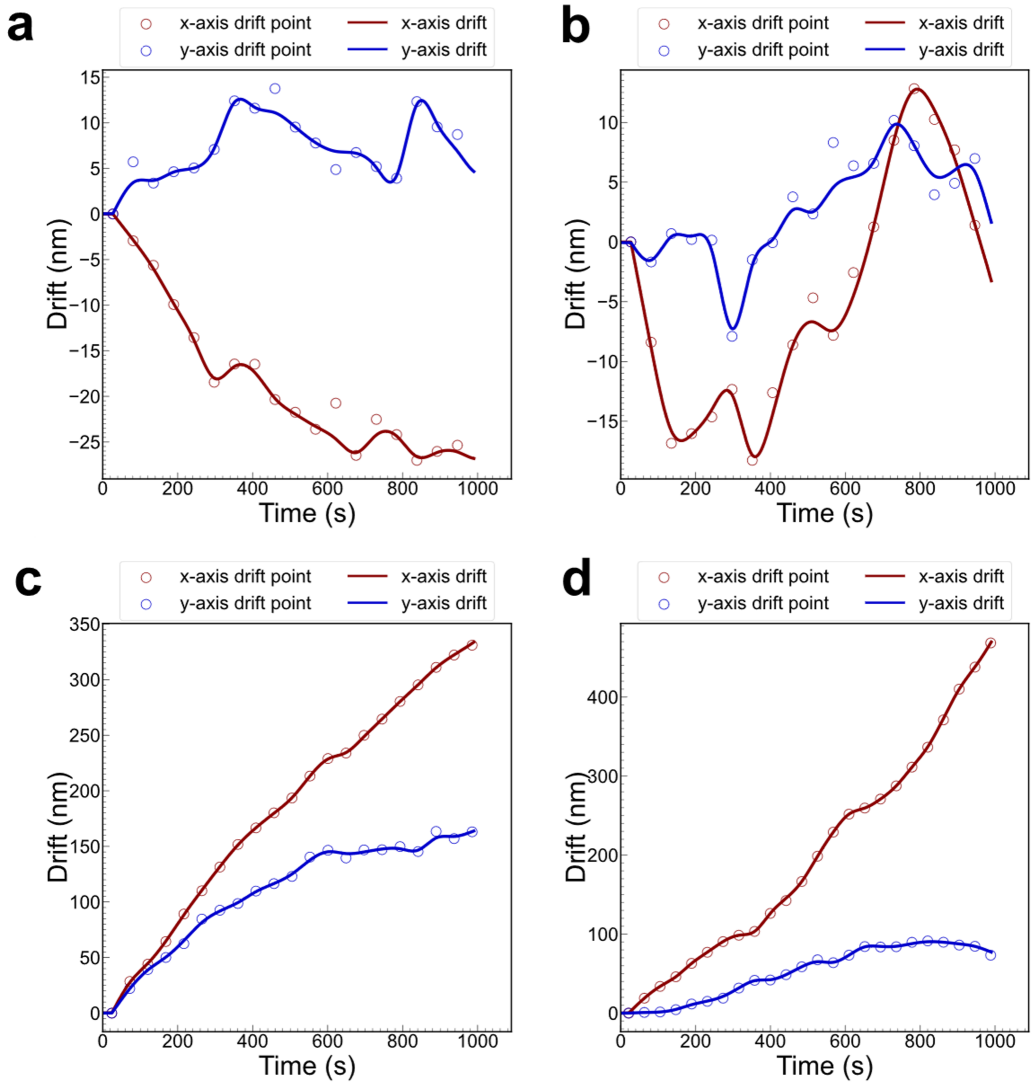

Fig. A.2: **Drift trajectories of the second and third image sequences from STORM of microtubules in Chapter 4 using the ROCS microscope and commercial microscope.** The format of the plots are the same as those in Fig. 4.7. The mean drifts are given in Fig. 4.7**c** (ROCS microscope) and Fig. 4.7**d** (commercial microscope). **a**–**b** Drift trajectories of the second repeat and third repeat, respectively, using the ROCS microscope. **c**–**d** Drift trajectory of the second and third repeats, respectively, using the commercial microscope.

The drift trajectories for the NPC image sequences are:

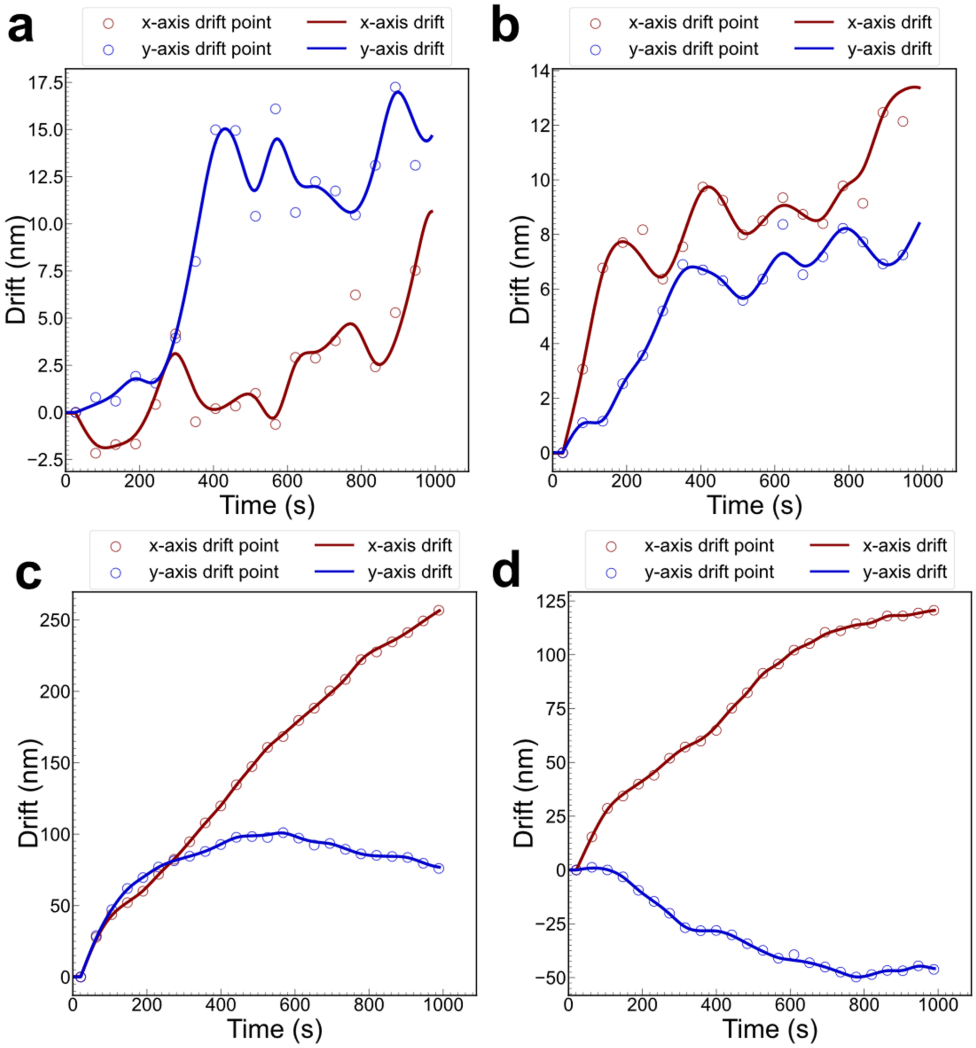

Fig. A.3: **Drift trajectories of the second and third image sequences from STORM of NPCs in Chapter 4 using the ROCS microscope and commercial microscope.** The format of the plots are the same as those in Fig. 4.7. The mean drifts are given in Fig. 4.11**c** (ROCS microscope) and Fig. 4.11**d** (commercial microscope). **a**–**b** Drift trajectories of the second repeat and third repeat, respectively, using the ROCS microscope. **c**–**d** Drift trajectory of the second and third repeats, respectively, using the commercial microscope.

A.3.2 STORM images of remaining datasets

The super-resolution images from only the first image sequence were shown for Figs. 4.7, 4.8, 4.11, and 4.12. The remaining images for microtubules and NPCs, with the ROCS and the commercial microscope, are shown here.

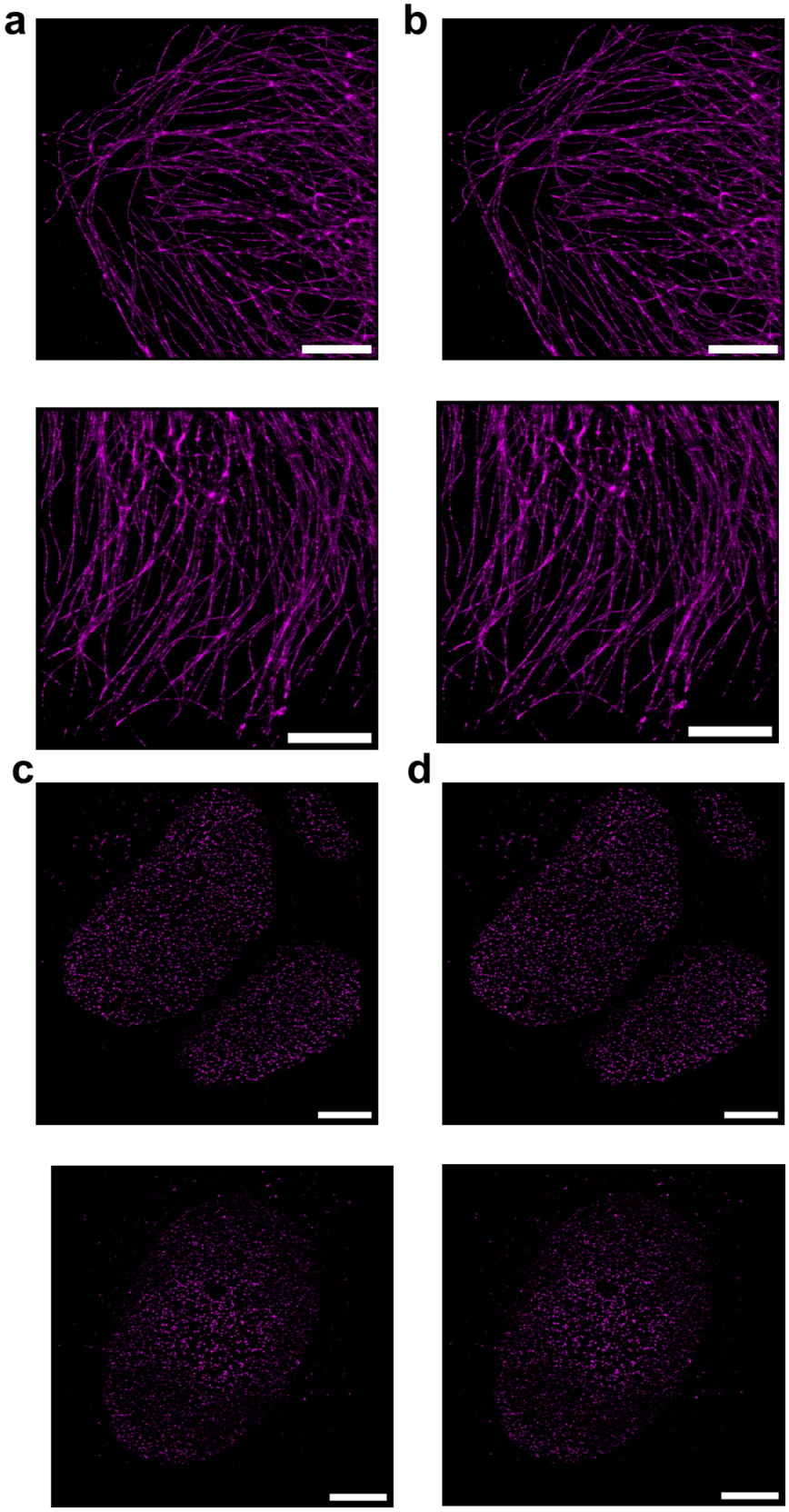

Fig. A.4: **Super-resolution images of the second and third datasets of microtubules and NPCs acquired with the ROCS microscope.** Scale bars: 5 µm. **a** Microtubule datasets 2 (top) and 3 (bottom) without drift correction. **b** Same order as **a**, with drift correction. **c** NPCs without drift correction. **d** NPCs with drift correction.

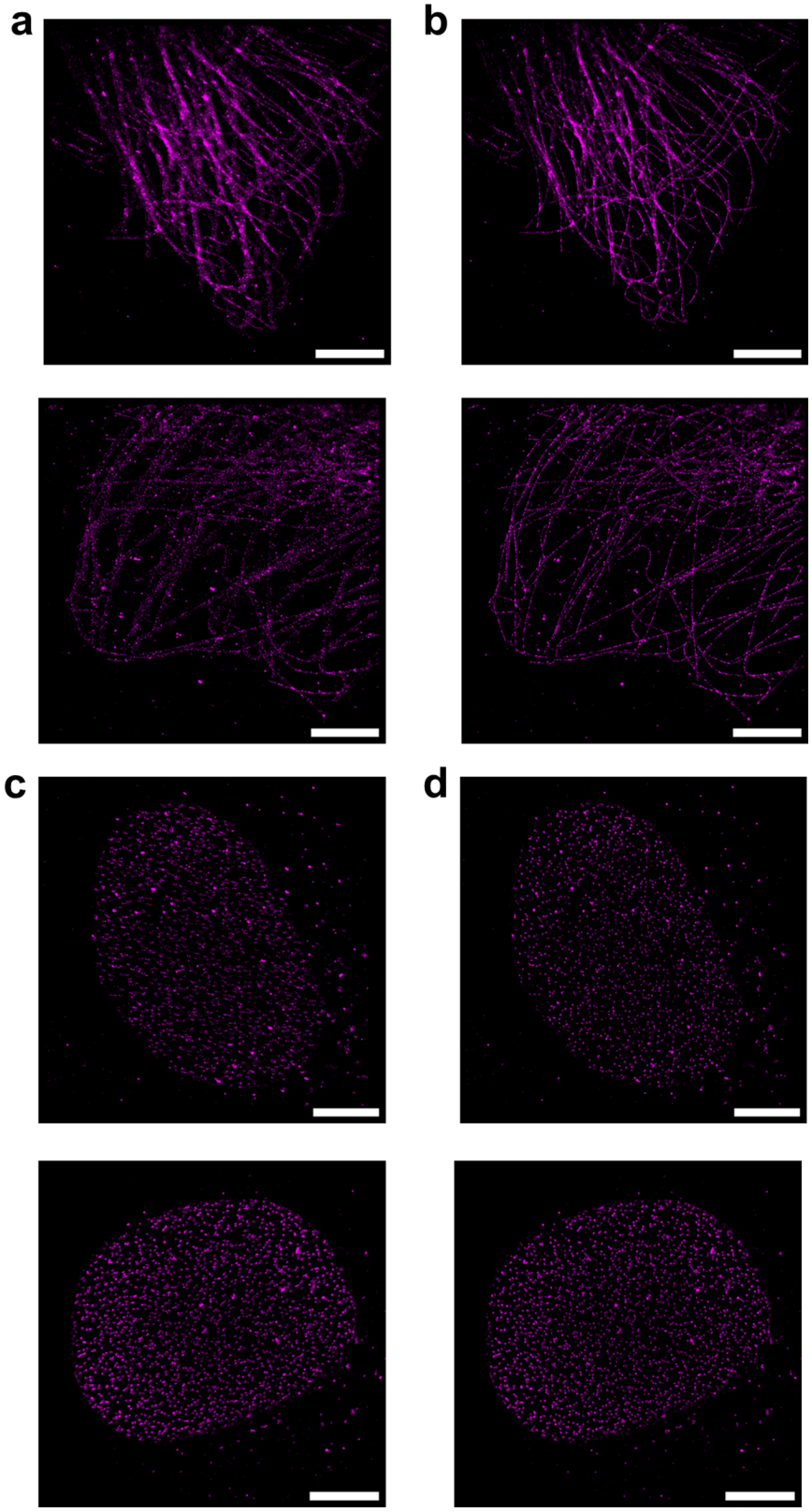

Fig. A.5: **Super-resolution images of the second and third datasets of microtubules and NPCs acquired with the commercial microscope (Zeiss, Elyra PS.1).** Scale bars: 5 µm. **a** Microtubule datasets 2 (top) and 3 (bottom) without drift correction. **b** Same order as **a**, with drift correction. **c** NPCs without drift correction. **d** NPCs with drift correction.

A.4 Supplementary information for Chapter 5

The reconstructions from the second dataset of STORM imaging of NPCs, with and without mirror-enhancement, are shown here.

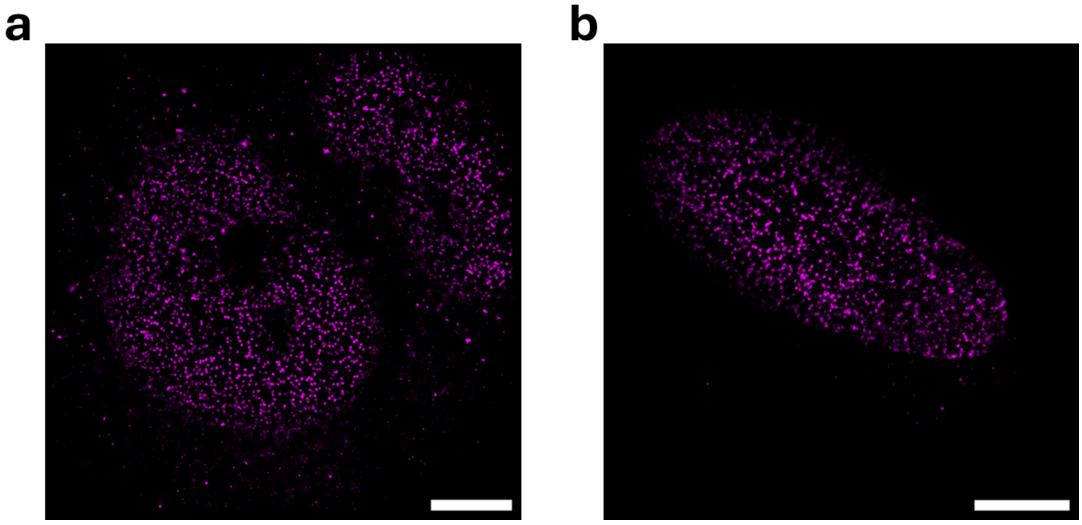

Fig. A.6: **Reconstructions from the second dataset of STORM imaging of NPCs.** Scale bars: 5 µm. **a** Reconstruction without mirror-enhancement. **b** Reconstruction with mirror-enhancement.

A.5 Supplementary information for Chapter 6

This section contains the DNA sequences of VB3, VB6, the anti-GFP nanobody, and the SNAP-tag. All sequences are listed from 5' to 3'.

VB3:

CAGGTTCAGCTGGTTGAATCTGGTGGTGGTTCTGTTCAGGCGGGTGACT
CTCTGCGTCTGTCTTGCGCGGCGTCTGGTAACACCTTCTCTATCAAAGT
TATGGGTTGGTACCGTCAGGCGCCGGGTAAACAGCGTGAACTGGTTGCG
GTTTCTACCAACTCTGGTGCGTCTGTTAACTACGCGAACTCTGTTAAAG
GTCGTTTCACCATCTCTATCGACTCTGTTAAAAAAACCACCTACCTGCA
GATGAACTCTCTGAAACCGGAAGACACCGCGGTTTACTTCTGCAACGCG
TACGACGGTCGTTACGAAGACTACTACGGTCAGGGTACCCAGGTTACCGTTTCT

VB6:

CAGGTTCAGCTGGTTGAATCTGGTGGTGGTCTGGTTCAGTCTGGTGGTT
CTCTGACCCTGACCTGCGCGGCGTCTGGTTTCACCTTCTCTGCGGCGTC
TATGCGTTGGGTTCGTCAGGTTCCGGGTAAAGGTCTGGAATGGGTTGCG
ACCATCGACGGTACCGGTGCGAACTCTTACTACTCTGAATCTGCGAAAG
GTCGTTTCACCATCTCTCGTGACAACGCGCGTAACACCCTGCGTCTGCA
GATGAACAACCTGAAACCGGACGACACCGCGGTTTACTACTGCGCGAAC
TTCGGTCGTAACTACTGGGGTAAAGGTACCCAGGTTACCGTTTCT

SNAP-tag

TCAGGCGACAAGGACTGCGAAATGAAGCGTACTACTCTGGATAGCCCGC
TTGGTAAGTTGGAGCTGTCCGGCTGCGAGCAAGGGCTTCATGAGATCAA
ATTGTTGGGTAAGGGTACAAGTGCTGCGGACGCTGTAGAAGTCCCTGCA
CCCGCCGCTGTGCTTGGAGGTCCCGAACCTTTAATGCAGGCGACCGCCT
GGCTGAACGCCTACTTTCATCAGCCGGAGGCTATCGAAGAATTTCCCGT
CCCGGCTCTGCACCACCCTGTGTTTCAACAAGAAAGTTTTACTCGTCAG
GTCCTGTGGAAACTGCTTAAGGTAGTTAAATTTGGAGAGGTAATCTCGT
ATCAACAGTTAGCGGCCTTAGCTGGCAACCCGGCAGCCACAGCAGCTGT
AAAAACGGCGCTGTCTGGAAACCCTGTGCCAATTCTTATTCCTTGTCAT
CGTGTTGTATCAAGTTCAGGTGCTGTGGGCGGCTACGAAGGAGGATTAG
CCGTAAAGGAATGGTTATTGGCGCACGAGGGGCACCGTCTTGGAAAGCCGGGTTTGGGT

Anti-GFP nanobody

GTACAGTTAGTTGAATCTGGTGGCGCTTTAGTACAGCCTGGTGGGTCCT
TACGCCTGAGTTGTGCTGCTTCGGGGTTCCCGGTTAATCGCTACAGCAT
GCGCTGGTATCGTCAAGCGCCTGGAAAAGAACGTGAATGGGTAGCCGGG
ATGTCGAGTGCCGGTGATCGCAGTAGCTACGAGGACTCCGTCAAAGGGC
GTTTCACCATTTCTCGCGACGACGCTCGTAACACTGTGTACTTGCAAAT
GAACAGCCTGAAACCCGAAGACACAGCAGTCTACTACTGTAATGTAAAT
GTAGGATTCGAGTACTGGGGCCAGGGAACGCAGGTAACGGTTTCGTCC

A.6 Supplementary information for Chapter 7

The reconstructions for the remaining datasets are shown here.

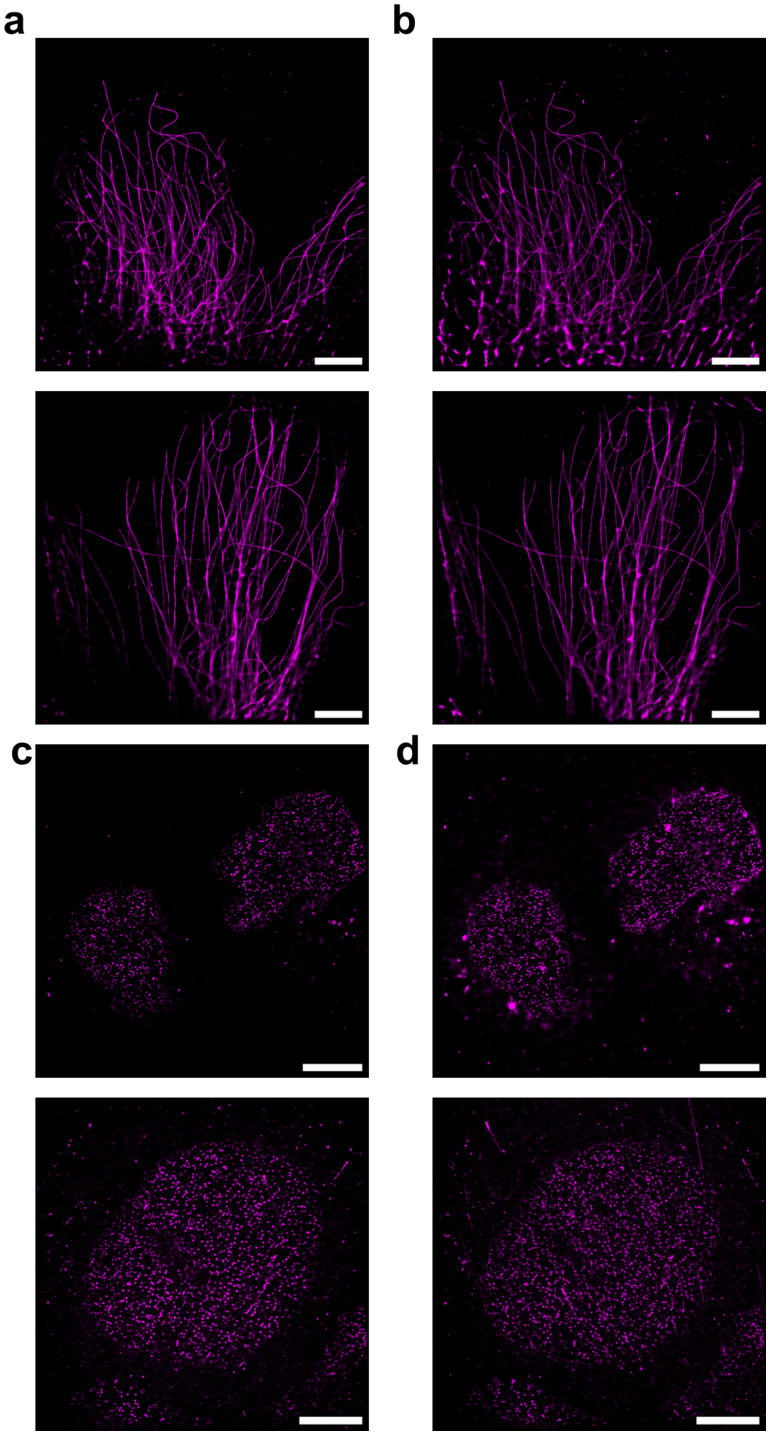

Fig. A.7: **Super-resolution images of the remaining datasets of microtubules and NPCs with and without denoising** Scale bars: 5 µm. **a** Microtubule datasets 2 (top) and 3 (bottom) without denoising. **b** Same order as **a**, following denoising. **c** NPC datasets 1 (top) and 3 (bottom) without denoising. **d** Same order as **c**, after denoising

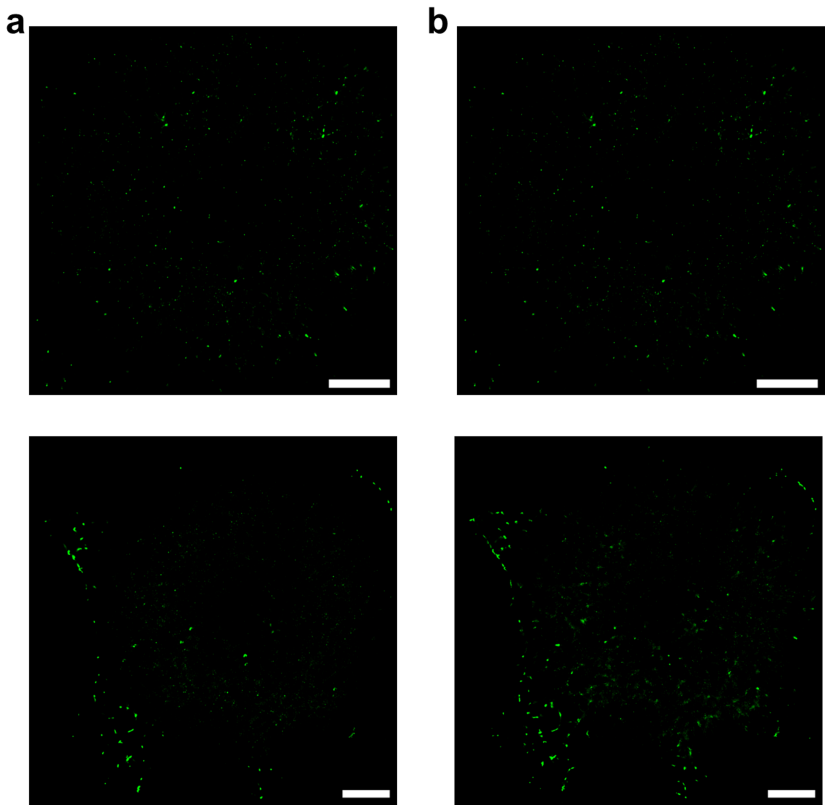

Fig. A.8: **Super-resolution images of the remaining datasets of ACE-2 receptor with and without denoising.** Scale bars: 5 µm. **a** ACE-2 receptor datasets 2 (top) and 3 (bottom) without denoising. **b** Same order as **a**, following denoising.

A.7 Supplementary information for Chapter 8

This section contains the sequences of ACE-2 receptor, and the SARS-CoV-2 spike protein used in the chapter. The STORM images of the negative control with and without denoising are also included.

ACE-2 receptor

ATGTCAAGCTCTTCCTGGCTCCTTCTCAGCCTTGTTGCTGTAACTGCTG
CTCAGTCCACCATTGAGGAACAGGCCAAGACATTTTTGGACAAGTTTAA
CCACGAAGCCGAAGACCTGTTCTATCAAAGTTCACTTGCTTCTTGGAAT
TATAACACCAATATTACTGAAGAGAATGTCCAAAACATGAATAATGCTG
GGGACAAATGGTCTGCCTTTTTAAAGGAACAGTCCACACTTGCCCAAAT
GTATCCACTACAAGAAATTCAGAATCTCACAGTCAAGCTTCAGCTGCAG
GCTCTTCAGCAAAATGGGTCTTCAGTGCTCTCAGAAGACAAGAGCAAAC
GGTTGAACACAATTCTAAATACAATGAGCACCATCTACAGTACTGGAAA
AGTTTGTAACCCAGATAATCCACAAGAATGCTTATTACTTGAACCAGGT
TTGAATGAAATAATGGCAAACAGTTTAGACTACAATGAGAGGCTCTGGG
CTTGGGAAAGCTGGAGATCTGAGGTCGGCAAGCAGCTGAGGCCATTATA
TGAAGAGTATGTGGTCTTGAAAAATGAGATGGCAAGAGCAAATCATTAT
GAGGACTATGGGGATTATTGGAGAGGAGACTATGAAGTAAATGGGGTAG
ATGGCTATGACTACAGCCGCGGCCAGTTGATTGAAGATGTGGAACATAC
CTTTGAAGAGATTAAACCATTATATGAACATCTTCATGCCTATGTGAGG
GCAAAGTTGATGAATGCCTATCCTTCCTATATCAGTCCAATTGGATGCC
TCCCTGCTCATTTGCTTGGTGATATGTGGGGTAGATTTTGGACAAATCT
GTACTCTTTGACAGTTCCCTTTGGACAGAAACCAAACATAGATGTTACT
GATGCAATGGTGGACCAGGCCTGGGATGCACAGAGAATATTCAAGGAGG
CCGAGAAGTTCTTTGTATCTGTTGGTCTTCCTAATATGACTCAAGGATT
CTGGGAAAATTCCATGCTAACGGACCCAGGAAATGTTCAGAAAGCAGTC
TGCCATCCCACAGCTTGGGACCTGGGGAAGGGCGACTTCAGGATCCTTA
TGTGCACAAAGGTGACAATGGACGACTTCCTGACAGCTCATCATGAGAT
GGGGCATATCCAGTATGATATGGCATATGCTGCACAACCTTTTCTGCTA
AGAAATGGAGCTAATGAAGGATTCCATGAAGCTGTTGGGGAAATCATGT
CACTTTCTGCAGCCACACCTAAGCATTTAAAATCCATTGGTCTTCTGTC
ACCCGATTTTCAAGAAGACAATGAAACAGAAATAAACTTCCTGCTCAAA
CAAGCACTCACGATTGTTGGGACTCTGCCATTTACTTACATGTTAGAGA
AGTGGAGGTGGATGGTCTTTAAAGGGGAAATTCCCAAAGACCAGTGGAT
GAAAAAGTGGTGGGAGATGAAGCGAGAGATAGTTGGGGTGGTGGAACCT
GTGCCCCATGATGAAACATACTGTGACCCCGCATCTCTGTTCCATGTTT

CTAATGATTACTCATTCATTCGATATTACACAAGGACCCTTTACCAATT
CCAGTTTCAAGAAGCACTTTGTCAAGCAGCTAAACATGAAGGCCCTCTG
CACAAATGTGACATCTCAAACTCTACAGAAGCTGGACAGAAACTGTTCA
ATATGCTGAGGCTTGGAAAATCAGAACCCTGGACCCTAGCATTGGAAAA
TGTTGTAGGAGCAAAGAACATGAATGTAAGGCCACTGCTCAACTACTTT
GAGCCCTTATTTACCTGGCTGAAAGACCAGAACAAGAATTCTTTTGTGG
GATGGAGTACCGACTGGAGTCCATATGCAGACCAAAGCATCAAAGTGAG
GATAAGCCTAAAATCAGCTCTTGGAGATAAAGCATATGAATGGAACGAC
AATGAAATGTACCTGTTCCGATCATCTGTTGCATATGCTATGAGGCAGT
ACTTTTTAAAAGTAAAAAATCAGATGATTCTTTTTGGGGAGGAGGATGT
GCGAGTGGCTAATTTGAAACCAAGAATCTCCTTTAATTTCTTTGTCACT
GCACCTAAAAATGTGTCTGATATCATTCCTAGAACTGAAGTTGAAAAGG
CCATCAGGATGTCCCGGAGCCGTATCAATGATGCTTTCCGTCTGAATGA
CAACAGCCTAGAGTTTCTGGGGATACAGCCAACACTTGGACCTCCTAAC
CAGCCCCCTGTTTCCATATGGCTGATTGTTTTTGGAGTTGTGATGGGAG
TGATAGTGGTTGGCATTGTCATCCTGATCTTCACTGGGATCAGAGATCG
GAAGAAGAAAAATAAAGCAAGAAGTGGAGAAAATCCTTATGCCTCCATC
GATATTAGCAAAGGAGAAAATAATCCAGGATTCCAAAACACTGATGATG
TTCAGACCTCCTTT

SARS-CoV-2 spike protein

ATGTTCGTGTTCCTGGTGCTGCTGCCTCTGGTGAGCAGCCAGTGCGTGA
ATCTGACCACCAGAACCCAGCTGCCTCCTGCCTACACCAATAGCTTCAC
CAGAGGAGTTTATTATCCCGATAAGGTGTTCAGAAGTAGTGTATTACAT
AGTACCCAGGACCTGTTCCTACCTTTCTTCAGTAACGTGACCTGGTTCC
ACGCCATCCACGTGAGCGGCACCAATGGCACCAAGAGATTCGACAATCC
TGTGCTGCCTTTCAATGACGGCGTGTACTTCGCCAGCACCGAGAAGAGC
AATATCATCAGAGGCTGGATCTTCGGCACCACCTTGGATTCCAAGACTC
AGAGCCTGCTGATTGTAAACAACGCTACAAATGTGGTGATCAAGGTGTG
CGAGTTCCAGTTCTGCAATGACCCTTTCCTGGGTGTTTATTATCATAAG
AACAACAAGAGCTGGATGGAGAGCGAGTTCCGCGTATATTCGTCGGCTA
ATAATTGCACCTTCGAGTACGTGAGCCAGCCTTTCCTGATGGACCTGGA
GGGCAAGCAGGGCAATTTCAAGAATCTGAGAGAGTTCGTGTTCAAGAAT
ATCGACGGCTACTTCAAGATCTACAGCAAGCACACACCCATTAATCTGG
TGAGAGACCTGCCTCAGGGCTTCAGCGCCCTGGAGCCTCTGGTGGACCT

GCCTATCGGCATCAATATCACCAGATTCCAGACCCTGCTGGCCCTGCAC

AGATCATATCTTACACCAGGCGATTCGTCAAGCGGTTGGACCGCTGGAG

CTGCGGCATATTACGTGGGCTACCTGCAGCCTAGAACCTTCCTGCTGAA

GTACAATGAGAATGGTACGATAACCGACGCAGTTGATTGTGCCCTGGAC

CCTCTGAGCGAGACCAAGTGCACCCTGAAGAGCTTCACCGTGGAGAAGG

GCATCTACCAGACCAGCAATTTCAGAGTGCAGCCTACCGAGAGCATCGT

GAGATTCCCTAATATCACCAATCTGTGCCCTTTCGGCGAGGTGTTCAAT

GCCACCAGATTCGCCAGCGTGTACGCATGGAACCGCAAGCGGATAAGCA

ATTGCGTGGCCGACTACAGCGTGCTGTACAATAGCGCCAGCTTCAGCAC

CTTCAAATGTTATGGTGTTTCGCCAACAAAGCTGAATGACCTGTGCTTC

ACCAATGTGTACGCCGACAGCTTCGTGATCAGAGGCGACGAGGTGAGAC

AGATCGCGCCAGGGCAGACCGGCAAGATCGCCGACTACAATTACAAGCT

GCCTGACGACTTCACCGGCTGCGTGATCGCGTGGAACTCTAACAATCTA

GATTCGAAAGTTGGAGGCAATTACAATTACCTGTACAGACTGTTCAGAA

AGAGCAATCTGAAGCCTTTCGAGAGAGACATCAGCACCGAGATCTACCA

GGCCGGCAGCACACCGTGTAATGGCGTGGAGGGCTTCAATTGCTACTTC

CCTCTGCAGAGCTACGGCTTCCAGCCTACCAATGGCGTGGGCTACCAGC

CTTACAGAGTGGTGGTGCTGAGCTTCGAGCTGCTGCACGCTCCCGCTAC

CGTGTGCGGCCCTAAGAAGAGCACCAATCTGGTGAAGAATAAGTGCGTG

AATTTCAATTTCAATGGTCTAACTGGAACGGGCGTGCTGACCGAGAGCA

ATAAGAAGTTTCTTCCCTTTCAACAATTCGGCAGAGACATCGCCGACAC

CACAGATGCTGTAAGAGACCCTCAGACCCTGGAGATCCTGGACATCACT

CCGTGTAGCTTCGGCGGCGTGAGCGTGATCACACCGGGTACCAATACCA

GCAATCAGGTGGCCGTGCTGTACCAGGACGTGAATTGCACCGAGGTGCC

TGTGGCCATCCACGCCGACCAGCTGACTCCCACTTGGAGGGTATATTCC

ACGGGAAGCAATGTGTTCCAGACCAGAGCCGGCTGCCTGATCGGCGCCG

AGCACGTGAATAATAGCTACGAGTGCGACATCCCTATCGGCGCCGGCAT

CTGCGCCAGCTACCAGACCCAGACCAATAGCCCTGGAAGCGCCAGCAGC

GTGGCCAGCCAGAGCATCATCGCCTACACCATGAGCCTGGGCGCCGAGA

ATAGCGTGGCCTACAGCAATAATAGCATCGCCATCCCTACCAATTTCAC

CATCAGCGTGACCACCGAAATATTACCAGTCTCCATGACCAAGACCAGC

GTGGACTGCACCATGTACATCTGCGGCGACAGCACCGAGTGCAGCAATC

TGCTGCTGCAGTACGGCAGCTTCTGCACCCAGCTGAATAGAGCCCTGAC

CGGCATCGCCGTGGAGCAGGACAAGAATACCCAGGAGGTGTTCGCCCAG

GTGAAGCAGATCTACAAGACTCCGCCGATCAAGGACTTCGGCGGCTTCA

ATTTCAGCCAAATACTCCCAGATCCAAGCAAGCCTAGCAAGAGGAGCTT

CATCGAGGACCTGCTGTTCAATAAGGTGACCCTGGCCGACGCCGGCTTC

ATCAAGCAGTACGGCGACTGCCTAGGTGATATTGCGGCAAGAGACCTGA

TCTGCGCCCAGAAGTTTAACGGTTTGACAGTACTACCTCCTCTGCTGAC

CGACGAGATGATAGCACAATATACGTCGGCATTGCTCGCTGGCACGATC

ACATCGGGCTGGACTTTCGGCGCCGGAGCAGCGTTGCAAATCCCTTTCG

CCATGCAGATGGCCTACAGATTCAATGGCATCGGCGTGACCCAGAATGT

GCTGTACGAGAATCAGAAGCTGATCGCCAATCAGTTCAATAGCGCCATC

GGCAAGATCCAGGACAGCCTGAGCAGCACCGCCAGCGCCCTGGGCAAGC

TGCAGGACGTGGTGAATCAGAATGCCCAGGCCCTGAATACCCTGGTGAA

GCAGCTGAGCAGCAATTTCGGCGCCATCAGTAGTGTACTCAACGATATC

CTGAGCAGACTGGACCCGCCAGAGGCCGAGGTGCAAATTGATCGTCTTA

TTACTGGCAGACTGCAGAGCCTGCAGACCTACGTGACCCAGCAGCTGAT

CAGAGCCGCCGAGATCAGAGCCAGCGCCAATCTGGCCGCCACCAAGATG

AGCGAGTGCGTGCTGGGCCAGAGCAAGAGAGTGGACTTCTGCGGCAAGG

GCTACCACCTGATGAGCTTCCCTCAGAGCGCTCCACATGGCGTGGTGTT

CCTGCACGTGACCTACGTGCCTGCCCAGGAGAAGAATTTCACCACCGCA

CCCGCAATCTGCCACGACGGCAAGGCCCACTTCCCTAGAGAGGGCGTGT

TCGTGAGCAATGGCACCCACTGGTTCGTGACCCAGAGAAATTTCTACGA

GCCTCAGATCATCACCACCGACAATACCTTCGTGAGCGGCAATTGCGAC

GTGGTGATCGGGATAGTCAATAATACTGTCTACGACCCTCTGCAGCCTG

AGCTGGACAGCTTCAAGGAGGAGCTGGACAAGTACTTCAAGAATCACAC

CAGCCCTGACGTGGACCTCGGTGATATTTCGGGAATCAATGCCAGCGTG

GTGAATATCCAGAAGGAAATTGATCGGCTCAACGAAGTGGCCAAGAATC

TGAATGAGAGCCTGATCGACCTGCAGGAGCTGGGCAAGTACGAGCAGGG

ATCAGGTTATATTCCTGAAGCTCCAAGAGATGGGCAAGCTTACGTTCGT

AAAGATGGCGAATGGGTATTACTTTCTACCTTTTTAAGCTTGCTGAATG

ACATATTCGAGGCCCAGAAGATTGAATGGCATGAGAAACATCACCATCA CCATCAC

A.7.1 STORM images of the negative control

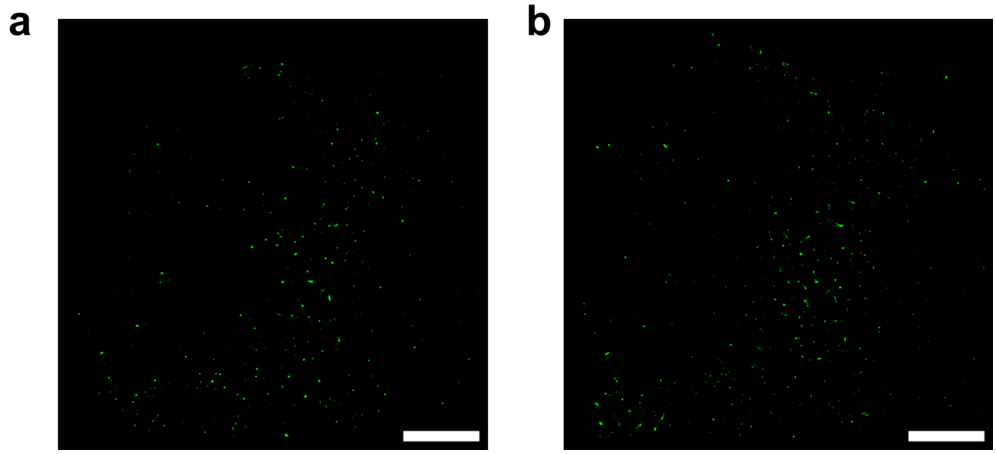

Fig. A.9: **Super-resolution images of the negative control of ACE-2-SNAP-ATTO 488.** Scale bars: 5 µm. **a** Negative control without denoising. **b** Negative control with denoising.